THE UNIVERSITY OF
WARWICK

AUTHOR: **David Collins** DEGREE: **Ph.D.**

TITLE: **X-ray Observations of Cataclysmic Variables**

DATE OF DEPOSIT: ....

I agree that this thesis shall be available in accordance with the regulations governing the University of Warwick theses.

I agree that the summary of this thesis may be submitted for publication.

I **agree** that the thesis may be photocopied (single copies for study purposes only).

Theses with no restriction on photocopying will also be made available to the British Library for microfilming. The British Library may supply copies to individuals or libraries. subject to a statement from them that the copy is supplied for non-publishing purposes. All copies supplied by the British Library will carry the following statement:

> "Attention is drawn to the fact that the copyright of this thesis rests with its author. This copy of the thesis has been supplied on the condition that anyone who consults it is understood to recognise that its copyright rests with its author and that no quotation from the thesis and no information derived from it may be published without the author's written consent."

AUTHOR'S SIGNATURE: ....

USER'S DECLARATION

1. I undertake not to quote or make use of any information from this thesis without making acknowledgement to the author.
2. I further undertake to allow no-one else to use this thesis while it is in my care.

DATE SIGNATURE ADDRESS

....

....

....

....

....

X-ray Observations of Cataclysmic Variables

by

David Collins

Thesis

Submitted to the University of Warwick

for the degree of

Doctor of Philosophy

Physics

May 2010

THE UNIVERSITY OF
WARWICK

”He who dares, wins.” - Winston Churchill

Contents

List of Tables

List of Figures

Acknowledgments

First I would like to thank my supervisor Peter Wheatley, for his help, support and guidance throughout my PhD, without whom, none of this would have been possible. I would also like to thank, Tom Marsh for his advice and support and for reading my thesis when he really did not have the time.

I would like to thank Jörn Wilms, for starting me off on the right path on my PhD. Without his numerous *RXTE* and IDL programs and various other scripts, guidance and assistance my work would have been a lot more arduous and time consuming.

I would like to give a special thanks to the people who made my PhD worth finishing, motivated me when I needed it and made difficult times in my PhD easier and enjoyable. You are all very special to me and I will not forget what you have given me: Monihar Dillon and Susana Barros, Jennifer Avila and of course my parents, brother and sister.

Declarations

I declare that the work presented in this thesis has not been submitted in any previous application for a degree at a university. The contents of this thesis represents my own work, except where references to other works are given.

Chapter 6 is based on work in preparation for publication.

Collins & Wheatley. ”The Evolution of U Gem Throughout Outburst”. *Collins & Wheatley 2010 in prep*

Chapter 7, is based on a refereed publication that was submitted during the course of my studies.

Collins & Wheatley. ”X-ray Observations of SU UMa Throughout Six Normal Outbursts”. *2010MNRAS.402.1816C*

Abstract

Cataclysmic variables are close binary systems where mass is accreted onto a white dwarf through an accretion disc. Approximately half the gravitational energy in the disc is released in a boundary layer as X-rays. X-rays originate from matter under the extreme and energetic conditions and provide a unique view of high energy processes. X-ray luminosities are sensitive to the accretion rate through the disc and to the conditions in the inner accretion zone. Accretion discs are wide spread throughout astronomy. The extraction of potential energy from accreted material is known to be the principal source of power in several types of system; quasars, galactic nuclei, binary X-ray sources, cataclysmic variables (CVs) and proto-planetary discs. CVs provide probably the best opportunity to study the accretion process in isolation.

Previous X-ray analysis of dwarf novae relied upon relatively short snap shot observations, which are unable to provide a full picture of the outburst cycle evolution. Multiple outbursts with far greater temporal accuracy and coverage than has ever been observed before are presented in this thesis. Pointed observations using the proportional counter array on the Rossi X-ray Timing Explorer of SS Cygni, U Gem and SU UMa are analysed.

The behaviour in the optical band is similar for the three systems in this thesis, however, a large distinction is seen in the X-ray band. The hard X-ray outburst flux in SS Cygni and SU UMa are quenched below the quiescent flux, while in U Gem it is unusually faint in quiescence brightening in outburst. The hard quiescent X-ray spectrum is replaced by an intense soft X-ray component in outburst for all dwarf novae. Analysis of U Gem suggests that X-rays originate from the inner accretion disc with a scale height not much greater than the disc thickness.

The start of the hard X-ray outburst is delayed behind the optical rise, this delay is roughly consistent for the three systems presented. This indicates that the origin of the heating wave in the accretion disc and the time it takes to propagate to the boundary layer are similar for these systems. The hard X-ray recovery also has a range of times, with the peak occurring as the optical flux reaches quiescence suggesting the cooling front reaches the boundary layer at the same time in relation to the end of the optical outburst.

The spectra for all three systems presented in this thesis are well described by a thermal plasma model with sub-solar abundances and are consistent with higher reflection during the hard X-ray suppression. This indicates that the disc is likely to be truncated in quiescence.

SS Cygni has a wide range of quiescent accretion rates. However, the X-ray flux in SS Cygni and U Gem always increases when the boundary layer transitions from both optically thick to thin, into outburst, and optically thin to thick, out of outburst. This is surprising, the flux is expected to decrease when the critical accretion rate is reached suggesting that the critical accretion rate when the boundary layer transitions is not fixed. The quiescent X-ray flux in SU UMa decreases and, with SS Cygni, is between $2-3$ orders of magnitude higher than predictions by the disc instability model.

Chapter 1

Introduction

1.1 Accretion Discs and Dwarf Novae

Accretion is a very powerful and ubiquitous phenomenon in the universe, examples can be seen in quasars, galactic nuclei, binary X-ray sources, cataclysmic variables (CVs) and protoplanetary discs.

In binary systems, as matter is transferred from one celestial body to another it can form a disc structure. As the matter is accreted the gravitational gradient gives rise to intense frictional heating. This structure, an accretion disc, is an extremely efficient way of turning gravitational energy into thermal energy. As material in the disc falls further into the potential well of the compact object it releases energy.

CVs are a class of semi-detached binary star systems, which consist of a white dwarf, the primary star, and a low mass main sequence star, the secondary, which are gravitationally bound and in orbit around one another. Because of the proximity of the two stars in close binaries matter can be transfered from one star onto the other leading to a broad range of astronomical phenomena. A characteristic feature of CVs are their brightness fluctuations which occur over a relatively short period of time. In a typical system the brightness of the CV may rise by several magnitudes in a day and then decay after a number of days, recurring every few weeks to months.

CVs provide probably the best opportunity to study the accretion process and are particularly useful in providing observational tests of theories of accretion. Their relatively close proximity allows them to be easily observed. CVs exhibit variability over short time scales allowing astronomers to be able to directly observe mass transfer and chart the evolution of the system. When it was realised that quasars and AGN were probably powered by accretion onto a central black hole it was clear that observational studies could be carried out in the much closer CV and X-ray binary population. The study of CVs can be used to gain a better understanding of the much more energetic events taking place in AGN.

1.2 Roche Lobe Geometry and Mass Transfer

Single stars, under the influence of only one gravitational field, are nearly spherical in shape. When a second gravitational field is brought into close proximity, for example in a binary, it will distort the gravitational potential that is experienced by any test particle located nearby. The large mass and low radial extent of the compact star is such that it remains spherical. However, the much less dense companion, commonly found in CV binaries, becomes distorted as it moves closer to the compact star (Kraft, 1962). One consequence of this is tidal locking, i.e., $P_{orb} = P_{spin}$. The distorted secondary star orbits with the same side facing the compact star and these tidal effects also circularise the orbit.

The potential surfaces surrounding the two stars is known as the Roche geometry and is defined as: the region surrounding each star in a binary system, within which any material is gravitationally bound to that particular star. Close to each star the surfaces are approximately spherical and concentric. Further from the stellar system the equipotentials are approximately ellipsoidal and elongated parallel to the axis joining the stellar centres. The Roche lobes of the two stars intersect at a Lagrange point, L_1, forming a two-lobed figure-of-eight shape with a star at the centre of each lobe. The L_1 point is the saddle point through which matter can flow from the secondary into the gravitational well of the compact star. The shape of the Roche geometry is determined entirely by the mass ratio (defined as M_2/M_1, the masses of the two binary components) with the overall scale given by the binary separation.

Figure 1.1 shows the equipotential lines produced by a compact star, of mass M_1, and a secondary, of mass M_2, orbiting about their common centre of mass, CM. $L_1 - L_3$ mark points

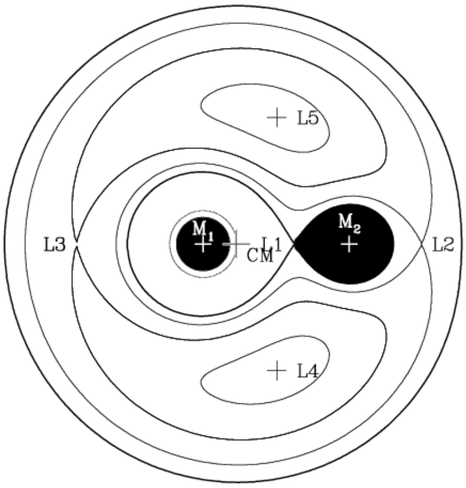

Figure 1.1: A cross section of the potential surfaces surrounding two bodies, M_1 and M_2, orbiting each other. $L_1 - L_5$ are Lagrangian points. This figure was adapted from Iben & Livio (1993).

of unstable local minima. L_4 and L_5 marks the position of the stable Lagrangian points, Coriolis forces due to the orbital motion stabilise synchronous orbits at these points. A perturbed particle will move away from the Lagrangian point, radial motions get deflected into tangential motion and tangential motion gets deflected into radial motion (relative to the global angular rotation). This causes the particle to orbit in a stable fashion about the Lagrangian point.

The potential experienced by a test particle with a position given by the vector $\mathbf{r}$ is determined by the sum of the potential of the two stars (with masses M_1 and M_2 located at r_1 and r_2) and the centrifugal force due to the rotation of the system. The potential of the system, Φ, at point $\mathbf{r}$ is approximated by (Pringle & Wade, 1985)

$$\mathbf{\Phi} = -\frac{GM_1}{|\mathbf{r} - \mathbf{r}_1|} - \frac{GM_2}{|\mathbf{r} - \mathbf{r}_2|} - \frac{1}{2}(\omega \wedge \mathbf{r})^2 \tag{1.1}$$

Where ω is the angular frequency of the orbit. A star of mass M_2 will come into contact with its Roche lobe either due to the binary separation decreasing or by swelling up due to stellar evolution. Any perturbation will cause material lying on the Roche lobe potential surface to be pushed over the L_1 point and into the potential well of the companion star, M_1, where it is eventually be captured by that star. A system like this is said to be semi-detached, and will efficiently transfer mass from M_2 to M_1 as long as M_2 remains in contact with its Roche lobe.

Since the lobes are not spherical an average radius is needed to characterise them. A suitable measure is given by the radius of a sphere containing the same volume as the lobe. An approximation is given by (Eggleton, 1983):

$$\frac{R_2}{a} = \frac{0.49q^{2/3}}{0.6q^{2/3} + ln(1 + q^{1/3})} \qquad \text{For all q} \tag{1.2}$$

The Roche lobes are defined by the binary separation, a, and the mass ratio, q, (defined as M_2/M_1), any change in these will alter the system. Any mass transferred between the pair will alter q and in the process alter the period, P, and a because of angular momentum redistribution in the system. It is important to know whether this will cause the Roche lobe of the mass losing star to shrink or expand. If the lobe shrinks it will remain in contact with the star and the resulting mass transfer will be self sustaining such that any mass transferred will cause the Roche lobe to shrink further. As more mass is transferred a runaway feedback loop is triggered resulting in unstable mass transfer. Should the lobe expand, mass transfer will be shut off unless some process is able to keep the star's surface in contact with the Roche lobe, such as angular momentum loss.

By conservation of angular momentum and mass

$$\frac{\dot{R}_2}{R_2} = \frac{2\dot{J}}{J} + \frac{2(-\dot{M}_2)}{M_2}\left(\frac{5}{6} - \frac{M_2}{M_1}\right) \tag{1.3}$$

For conservative mass transfer, i.e., setting $\dot{J} = 0$ and remembering that $\dot{M}_2 < 0$, moving mass towards the more massive star causes the Roche lobe of the secondary to expand if $q < 5/6$. More mass is placed closer to the centre of mass of the system resulting in the remaining mass moving to a wider orbit conserving angular momentum. Conversely moving matter from the more massive to the less massive star causes the Roche lobe to shrink. Changing the mass ratio will also affect the binary separation. Sustained and stable mass transfer onto the more massive white dwarf is only possible through angular momentum loss or evolution of the companion star.

1.3 Angular Momentum Loss Mechanisms

In CVs mass is transferred from the less massive secondary to the more massive white dwarf. Mass transfer in this type of system will increase the radius of orbit causing an increase in the size of the Roche lobe of the secondary star. This results in the Roche lobe detaching from the secondary causing the accretion to cease. In order for Roche lobe contact to be maintained and stable mass transfer to continue the orbital separation must decrease, which occurs through the loss of angular momentum. The following mechanisms are believed to be responsible for angular momentum loss and thus drive mass transfer:

1.3.1 Magnetic Braking

Magnetic braking is the currently favoured angular loss mechanism for close binaries with a period above 3 hours (Verbunt & Zwaan, 1981). Red dwarfs have a strong magnetic field which interacts with its stellar wind. As ionised particles, ejected in the stellar wind, flow along the magnetic field lines they are accelerated up to high speeds before being shot into space. A substantial amount of angular momentum is lost which retards the spin of the secondary star. Due to tidal forces in the binary, the secondary and its magnetic field rotate with a period locked to the orbital period of the system. This loss in angular momentum from the secondary results in angular momentum being extracted from the binary, shrinking the orbital radius as a result. The theoretical rates of mass transfer via magnetic braking are typically $10^{-9} - 10^{-8}\mathrm{M}_{\odot}\mathrm{yr}^{-1}$ (Howell et al., 2001).

The efficiency of magnetic braking is uncertain. However, following the standard scenario of magnetic braking of Verbunt & Zwaan (1981) and Rappaport et al. (1983) the angular momentum loss rate from the system due to magnetic braking, $\dot{J}_{MB}$, is given by:

$$\dot{J}_{MB} = -3.8 \times 10^{30} M_2 R_{\odot}^4 \left(\frac{R_2}{R_{\odot}}\right)^{\gamma} \left(\frac{2\pi}{P_{\rm orb}}\right)^{\gamma} \tag{1.4}$$

where γ governs the efficiency of the magnetic braking process, a value of $\gamma = 2$ is the most frequently used in CV evolution. Evolution proceeds on the orbital angular momentum loss time scale (Kolb & Stehle, 1996).

$$t_{MB} = -\frac{J}{\dot{J}_{MB}} = 2.2 \times 10^{9} \frac{M_1}{(M_1 + M_2)^{1/3}} r_2^{-4} P_d^{10/3} yr \tag{1.5}$$

1.3.2 Gravitational Braking

At short orbital periods gravitational radiation, first suggested by Kraft et al. (1962), becomes an important mechanism for sustaining the angular momentum loss. In accordance with general relativity, matter causes space to curve. The warping of space caused by the orbiting of a close binary system causes ripples to propagate in a periodic wave. As the energy needed to generate the wave is extracted from the binary orbit the two stars spiral inward. The rate of mass loss due to gravitational radiation is around $10^{-10}\mathrm{M}_{\odot}\mathrm{yr}^{-1}$ in short-period CVs (Howell et al., 2001).

The rate at which angular momentum is lost to radiation of gravitational waves, $\dot{J}_{GR}$, from Einstein's quadrupole formula is:

$$\dot{J}_{GR} = -\frac{32G^{7/3}}{5c^5} \frac{M_1^2 M_2^2}{(M_1 + M_2)^{2/3}} \left(\frac{2\pi}{P_{\mathrm{orb}}}\right)^{7/3} \tag{1.6}$$

Evolution proceeds due to gravitational braking on the orbital angular momentum loss time scale (Kolb & Stehle, 1996).

$$t_{GR} = -\frac{J}{\dot{J}_{GR}} = 3.8 \times 10^{11} \frac{(M_1 + M_2)^{1/3}}{M_1 M_2} P_d^{8/3} yr \tag{1.7}$$

Typical evolutionary time-scales for CVs to evolve from $P_{orb} \sim 10$ to ~ 3 hours via magnetic braking are $\sim 10^8$ years. Evolution takes $\sim 10^9$ years to evolve through the period gap via gravitational braking (Kolb & Stehle, 1996).

1.4 Dwarf Nova

Dwarf novae are named after their outbursts where the optical flux increases dramatically over a few days every few months; they are weakly magnetised cataclysmic variables. The most obvious characteristic giving rise to the name 'cataclysmic', is a rise in intensity by as much as several magnitudes in the space of a day or so. They stay bright for about a week before declining to quiescence. This cycle repeats on a regular basis. For a comprehensive review of

CVs see Warner (1995) and more recently Hellier (2001). In these systems the mass transfer rate from the secondary is thought to occur at a constant rate and the outbursts are thought to be triggered by a thermal-viscous instability. This instability greatly increases the accretion rate in the disc surrounding the white dwarf primary (Osaki, 1996). See Section 1.5.3 for more discussion on the disc model. It is believed that similar behaviour of many X-ray binaries is also due to this accretion disc instability (Lasota, 2001). The increased accretion onto the white dwarf both increases the luminosity and removes $\sim$ 10 per cent of material from the accretion disc allowing the system to become stable again and drop back into quiescence. Their relative brightness and proximity makes accretion discs in dwarf novae unusually accessible.

Figure 1.2 shows the American Association of Variable Star Observers, *AAVSO*, optical history of the dwarf novae SS Cygni, Z Cam and SU UMa over the past 10 years (1998 to 2008). The y axes of all plot panels have the same scale to highlight the differences in the visual magnitudes between the three objects, as well as the similarities. Peculiarities for each of the systems plotted can clearly be seen.

1.4.1 Dwarf Nova Classification

Non-magnetic cataclysmic variables are divided into several sub-classes due to the differing properties they exhibit. Many of their properties are based on their orbital periods and mass accretion rates through the disc. The first to be discovered were novae. Nova outbursts are caused by the ignition of hydrogen rich material that has accreted onto the white dwarf surface causing a thermonuclear runaway (Kraft, 1964). This gives rise to an enormous outburst 6 to 19 magnitudes in amplitude over a period of months or years. Dwarf novae outbursts, originating in an accretion disc, are not as spectacular as those of the novae but occur more regularly. Figure 1.3 shows a detailed view of the different behaviour of non-magnetic DN outbursts.

Dwarf novae are further divided into three sub-groups: U Geminorum (U Gem) stars, Z Camelopardalis (Z Cam) stars and SU Ursae Majoris (SU UMa)stars. Typically, U Gem dwarf novae brighten every few weeks to few months, remaining bright for several days before returning to quiescence and repeating the cycle (Cannizzo & Mattei, 1992).

Z Cam stars are more unpredictable and complex in their behaviour than U Geminorum

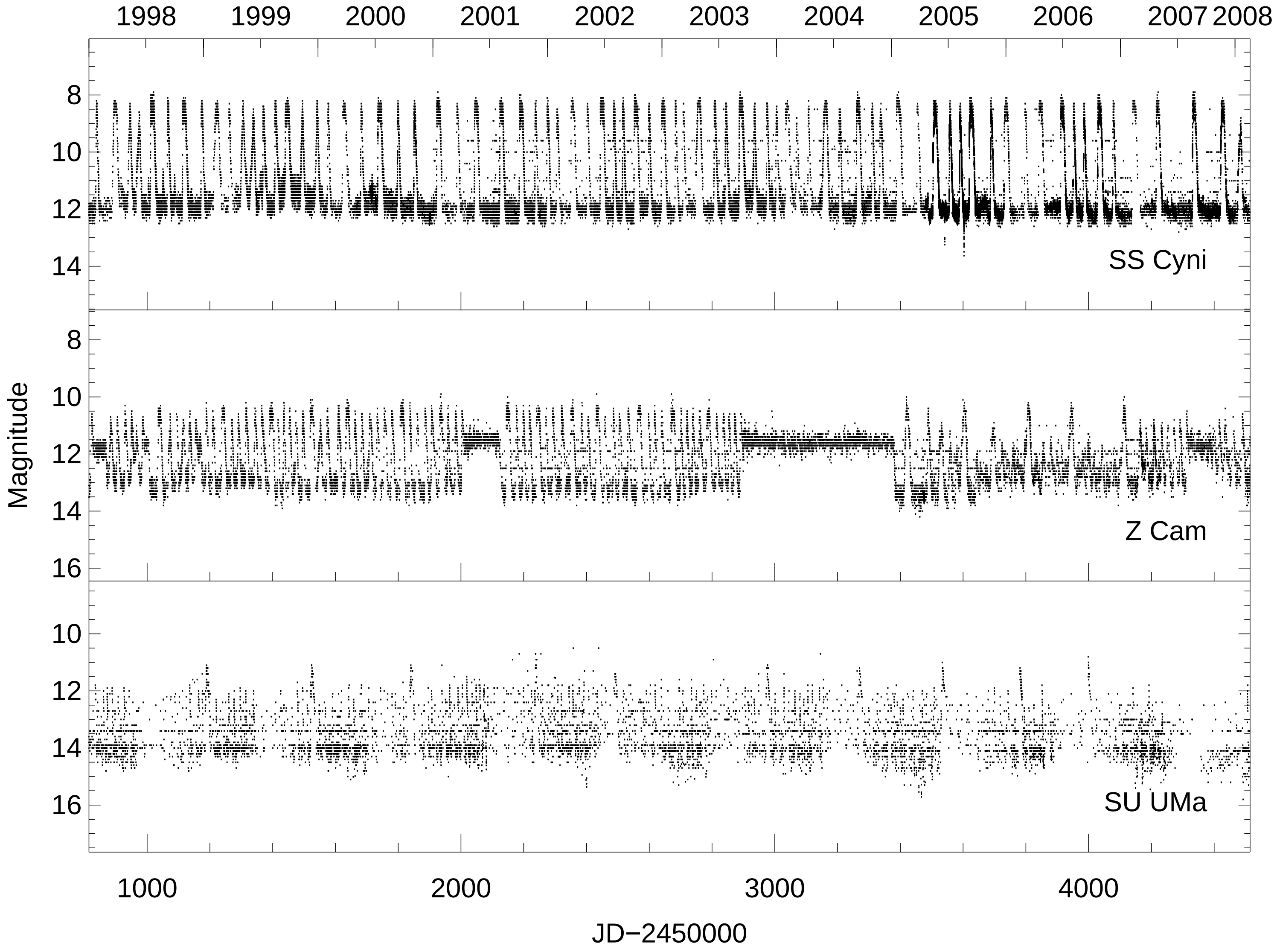

Figure 1.2: 10 year *AAVSO* lightcurves of SS Cygni (top), Z Cam (middle) and SU UMa (bottom). Long and short outbursts can be seen in the SS Cygni lightcurve, standstills in the outbursts can clearly be seen in the Z Cam lightcurve and the higher amplitude longer superoutbursts can be seen in the SU UMa lightcurve.

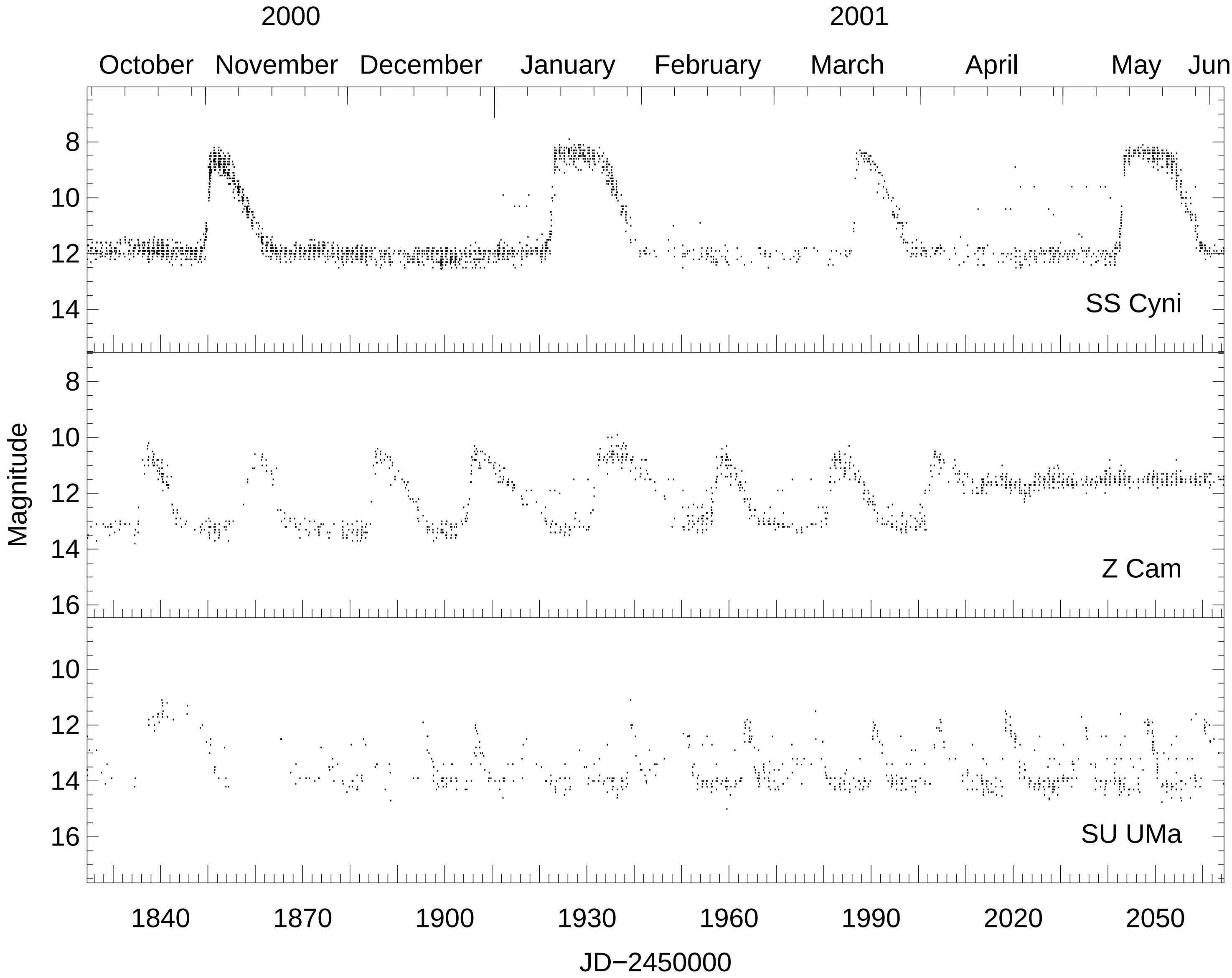

Figure 1.3: Detailed view of the *AAVSO* lightcurves of SS Cygni (top), Z Cam (middle) and SU UMa (bottom) from Figure 1.2.

stars. Z Cam stars show normal, U Gem type outbursts, however they are distinguished by stand-stills (Meyer & Meyer-Hofmeister, 1983). Some outbursts end in stand-stills in which the brightness remains constant roughly 1 magnitude below maximum light anywhere from a few days to 1000 days. The average energy output in a standstill is larger than that during an outburst cycle (Oppenheimer et al., 1998).

SU UMa stars, along with showing U Gem type outburst, also display superoutbursts occurring typically every $3 - 10$ cycles. Superoutbursts are slightly longer lasting and brighter by $\sim 1 - 2$ magnitudes. A hump shaped modulation can also be seen near the superoutburst maximum with a period a few per cent longer than the orbital period (see Section 1.5.3 where this is discussed further). At quiescence the SU UMa stars appear to form a natural extension of U Gem stars to shorter orbital periods. With the exception of TU Men, all of the SU UMa stars have $P_{orb} \lesssim 2$ hours. This class is further divided into ER Ursae Majoris (ER UMa) (Osaki, 1996), with a short duration between superoutbursts, and WZ Sagittae (WZ Sge) (O'Donoghue et al., 1991), with a long period between superoutbursts. The peak amplitude of superoutbursts is also larger.

Nova-like variables are stable in nature; their accretion discs are believed to be in a permanent high state (Warner, 1995). As a result of the high rate of mass transfer in the disc nova-like variables are seen to be very luminous. The overall brightness varies only slightly about its mean level. Finally, permanent superhumpers are short period nova-like variables which show a permanent hump shaped modulation in their light curve, as seen in SU UMa type dwarf nova.

Magnetic cataclysmic variable systems are cataclysmic binaries in which the white dwarf primary has a strong magnetic field. The magnetic field is strong enough to prevent an accretion disc from extending down to the surface of the white dwarf or may even prevent the formation of an accretion disc. Instead, gas is accreted onto the poles of the white dwarf primary star. The systems in this thesis are non-magnetic cataclysmic variables, therefore the focus of this chapter will be non-magnetic cataclysmic variables.

1.4.2 Dwarf Nova Formation and Evolution

Stars destined to become cataclysmic variables begin as binaries separated by a few hundred solar radii, orbiting every $\sim$ 10 years. The more massive star, the primary, evolves more rapidly since the greater mass of its core ensures a higher temperature and pressure causing a faster thermonuclear evolution. As the star evolves it becomes a giant filling its Roche lobe and thus overflowing onto its companion (Kraft, 1962), the secondary, through the L1 point (Section 1.3). Unstable mass transfer proceeds since matter is transferred away from the centre of mass of the binary towards the secondary causing the binary separation to shrink (Section 1.2). The secondary cannot accommodate the high rate of mass transfer and matter piles up until the binary is enveloped in a cloud. In this ’common envelope’ (CE) phase the secondary companion is effectively orbiting inside of a red giant (Paczynski, 1976; Iben & Tutukov, 1993). The orbital evolution inside the envelope is then driven by dynamical friction which extracts energy and angular momentum. Thus the orbital energy of the binary is used to expel the envelope leading to the binary gradual spiralling inwards. During this phase of evolution the orbital separation may decrease by as much as a factor of 100 (Iben & Livio, 1993). Figure 1.4 shows a graphic illustration of this process.

If after the common envelope phase the orbital separation of the binary is too large for the main sequence secondary to be in contact with its Roche lobe then the system is detached. Some form of angular momentum loss will be required, as described in Section 1.3, before mass transfer is able to begin. As the binary separation decreases and the secondary comes into contact with its Roche lobe matter will be transferred through the L1 point from the secondary to the primary forming an accretion disc, see Section 1.2.

CV evolution proceeds via magnetic braking for longer period systems ($P_{orb} \gtrsim 3$ hours) (see Tutukov et al., 1982; Hjellming & Webbnik, 1987; Ivanova & Taam, 2004; Postnov & Yungelson, 2006, and references therein for a detailed description). Between $P_{orb} \sim 2 - 3$ hours there is an abrupt drop in the number of observed systems. The dearth of observed systems is known as the period gap. Binaries evolve down to $P_{orb} \sim 3$ hours via magnetic braking at which point the secondary star is thought to become completely convective and magnetic braking is deemed no longer effective and shuts off (Spruit & Ritter, 1983; Rappaport et al., 1983; Taam &

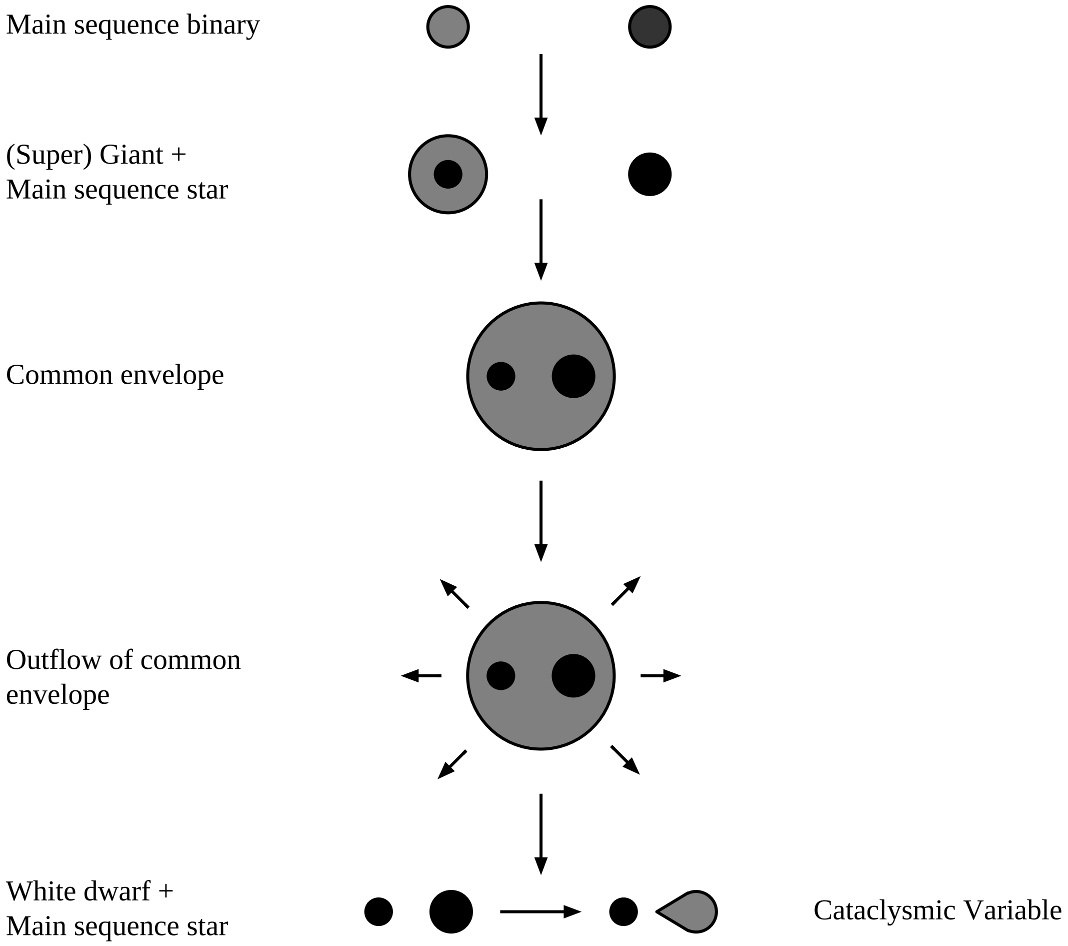

Figure 1.4: The formation of a close binary system. Two stars initially at a large separation evolve into contact through a common envelope phase producing a detached binary. Angular momentum loss will bring the detached binary into contact. This figure was adapted from Postnov & Yungelson (2006).

Spruit, 1989). With the mechanism driving the evolution of the binary no longer able to remove angular momentum, the secondary finds itself driven out of equilibrium with a radius too large for its mass. The secondary, unable to remain in contact with its Roche lobe, contracts preventing further mass transfer. For mass transfer to resume the orbital separation must decrease, reducing the size of the Roche lobe bringing it back in contact with the surface of the secondary. After magnetic braking has shut off the system evolves by gravitational radiation removing angular momentum and causing the orbit to shrink. At $P_{orb} \sim 2$ hours contact is made with the Roche lobe again and mass transfer resumes.

As the binary system evolves to shorter and shorter periods it reaches an observed minimum of $P_{orb} \sim 78$ minutes (Paczyński, 1971; King, 1988). The mass of the secondary star has become so low ($\sim 0.08 M_{odot}$) that hydrogen fusion ceases. At this point the very low mass secondary is degenerate and the removal of mass causes the star to expand. This results in a widening of the binary separation and a lengthening period. Eventually the mass of the secondary becomes so low that the evolution of the binary slows down becoming difficult to detect resulting in a brown dwarf orbiting a white dwarf (Littlefair et al., 2006a,b).

1.4.3 Radiation Processes Around a White Dwarf

The boundary layer is a small radial extent between the accretion disc and central star where accreting material is slowed from a near Keplerian angular velocity to the angular velocity of the central star. The radial extent of the boundary layer is $\sim H$, the scale height of the disc (Patterson & Raymond, 1985a). As the accreting material is slowed the kinetic energy, accounting for up to half the total energy in the disc, is radiated away. Due to the size and amount of energy liberated the boundary layer temperature is significantly higher than that of the remainder of the disc and as a result emits in the X-ray band.

If the accretion rate, and therefore surface density in the disc, are high enough (such as dwarf novae in outburst), the boundary layer will be optically thick. This allows energy to be radiated efficiently and primarily in the extreme ultraviolet and soft X-ray band-passes (kT of order $10-100$ eV) (Pringle, 1977). At low mass accretion rates, and also disc surface density, the boundary layer will be optically thin, cooling very inefficiently resulting in hard X-ray emission

($10^5 - 10^8$ K) (Pringle & Savonije, 1979; King & Shaviv, 1984; Patterson & Raymond, 1985a).

The structure of the boundary layer is poorly understood and theoretical modelling is complicated due to the strong shearing and turbulence present in the accretion flow which must be accounted for. A number of widely different models have been proposed, including a disc like boundary layer (Narayan & Popham, 1993), a coronal siphon flow (Meyer & Meyer-Hofmeister, 1994) and a hot settling flow (Medvedev & Menou, 2002). Detailed theoretical models of the boundary layer emission are not well developed due to the complexity of modelling between the disc and the white dwarf surface.

Continuum Emission

For an optically thick boundary layer the gas cools efficiently and collapses quickly on to the white dwarf surface, the luminosity emerges at the black-body temperature. Conversely, if the gas is optically thin, then radiative cooling is much less efficient and the gas can be heated up to much higher temperatures before reaching equilibrium. The primary mechanism of X-ray production is then via free-free emission. When an electron experiences a change in velocity due to the electric field of a nearby nucleus it emits an X-ray photon resulting in continuum emission commonly known as bremsstrahlung, or braking radiation. The left image of Figure 1.5 illustrates this mechanism.

In a uniform plasma, thermal electrons with a temperature T_e are distributed according to the Maxwell-Boltzmann distribution. Free electrons are constantly producing Bremsstrahlung radiation in collisions with the ions giving a characteristic continuous spectrum. The power density, P_{brems}, produced is dependent on the number density of electrons, n_e, and ions, n_Z, present in the plasma and on their temperature, T:

$$P_{brems} = \frac{8}{3}\left(n_e r_e^3\right)^2 \left(\frac{k_B T}{m_e c^2}\right)^{1/2} \left(\frac{m_e c^3}{r_e^4}\right) z_{eff} \alpha K \tag{1.8}$$

where Z_{eff} is the effective ion charge state, α is the fine structure constant, K is a number (~ 3). The bombarding electrons can also eject inner shell electrons from a target atom resulting in higher shell electrons making transitions into the lower shells. In making such transitions photons are emitted at discrete energies. However, in a hot plasma, such as in the boundary

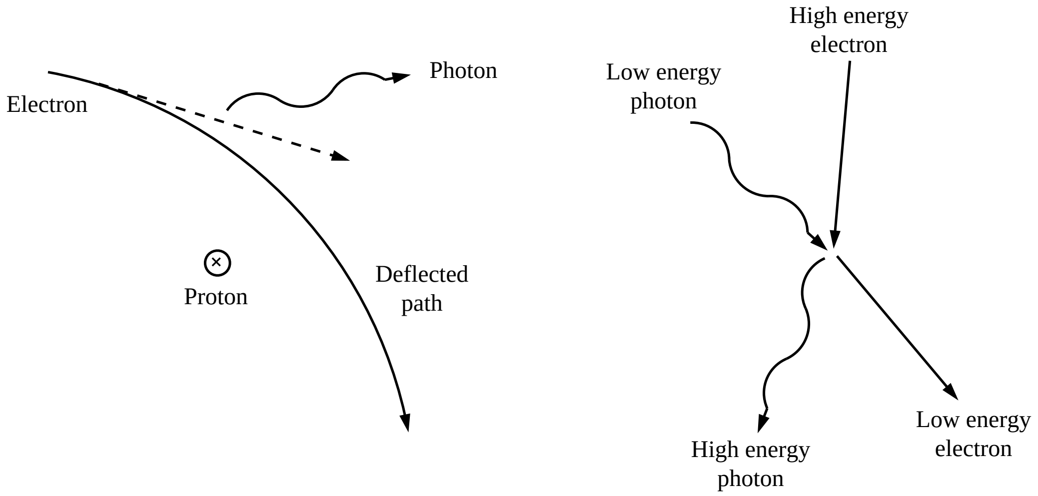

Figure 1.5: The mechanisms of producing hard X-rays. Bremsstrahlung radiation (left) is the primary process for producing X-rays in non-magnetic CVs and Compton scattering (right) producing a hard X-rays spectrum from high energy electrons.

layer, the atoms are almost entirely ionised. After an electron is ejected, the atom remains ionised until it recombines with an electron producing line emission at an energy dependent on the ionisation state (and hence temperature) of the material. The energy of the photon is the difference between original energy of the electron and the energy of the bound state producing line emission.

Iron line complex

Spectroscopic analysis of the X-ray line emission from a hot plasma can provide valuable information, such as the ionisation processes (photoionisation and/or collisional ionisation), the elemental abundances and the ionisation balance. For a high temperature plasma in ionisation equilibrium the most intense thermal line emission occurs between $6 - 7$ keV. The emission originates from Fe Kα emission consisting of an Fe XXV line (He like) at 6.7 keV comprising of three subcomponents (a resonance line, two intercombination lines and a forbidden line) and a Fe XXVI line (H like) at 6.9 keV comprising of two subcomponents.

The strengths of each component is dependent on the temperature of the plasma. At higher temperatures the H like line emission will be dominant, while at lower temperatures the

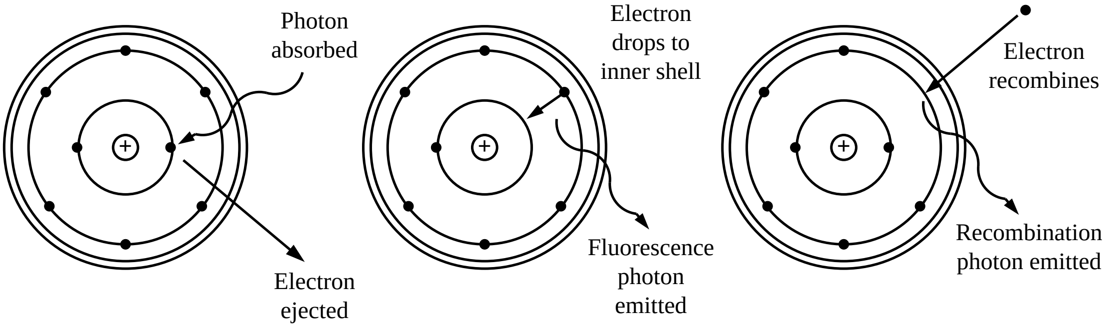

Figure 1.6: Atomic processes relevant to X-ray astronomy. The left image shows photon absorption. The middle image shows a fluorescent photon being emitted as an electron drops into the energy level vacated by an ejected electron. The right image shows the free-bound absorption process producing continuum emission with an energy dependent on the gas ionisation state.

line profile switches and the He like emission becomes dominant. It should be noted that the *RXTE PCA* detector (see Chapter 2) has a moderate spectral resolution potentially resulting in the 6.4 (see the following sub section) and 6.7 keV emission lines becoming blended in the detector.

Reflection

Intense X-ray radiation illuminating a cool plasma is reprocessed. Photons are reflected by the plasma and re-emerge with a spectrum altered by bound-free absorption and Compton scattering. Reflection is energy dependent: at low energies the scattering probability is decreased by photoelectric absorption, below 10 keV bound-free absorption dominates producing a characteristic 6.4 keV iron fluorescence line with corresponding absorption above 7.1 keV, the mechanism can be seen in Figure 1.6. As the incident photon energy increases Compton scattering becomes increasingly important; the right hand image in Figure 1.5 shows the Compton scattering mechanism. Above 10 keV Compton scattering dominates, causing a hardening of the spectrum between $\sim 10-30$ keV seen as a broad spectral ’bump’ (Magdziarz & Zdziarski, 1995). Compton scattering is also highly dependent on the viewing angle and harder photons are preferentially observed as the angle of observation increases.

1.5 Accretion in Dwarf Novae

1.5.1 Accretion Disc Formation

A consequence of Roche lobe overflow is mass transfer. The mass that is transferred has a high specific angular momentum and thus cannot directly accrete onto the mass-capturing star. The material leaves the secondaries Roche lobe and heads towards the primary through the L_1 point due to thermal pressure from the stellar atmosphere. The stream has such a high specific angular momentum that the primary sees it moving orthogonally to the line connecting the centre of the stars. The stream can be approximated to a single particle with a given angular momentum falling into the gravitational field of the primary alone.

The particle falls under the influence of the primary's gravitational field making an elliptical orbit, the presence of the secondary causes the orbit to precess. A continuous stream taking this orbit would impact with itself resulting in shocks that dissipate the energy of the stream (Lubow & Shu, 1975). The stream would then settle into the lowest energy configuration in the potential well of the star, a circular orbit, at a radius such that the angular momentum is equal to that of the L_1 point. This radius is known as the circularisation radius. Dissipative processes then cause the ring to spread (Pringle, 1981).

The time-scale on which the gas in the disc can redistribute angular momentum is much longer than that of radiative dissipation. As a result material loses as much energy as it can for a particular orbit then moves to a lower orbit by transferring angular momentum to larger radii. Material orbiting in this fashion is called an accretion disc. A small amount of mass takes the angular momentum to large radii, while the mass moves further into the potential well. See Section 1.3.

1.5.2 Accretion Disc Theory

The extraction of gravitational potential energy from material accreted through a disc onto a gravitational body is now known to be the principal source of power in several types of close binary systems. This is believed to provide the power supply in quasars, galactic nuclei, binary X-ray sources, cataclysmic variables (CVs) and proto-planetary discs. For a body of mass M

and radius R_* the gravitational potential energy released by the accretion of a mass, m, onto its surface is

$$\Delta E_{acc} = \frac{GMm}{R_*} \tag{1.9}$$

The efficiency of accretion as an energy release mechanism is strongly dependent on the compactness of the accreting object. The larger the ratio M/R_* the greater the efficiency. The luminosity from the disc, L_{disc}, equals the gravitational potential energy released per unit time and is equal to

$$L_{disc} = \frac{GM_1\dot{M}}{2R_\star} = \frac{1}{2}L_{acc} \tag{1.10}$$

Where G is the gravitational constant, M_1 is the mass of the accreting body, $\dot{M}$ is the rate mass is transferred through the disc and $R_\star$ is the radius of the primary. This assumes a thin disc in a Keplerian circular orbit.

Only half the energy stored in the accretion disc is radiated by the disc. As the accreting material close to the star is slowed, from the Keplerian velocity of the disc to that of the white dwarf, the remaining energy is radiated in the boundary layer, the interface between the disc and star surface.

1.5.3 Disc Instability Model

Ever since the origin of DN outbursts was known to arise in the disc surrounding the white dwarf there has been an effort to understand the processes involved in causing the observed outbursts. The Disc Instability Model (DIM) contains all the understanding gleaned from observational and theoretical studies. This model is an attempt to characterise and predict the outburst cycle. For detailed reviews on the disc instability model see Smak (1984b); Cannizzo (1993); Osaki (1996); Lasota (2001) and references therein.

An accretion disc is not a rigid body; each annulus is in a Keplerian orbit. There exists differential rotation between the disc annuli and each annulus orbits with a different angular velocity. Bulk flow of fluid is accompanied with turbulent and chaotic motion that generates stresses in the disc. The shear of viscosity transports angular momentum outwards enforcing co-rotation between annuli (Hōshi, 1979). The slower outer annuli are sped up and the faster inner annuli are slowed down causing angular momentum to be transported outwards. During this process the inner annuli lose angular momentum causing them to drop further into the potential well releasing gravitational potential energy.

In 1973 Shakura & Syunyaev hypothesised that the viscosity was due to vertical eddies inside the disc. The eddies cannot exceed the vertical scale height of the disc, H, in size. The turbulent velocity of these eddies must also be below the sound speed, c_s, otherwise the turbulence will be thermalised. Known as the α-prescription, it allows for ignorance about the viscosity, ν, to be encapsulated inside of the parameter α by:

$$\nu = \alpha c_s H \tag{1.11}$$

In 1974 Osaki proposed a model that suggested dwarf nova outbursts were caused by intermittent accretion of matter onto the white dwarf by some, unknown at that time, instabilities within the disc. He proposed that the mass-transfer rate from the secondary is constant, but mass is not accreted onto the central white dwarf during quiescence and is stored in the outer parts of the disc. If the mass stored reaches a critical amount, an instability within the disc sets in and a significant amount of mass is then suddenly accreted onto the white dwarf.

Thermal Instability

The physical mechanism responsible for the disc outburst was proposed by Hōshi (1979) and Meyer & Meyer-Hofmeister (1981). They showed that the accretion disc becomes thermally unstable due to partial hydrogen ionisation and outbursts occur when the disc transitions from a convective to radiative energy transport mechanism exhibiting bi-stable states. This is due to the increasing ionisation at higher temperatures. The accretion disc moves between these two states discontinuously showing a limit-cycle characterised by a well known S-shaped thermal equilibrium curve, see Figure 1.7. The behaviour seen in the disc is that of a limit cycle with alternating long-lived low viscosity states with low accretion rates and short-lived high viscosity states with high accretion rates. The solid line shows the two thermally stable equilibrium states,

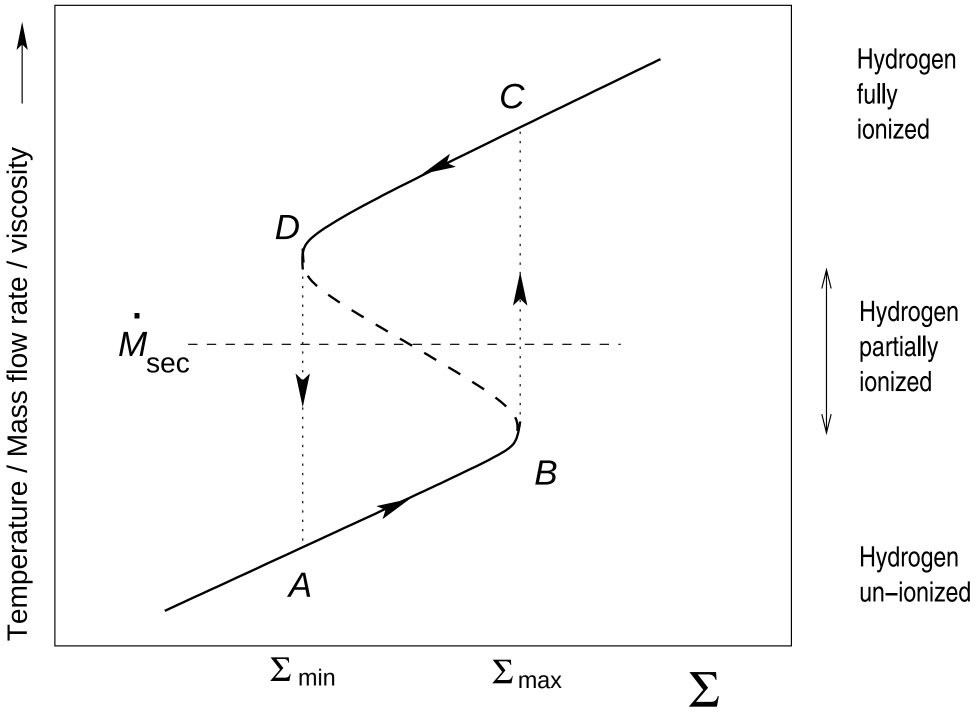

Figure 1.7: The limit cycle, showing the local behaviour of an annulus in the accretion disc. The branch AB is the low equilibrium state, branch CD is the high equilibrium state and lines BC and DA represent the path taken by the disc when it moves off a stable branch.

the dashed line shows the thermally unstable equilibrium state. This discussion is purely local to each annuli in the disc.

The low branch, AB on Figure 1.7, represents the cool, convective state. The annulus is formed from neutral hydrogen giving it a low opacity, thus it is optically thin. This branch is thermally stable, a small perturbation in viscosity in a region of the disc would drain that region lowering the density and reducing the viscous heating. The temperature then drops back to equilibrium. The annulus has low viscosity causing the mass transferred into it to accumulate. As material builds up the surface density, Σ, increases until it reaches a critical surface density, Σ_{max}, where the annulus becomes partially ionised. At this point the thermal instability develops. The annulus moves to the middle branch where it is thermally unstable and heating dominates cooling; a small increase in temperature will cause the annulus to quickly transition into its hot state on the upper branch.

With the disc partially ionised, the opacity, κ, becomes very important and is very sensitive to temperature ($\kappa \propto T^{10}$) (Hōshi, 1979). A small increase in the temperature of the disc will make the opacity rapidly increase, trapping heat and feeding back, making the temperature rise even further until the disc is fully ionised. At this stage the opacity loses its sensitivity to temperature.

Once in the high state, CD on Figure 1.7, the annulus is hot and fully ionised causing it to have a high opacity. It is therefore optically thick and as a result there are a greater number of interactions between photons and ionised particles in the disc. This impedes the flow of radiation and gives rise to high viscosity. This branch is radiative and cooling dominates heating, the annulus is thermally stable, as on the low branch. In the hot, highly viscous state the inward flow of material through the disc exceeds that being added from the secondary. The state cannot be sustained and eventually matter drains from the annulus until the surface density reaches the critical surface density, Σ_{min}. At this point, D, the temperature drops and recombination of the ionised gas occurs, the disc returns to its cold state.

Between outbursts, the material supplied by the secondary component is stored in the relatively cool disc. This eventually leads to a local thermal instability which results in the increase of the viscosity and of the local accretion rate. As the instability propagates across the disc, in the form of a heating wave, the global increase in the accretion rate is observed as an outburst. Similarly, a cooling wave spreads when an annulus has been drained sufficiently to have its surface density drop below the minimum critical surface density. This always occurs at the outer disc since this is where the surface density is the highest.

During the period when all annuli in the disc are on their hot branch, with high accretion rates, only $\sim$ 10 per cent of the material in the disc has time to be accreted onto the central white dwarf. Much of the remaining material simply flows inward due to the heating wave and expands as the cooling wave propagates through the disc.

Balbus-Hawley Instability

A weak field instability was first discussed by Chandrasekhar (1960, 1961) and Shakura & Syunyaev (1973), but it was not until the work of Balbus & Hawley (1991) that it received fresh impetus as a mechanism of transporting angular momentum in accretion discs. They showed that a magnetic field is unstable if the angular momentum of the fluid increases outward. A magnetic field line permeating the disc will be coupled with ionised gas. A perturbation will result in the field line becoming radially distorted; this distortion increases in size as the field line experiences opposing forces from neighbouring annuli stretching it. The increased magnetic tension acts to enhance the instability increasing the efficiency of angular momentum transport between adjacent annuli. This instability is an effective way of transporting mass and angular momentum in the disc.

The Balbus-Hawley instability is strongly dependent on the coupling between the magnetic field in the disc and the disc material. This occurs when the disc is hot and ionised. When the disc is cold the instability effectively shuts down. In the cold state the secondary transfers material into the accretion disc, as it does the surface density grows causing the temperature to rise. At near 10^4 K the hydrogen in the disc begins to ionise, allowing the Balbus-Hawley instability to increase the magnetic viscosity in the disc. This significantly increases the mass flow through the disc, or accretion rate, and effectively transports angular momentum outwards.

Tidal Instability

The outburst types that are seen in many dwarf nova cannot be fully explained by the standard DIM using the thermal instability explained above. Short period dwarf nova display standard disc instability behaviour with normal outbursts lasting ~ 3 days but also show less frequent superoutbursts lasting $\sim 10-18$ days. However, the rise to superoutburst cannot be distinguished from the rise of a normal outburst. Superoutbursts are longer in duration and $\sim 1-2$ magnitude brighter than the normal outburst. A hump shaped modulation also appears near the superoutburst maximum with an amplitude of $20-30$ per cent of the total brightness. The superhump period is $\sim 2-3$ per cent Patterson et al. (2005) longer than the orbital period of the system. Therefore, by observing the superhumps, an orbital period of the system can obtained.

To reproduce these observed characteristics modifications need to be made to the standard instability model. Vogt (1982) first proposed that superhumps were caused when the disc becomes elliptical during superoutburst and that the elliptical disc would precess on a time-scale much longer than the orbit. Simulations by Whitehurst (1988) showed that for systems with extreme mass ratios, $q \lesssim 0.33$, the disc becomes elliptical and begins to precess. In almost all cases, systems of this type have been found to have orbital periods of less than two hours.

With each successive outburst the size of the accretion disc increases until the proximity of the edge of the disc gets closer to the orbiting secondary. The secondary tidally interacts with the disc producing a significant torque that acts as a sink severely depleting the angular momentum in the disc. This limits the radial extent of the outer disc to the tidal truncation radius. Most of the disc mass is then accreted onto the white dwarf producing a brighter and longer super-outburst. In this scenario resonances of the separate orbits of the disc and secondary become important, however, due to restrictions of mass ratios attainable in binary systems it is the 3:1 resonance ratio of the disc to secondary orbit that is important. For every 3 orbits made by the gas in the disc the secondary makes one complete orbit providing a driving force, known as the tidal instability. The tidal interaction causes material in Keplerian orbits in the disc to intersect leading to shearing in the disc. The shearing interaction of the material produces dissipation which is observable as a photometric modulation. This additional instability is thought to be the origin of elliptical discs in outburst.

1.6 X-ray Observations of Dwarf Novae

1.6.1 Dwarf Novae

The first dwarf nova to be discovered, and the prototype of its sub-class, was U Gem, discovered by Hind & Hansen in 1855. It has an optical range of magnitude 14 at quiescence rising to magnitude 9 during outburst (Szkody & Mattei, 1984). Its high inclination results in absorption dips in the light curves making it possible to study the origin of the X-ray emission and the physical structure of the disc (Mason et al., 1988; Szkody et al., 1996). The X-rays in U Gem are also brighter during outburst and not quenched as is seen in other DN making it an interesting system to observe (Swank et al., 1978; Cordova & Mason, 1984; Mattei et al., 2000).

Belonging to the same class, SS Cygni, was discovered in 1896 (Pickering & Fleming, 1896) and has undoubtedly been one of most observed variable stars in the night sky. Amateur astronomers have continuously observed SS Cygni over the past 100 years without missing a single outburst. This is due largely to the fact that it is the brightest of the U Gem dwarf novae class with an optical range of $m_v \sim 12 - 8$ mag. Both these systems with their close proximity (96.4 ± 4.6 pc for U Gem and 166.2 ± 12.7 pc for SS Cygni (Harrison et al., 1999)) and regular outbursts between 50 and 100 days make them ideal candidates for studying.

SU Ursae Majoris (SU UMa) is also the prototype of its sub-class. It was discovered by Ceraski in 1908 (Ceraski, 1908). Unlike U Gem and SS Cygni this system resides below the period gap with a period of $P_{orb} = 109.9 \pm 0.1$ minutes (Thorstensen et al., 1986). In addition to exhibiting U Gem type outbursts SU UMa also displays the superoutburst and superhump phenomenon described in Section 1.5.3. Its variations occur on a shorter time-scale than either SS Cygni or U Gem. Narrow outbursts occur every 11 to 17 days lasting $1 - 3$ days. Superoutbursts occur every $3 - 10$ normal outburst cycles, approximately every 153 to 260 days with a duration of $10 - 18$ days. SU UMa typically varies from a minimum of magnitude 15 to a maximum of magnitude 10.8 during superoutburst.

The outbursts observed in these systems are thought to be triggered by a thermal-viscous instability in the accretion disc surrounding the white dwarf primary (Osaki, 1996). See section 1.5.3 for further discussion.

1.6.2 X-ray Studies

SS Cygni was the first dwarf novae to be detected in the X-ray band. Detected by Rappaport et al. (1974) in soft X-rays, between $0.15 - 0.28$ keV and $0.4 - 0.85$ keV, during a scanning rocket flight. It was later detected again by Heise et al. (1978) where it was observed to emit both soft ($0.16 - 0.284$ keV) and hard ($1 - 7$ keV) X-ray components. Observations by Ricketts et al. (1979) and Watson et al. (1985) provided a more detailed picture of the X-ray behaviour and showed that the soft X-ray emission was well correlated with the optical outburst, whilst the hard X-rays were equally strongly anti-correlated and quenched to below quiescent levels (discussed in Section 1.4.3). The most complete multi-wavelength coverage of an outburst was presented by Wheatley et al. (2003) who analysed the flux evolution through an entire outburst, resolving the rise to outburst. Using X-ray, extreme UV (EUV) and optical bands the correlation of optical and

EUV and the anti-correlation with the hard X-ray band was seen in great detail. The observed quiescent luminosity corresponded to an accretion rate about two and a half orders of magnitude higher than predicted by the DIM (Meyer & Meyer-Hofmeister, 1994). In studying archival SS Cygni data, from the *Ginga* and *ASCA* satellites, Done & Osborne (1997) found single and multi-temperature plasma models with line emission and a reflection component to represent the data well. They claimed there to be a larger contribution from the reflection component in the softer outburst spectra supporting models where the inner disc is truncated (Disc truncation is discussed further in Section 1.7).

Observations of eclipsing system HT Cas during quiescence provides evidence for hard X-ray emission arising from the boundary layer (Mukai et al., 1997). The observed X-ray eclipses were found to be short and compatible with total eclipses indicating an X-ray emission region of <1.15 times the size of the white dwarf. Currently, it is not known where hard X-rays originate from in outburst. Patterson & Raymond (1985a) suggested that the hard X-rays are produced in an optically thin region surrounding an optically thick boundary layer. However, observations of OY Car during superoutburst did not detect an eclipse in the soft X-ray band providing evidence for an extended X-ray source (Naylor et al., 1988; Pratt et al., 1999). Observations in the EUV band by Mauche & Raymond (2000) also show a lack of eclipse in outburst, they suggest the extended source originates from optically thick radiation being scattered into the line of sight by an accretion disc wind. Observations of VW Hyi over a two month period by van der Woerd & Heise (1987), found the spectral shape during outburst to be remarkably constant while the fluxes changed by two orders of magnitude. They concluded that the observations were consistent with a spectrum comprising of multiple components, possibly with emission from an optically thin extended region surrounding the white dwarf.

The spectral parameters of 32 cataclysmic variables observed with the *Einstein* satellite were determined by Eracleous et al. (1991). An optically thin thermal bremsstrahlung model was found to describe the data well, indicating the X-ray emitting region is a hot optically thin boundary layer region. Later, all available non-magnetic CVs from the *ROSAT PSPC* archive were presented by van Teeseling et al. (1996) finding that there was no correlation between the temperature and X-ray luminosity, emission measure or X-ray luminosity. This is difficult to explain if the X-rays are emitted by the boundary layer. Also the ratio of X-ray to UV+optical flux was found to be anti-correlated with the accretion rate[1], which is not consistent with simple boundary layer models. However, evidence for anti-correlation between the observable emission measure and orbital inclination in the X-rays indicate that the emitting region is very close to the white dwarf.

Work by Yoshida et al. (1992) on SS Cygni and U Gem data found the energy spectrum, during quiescence, to be well reproduced by a thermal bremsstrahlung continuum. Baskill et al. (2005) presented 34 non-magnetic cataclysmic variables in outburst and quiescence, including SS Cygni, U Gem and SU UMa. Like SS Cygni, the brighter systems favoured the inclusion of an emission line at 6.4 keV from neutral iron. The outburst emission from the dwarf novae was found to be weighted towards lower temperatures. Using high resolution data taken from the *Chandra* satellite using the High Energy Transmission Grating (*HETG*) Mukai et al. (2003) found seven systems to be well fit with either a cooling flow model or a photoionised continuum with all having strong H and He like ion emission. The presence of an iron fluorescence line and a number of thermal emission lines from a broad range of ions in the spectra of six dwarf novae was found by Rana et al. (2006). The prominent fluorescent iron line, seen in many non-magnetic CVs, indicates the presence of a significant reflection component. The equivalent width of this line is also consistent with a reflection origin. The presence of a strong Fe `XXV` triplet at 6.7 keV is a common feature in the hard X-ray spectra of non-magnetic CVs. The triplet is present in outburst and quiescence indicating plasma temperatures of $\gtrsim 3 \times 10^7$ K. The ratio of the Fe `XXVI/XXV` lines indicates a higher ionisation temperature during quiescence than in outburst. H and He like emission from a number of ions was also found by Okada et al. (2008) and emission lines were found to be narrower during quiescence suggesting that the lines arise from the entrance of the boundary layer. The line emission from ten CVs observed during quiescence using *XMM-Newton* indicate that X-rays are emitted from a cooling plasma settling onto the white dwarf, excluding the presence of an extended X-ray emitting corona (Pandel et al., 2005).

---

[1] Accretion rates were calculated from bolometric fluxes based on flux measurements in the energy range 0.1 – 2.4 keV and used distances given by Warner (1987).

1.7 Disc Model Issues

Compared to early models the current Disc Instability Model (DIM) has become rather complex. With the addition of physical mechanisms not taken into account in the original model the current version is able to describe many aspects of the dwarf nova outburst cycle: irradiation, evaporation, stream impact heating and mass transfer variations.

Irradiation from the hot central body (Hameury et al., 1999; Schreiber & Gänsicke, 2001) changes the relation between the mid-plane and surface temperature of the disc. This irradiation will stabilise the inner disc when the central disc temperature is pushed above the hydrogen ionisation range. At larger radii irradiation will destabilise the outer disc by increasing the mid-plane temperature bringing it close to hydrogen partial ionisation. Smak (2000) plotted the ratio of mean irradiation to the secondary's intrinsic flux finding that DN not showing superoutbursts had a ratio less than 10. Systems with superoutburst have a much larger ratio of greater than 20 indicating that irradiation plays a crucial role in superoutburst systems.

Evaporation of the inner disc into a corona (Meyer & Meyer-Hofmeister, 1994) provides a means for the white dwarf to accrete during quiescence. The inner disc is evaporated by a siphon flow into a corona. The matter retains its angular momentum which supports it against the gravitational pull of the white dwarf and can then be accreted solving the problem of the intense X-rays observed from CVs during quiescence.

Stream impact heating and *tidal dissipation* respectively heat and truncate the outer disc (Buat-Ménard et al., 2001a). The gas stream from the secondary hits the accretion disc, creating a bright spot that heats the outer disc. It allows outside-in heating waves to occur for lower mass transfer rates. The outer radius of the disc is truncated by tidal effects for close binaries and angular momentum transported through the disc is returned to the binary orbit. A range of mass transfer rates are obtained where the model produces alternating short and long outbursts. The outer fraction of the gas stream from the secondary is able to skim over and under the outer disc while the inner fraction of the gas stream bores into the outer disc and is stopped (Schreiber & Hessman, 1998). The overflowing stream interacts with the heating and cooling fronts. However, significant overflow is required to change the outburst.

Mass transfer variations (Smak, 1999; Schreiber et al., 2000; Buat-Ménard et al., 2001b) can occur on almost every possible time scale leading to the disc exhibiting differing outburst profiles. Models with the mass transfer variations during outburst show that moderate enhancement of the mass transfer rate correspond to narrow outbursts and major enhancement of the mass transfer rate correspond to wide outbursts.

Despite these additions to the DIM there are still a number of areas that require improvement before the predictions made by the model can be properly tested. It was realised quite early in the development of the DIM that in order to reproduce observed amplitudes and durations the parameter α must have different values in outburst and quiescence, requiring two separate S-curves to be used (Smak, 1984a).

An artifact of using the same α value on the upper and lower branches is that the DIM produces small amplitude variations in the disc luminosity instead of dwarf nova type lightcurves. This indicates that the parameter α must have different values in outburst and quiescence, however, this has yet to be confirmed. The DIM is also unable to produce a sequence of narrow and wide outbursts of roughly the same amplitude, however, mass-transfer enhancements may be able to solve this (Smak, 1999).

The single largest issue confronting the DIM today is quiescence (Lasota, 2001). The DIM predicts low quiescent temperatures ($\lesssim$ 4000 K) (Gammie & Menou, 1998) below the critical value needed for the Balbus-Hawley instability to operate. However, quiescent DN emit an impressive quantity of hard X-rays with luminosities of $10^{30} - 10^{32}$ ergs s^{-1} (Verbunt et al., 1997). X-ray eclipsing systems clearly show that the X-rays are emitted by the accretion flow close to the white dwarf (Mukai et al., 1997). Thus for the DIM to be valid another viscosity mechanism must be in operation during quiescence. The low predicted quiescent temperatures also do not correspond with observation (Wood et al., 1986, 1989).

A further problem of the DIM is the quiescent disc, if it were to extend down to the surface of the white dwarf and the X-rays emitted by a hot boundary layer, the required accretion rates would be about two and a half orders of magnitude higher than those allowed by the DIM (Meyer & Meyer-Hofmeister, 1994). Reviewing the disc instability model, Lasota (2001) states that the truncation of the inner accretion disc is a necessary ingredient in the explanation of quiescent X-ray fluxes. Holes present in the inner disc can be formed in a number of ways: magnetic fields (Livio & Pringle, 1992); evaporation into a siphon flow (Meyer & Meyer-Hofmeister, 1994); or an Advection Dominated Accretion Flow (Menou, 2000). Truss et al. (2004) presented two-dimensional accretion disc models achieving the same effect with a small portion of the disc remaining in a high-viscosity state. The DIM also predicts that quiescent fluxes are increasing, however observations show that they are constant or decreasing (McGowan et al., 2004).

The DIM can describe many aspects of the DN outburst cycle if it is complemented by additional physical mechanisms not taken into account in the original version. However, before the DIM can be considered as providing a credible description of DN outbursts these problems described above must be solved.

Chapter 2

Rossi X-ray Timing Explorer

2.1 The History of X-ray Astronomy

X-ray observations of astronomical sources are possible only from space based observatories because X-rays are absorbed in the Earth's atmosphere. Only 10 cm of air (at atmospheric pressure) is enough to stop 90 per cent at an energy of 3 keV (Seward & Charles, 1995). Thus the field of X-ray astronomy relies upon space based observations, using either sounding rockets or satellites carrying X-ray detectors. The first astronomical object outside the Solar System discovered to emit X-rays was Scorpius X-1 in the constellation of Scorpius (Giacconi et al., 1964). It was detected using a sounding rocket which was the primary means of observing X-rays from space in the 1960s. See Seward & Charles (1995) for a detailed look at the history of X-ray astronomy.

The first orbiting mission dedicated to celestial X-ray astronomy (able to observe for more than a few minutes) was *Uhuru*. Launched in 1970 (Giacconi et al., 1971), *Uhuru* had a simple complement of instrumentation covering the energy range 2 – 20 keV. It was designed to continue the broad surveys of the sky for X-ray sources. This was followed in the late 1970s and early 1980s by larger missions *HEAO 1*, *ANS*, *Einstein* and *EXOSAT*. In the late 1980s *Ginga* discovered X-ray transient black hole candidates and followed their spectral evolution (Koyama, 1988; Tsunemi et al., 1989). Then, in the 1990s the *ROSAT* survey detected more than $100,000$ X-ray objects (Aschenbach, 1991; Watson, 1995) and the *ASCA* mission made the first high resolution measurements of the X-ray spectra of these objects (White, 1995; Inoue, 2001). Launched in the mid 1990s, the Rossi X-ray Timing Explorer studied their timing properties on time scales from microseconds to months in a broad spectral range from 2 – 250 keV (Zhang et al., 1996; Reig & Coe, 1998; Giles et al., 1998; Rana & Singh, 2003). Following these successful missions the turn of the century saw the launch of the *Chandra* and *XMM-Newton* observatories which brought high-resolution imaging and spectroscopy (Marshall, 2000; Charles, 2002) and *Suzaku/Astro-E2*, launched in 2005 (Mitsuda et al., 2007). These current and past missions represent a vast improvement in detector technology and have allowed X-ray astronomers to learn a great deal about the high energy universe.

2.2 Rossi X-ray Timing Explorer

The Rossi X-ray Timing Explorer (*RXTE*), (Figure 2.1 shows a sketch of the satellite), was placed into orbit by a Delta II Rocket from Cape Canaveral on December 30, 1995. It was placed into a circular orbit at an altitude of 580 km with an inclination of 23 degrees corresponding to a 96 minute period. Since then the orbit has decayed to $\sim$ 490 km; this is thought to be due to the increased drag due to the expansion of the Earth's atmosphere caused by increased solar activity associated with the solar cycle (Jahoda et al., 2006).

RXTE was designed to observe in high time resolution with moderate spectral resolution from 2 – 250 keV. See Bradt (1982) for a description of the scientific objectives. It carries two pointed instruments, the Proportional Counter Array (*PCA*) covering the 2 – 60 keV range of the energy spectrum and the High Energy X-Ray Timing Experiment (*HEXTE*) covering the 20 – 250 keV energy range. The *RXTE* also carries a continuously scanning All Sky Monitor (*ASM*) capable of observing the X-ray sky once every orbit in the 2 – 10 keV energy band. The satellite has a 7 hour response time to an *ASM* triggered event. See Bradt et al. (1990) for a pre-launch summary of the satellite's instruments and capabilities.

The *RXTE* is capable of moving $\sim$ 6 degrees min^{-1} and the *PCA*/*HEXTE* field of view can be pointed to any position on the sky on any day of the year provided the angle to the sun is $>$ 30 degrees. The *PCA* and *HEXTE* both have a 1 degree full width at half maximum

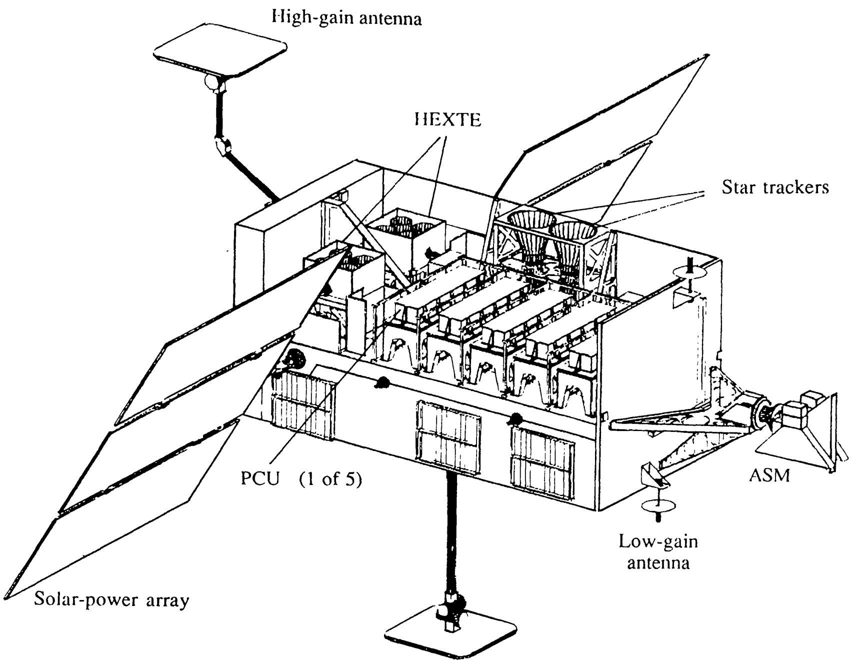

Figure 2.1: Rossi X-ray Timing Experiment, *RXTE*. Figure taken from Bradt et al. (1993).

(FWHM) field of view. Data is telemetered using the Tracking Data Relay Satellite System, it is possible to maintain contact with the spacecraft for approximately 70 – 80 per cent of each orbit. Data transmission is quasi-continuous, nominal telemetry rates are of the order of 20 kbps for the *PCA*, 5 kbps for *HEXTE* and 3 kbps for the *ASM*, with rates of up to 256 kbps possible. A very extensive technical description of the instruments is given in Appendix F of the National Aeronautics and Space Administration (NASA) Research Announcement for *RXTE* (NASA 1997[1]).

The *RXTE* has a complement of three experiments aboard, each with their own purpose. This thesis is only concerned with data taken with the *PCA* therefore the *HEXTE* and *ASM* experiments will only be described briefly here. A more detailed description of the *PCA* is given in Section 2.3.

The first experiment on board *RXTE* is the *ASM*, which can provide a transient event alert for the *PCA*/*HEXTE* instruments and provides a base for long term studies. It consists of

---

[1] http://heasarc.gsfc.nasa.gov/docs/xte/RXTE_tech_append.pdf

three position sensitive proportional counters mounted on an assembly that can be rotated. It has a combined effective area of 90 cm^2 sensitive to energies of $1.5 - 12$ keV and can scan 80 per cent of the sky in 90 minutes with a field of view of 6×90 degrees. A technical description and the first results are presented by Levine et al. (1996).

The *HEXTE* forms the high energy component of the *RXTE* mission. *HEXTE* is a descendent of the *HEAO 1* A4 experiment (Ungut et al., 1978). The *HEXTE* experiment consists of two independent scintillation counter clusters covering the energy range of $15 - 250$ keV. An X-ray photon traverses a sodium iodide crystal creating scintillations which are then amplified in a photomultiplier tube. *HEXTE* has a $10\mu s$ temporal resolution with an effective area of 800 cm^2 and field of view of 1 degree FWHM. The in-flight performance is discussed by Rothschild et al. (1998).

2.3 Proportional Counter Array

2.3.1 The Detector

The Proportional Counter Array (*PCA*), built by the Goddard Space Flight Centre (GSFC) Laboratory, is a 50 per cent scaled up version of the *HEAO 1 A-2 HED* sealed detector (Rothschild et al., 1979). The *PCA* consists of five identical non-imaging Proportional Counting Units (*PCU*) with a combined effective area of 6250 cm^2. Since the *PCA* is not position sensitive each *PCU* is fitted with a mechanical collimator, which screens out contaminating light and provides a field of view of 1 degree FWHM. Beneath the collimators sits an aluminium coated window and a second window creates a sealed propane filled front volume containing the first anode layer. The volume contains 20 anodes separated by thin solid aluminium walls. The front layer serves as a front entrance anti-coincidence layer, rejecting non X-ray events, such as electrons, entering the detector through the front window.

Beneath the propane volume is a xenon/methane (with a $90/10$ per cent mixture) volume. The xenon volume contains 80 anodes in four layers separated by wire wall cathodes with 20 anodes in each layer. The bottom layer and the outermost anodes of the top three xenon layers form a veto detection layer rejecting events that enter the detector through the sides and back rather than through the detector window. Events simultaneously detected on two independent anode chains are also vetoed. Beneath the last layer is a back plate also providing some shielding from events created in the calibration volume. An Americium-241 source is mounted on the back plate with two more anodes to provide a low level energy calibration signal. Calibration is discussed further is Section 2.3.2. Each *PCU* is also passively shielded to reduce the cosmic X-ray background flux and absorb hard X-ray events generated in the spacecraft by cosmic ray impacts. Figure 2.2 shows an exploded view of the *PCU* assembly. A description of the *PCA* is given by Bradt et al. (1993) and Glasser & Odell (1994).

Each *PCU* has three xenon detector layers. In the soft band (<10 keV) the top layer detects roughly 90 per cent of the cosmic photons. X-ray photons originating from harder sources create proportionately more events in the lower layers. For weak sources, selecting events from only the first layer will yield higher signal-to-noise than the second, third or any combination and the nature of non-source X-rays that contribute to the instrumental background depends less on layer. See section 2.3.3 for a more in depth discussion about the instrument background.

An X-ray is detected in a *PCU* when an incoming photon of sufficiently high energy enters through the window and interacts with the counter gas. This interaction happens via the photoelectric effect; when an incident X-ray photon is absorbed an electron is ejected creating an electron-ion pair in the detector gas. The electron ejected in the initial photoionisation is energetic enough to cause further ionisation. The number of primary electrons created is proportional to the energy of the incident photon.

The primary electrons, created by the X-ray photon, drift towards the anode undergoing ionising collisions creating a cascade of ion pairs in an avalanche. The electric field amplifies the charge from the original primary electrons into a cloud of electrons that surround the anode forming a measurable pulse. The size of the charge pulse is measured and placed within a finite voltage increment. This increment is the detector channel. The pulse is dependent on the detector operating voltage and the energy deposited by an incident photon or particle. The higher the operating voltage, the larger each avalanche becomes and the larger the pulse generated. The greater the energy deposited in the detector gas the larger the number of primary electrons created, therefore more avalanches are produced resulting in a larger electron cloud.

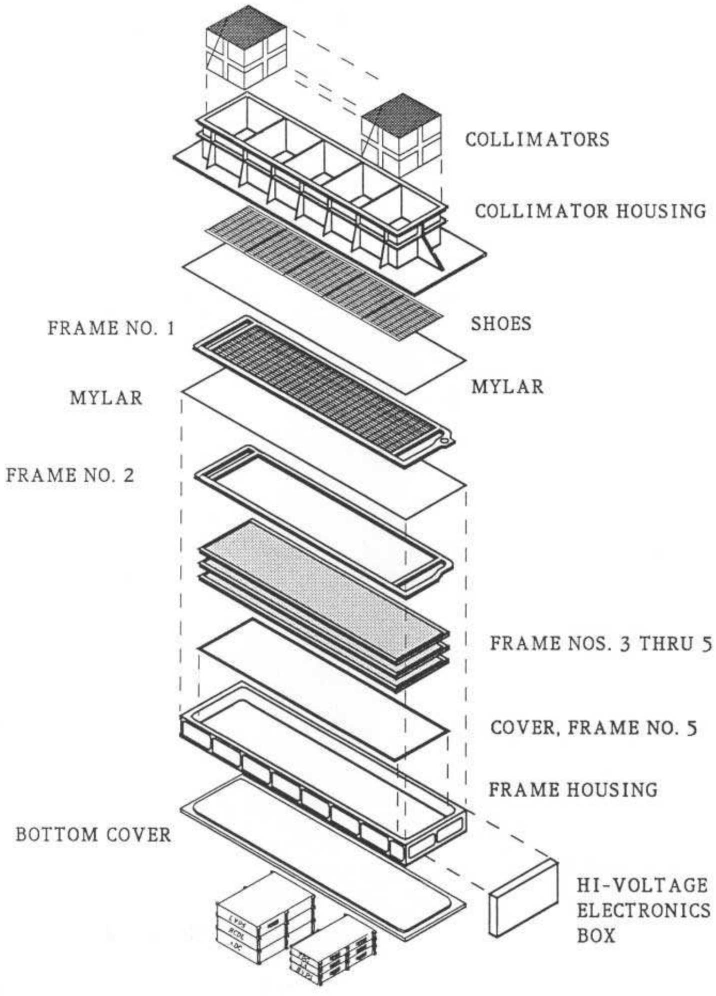

Figure 2.2: Assembly view of one *PCU* detector. Frame 1 denotes the propane veto layer. Frame 2 is the first xenon layer and Frames 3 – 5 define the third, fourth and xenon veto layer. Figure taken from Jahoda et al. (2006).

The frequency of pulses measured for all channels creates a pulse height distribution which is a good approximation for the spectrum being observed.

Recombination of an electron and the detector gas will emit a photon capable of re-ionising the gas, therefore producing pulses that are not related to the incident photon. To prevent this a small quantity of an organic gas, with a weaker electron affinity than the detector gas, is used to quench these events. The detector gas will take an electron from the organic gas and the energy liberated when the organic gas recombines at the cathode causes the molecule to dissociate before it is able to emit a photon. The quench gas is thus gradually consumed.

2.3.2 The Response Matrix

The response matrix provides information about the probability that an incident photon of a particular energy will be observed in a particular instrument channel. A discussion of the in orbit performance and calibration of the *PCA* can be found by Jahoda et al. (1996) and Jahoda et al. (2006). The detector response matrix captures non-linearities in the detector and must account for:

1. The *energy to channel relationship* which is non-monotonic at energies close to absorption edges. The mean energy absorbed above an edge is greater than the mean energy just below the edge; energy goes into the potential energy of the absorbing atom resulting in the photoelectron having less kinetic energy and so producing a smaller avalanche. Data suitable for parameterising the energy scale and monitoring variations (Jahoda et al., 2006) comes from three regularly observed sources.

    - Each *PCU* contains a small Americium-241 source along with two dedicated anodes in a parasitic proportional counter referred to as the alpha counter. The Americium-241 provides continuous calibration lines with energies between 13 and 60 keV. The source undergoes an alpha decay emitting several X-ray lines. The alpha particle is detected and tagged by a the alpha counter and the X-rays lines are captured in the xenon layer. A set of 6 Gaussians provides an excellent fit allowing the gain and resolution to be monitored.

- The supernova remnant Cassiopeia A has a bright, strong iron line easily visible in the *PCA* count spectra, a power-law fit to the continuum and Gaussian line between 4 and 9 keV can be fit to the data. The fit energy centroid can be unambiguously converted to a mean channel.
- Due to diffusion a small amount of xenon is present in the front propane layer. Regular monitoring of the Crab Nebula allows the measurement of energies near the xenon L edge, at 4.78 keV. Fits in energy can be used to determine the energy to channel relationship.

2. The *quantum efficiency* is a measure of how efficient the device is at converting photons hitting the device into photoelectrons that can be detected. To model the quantum efficiency of the detector each *PCU* is treated as a series of parallel slabs of material. Various parameters, including the amount of xenon, amount of xenon in the propane layer, rate of change of xenon in the propane layer, thickness of xenon between layers, amount of propane in the first gas volume and the thickness of front window are specified in the matrix generation configuration file. Parameter values can be found in table 3 of Jahoda et al. (2006). Frequent observations of the Crab Nebula were used to estimate the best values for the parameters, which were averaged over time and *PCU*.

3. The detector also detects *additional 'false' escape peaks* as well as detecting authentic lines from the source. An incident X-ray photon with energy above the absorption edge displaces a K or L alpha electron from an atom. If the fluorescence produced by the atom escapes from the detector the measured signal is interpreted as coming from a lower energy photon. The energy of this photon, E_{esc}, is the difference between the incident photon, E_i, and the energy of the lost fluorescence photon, E_f, $E_{esc} = E_i - E_f$.

The width of the photopeak corresponds to the energy resolution of the detector, which goes as $\Delta E/E = 0.17(E/6keV)^{1/2}$ where ΔE is the FWHM. The matrix also accounts for events that can be rejected because the photoelectron travels into a neighbouring anode volume.

The anodes in the xenon volume were initially set to a nominal +2050 V which has since been reduced. After 70 days in orbit, two of the 5 detectors showed evidence of gentle

Table 2.1: Dates and voltages for the epochs during the *RXTE* mission.

				Voltage		
Epoch	Start date (UT)	PCU 0	PCU 1	PCU 2	PCU 3	PCU 4
1	Launch	2030	2030	2026	2027	2048
2	1996 Mar 21, 18 : 34	2010	2010	2006	2007	2007
3A	1996 Apr 15, 23 : 06	1990	1990	1986	1987	1988
3B	1998 Feb 09, 01 : 00	-	-	-	-	-
4	1999 Mar 22, 17 : 39	1970	1970	1966	1967	1968
5	2000 May 12, 01 : 06	-	-	-	-	-

breakdown, to prevent further occurrences the gain was lowered by 35 per cent on all detectors and the detectors were operated at a warmer temperature. The overall gain setting has been changed twice since launch for operational reasons. Changes in the operating voltages mark periods of discontinuity in the detector response, referred to as epochs. Table 2.1 shows the dates of each epoch. The satellite orbit began to decay noticeably midway through epoch 3 so the epoch was split to distinguish background models with different time dependences; epoch 5 was also split into three sub epochs. The anodes of the main detector are connected alternately so each layer has two anode chains. The electronic system uses this to monitor the gain. The propane veto layer forms one chain and is maintained at a higher nominal voltage of +2800 V to compensate for higher gas leakage.

The net effective area and the effective area of the first layer of the *PCA*, as a function of energy, is shown in Figure 2.3. The useful energy range of the *PCA* is from $\sim$ 2.5 keV to $\sim$ 50 keV. The small jumps in the effective area in the lower energy range are the xenon L edges, with energies of 4.78, 5.10, 5.45 keV. The strong decrease below 34.6 keV is the xenon K edge. Just above the edges more energy goes into potential energy associated with the absorbing atom. The photoelectron has less kinetic energy and the number of electrons produced in the absorbing gas is smaller.

2.3.3 Detector Background

The *PCA* is a non-imaging instrument and for both light curves and spectroscopy the background must be subtracted based on an a priori model background. The background is generally defined

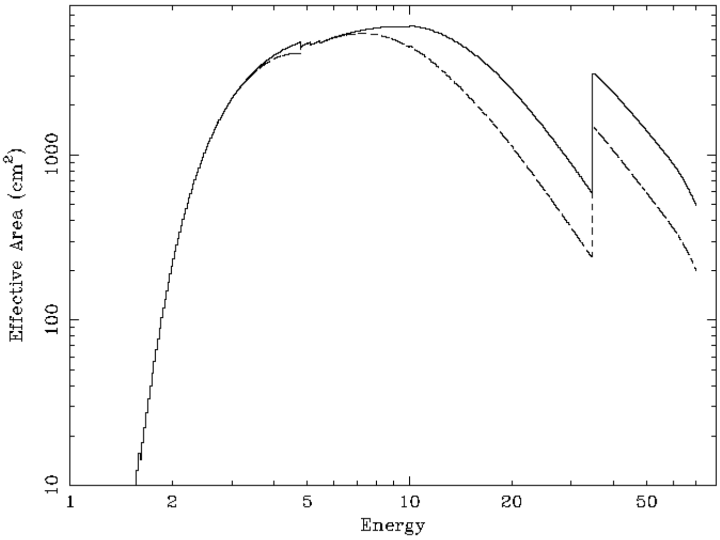

Figure 2.3: The upper curve shows the total effective area of the *PCA*. The lower curve shows the effective area of only the top xenon layer. Both curves are summed over 5 *PCU*.

as any non-source counts which includes:

1. Interaction of cosmic rays, such as protons, alpha particles and electrons, with the detector.
2. Induced radioactivity in the spacecraft from isotopes produced by spallation during transition through regions of high charged particle density.
3. Cosmic X-ray background produced by the superposition of many weak active galactic nuclei (Fabian & Barcons, 1992, and references therein).
4. With data of high spectral resolution and somewhat poorer S/N, weak lines are not measurable and must be disregarded, complicating the determination of the detector background counting rate. This can lead to an overestimation in the background, causing the intensities of spectral lines to be underestimated.

It is typical that these components vary in time and must be parameterised. The first two components constitute the internal detector background. Model parameters are adjusted to fit a set of dedicated *PCA* observations of the blank-sky. Section 3.3.2 in Chapter 3 contains a more detailed discussion of the modelling of the detector background. Several design features lead to a lower and less variable background than in previous missions. The *PCU*s use an aluminium collimator rather than iron and the lower Z material has a lower interaction cross section with particles and γ rays. Each *PCU* also has a graded shield constructed of tin and tantalum to provide passive additional background reduction.

An area of the Earth's magnetic field that is particularly weak resulting in a high charged particle flux is known as the South Atlantic Anomaly (SAA). The low Earth orbit of *RXTE* must pass through the SAA enduring high charged particle flux rendering the instrumentation unusable. It must be shut down for this period because the charged particle density is so high that the detector risks being severely damaged if it is activated. Highly charged particles would swamp the high voltage anodes causing serious breakdown problems. The low Earth orbit also minimises cosmic ray fluxes and charged particle backgrounds which are higher at the Earth's poles than the equator. A sun-shield also prevents direct illumination of scattered solar X-rays. The front propane layer reduces the background due to electrons and combined with the outer anodes and the last xenon layer in the xenon volume forms an anti-coincidence layer surrounding the main detector volume. The background reduction and anti-coincidence features reduce the internal background by a factor of 20 (Glasser & Odell, 1994).

The history of X-ray detectors in astronomy and in particular the *RXTE* mission were discussed in this chapter along with the principles behind the detectors on board the satellite. Data acquisition and technical aspects determining the calibration of the *PCA*, such as factors that contribute towards the background as well as how the energy to channel relationship is calculated amongst other factors used to calculate the *PCA* response matrix, were also discussed. The process of creating light curve and spectral files for analysis is discussed in Chapter 3.

Chapter 3

Data Reduction and Analysis

This chapter describes how the data, acquired in Chapter 2, are screened to remove periods of bad data. The process of creating light curve and spectral files and the corresponding background and response files for analysis, including corrections for deadtime in the detector are also discussed.

Data reduction is performed using the `FTOOLS` library (Blackburn, 1995) supplied by the High Energy Astrophysics Science Archive Research Centre[1] (`HEASARC`). A set of recipes containing information about the various aspects of reducing *RXTE* data can be found in `The` *`RXTE`* `Cook Book`[2]. More information pertaining to the *RXTE* data files, *PCA* Issues, data screening, extracting light curves and spectra and the time systems used can be found in `The ABC of XTE`[3].

3.1 Experiment Data System

The final on-board instrument is the Experiment Data System (*EDS*). The *EDS* is a microprocessor-based electronics package that controls data acquisition and formatting for the *PCA* and *ASM*. It consists of eight event analysers (*EA*s), of which six are dedicated to processing *PCA* data and the remaining two process the *ASM* data. The *EA*s analyse incoming data streams in parallel capable of recording up to 10 different configurations to tailor the observation to the scientific

---

[1] http://heasarc.gsfc.nasa.gov/ftools

[2] http://heasarc.nasa.gov/docs/xte/recipes/cook_book.html

[3] http://heasarc.nasa.gov/docs/xte/abc/front_page.html

goals.

For every observation data is collected in two standard modes providing a common format for instrument monitoring. This makes archival research easier and makes it possible to compare observations of different sources. The Standard 1 format has a time resolution of 0.125s with no energy information, while the Standard 2 format has a time resolution of 16s and 129 energy channels covering the full energy range of the *PCA* detectors.

Despite the large number of possible data configurations (over 650[4]) there are two basic data formats for science data: science array containing regularly spaced binned data and science event containing data for each event registered.

The data presented in this thesis uses the standard 2 configuration since it has good temporal and spectral resolution, therefore this chapter will focus on the extraction of this format. The xenon volume contains three layers that are treated separately; since the objects presented in this thesis are faint only the top layer will be used. The top layer has the advantage that it detects 90 per cent of the cosmic photons, but has only 50 per cent of the internal background improving the signal to noise for fainter objects.

3.2 Screening

The first step in reducing data is to create a filter file. The filter file spans the entire observation and contains housekeeping data that can be used to identify periods of good data. `xtefilt` is used to generate the filter file. The filter file contains the status of the instrument during the observation and using the `FTOOL maketime` events can be screened from the science data. A Good Time Interval (`GTI`) file is created based on logically combining screening criteria. The following criteria were used:

- The number of *PCU*s on. Some of the *PCU*s suffer breakdown and automatically switch themselves off if they are not regularly rested. This means that any individual observation may contain data ranging from 1 to 5 *PCU*s. Observations in this thesis were extracted

---

[4] a full list of available configurations is available via anonymous FTP at legacy.gsfc.nasa.gov

individually for all *PCU* combinations during each observation and scaled for a count rate for 3 *PCU*s, the most common number of *PCU*s on at any one time.

- Elevation. The instantaneous angle between the Earth's limb and the target subtended by the spacecraft. The Earth's atmosphere absorbs X-rays at preferentially lower energies so the source spectrum becomes distorted at low elevation angles. The elevation angle will also show Earth occultations. Data with an elevation less than 10 degrees was filtered.
- Pointing offset. The difference in detector pointing and object position changes regularly by a small factor ($\sim 10^{-3}$ degrees) due to the *HEXTE* rocking. There may also be slew data included at the start or end of the data set. An offset of less than 0.01 degrees was used.
- `SAA` passages. High particle fluxes during `SAA` passages induce radioactivity in the detector that dramatically increase the background, lowering the signal to noise, especially important for the weak sources presented in this thesis. Data up to 10 minutes after the `SAA` passage was discarded.
- Electron contamination. The *PCA* is subject to contamination from electrons trapped in Earth's magnetosphere or from increased solar activity. Such electrons are measured in the anti-coincidences layers of the detector but increase the background at low energies. Data is screened and not used with an electron ratio, the ratio of veto rates in the detector, above 0.1.

Figure 3.1 shows a plot overview of a section of the 1996 *RXTE* observation of SS Cygni. The top panel shows the light curve, the middle panel shows the electron background, where the dotted line represents the upper discriminator level used to extract the data. The bottom panel shows the state of the instrument during the observation including how many *PCU*s were switched on or off and their duration. It also shows `SAA` passages (if any). The `GTI` shows the good time used in the extraction process.

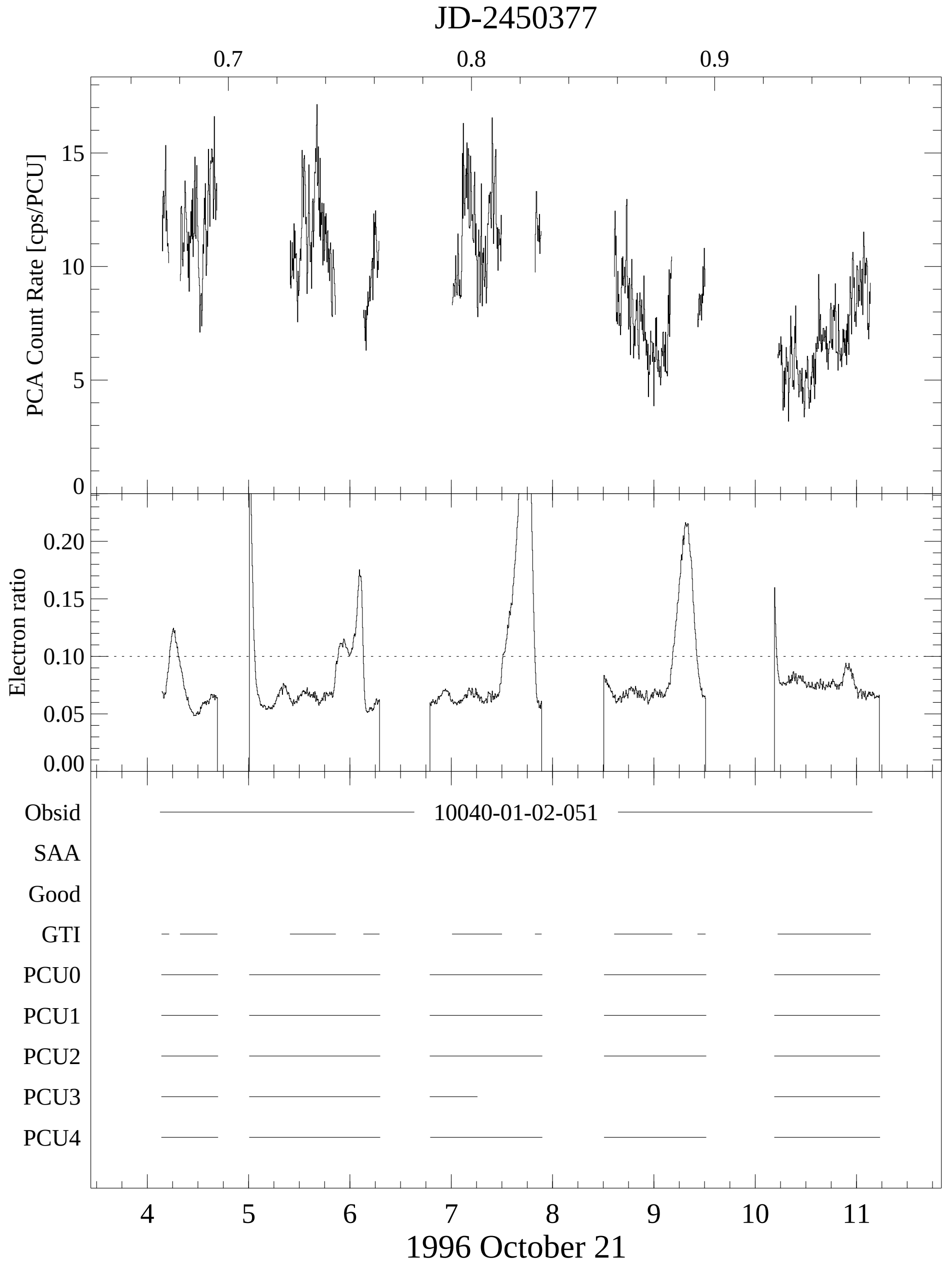

Figure 3.1: A section of the 1996 *RXTE* observation of SS Cygni. The top plot shows the *PCA* light curve, below is a plot of the electron ratio with the dotted line representing the screening criteria used in the data extraction process. The bottom panel shows a representation of the state of the *PCU*s with a solid line being when the detector is switched on. The `GTI` is the good time that was used in the extraction process.

3.3 Extracting Data Files

3.3.1 Source Files

Light curve and spectral files are both created using either `saextrct` for science array data or `seextrct` for science event data. The file created, from the `GTI` information, chosen detector, layers is a standard Level 2 FITS file.

3.3.2 Background

The *PCA* is a non-imaging instrument and for both light curves and spectroscopy thus the background must be based on an a priori model. The `FTOOL` `pcabackest` is used to create the synthetic background. The files generated are very similarly to Standard 2 data files so can be extracted via the process explained above using `saextrct`.

The background models for the *PCA* have components quite similar to those for the *Ginga* Large Area Counters (Hayashida et al., 1989). Model files contain data from several high latitude background pointing observations sorted by quantities such as position of the spacecraft with respect to the `SAA`. Modelling matches the observation conditions to that of the background model file. Currently there are two models used, depending on count rate: the faint sources model, $L7/240$[5] model, is used for rates $\lesssim 40$ counts s^{-1} pcu^{-1}, otherwise the bright `VLE` model is used.

Current background models have linear dependencies on $L7$ (or `VLE`) rate, the radioactive decay term and mission elapsed time. For each channel, i, the background model is

$$BKG_i = A_i + B_i \times L7 + C_i * DOSE + D_i \times (t - t_0) \tag{3.1}$$

A_i, B_i, C_i, D_i are the fit coefficients $L7$ is the $L7$ rate in a *PCU*, $DOSE$ is the particle dosage summed over individual passages through the `SAA` and decayed by a 240 minute folding timescale, t is the epoch time. The parameters in the model are adjusted to fit a set of dedicated *PCA* observations of the blank-sky. Once a good fit is achieved the model can be applied to other obser-

---

[5] $L7$ is the name of the housekeeping rate that characterises the X-ray background well. 240 refers to a radioactive decay timescale of approximately 240 minutes describing the combined effect of several radioactive elements.

vations. Jahoda et al. (2006) fit multiple, dedicated *PCA* background pointings. Each pointing had a slightly different set of fit coefficients so a weighted average was taken, therefore the background model represents an 'average' patch of high latitude sky. The remaining count-rate variations after background subtraction is measure of systematic error. Due to the large effective area of the *PCA* the error is dominated by systematic error rather than Poisson error.

The statistical error on the background is related to the amount of data that went into the background model and not the length of the observation[6]. Thus the error on the background spectrum generated by `pcabackest` is overestimated and incorrect[7] since it is based on the average of a huge amount of data. For observations of faint sources the systematic errors in the count rates are reported by Jahoda et al. (2006) who determined that un-modelled variations in the instrumental background is <2 per cent below 10 keV and <1 per cent between 10 – 20 keV.

A qualitative way to check how good the background model is shown in Figure 3.2. The source spectrum is plotted without subtracting the background, with the predicted background spectrum over plotted. For objects in this thesis the spectrum above 20 – 30 keV is dominated by the background. The source and background spectra can be compared at these higher energies. For a realistic background estimation the source and background spectra should lie on top of one another. Figure 3.2 shows above ~ 25 keV the predicted background is a good representation of the true detector background.

Deadtime

Each *PCU* can only process one event at a time. The processing takes a finite amount of time (approximately $10\mu s$ for lower energy X-rays) rendering the detector unable to process another event. This limitation results in detector deadtime, which is dependent on count rate. For low count rates the deadtime will occur in gaps during events, however, at higher count rates as the time between events approaches the deadtime a number of events will arrive before the detector can detect them. This results in a count rate that is lower than expected, the signature of deadtime.

---

[6] http://astrophysics.gsfc.nasa.gov/xrays/programs/rxte/pca/chisquare.html

[7] http://astrophysics.gsfc.nasa.gov/xrays/programs/rxte/pca/chisquare.html

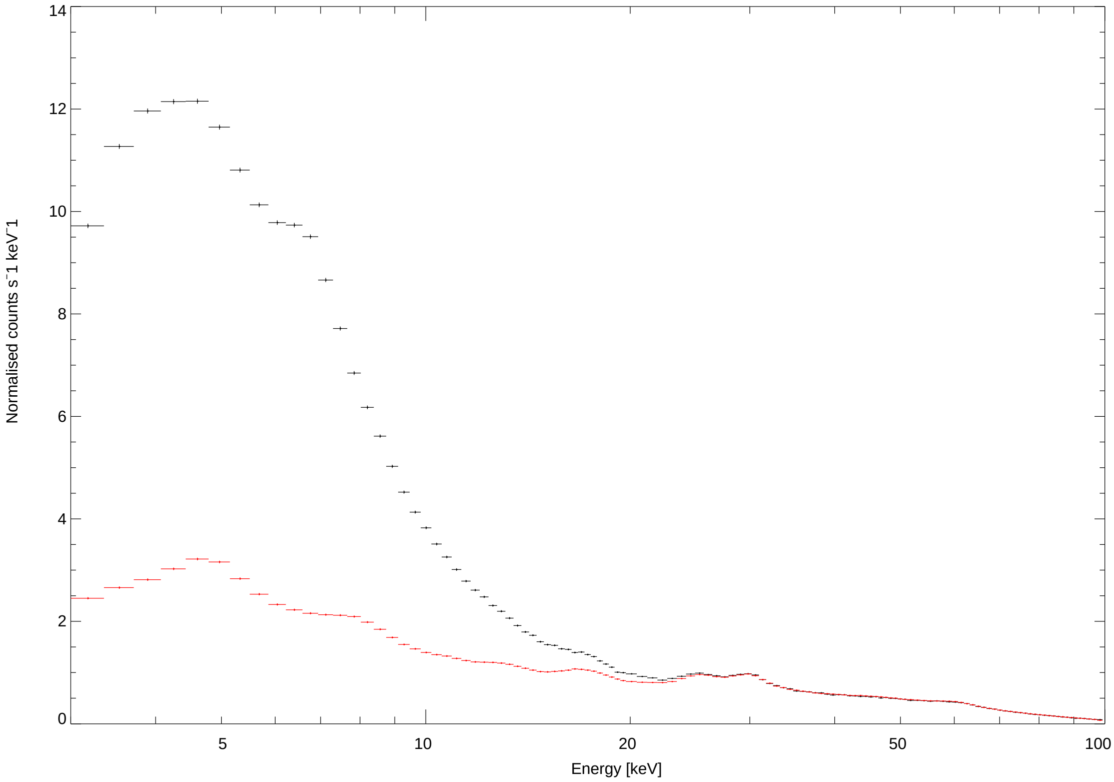

Figure 3.2: The source spectrum, before background subtraction, is shown in black and the estimated background spectrum calculated by `pcabackest` is shown in red during an outburst of SS Cygni.

The deadtime fraction is calculated as the total count rate multiplied by the length of deadtime caused by an event in the *PCU*. Events include: good xenon events detected once in the main volume; propane events detected in the propane veto layer; coincident events (mostly due to particles) that are detected in more than one anode simultaneously; very large events (`VLE`) which deposit $\gtrsim$ 75 keV in the detector possibly causing saturation. When a `VLE` event occurs in an anode chain the detector has a preset deadtime window of duration to allow the large event to clear the detector. This deadtime window must be taken into account in calculating the overall deadtime. Deadtime is not the sum of the individual *PCU* deadtimes since an event in one *PCU* does not cause deadtime in another *PCU*.

All events cause deadtime in the detector and must be taken into account. The deadtime fraction is calculated as the sum of the count rates of all events described above multiplied by their respective number of events. This is then divided by the number of detectors on during the observation. The deadtime correction is then the inverse of 1 minus the deadtime fraction (`DTF`).

$$DTF = \frac{\text{count rate} \times N_{counts}}{N_{pcu}} \tag{3.2}$$

The exposure must then be adjusted accordingly by dividing by the deadtime correction (`DCOR`).

$$DCOR = \frac{1}{(1 - DTF)} \tag{3.3}$$

The corrected exposure is then written to the spectrum file. The exposure in the background spectrum must also be corrected, however, the count rate generated by `pcabackest` (Section 3.3.2) is used instead of the xenon volume source rate. The same factors used to calculate the detector deadtime are also used to calculate the background deadtime. The count rates for systems presented in this thesis are low enough that the deadtime will not make a significant impact.

3.3.3 Response

The response matrix is dependent on several factors intrinsic to the detector at the time of the observation. For this reason it is very important to match the instrument response to the correct mission epoch. *PCA* response matrices are divided in two parts to independently model factors that effect the detector response: the Redistribution Matrix Function (`RMF`) accounts for the redistribution of photon energy amongst detector channels by the detecting medium; and the Ancillary Response File (`ARF`) accounts for the detector windows and collimator response. The two matrices are created and then combined, using `pcarmf`, into a single response matrix (`RSP`) to be used by `XSPEC` for spectral analysis.

The energy calibration matrix is determined from which detectors and layers were used to extract the source spectrum as well as the high voltage gain in the detector, a slow drift in the detector gain is also accounted for. Any corrections required by the *EDS* are applied and the matrix is then binned according to the binning in the input spectrum file. The response also takes into account an offset in the instrument pointing and spacecraft jitter during the observation in an ancillary response matrix.

Systematic effects in the detector response are still not well understood. Detailed analysis by Jahoda et al. (2006) determined that the energy calibration has deviations of <1 per cent using power law fits to the Crab Nebula. It is common to find many authors applying a systematic error of between $0 - 2$ per cent to *RXTE* data (see Table 4.3 in Chapter 4). Further analysis to understand the systematic error required by the data is presented in Section 4.4.1 in Chapter 4 and Section 7.4 in Chapter 7. It was found that a systematic of 0.5 per cent was suitable on the data and also 0.5 per cent on the background.

3.4 Combining Spectra

The extraction process described above creates several data files, one of each light curve and spectrum file with associated background and response files corresponding to every configuration of the satellite during the observation. A configuration change can be caused by a detector being cycled off and on to reduce break down. To properly analyse the spectra it must first be combined into a single file.

Since photon arrival times are lost during the extraction process it is not possible for spectral fitting programs to be able to determine the number of *PCU*s data was collected on. This makes it important that spectra should only be combined when all data is in the same spectral state to be able to calculate the correct instrument response. Combining the source and background data files is straightforward: the total counts is the sum of the individual counts and the total exposure is the sum of the individual exposures in each respective file. The corresponding responses should be combined by weighting the background-subtracted counts, rather than by exposure.

Using `mathpha`, from the `FTOOLS` package (Blackburn, 1995), mathematical operations can be performed on spectral data files, thus it can be used to combine the separate spectral files into a single file. Then `grppha` is used to redefine the binning and the systematic errors associated with each channel in the spectral file.

3.5 Spectral Analysis

The detector measures photons counted, C, within a detector channel, I, this can then be used to calculate the spectrum of the source, $f(E)$. Before the spectrum of the source can be predicted characteristics of the instrument must be taken into account, this is encapsulated in the instrument response $R(E, I)$. It gives the probability of a photon with energy E being detected in channel I. (The detector response is discussed in depth in Sections 2.3.2 and 3.3.3). The spectrum is related to the actual source spectrum by

$$C(I) = \int_0^\infty f(E)R(I, E)dE \tag{3.4}$$

The complexity of the response matrix in Equation 3.4 prevents direct calculation of the source spectrum. An alternative approach is to choose a model spectrum and use Equation 3.4 and fold it through the X-ray detector response.

By minimising the deviation between the predicted model spectrum and measured data it is possible to obtain a 'best fit' to the data. The minimisation is typically done by a Levenberg-Marquardt algorithm, see Bevington & Robinson (1992). The most commonly used fit statistic for determining the best fit model is χ^2, which is defined as follows

$$\chi^2 = \sum \left(\frac{C(I) - C_p(I)}{\sigma(I)} \right)^2 \tag{3.5}$$

Where $C_p(I)$ is the predicted counts and $\sigma(I)$ is the error for channel I. The count rates (per *PCU*) for the systems presented in this thesis are high enough to ensure that the χ^2 statistic is appropriate. The χ^2 statistic allows us to easily determine the level of confidence in the resulting fit. As a general rule of thumb the reduced χ^2 (χ^2 per degrees of freedom, ν, which is calculated as the number of channels minus the number of model parameters) should be approximately equal to 1. A χ^2_ν much above one indicates a poor fit, which may be due to the wrong model being chosen or the uncertainties on the data being under estimated. Similarly a χ^2_ν less than one indicates that the model is over parameterised or the errors on the data have been over estimated.

To calculate the uncertainty (confidence interval) of an interesting model parameter that parameter is fixed at a new value and a new best fit is found, resulting in a new χ^2. The chosen parameter is then varied and re-fit until a fit is found such that the chi-squared has increased by the required $\Delta\chi^2$. The confidence interval are tabulated by Lampton et al. (1976).

Table 3.1 contains a list of the data sets that were analysed in this thesis. It presents the observation proposal number, year of observation and data of the observation, the number of continuous segments in the observation, the exposure time and the gain setting the *PCA* was in during the observation.

Table 3.1: Log of pointed *RXTE*/*PCA* observations for all objects studied in this thesis.

Object	Proposal ID	Year	Start - End date	Number of observations	Total exposure [ks]	Gain epoch
SS Cygni	P10040	1996	Oct 09 - Oct 21	25	282	3
	P20033	1997	Mar 01 - Jul 02	42	83	3
	P40012	1999	Jun 07 - Jun 21	20	73	4
	P50011	2000	Mar 05 - Jun 03	185	171	4,5
	P50012	2000	Aug 23 - Jan 18	15	55	5
	P90007	2004	Sep 19 - Jan 25	33	178	5
U Gem	P20035	1997	Nov 07 - Dec 01	25	208	3
	P80011	2004	Feb 27 - Mar 14	24	155	5
SU UMa	P60005	2001	Mar 25 - Jun 21	193	336	5

Chapter 4

Spectral Analysis of SS Cygni in Outburst

4.1 Introduction

SS Cygni was the first dwarf nova to be detected in the soft X-ray band during a scanning rocket flight (Rappaport et al., 1974). It was later observed to emit in both soft and hard X-rays (Heise et al., 1978). Further observations provided a more detailed picture of the X-ray behaviour; the soft X-ray emission was seen to be well correlated with the optical outburst, whilst the hard X-rays were equally strongly anti-correlated and quenched to below the quiescent level (Ricketts et al., 1979; Watson et al., 1985).

Theoretical explanations for this behaviour were given by Pringle (1977), Pringle & Savonije (1979) and Patterson & Raymond (1985a). They showed that as the dwarf novae system enters outburst the accretion rate and the X-ray emission from the boundary layer also increases. The boundary layer becomes optically thick to the hard X-rays and only thermalised soft X-rays are emitted, resulting in a softer X-ray component as the accretion rate becomes much larger than 10^{16} g s^{-1}.

Observations of SS Cygni made during quiescence, using the *Ginga* satellite, showed that the energy spectrum was well reproduced by a thermal bremsstrahlung continuum with iron line emission (Yoshida et al., 1992). The iron line centre, at 6.88 keV, was inconsistent with the fitted plasma temperature of 17 keV. It was suggested that either the plasma was not in ionisation equilibrium or the line energy was a blend of lines from other iron states. Later work, also using data from *Ginga* when the source was in decline from outburst, showed that a similar model required a large equivalent width, which could not be generated by the blending of different ionisation states (Ponman et al., 1995). A two-temperature model for the hot plasma was suggested.

Archival spectra of SS Cygni, from the *Ginga* and *ASCA* satellites during quiescence and outburst, were fitted with single and multi-temperature thermal plasma models. A reflection component was also fit and was found to have a larger contribution in the outburst spectrum supporting models where the inner disc is disrupted (Done & Osborne, 1997). The observed accretion rates would be about two and a half orders of magnitude higher than predicted by the disc instability model, (e.g., Hameury et al., 2000), if the X-rays are emitted by a hot boundary layer that extends down to the white dwarf surface (Pringle & Savonije, 1979; Tylenda, 1981; Patterson & Raymond, 1985b).

Multi-wavelength observations covering the transition into and out of outburst were simultaneously observed in the optical, extreme ultraviolet and hard X-ray bands by Wheatley et al. (2003). These observations allowed the flux evolution through outburst to be analysed. The X-ray rise occurred 0.9 – 1.4 days after the optical and 0.6 days before the extreme ultraviolet rise. The coincidence of the X-ray fall and extreme ultraviolet rise indicates that both components originate in the boundary layer. Quasi periodic oscillations were also detected in the *EUVE* light curves. Mauche et al. (2001) suggested that the oscillations originated in the boundary layer. Quasi periodic oscillations were not detected in the X-ray band, which were most likely too hard to be observed.

SS Cygni was observed in X-rays using the *ASCA* satellite during an anomalous outburst, the X-ray count rate was found to be higher in optical outburst than in quiescence rather than suppressed (Baskill et al., 2005). The observations took place during an unusually faint quiescent period. In addition the X-ray spectrum during outburst was softer than during quiescence as expected. The high spectral resolution of the *ASCA* CCD detectors were used to constrain a multi-temperature emission model for SS Cygni. Baskill et al. (2005) found that the outburst spectrum was clearly dominated by contributions from cool gas accounting for the low hardness ratios of dwarf novae in outburst. Spectral fitting also favoured the inclusion of an iron emission line at 6.4 keV which was taken as an indication of a reflection component in the spectrum. A reflection component was not modelled because of the low effective area of the *ASCA* detectors above 10 keV.

Observations of SS Cygni using the *Chandra HETG* found the quiescent spectrum to be well reproduced by a cooling flow model, indicating that the source of X-rays is a cooling plasma settling onto the white dwarf (Mukai et al., 2003). During both outburst and quiescence X-ray emission lines were resolved for the first time (Rana et al., 2006). The spectrum required a strong fluorescent line in quiescence indicating the presence of a reflection component, the equivalent widths of the lines were also consistent with a reflection origin. In outburst and quiescence the Fe `XXV` triplet (at 6.7 keV) was found to be present indicating plasma temperatures of $\gtrsim 3 \times 10^7$ K while the ratio of Fe `XXVI/XXV` indicated a higher ionisation temperature during quiescence than in outburst. In quiescence the spectrum was dominated by hydrogen like line emission which was replaced by helium like line emission in outburst (Okada et al., 2008). In quiescence the line emission was found to arise from the boundary layer.

Outburst and quiescent observations using the *XIS* detector on the *Suzaku/Astro-E2* satellite were well fit using a multi-temperature thermal plasma model, narrow 6.4 keV iron line and reflection component (Ishida et al., 2009). The temperature of the plasma during quiescence was found to be significantly higher than that during outburst and a sub-solar abundance of heavier elements was found. The reflection component was also found to be higher in quiescence, attributed to reflection from both the accretion disc and white dwarf surfaces. This is puzzling suggesting that the disc does extend down to the white dwarf surface during quiescence, contradicting the conclusions of Done & Osborne (1997).

This chapter explores the evolution of spectral parameters, with reflection being of particular interest, of SS Cygni during outburst. In Section 4.3, the time series analysis first discussed by Wheatley et al. (2003), is briefly revisited before detailed spectral analysis of the 1996 outburst is presented. Two representative spectra are used to create a model which is then tested with all spectra in Section 4.4.

4.2 Observations

The observations of SS Cygni began on 1996 October 9, continuously for 2 days, coinciding with the beginning of an outburst and for 3 days at the end of outburst and are shown in Table 4.1. The total exposure was 118 ks and 164 ks respectively, with gaps only due to Earth occultations and the passage of the spacecraft through the South Atlantic Anomaly (SAA). Data were measured using the proportional counter array (*PCA*) experiment on *RXTE* (Bradt et al., 1993). Consisting of 5 identical xenon-filled proportional counter units (*PCU*) (Jahoda et al., 1996) sensitive to X-rays in the energy range $2 - 60$ keV. See Chapter 3 for a more detailed description.

The *RXTE PCA* provides low-resolution X-ray spectroscopy. For spectral analysis, the data were extracted using the `FTOOLS` package, version 6.1.2, provided by the High Energy Astrophysics Science Archive Research Centre[1]. Only the top xenon layer was used and the *PCA* data were extracted in Standard-2 binned mode. `saextrct` version 4.2e was used to produce light curves with a time resolution of 16 seconds and spectral files binned into 129 channels. Data were excluded where the elevation above the Earth's limb was less than 10 degrees, the ELECTRON2 ratio was greater than 0.1 and the time since SAA passage was under 10 minutes. See Chapter 3 for a more detailed explanation of the extraction process. The background and response matrix were estimated using `pcabackest` version 3.0 and `pcarsp` version 10.1. Data from different detector configurations were extracted as separate spectra and re-binned using `rbnpha`, version 2.1.0. Spectral fitting was carried out using the `XSPEC` (Arnaud, 1996) fitting package version 11.3. All error bars quoted are $\Delta\chi^2 = 1$ (68 per cent confidence level for one free parameter).

The X-ray light curves will be compared with the long term optical light curves obtained by the American Association of Variable Star Observers[2] (*AAVSO*). The *AAVSO* is an amateur organisation who monitor a large number of variable stars, mainly in the visual band. They provide an invaluable resource, with a continuous record of observations dating back to the

---

[1] http://heasarc.gsfc.nasa.gov/ftools

[2] http://www.aavso.org

Table 4.1: Log of pointed *RXTE*/*PCA* observations of SS Cygni used in this analysis.

Proposal ID	Year	Start - End date	Number of observations	Total exposure [ks]	Gain epoch
P10040	1996	Oct 09 - Oct 21	25	282	3

discovery of SS Cygni (Pickering & Fleming, 1896).

4.3 Analysis of Representative Spectra

The *AAVSO* optical light curve along with the *RXTE* X-ray light curve and hardness ratio beneath is shown in Figure 4.1. As is typical with fast-rise outbursts of SS Cygni the optical light curve initially rose slowly then more rapidly until reaching a maximum of approximately $m_{vis} \sim 8.5$ mag. The light curve remained at its maximum for about 1 day before starting its decline and returning to quiescence, nearly 13 days after the start of the outburst on JD 2450366. The rise in the X-ray was delayed by 0.9 – 1.4 days after the start of the outburst (Wheatley et al., 2003). Almost as soon as the X-ray maximum was reached the flux declined to near zero in 3 hours. The recovery out of outburst took a day and a half.

To examine the spectral variation in the hard X-ray flux the *RXTE* counts were divided into soft, S, and hard, H, bands, to form the hardness ratio, H/S. The bands were roughly split so there was an equal number of counts in each band; $2.3-4.8$ keV in the soft band and $4.8-20.3$ keV in the hard band. The quiescent spectrum was hard which rapidly became soft in outburst on JD 2450367, the H/S softened from 1.2 to 0.9, with a slow transition back to quiescence.

When `saextrct` generates the data files the error is calculated as the square root of the number of counts in the data file. This is correct for the data, however, the background is estimated from the average of a huge amount of data and so the resulting error on the background is overestimated[3]. The statistical error on the background is related to the amount of data used to create the background model and not the length of the observation. For initial fitting the background error column was set to zero. Since this underestimates the error on the background it will result in the reduced χ^2_ν being greater than 1. The systematics will be further studied in

---

[3] http://astrophysics.gsfc.nasa.gov/xrays/programs/rxte/pca/chisquare.html

Section 4.4.1 in this chapter and in Chapter 7.

Two spectra were taken, one before and one after the first dramatic spectral change. The chosen spectra are labelled in Figure 4.1 and will be referred to as *spectrum* 1 and *spectrum* 2 throughout this chapter. These representative spectra were fit with a single temperature model upon which components were progressively added to develop a complex model that described both states well.

4.3.1 Single Temperature Model Fits

Both spectra were poorly represented by a single temperature thermal plasma model (mekal in `XSPEC` Mewe et al., 1985, 1986; Liedahl et al., 1995). The top plot of Figure 4.2 shows the data and the model for the two spectra. Label 1 represents the spectrum prior to the spectral change and label 2 represents the spectrum after the spectral change. Their respective residuals can be seen in panels A and B. The fits are unacceptable with a χ^2_ν of 13 (43 d.o.f) for both spectrum 1 and 2. See table 4.2 for the full list of all best fit parameters for this and all other models.

The residuals for the single temperature plasma model in Figure 4.2 show an excess at around 6.5 keV and a deficit at $7-8$ keV. This was also found by Done & Osborne (1997) using data from the *Ginga* satellite and by Wheatley et al. (2003). The excess in the data at 6.5 keV shows compelling evidence for a 6.4 keV fluorescence line, therefore a narrow Gaussian component fixed at 6.4 keV for neutral iron was added to the model. More recent studies by Mukai et al. (2003) and Rana et al. (2006), using data from the *Chandra HETG*, and Okada et al. (2008), using data from *Suzaku/Astro-E2*, also detected a prominent fluorescence line.

The deficit seen near $7-8$ keV may be due to excess thermal line emission from the thermal plasma model. Reducing the strength of the thermal lines can be achieved by increasing the continuum temperature or by lowering the metal abundances. Increasing the model temperature would make the lines weaker, however, a higher temperature model would not fit the continuum. At temperatures of $7-8$ keV iron can be found in He and H like ionisation states emitting at 6.7 and 6.95 keV, reducing the abundances will reduce the emission from these states. Done & Osborne (1997) found that the relative abundance of iron with respect to lighter elements was smaller than the solar values, with best fits of $0.35-0.5$ solar (relative to abundances of

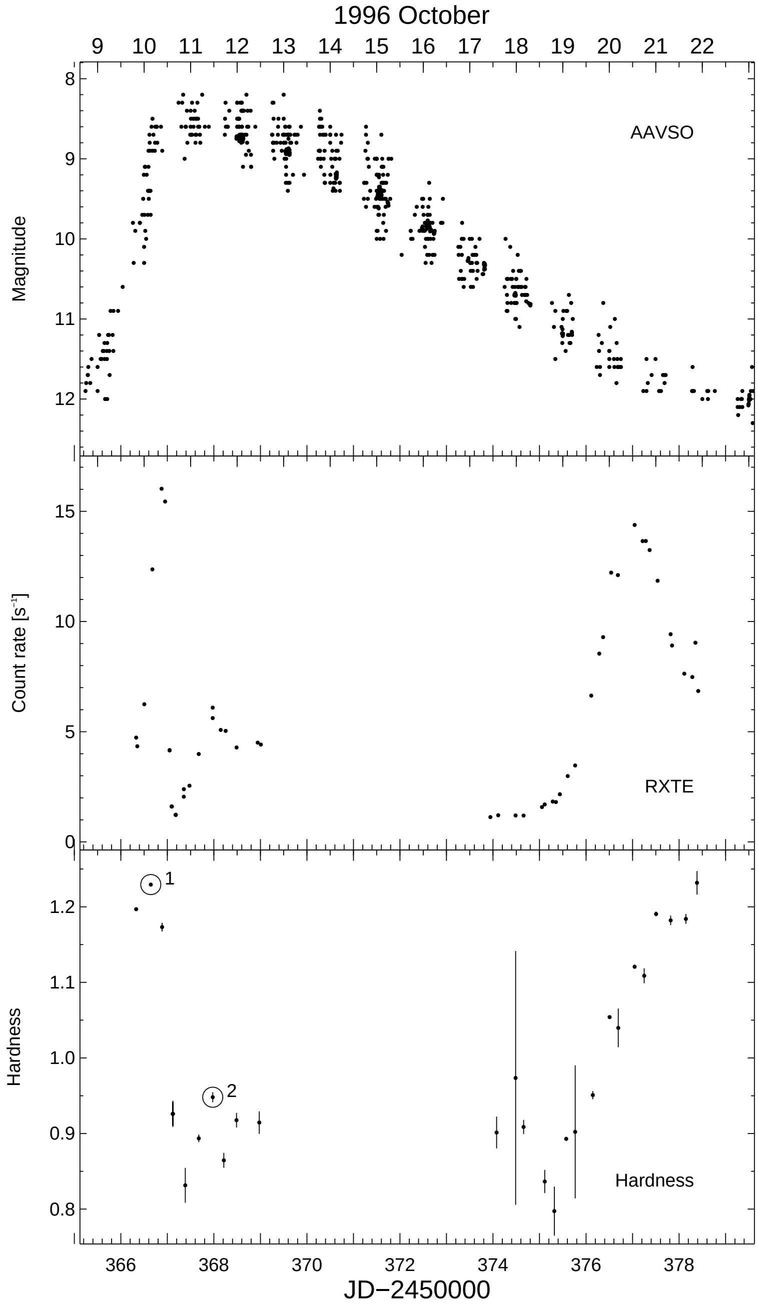

Figure 4.1: Simultaneous *AAVSO*, *RXTE* observations along with the hardness ratio. Labels 1 and 2 denote the representative spectra that were chosen to determine the best fitting models of before and after the dramatic spectral change seen in the data. The fits of these two spectra can be seen in Figure 4.2.

Anders & Grevesse, 1989). Baskill et al. (2005) also found a significant improvement to their χ^2 when they allowed the model abundances to be fit as a free parameter, resulting in sub solar abundances of 0.55 and 0.76 for outburst and quiescence respectively. The data were fitted with the free abundances with a similar improvement to the χ^2. Both spectral abundances were lower than solar levels at 0.54 and 0.45 solar respectively, resulting in a significant improvement. The F-test is used to estimate the significance of the addition of a model component. If the F-test probability is low then it is reasonable to add the extra model component. The F-test probability was smaller than 10^{-17} for both spectra with χ^2_ν of 1.53 (41 d.o.f) and 2.36 (41 d.o.f) for spectrum 1 and 2 respectively. The residuals can be seen in Figure 4.2, panels C and D. Best fit χ^2_ν values can be seen on the same figure at the end of each respective residual panel. The best fit parameters for this model can be found in Table 4.2 along with the best fit parameter values from the other models used.

4.3.2 Improving the Model

The need for a 6.4 keV line is highly suggestive of Fe Kα fluorescence emission due to illumination of cold gas, which is a strong indication that there is Compton scattering of X-rays. The equivalent widths were also consistent with those expected from a semi-infinite, plane parallel cold slab irradiated by an external source of X-rays (George & Fabian, 1991). Figure 4.2, panels E and F, shows the single temperature thermal plasma model with a narrow 6.4 keV emission line, free abundances and a reflection component (calculated from the code of Magdziarz & Zdziarski, 1995). The reflector abundances were tied to the abundances of the plasma model.

The addition of the free reflection caused both spectra to be fit with lower temperature and equivalent widths, as expected (also found by Done & Osborne, 1997). The reflection component made a greater improvement to the fit of spectrum 1 resulting in a χ^2_ν of 1.40 (40 d.o.f) with an F-test probability of 3×10^{-2}. There was no improvement in spectrum 2 and the best fit resulted in an unacceptable χ^2_ν of 2.37 (40 d.o.f). This component also failed to fully remove a faint residual excess present near $7 - 8$ keV in both spectra.

To investigate the nature of the faint $7 - 8$ keV deficit the reflection component was replaced with an absorption edge, with the edge energy fixed at 7.11 keV corresponding to the

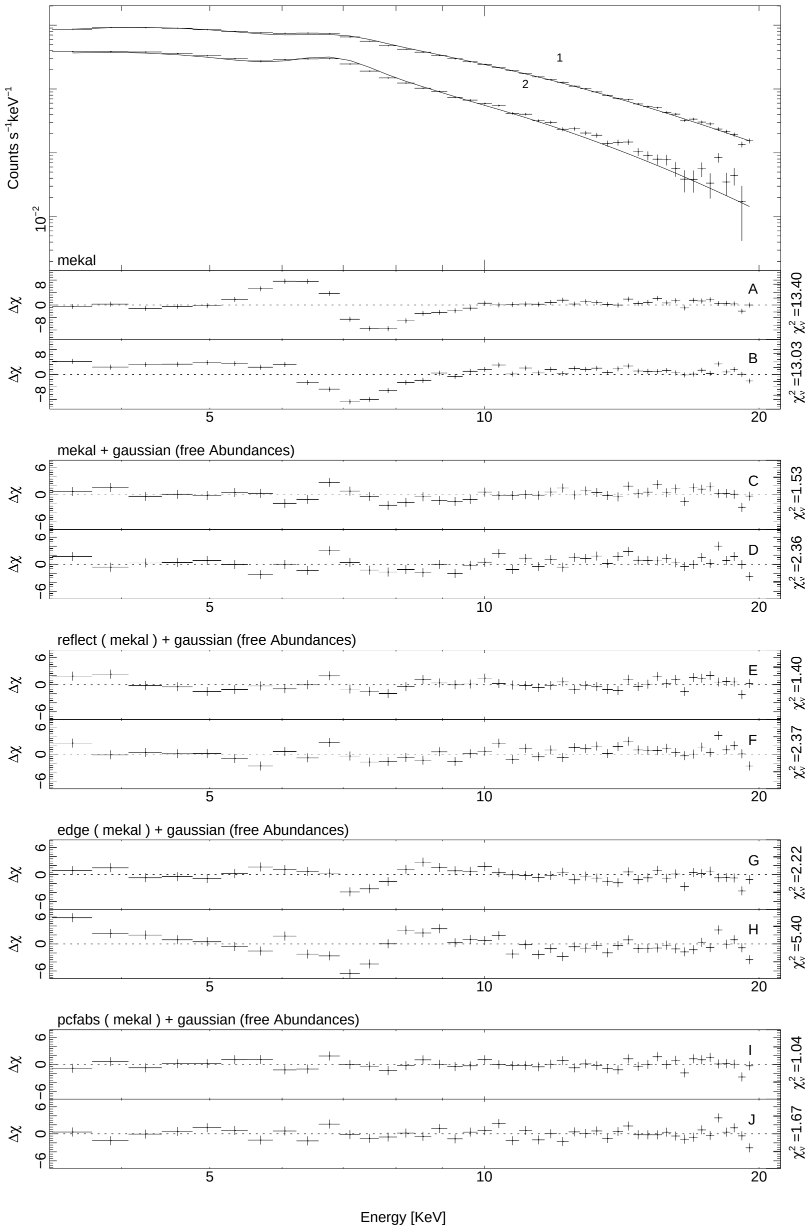

Figure 4.2: The top panel shows the data (crosses) and the single temperature continuum (curve) for the two representative spectra before to and after the first dramatic spectral change seen in the outburst data. They are the spectra labelled in Figure 4.1 as 1 (top), before the spectral change and 2 (bottom) after the spectral change. The plots below show the residuals for this model and fits to subsequent models. The upper and lower panels correspond to spectrum 1 and 2 respectively. The model, as used in `XSPEC`, is labelled above the pair of residuals, with the reduced χ^2 at the end of the individual panel.

Table 4.2: Best fit parameters for the representative spectra for all models used in the fitting. The data in this table refers to the residuals that can be seen in Figure 4.2. All errors are 68 per cent confidence for one parameter of interest ($\Delta\chi^2$ = 1.0).

Model[a]	χ^2_ν		kT [keV]		EW [eV]		A		R/τ_{max}[b]		nH [atoms cm^{-2}]		CvrFrac	
	1[c]	2[d]	1	2	1	2	1	2	1	2	1	2	1	2
m	13 (43)	13 (43)	16.8	6.3	-	-	-	-	-	-	-	-	-	-
mg	1.53 (41)	2.36 (41)	17.7	6.7	195	182	0.54	0.45	-	-	-	-	-	-
mRg	1.40 (40)	2.37 (40)	$14.3^{+0.6}_{-0.7}$	$6.3^{+0.2}_{-0.2}$	312^{+35}_{-30}	316^{+65}_{-72}	$0.46^{+0.01}_{-0.03}$	$0.44^{+0.03}_{-0.02}$	$1.1^{+0.3}_{-0.2}$	$0.7^{+0.4}_{-0.5}$	-	-	-	-
meg	2.22 (40)	5.40 (40)	$18.9^{+0.2}_{-0.2}$	$8.4^{+0.2}_{-0.1}$	202^{+16}_{-18}	$0.00^{\infty}_{0.00}$	$0.48^{+0.02}_{-0.04}$	$0.46^{+0.04}_{-0.03}$	$0.26^{+0.02}_{-0.02}$	$1.12^{+0.1}_{-0.1}$	-	-	-	-
mpg	1.04 (39)	1.67 (39)	$14.9^{+0.9}_{-0.9}$	$6.1^{+0.2}_{-0.2}$	280^{+35}_{-31}	167^{+32}_{-28}	$0.49^{+0.04}_{-0.04}$	$0.46^{+0.03}_{-0.03}$	-	-	106^{+32}_{-18}	204^{+53}_{-47}	$0.37^{+0.05}_{-0.08}$	$0.93^{+0.1}_{-0.1}$

---

[a] All models comprise of one or more of the following components:
m=mekal, R=free reflection, e=edge, p=partial covering absorber, g=gauss

[b] To save space in the table the upper column represents R and the lower column represents τ_{max}

[c] Columns labelled 1 represent best fit values of spectra 1 from Figures 4.1 and 4.2.

[d] Columns labelled 2 represent best fit values of spectra 2 from Figures 4.1 and 4.2.

K-shell edge energy of neutral iron. Although this model is not physically realistic it is, however, useful to parameterise the system. Figure 4.2, panels G and H, show the residuals for this fit. After the addition of the edge component to the model the fits resulted in a poorer χ^2_ν for both spectra with χ^2_ν of 2.22 (40 d.o.f) and 5.40 (40 d.o.f) in spectrum 1 and 2 respectively.

The absorption edge most likely did not account for the absorption in the correct part of the spectrum. The edge component was replaced by a partial covering fraction, to model a partially absorbed X-ray source such as a disc in the line of sight between the detector and X-ray source. The addition resulted in a significant improvement to both fits, resulting in a χ^2_ν of 1.04 (39 d.o.f) for spectrum 1 and a χ^2_ν of 1.67 (39) for spectrum 2. Figure 4.2, panels I and J, show the residuals for this fit. Performing an F-test calculation between the thermal plasma model with emission line, the current model shows that the improvement is significant with probabilities of 2×10^{-4} and 4×10^{-4} for spectra 1 and 2 respectively.

4.4 Full Spectral Analysis

Using two representative spectra in Section 4.3.2 a model was created that was able to describe the data. To further improve this model all data needs to be taken into account. The data was split into 23 spectra to give a good combination of time resolution and signal-to-noise. This allows the evolution of the χ^2_ν and model parameters to be studied throughout the outburst. The best fit parameters for the representative spectra to all models as well as the χ^2_ν based on fits to all spectra are presented Table 4.4. All fits were performed using systematics discussed in Section 4.4.1. This table also includes the single temperature thermal plasma model and 6.4 keV line with and without the partial covering absorber for comparison.

4.4.1 Detector Systematic Error

Only the final model in Section 4.3.2 was able to provide a satisfactory fit to spectrum 1 and none of the models resulted in an acceptable fit to spectrum 2. All models in Figure 4.2 exhibit residuals at the same energies, for example small peaks just below 7, 10 and near 20 keV and dips between $7 - 8$ and just above 10 keV. These residual features indicate that either the model is incorrect or un-modelled systematic features remain in the data. Extensive analysis of the calibration and background model for the *PCA* was carried out by Jahoda et al. (2006). They determined that the energy calibration has deviations of ≤ 1 per cent from power law fits to the Crab Nebula and unmodeled variations in the instrumental background at ≤ 2 per cent below 10 keV and ≤ 1 per cent between 10 – 20 keV. Reviewing the literature it is common to find many authors add a systematic error to compensate for properties of the detector that are still poorly understood, see Table 4.3 for a list of references for systematics used and a resulting χ^2_ν.

Instruments, such as the *PCA*, with a large effective area have a high signal to noise. The resulting systematic error associated with the detector response is dominated by uncertainties in the calibration rather than the Poisson errors. To obtain reasonable spectral parameters, the systematic error of the instrument must to be taken into account.

A series of fits were made with the systematic error selected in the range 0 – 2 per cent, as identified by Jahoda et al. (2006). The data were fitted using the current best model: a thermal plasma model with free abundances and a narrow emission line fixed at 6.4 keV with a partial covering absorber. Figure 4.3 shows the cumulative histogram plots of the best fit χ^2_ν distributions, with the cumulative plot of the χ^2 distribution (curve) on the same plot. The plots show that a systematic error of 0 and 0.1 per cent underestimates the error resulting in distributions that are greater than 1. Similarly a systematic error of between 1.3 and 2 per cent overestimate the error and result in distributions that are less than 1. A systematic error between 0.3 and 1 per cent produces a distribution that is closest to a χ^2 distribution, with a systematic error of 0.5 per cent producing the best result. Since this is within the range identified by Jahoda et al. (2006) and produced acceptable fits to the model, this value was adopted and applied to all data.

A systematic error of 0.5 per cent was chosen and applied to the data. Analysis of the fainter SU UMa data in Section 7.4 in Chapter 7, where the background dominates the data, found that a systematic error of 0.5 per cent was also required on the background. It should be noted that adding a uniform systematic error is incorrect and that the errors are demonstrably energy dependent. However, a uniform systematic results in good χ^2_ν. Fitting the representative spectrum with the systematics applied to the data reduced the χ^2_ν for all models in Figure 4.2.

Table 4.3: Systematic error used in previous *RXTE* data analysis with an approximate χ^2_ν achieved by fitting the systematic error. References with multiple systematics used systematics based on the channel range.

Systematic error [%]	Reference	χ^2_ν	Comments
0	Hanke et al. (2009)	-	-
0.8	Prat et al. (2009)	-	-
0.5	Nowak et al. (2008)	1.2	-
0.5	Suchy et al. (2008)	0.8	-
0.1	McBride et al. (2007)	0.74	-
0.3	Rothschild et al. (2006)	0.8 – 1.2	Reduced systematic until $\chi^2_\nu = 1$
0.5	McBride et al. (2006)	1.2	-
0.5	Wilms et al. (2006)	-	Calibration effects still present
0.5	Markoff et al. (2005)	-	-
0.5	Pottschmidt et al. (2005)	1	-
0.5	Nowak et al. (2005)	1.2	Most $\chi^2_\nu = 1.2$, as low as 0.6
0.5	Paizis et al. (2005)	1	Energy range 3 – 13 keV
1/0.5/2/5	Kuster et al. (2005)	-	-
1/0.5/2/5	Kreykenbohm et al. (2004)	2	$\chi^2_\nu = 0.7 - 5$, none near 1
1/0.5/2/5	Pottschmidt et al. (2003)	1 – 2	-
0.3	Pottschmidt et al. (2003)	0.9	-
0.4	Coburn et al. (2002)	1	Reduced systematic until $\chi^2_\nu = 1$
0.3/1/0.5/1/2	Kreykenbohm et al. (2002)	1 – 2	
0.3	Heindl et al. (2001)	1	-
0.25	Gruber et al. (2001)	1	-
0.3/0.4/2.4	Coburn et al. (2001)	1	Reduced systematic to get $\chi^2_\nu = 1$
1	Benlloch et al. (2001)	0.4 – 0.7	-
1/0.5/2/5	Nowak et al. (2001)	2	-
2	Coburn et al. (2000)	1	-
1/0.5/2/5	Wilms et al. (1999)	0.4 – 1.2	-
1	Heindl et al. (1999)	-	Reasonable fit
1	Stelzer et al. (1999)	1.5	-
2	Dove et al. (1998)	1.5	-

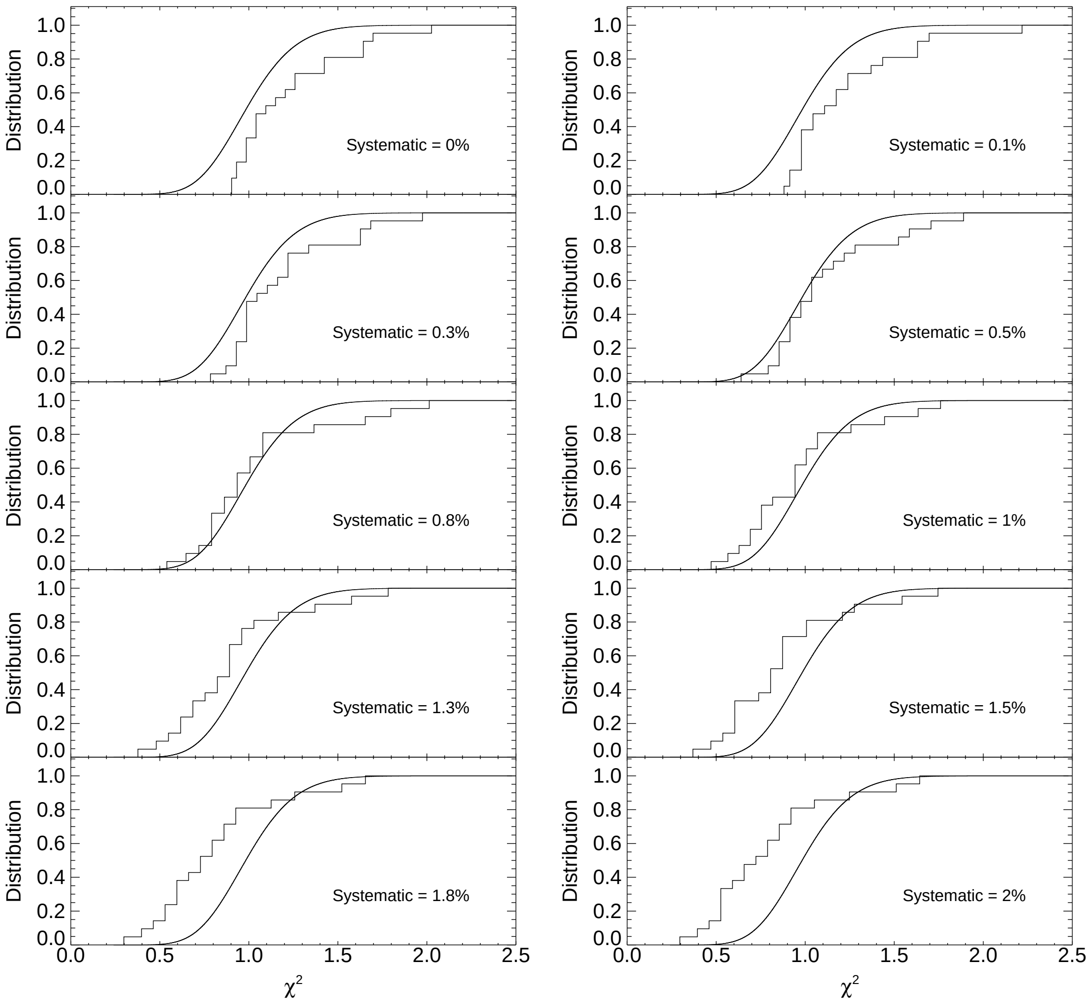

Figure 4.3: Cumulative histogram plots of χ^2_ν resulting from fits of all spectra to the thermal plasma model with a narrow emission line with partial covering absorption. The background systematic error is fixed at 0 for all fits while the detector systematic is varied from 0 – 2 per cent. The cumulative χ^2 distribution (curve) is also plotted.

However, the only model to fit both spectra well was the thermal plasma model with a narrow emission line and a partial covering absorption component. This model resulted in a χ^2_ν of 0.96 (39 d.o.f) for spectrum 1 and a χ^2_ν of 1.48 (39 d.o.f) for spectrum 2. Although the χ^2_ν for spectrum 2 was still high the χ^2_ν histogram of all spectra shows that this is broadly consistent with a χ^2_ν distribution.

4.4.2 Reflection

Adding a reflection component, with the reflection albedo fixed at 1 and the reflector abundances tied to the abundances of the plasma model, to the single temperature model with partial covering absorber and 6.4 keV line did not result in an improvement to the representative spectra. This model also did not improve the overall χ^2_ν when applied to all data (See the total χ^2_ν column in Table 4.4). Allowing the reflection to be a free parameter only improved spectrum 1, however it did significantly improve the total χ^2_ν of the fit to all the spectra. An F-test resulted in a probability of 1.0×10^{-8}. Freeing the reflection component resulted in both the reflection and covering fraction contribution in spectrum 2 being larger than that of spectrum 1. This was also accompanied by an increase in the equivalent hydrogen column. The reflection, however, was not well constrained (also found by Done & Osborne, 1997). Although it is highly unlikely for the metal abundances to change during the observation the abundance parameter for all spectra were fit as a free parameter and independently. Fitting the spectra independently allowed the minimisation to converge in a reasonable time. See Table 4.4 for the full list of all best fit parameters for this and all other models applied to all spectra. Fits to all the data using the single temperature model and partial covering component with 6.4 keV and free reflection component can be seen in Figure 4.4.

Throughout the outburst the flux was well constrained, the best fit temperature of spectrum 1 was higher than spectrum 2. The trend of all the data showed that as the system entered outburst the temperature rapidly dropped as the flux quickly rose before being quenched. The hard X-ray flux remained close to zero until the end of the outburst when both the temperature and flux began to climb. The flux reached its peak and declined back to its quiescent value while the temperature continued to climb reaching its peak at the end of the observation. The reflection and covering fraction both increased as the X-rays became quenched at the start of outburst and declined at the end of the observation when the X-rays recovered. The hydrogen column, within error, was consistent with being constant throughout the observation. It is unclear whether there is any pattern in the 6.4 keV line equivalent widths through the outburst and within the error there is only weak evidence for variability. These equivalent widths, within the error, are also broadly consistent with those found previously, (e.g., Done & Osborne, 1997; Rana et al., 2006; Okada et al., 2008)

4.4.3 Multi-Temperature Model Fits

Although the fits in Sections 4.3.2 and 4.4.2 show that a single temperature model represents the data well, fits by Done & Osborne (1997), Baskill et al. (2005) and Okada et al. (2008) were found to be more statistically acceptable using a multi-temperature continuum. Therefore the single temperature continuum model was replaced with a multi-temperature model, cemekl in `XSPEC` (built from the mekal code, Singh et al., 1996). The emission measure follows a power law in temperature, proportional to $(T/T_{max})^{\alpha}$. This allows a full range of temperatures to be fit with T_{max} and α fit as free parameters.

As with the single temperature fits, the residuals required an emission line fixed at 6.4 keV and free metal abundances. Compared to the single temperature analog, the multi-temperature model produced better fits, with a χ^2_ν of 0.94 (40 d.o.f) and 1.61 (40 d.o.f) for spectra 1 and 2 respectively and a total χ^2_ν of 1.12 (920 d.o.f) (see Table 4.4).

The requirement of the 6.4 keV line is an indication of Fe Kα fluorescence emission due to illumination of cold gas. Adding a fixed reflection component to the model with the reflector abundances tied to the abundances of the plasma model produced a good fit for spectrum 1, with a χ^2_ν of 0.96 (40 d.o.f), but resulted in a poor fit to spectrum 2 of χ^2_ν of 1.42 (40 d.o.f), however, the model was a good fit to all the data with an overall χ^2_ν of 1.05 (920 d.o.f). The overall best fit was significantly improved when the reflection was allowed to be a free parameter resulting in a best fit χ^2_ν of 1.01 (897 d.o.f). An F-test resulted in a probability of 7.0×10^{-5}. The best fit to spectrum 1 improved, with a χ^2_ν of 0.85 (39 d.o.f), no improvement was seen for spectrum 2. The best fit values for the temperature and α, of both spectra, were consistent with the quiescent

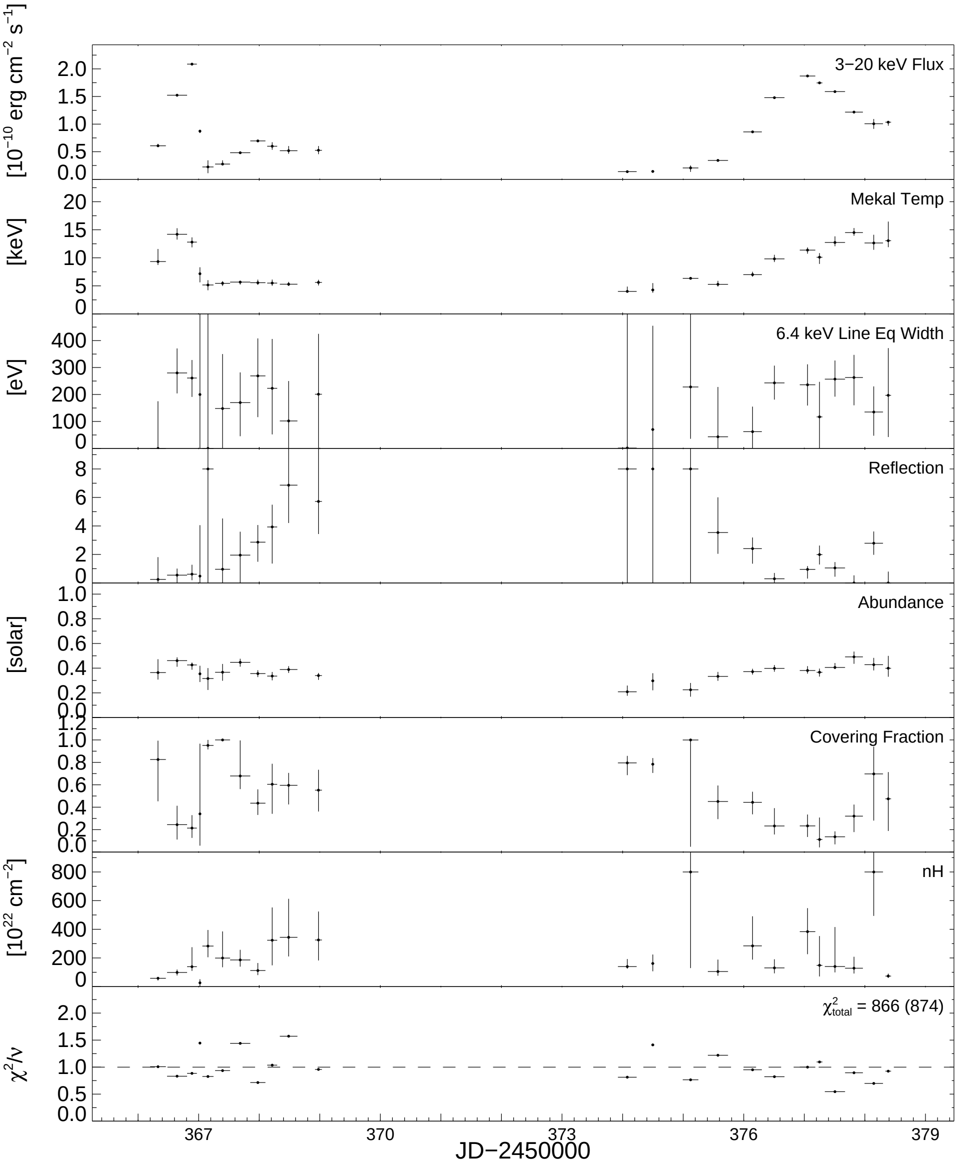

Figure 4.4: Results of fitting the twenty three spectra with a single temperature model with free abundances, partial covering component, fixed 6.4 keV emission line and a free reflection component. All errors are 68 per cent confidence for one parameter of interest ($\Delta\chi^2$ = 1.0).

Table 4.4: Best fit parameters for the representative spectra for all models used in the fitting. The first two models are included from Table 4.2 with new χ^2_ν calculated using the systematics from Section 4.4.1. All errors are 68 per cent confidence for one parameter of interest ($\Delta\chi^2 = 1.0$).

Model[a]	χ^2_{tot}	χ^2_ν		kT/T_{max} [keV]		EW [eV]		A		α		R	
		1[b]	2[c]	1	2	1	2	1	2	1	2	1	2
mg	1.23 (943)	1.17 (41)	2.00 (41)	17.9	6.7	201	184	0.53	0.45	-	-	-	-
mpg	1.06 (897)	0.96 (39)	1.48 (39)	$14.9^{+1.1}_{-0.9}$	$6.1^{+0.2}_{-0.2}$	280^{+39}_{-39}	167^{+42}_{-33}	$0.49^{+0.05}_{-0.04}$	$0.46^{+0.03}_{-0.03}$	-	-	-	-
mprg	1.06 (897)	0.94 (39)	1.52 (39)	$12.2^{+0.4}_{-0.2}$	$6.2^{+0.2}_{-0.2}$	118^{+30}_{-28}	164^{+50}_{-58}	$0.40^{+0.03}_{-0.01}$	$0.45^{+0.03}_{-0.03}$	-	-	1.00	1.00
mpRg	0.99 (874)	0.83 (38)	1.44 (38)	$14.2^{+1.1}_{-0.9}$	$5.7^{+0.2}_{-0.4}$	280^{+89}_{-86}	170^{+107}_{-127}	$0.46^{+0.03}_{-0.05}$	$0.45^{+0.03}_{-0.04}$	-	-	$0.6^{+0.5}_{-0.6}$	$2.0^{+1.6}_{-2.0}$
cg	1.12 (920)	0.94 (40)	1.61 (40)	$28.8^{+3.6}_{-3.0}$	$10.7^{+1.4}_{-0.7}$	179^{+10}_{-11}	212^{+25}_{-21}	$0.58^{+0.04}_{-0.04}$	$0.53^{+0.04}_{-0.04}$	$1.57^{+0.41}_{-0.33}$	$0.92^{+0.28}_{-0.36}$	-	-
crg	1.05 (920)	0.96 (40)	1.42 (40)	$15.3^{+1.8}_{-0.6}$	$9.0^{+0.7}_{-0.7}$	111^{+11}_{-11}	163^{+24}_{-26}	$0.42^{+0.02}_{-0.03}$	$0.48^{+0.03}_{-0.03}$	$2.95^{+1.31}_{-0.63}$	$0.83^{+0.36}_{-0.27}$	1.00	1.00
cRg	1.01 (897)	0.85 (39)	1.42 (39)	$18.7^{+3.4}_{-1.9}$	$8.2^{+0.9}_{-0.5}$	152^{+19}_{-16}	117^{+41}_{-40}	$0.48^{+0.04}_{-0.04}$	$0.46^{+0.04}_{-0.03}$	$2.76^{+1.88}_{-0.34}$	$0.62^{+0.36}_{-0.36}$	$0.5^{+0.1}_{-0.2}$	$2.0^{+0.9}_{-1.1}$
cpg	1.02 (874)	0.83 (38)	1.46 (38)	$28.7^{+3.8}_{-6.9}$	$6.2^{+0.2}_{-0.3}$	170^{+249}_{-70}	$173^{+\infty}_{-173}$	$0.46^{+0.05}_{-0.04}$	$0.46^{+0.03}_{-0.03}$	$0.72^{+1.06}_{-0.37}$	$10.0^{+0.0}_{-0.0}$	-	-
crpg	1.00 (874)	0.84 (38)	1.44 (38)	$16.5^{+1.4}_{-1.4}$	$11.6^{+1.0}_{-1.1}$	219^{+126}_{-104}	$258^{+\infty}_{-150}$	$0.43^{+0.05}_{-0.03}$	$0.52^{+0.04}_{-0.04}$	$2.70^{+7.30}_{-1.24}$	$0.01^{+0.23}_{0.00}$	1.00	1.00

---

[a] All models comprise of one or more of the following components m=mekal, r=fixed reflection, R=free reflection, g=gauss, e=edge, A=free Abundance

[b] spectra 1 the leftmost of the pair of parameters

[c] spectra 2 the rightmost of the pair of parameters

and outburst fits of Done & Osborne (1997), for fits using the same model. The best fit reflection parameters of the representative spectra indicate a larger amount of reflection in outburst than quiescence in support of Done & Osborne (1997). They found the reflection during outburst to be 2.2, consistent with spectrum 2 which fit with a reflection of $2.0^{+0.9}_{-1.1}$. Their quiescent reflection was 0.7, consistent with spectrum 1 which fit with a reflection of $0.5^{+0.1}_{-0.2}$. Multi-temperature models including a partial covering fraction were also fit, these models were not used for further analysis as the data were not able to constrain the model. See Table 4.4 for the full list of all best fit parameters for this and all other models.

As the system entered outburst the temperature rapidly dropped while the flux quickly rose before being quenched. The hard X-rays remained close to zero until the end of the outburst when both the temperature and flux began to climb. The flux reached a peak before declining back to quiescent, while the temperature continued to climb reaching a peak at the end of the observation. See Figure 4.5 for a plot of the best fit parameters. The multi-temperature continuum provides a more realistic description of the continuum, however the large errors, e.g., α, indicate that the model is barely constrained by the data. The best fit α parameters were also larger than expected, fits by Baskill et al. (2005) resulted in α of 0.16 ± 0.06 in outburst and 1.41 ± 0.09 in quiescence. However, Done & Osborne (1997) had a best fit of $0.51^{+0.35}_{-0.25}$ in outburst and also had a high α in quiescence of $2.9^{+\,\mathrm{inf}}_{-1.4}$. The spectra in Figure 4.5 (without error bars on the time axis) were poorly constrained and the best fits extend past the axis range. The contribution from the reflection continuum was not well constrained but suggests that the reflection increased at the start of the X-ray suppression and then declined as the hard X-rays recovered. It is unclear whether there is any pattern in the 6.4 keV line equivalent widths through the outburst and within the error there is only weak evidence for variability. The best fit abundances reassuringly have very similar values of ~ 0.4 solar for all spectra.

In both the single and multi-temperature fits the spectra had a lower temperature during the outburst and favoured sub-solar abundances of ~ 0.4 solar. Both models, within error, had consistent 6.4 keV line strengths of ~ 200 for the single temperature model and ~ 150 eV for the multi-temperature model, strongly indicating the presence of a reflection continuum in the spectra (George & Fabian, 1991). The higher covering fraction and hydrogen column during

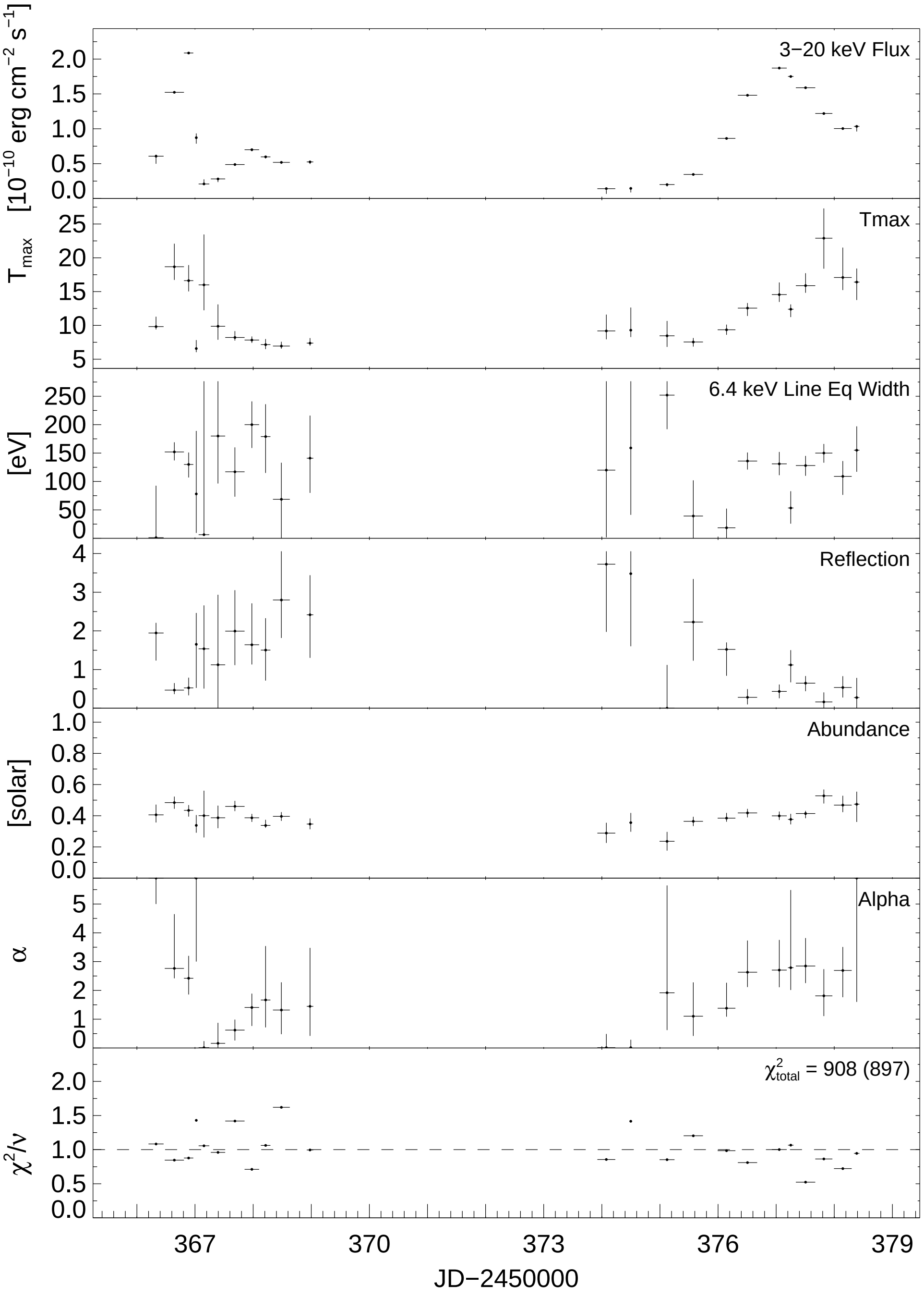

Figure 4.5: Results of fitting the twenty three spectra with a multi-temperature model with free abundances, fixed 6.4 keV emission line and a free reflection component. All errors are 68 per cent confidence for one parameter of interest ($\Delta\chi^2$ = 1.0).

outburst in the single temperature fits provide some evidence of an increased amount of absorbing gas during this period, possibly from observing hard X-rays through the disc, however this component is not needed by the multi-temperature models. When fitting reflection, the spectra favour a higher reflection in both models, however it is not well constrained in either.

4.4.4 Model Reflection

Only photons above 7 keV have enough energy to produce fluorescence photons that contribute to the 6.4 keV line emission required by the data. The 6.4 keV line provides evidence of photoionisation which is a strong indication of Compton scattering of X-rays. Spectral fits are also consistent with a reflection component being present in the data. Since the 6.4 keV line can only be produced by photons with a higher energy it is possible to get a better understanding of the reflection in the system by plotting the flux above 7 keV with the line normalisation. If the amount of reflection in the system is constant then, as the continuum emission increases the line emission will also increase. Thus the gradient of a best fit line is representative of the reflection in the system. As the flux from the X-ray source decreases the number of photons producing fluorescence line photons also decreases, thus the best fit line is expected to have an intercept that passes near to zero.

The line normalisation and the line flux above 7 keV is plotted in Figure 4.6 for the single temperature model with 6.4 keV line and a partial covering absorber. The solid line shows the best fit to all spectra, the spectra are also numbered sequentially in time (see Figure 4.4). It is clear that spectra numbered 7 – 11 do not fit this line. The dotted lines represent separate line fits. The steep line is composed of the spectra above the initial line fit as well as the group of spectra with low 7 – 20 keV flux. The spectra with high line normalisation were observed just after the hard X-rays suppression, spectra 5 and 6, observed immediately after the suppression, also fit this steeper line. These spectra are consistent with observations of the U Gem outbursts where more reflection was seen during outburst (Figure 6.14 in Chapter 6). The second line is composed of all spectra excluding those above the initial line fit. The residuals between the respective dotted best fit line and the data are plotted in the bottom panel. The two line fits resulted in gradients of 0.107 ± 0.009 and 0.053 ± 0.002 respectively (intercepts were

-0.007 ± 0.005 and -0.027 ± 0.003 respectively). The steeper gradient between the pair of line fits shows that there is a greater amount of reflection in the outburst spectra, i.e., more 6.4 keV photons were produced from photons with energy ≥ 7 keV during the period these spectra were observed.

The single temperature model used for Figure 4.6 may over predict the 6.4 keV line in outburst. At lower temperatures there will be more He like emission which may be fit by the 6.4 keV line. The multi-temperature model allows a range of temperatures to be fit resulting in a more realistic determination of the thermal lines. Therefore, the line normalisation and the line flux above 7 keV is also plotted for the multi-temperature model in Figure 4.7. This model includes a reflection component that accounts for the reflected photons, which should be removed from the data leaving only the photons that can cause reflection. After a best fit to the model was found the reflection parameter was then set to zero and the flux was calculated.

As with the single temperature plot the solid line shows the best fit to all spectra, again a number of spectra do not fit this line. The dotted lines represent separate line fits using only the spectra that lie above the solid line, whilst the second line fit is made using the remaining data. The residuals between the respective dotted best fit line and the data are plotted in the bottom panel. The line fits resulted in gradients of 0.107 ± 0.002 and 0.054 ± 0.003 respectively (intercepts were -0.008 ± 0.004 and -0.051 ± 0.003 respectively). Both Figures 4.6 and 4.7 have consistent gradients and are consistent with more reflection at the beginning of the outburst when the hard X-rays were quenched. However, it is possible that as the system entered outburst more cooler gas was present in the boundary layer there resulting in an increase in the helium like (at 6.7 keV) thermal line emission, which was blended by the detector and fit by the 6.4 keV line resulting in stronger line equivalent widths.

4.4.5 X-ray Luminosity

The spectra observed on JD 2450366.3 and 2450366.9 were used to calculate the luminosity and accretion rates representing the system in quiescence and outburst, immediately before the disc became optically thick to its own radiation. Fluxes were calculated from the best fitting model over the energy range $2 - 20$ keV. Broadband fluxes were also calculated by integrating over

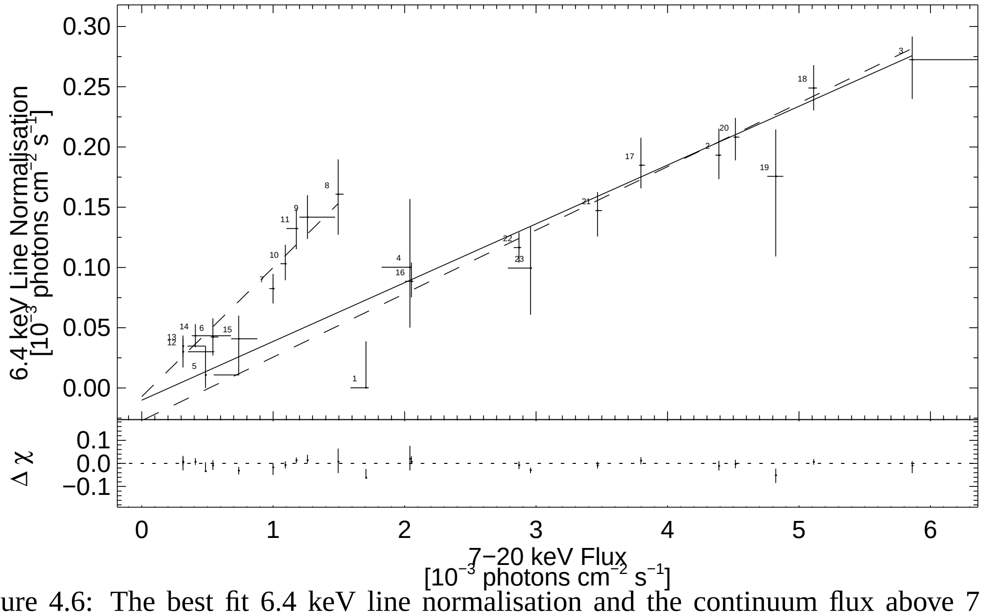

Figure 4.6: The best fit 6.4 keV line normalisation and the continuum flux above 7 keV to the single temperature model with partial covering fraction, 6.4 keV emission line and free abundances. The best fit line to all the data and separate best fit lines fitting the separate gradients are plotted along with their residuals. All errors are in the 68 per cent confidence interval for one parameter of interest ($\Delta\chi^2 = 1.0$).

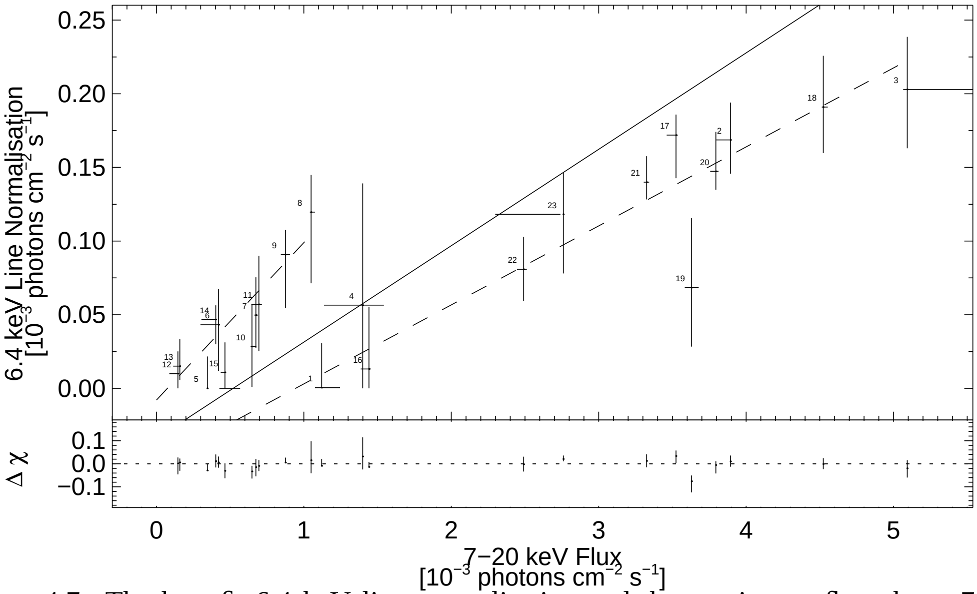

Figure 4.7: The best fit 6.4 keV line normalisation and the continuum flux above 7 keV to the multi-temperature model with free reflection component, 6.4 keV emissions line and free abundances. The best fit line to all the data and separate best fit lines fitting the separate gradients are plotted along with their residuals. All errors are in the 68 per cent confidence interval for one parameter of interest ($\Delta\chi^2 = 1.0$).

Table 4.5: Fluxes, luminosities and associated accretion rates for SS Cygni.

Time	Flux[a]		Luminosity[b]	Accretion rate[c]
[JD]	[2 – 20 keV]	[0.01 – 100 keV]		
2450366.3	6.2	11	3.6	3.4
2450366.9	21	38	11	12

[a] $\times 10^{-11}$ ergs s^{-1} cm^{-2}

[b] $\times 10^{32}(d/166pc)^2$ ergs s^{-1}

[c] $\times 10^{15}$ g s^{-1}

the energy range 0.01 – 100 keV. Fluxes are presented in Table 4.5 along with the luminosities and associated accretion rates. Assuming a distance of 166.2 ± 12.7 pc for SS Cygni (Harrison et al., 1999) and using the 0.01 – 100 keV fluxes, the corresponding luminosity was calculated to be $3.6 \times 10^{32}(d/166pc)^2$ ergs s^{-1} and $11 \times 10^{32}(d/166)^2$ ergs s^{-1}. Using the relation $L = GM_{wd}\dot{M}/2R_{wd}$ and assuming the mass of the white dwarf in SS Cygni is $M_{wd} = 0.82M_{\odot}$ and $R_{wd} = 5.9 \times 10^8$ cm (Bitner et al., 2007), accretion rates were calculated. The accretion rates corresponding to the luminosities were calculated to be 3.4×10^{15} g s^{-1} in quiescence and 1.2×10^{16} g s^{-1} immediately before the hard X-rays were quenched.

4.5 Updated Software Release

Improved PCA response matrix software and calibration database files were released after this analysis was performed. Changes were made to both the energy-to-channel relationship and the modelling of L-escape lines. Cumulative histogram plots using the new software and a systematic error selected in the range 0 – 2 per cent are shown in Figure 4.8 using the preferred models from the previous analysis. A thermal plasma model with free abundances and a narrow emission line fixed at 6.4 keV with a partial covering was used. Comparing this figure with Figure 4.3 shows that the new software does result in an overall improvement to the spectral fits using lower systematic errors.

Figure 4.9 shows the average residuals for all 23 spectra from fits to the four most realistic and best fitting models (labelled). As before (Section 4.3.1) all models presented in this figure are fitted with a background systematic error of 0 per cent and with source systematic

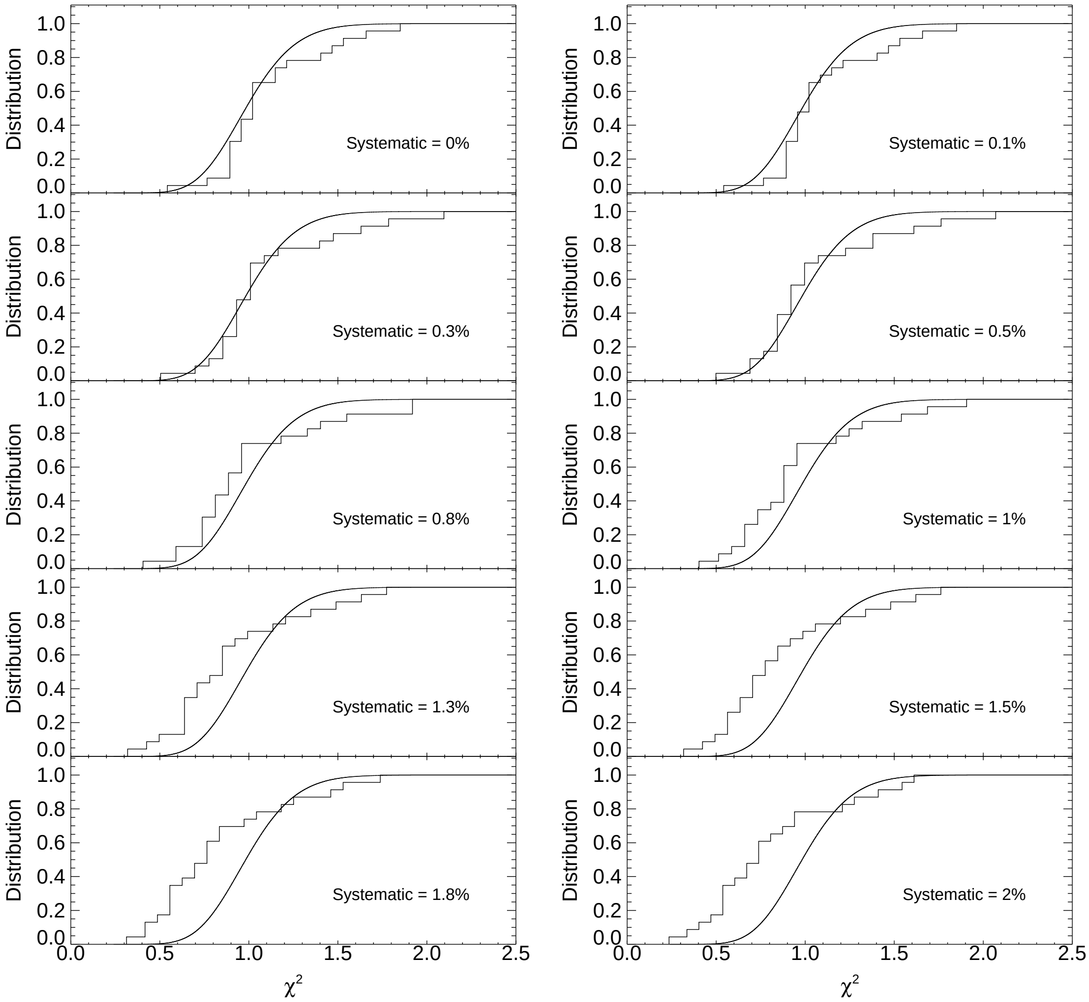

Figure 4.8: Cumulative histogram plots of χ_ν^2 resulting from fits of all spectra to the thermal plasma model with a narrow emission line with partial covering absorption using the improved response matrix software and calibration database. The background systematic error is fixed at 0 for all fits while the detector systematic is varied from 0 – 2 per cent. The cumulative χ^2 distribution (curve) is also plotted.

error of 0 per cent. The multi-temperature model is also fit with 0 per cent systematic error, despite the previous fit using a 0.5 per cent systematic error on the source and background, to compare these residuals with the other models. The average residuals show systematic features present in all spectra. The χ^2_ν at the end of each plot represents the sum of the χ^2_ν for all spectra divided by the sum of the total degrees of freedom. The left column use the previous response and calibration files, while the right column uses the new response and calibration files.

The new detector response and calibration provide a better description of the systematic features introduced by the detector, clearly reducing the residuals in all four models in all channels below $\sim$ 8 keV. However, based on these fits the updated response and calibration database release does not change the results in Sections 4.3.1 and 4.4.3.

4.6 Discussion

A total of 293 ks of data beginning on 1996 October 9 and ending on 1996 October 21 of SS Cygni were presented. During the outburst evolution, the hard X-ray flux quickly rose at the start of the observation before being rapidly quenched and softening. Near the end of the outburst the hard X-rays began to recover, the spectrum hardened and the flux rose to a peak before reaching quiescence. Good fits were achieved with both single and multi-temperature plasma models. All spectra required the addition of a fixed 6.4 keV line and free metal abundances. The single temperature model also required an additional partial covering absorber to achieve a good χ^2_ν for all spectra. The need for a 6.4 keV line is highly suggestive of Fe Kα fluorescence emission due to illumination of cold gas, which is a strong indication that there is Compton scattering of X-rays. The equivalent widths were consistent with that of a reflection origin and the high nH and covering fraction, in the single temperature fits, during the suppression also suggests that some hard X-rays were observed through the disc. Adding a reflection continuum to the model significantly improved the best fits. Both the single and multi-temperature models favoured a higher reflection during the hard X-ray suppression, $2.0^{+1.6}_{-2.0}$ and $2.0^{+0.9}_{-1.1}$ in outburst and $0.6^{+0.5}_{-0.6}$ and $0.5^{+0.1}_{-0.2}$ in quiescence, for the single and multi-temperature model respectively. The reflection parameter was not well constrained for either model and the error bars for the single temperature

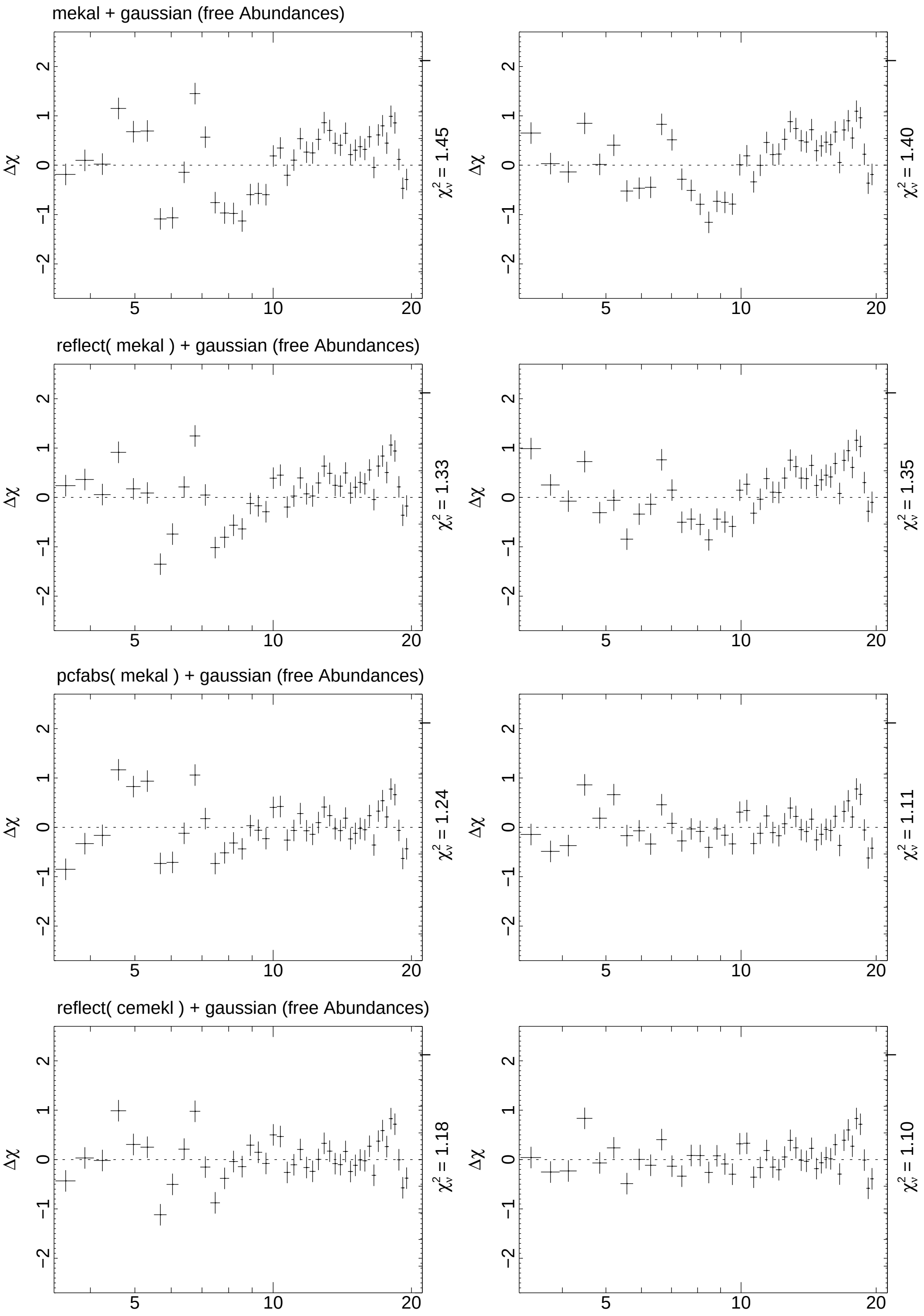

Figure 4.9: Averaged residuals resulting from fits of all spectra with the labelled model using the old (left) and improved (right) response matrix software and calibration database.

model overlap, however, increased reflection in the multi-temperature model is significant. This is also consistent with increase in reflection observed in plots of the 6.4 line normalisation and the flux above 7 keV. This is consistent with reflection fits by Done & Osborne (1997). They found a reflection of 2.2 in outburst and 0.7 in quiescence for their multi-temperature model (no errors were given).

Further evidence for reflection comes from the line fits of the 6.4 keV line normalisation and the model flux above 7 keV, only flux above 7 keV has enough energy to be able to produce fluorescence photons. A higher fraction of fluorescent photons were created from the continuum flux in the spectra immediately following the suppression. Approximately 10 per cent of the flux were fluorescent photons, compared to approximately 5 per cent before the suppression and at the end of outburst. The spectra at the end of outburst were consistent with the same fraction of fluorescent photons as quiescence. A high fraction of fluorescent photons was also seen in U Gem after the boundary layer entered outburst in Chapter 6 (see Figure 6.14.)

The luminosity at the start of the observation (a good estimate of the quiescent luminosity), was 3.6×10^{32} ergs s^{-1}. The luminosity at the peak of the flux at the start of outburst was calculated at 11×10^{32} ergs s^{-1}. This is presumably the moment when the optically thin boundary layer became optically thick to its own radiation. The corresponding accretion rates were 3.4×10^{15} g s^{-1} and 1.2×10^{16} g s^{-1} respectively. The outburst accretion rate is consistent with the expected critical value of 2×10^{16} g s^{-1} for outburst (Pringle & Savonije, 1979). If the quiescent disc were to extend down to the white dwarf surface and if the X-rays are emitted by a hot boundary layer (Pringle & Savonije, 1979; Tylenda, 1981; Patterson & Raymond, 1985b), then the required accretion rates would be about two and a half orders of magnitude higher than predicted by the disc instability model, (e.g., Hameury et al., 2000). During outburst, U Gem had an accretion rate of 3.7×10^{14} g $s^{-}1$ and 5.5×10^{14} g $s^{-}1$ for the 1997 and 2004 outbursts (see Chapter 6). The average SU UMa quiescent accretion rate was 4.2×10^{15} g s^{-1} (see Chapter 7).

Current theory suggests that a hole is required to develop in the inner accretion disc during quiescence, (e.g., Lasota, 2001). The observed accretion rate is about two and a half orders of magnitude higher than predicted by the disc instability model, (e.g., Hameury et al., 2000), if the X-rays are emitted by a hot boundary layer that extends down to the white dwarf surface (Pringle & Savonije, 1979; Tylenda, 1981; Patterson & Raymond, 1985b). As the disc enters outburst the accretion rate increases and material in the disc fills the truncated boundary layer causing the hard X-ray flux to increase. The correlated increase in the reflection and quenching of hard X-rays suggests that the boundary layer begins to fill, increasing the reflection, as the hard X-ray emitting region becomes optically thick. The time frame for the hard X-ray emitting region to become quenched is approximately 4 hours in the case of the outburst presented here. Similarly at the end of outburst, the hard X-rays recover and the boundary layer transitions from an optically thick to optically thin state. This is surprising, it would be expected that the reflection should, for example, decrease after the spectrum hardens at the end of the hard X-ray suppression and not at the same time as is observed. At the end of the hard X-ray suppression the spectrum hardens indicating that the truncated region should have emptied. This suggests that the observed changes in the spectrum may be due to the boundary layer itself and not disc truncation. Holes present in the inner disc could be formed in a number of ways: magnetic fields (Livio & Pringle, 1992); evaporation into a siphon flow (Meyer & Meyer-Hofmeister, 1994); or an Advection Dominated Accretion Flow (Menou, 2000). Truss et al. (2004), presented two-dimensional accretion disc models achieving the same effect with a small portion of the disc remaining in a high-viscosity state.

4.7 Conclusions

Previous analysis of the X-ray properties of SS Cygni have relied upon relatively short snap shot observations during either quiescence or outburst. Analysis of snap shots makes it difficult to determine how the spectrum evolves between the hard and soft state in quiescence and outburst.

Analysing extensive X-ray data of SS Cygni during the 1996 outburst using pointed *RXTE*/*PCA* observations and *AAVSO* (optical) observations, it has been possible to study the spectral behaviour with far greater temporal accuracy than has ever been done before. The data presented here covered an entire transition from quiescence into outburst and the reverse transition from outburst back to quiescence.

Good fits were found with a single temperature plasma model, free abundances, a 6.4 keV line and partial covering absorber. The data are also consistent with a multi-temperature thermal plasma continuum and with a reflection component present.

The evolution of the spectral parameters shows that there is evidence for an increase in the reflection during outburst. The change in reflection also occurs at the same time as the spectrum changes. The increased reflection observed suggests that there is additional reflecting material present during outburst. This is consistent with a truncated inner disc during quiescence.

Chapter 5

The Quiescent Evolution of SS Cygni

5.1 Introduction

SS Cygni enters outburst approximately every 50 days, with a bimodal distribution in the duration of approximately 7 and 14 days (Cannizzo & Mattei, 1992). The remaining $\sim$ 75 per cent of the time accounts for quiescence. The length of time spent in quiescence makes a study of this period very important in the understanding of the photometric and spectroscopic evolution of the system.

Quiescence has been described as the ’Achilles heel of the disc instability model’ by Lasota (2001) and the disc instability model (DIM) is not able to accurately describe this section of the outburst cycle. If the quiescent disc were to extend down to the white dwarf surface and if the X-rays are emitted by a hot boundary layer (Pringle & Savonije, 1979; Tylenda, 1981; Patterson & Raymond, 1985b), then the required accretion rates would be about two and a half orders of magnitude higher than predicted by the disc instability model, (e.g., Hameury et al., 2000). accretion rate in the quiescent accretion disc is dependent on the radius the gas in the disc is accreted at. Therefore, the removal of the inner disc by magnetic stress (Livio & Pringle, 1992) or evaporation (Meyer & Meyer-Hofmeister, 1994; Menou, 2000) or by other means makes the truncation of the disc an important ingredient in the DIM resolving the discrepancy between observation and theory.

Previous studies have been based upon a number of snapshot observations with short

Table 5.1: Pointed *RXTE*/*PCA* observations.

Proposal ID	Year	Start - End date	Number of observations	Total exposure [ks]	Gain epoch
P20033	1997	Mar 01 - Jul 02	42	83	3
P40012	1999	Jun 07 - Jun 21	20	73	4
P50011	2000	Mar 05 - Jun 03	185	171	4,5
P50012	2000	Aug 23 - Jan 18	15	55	5
P90007	2004	Sep 19 - Jan 25	33	178	5

durations, making it difficult to draw firm conclusions about the quiescent X-ray evolution. This chapter explores the long and short term evolution of the quiescent X-rays over a number of well sampled outburst cycles spanning several years. Thanks to the high signal to noise of the data complex spectral models are constrained providing a better and more detailed understanding of the quiescent state. The transitions for a number of outbursts are also studied along with the accretion rates during the transition and in quiescence.

5.2 Observations

The observations of SS Cygni used for the analysis in this chapter are shown in Table 5.1. The observations spanned from approximately 2 to 5 months having total exposures of 55 to 178 ks. Data were measured using the proportional counter array (*PCA*) experiment on *RXTE* (Bradt et al., 1993).

For details of the extraction criteria and software used in this chapter see Section 4.2 in Chapter 4. Data for this chapter were extracted using an updated version (version 6.7) of the `FTOOLS` package.

5.3 Time Series Analysis

5.3.1 Outburst Lightcurves

Figures 5.1 to 5.5 show contiguous *AAVSO* and *RXTE* observations along with their X-ray hardness ratio and variability. The calculated variability is plotted along with the expected variability (solid line) based on counting statistics alone. The hardness ratio, H/S, was formed by dividing the counts into a soft, S, and hard, H, band. The bands were roughly split so there were an equal number of counts in each band; 2.3 – 4.8 keV in the soft band and 4.8 – 20.3 keV in the hard band. The data sets used to produce these plots along with details of the number of observations, exposure time and satellite epoch are listed in Table 5.1.

P20033, March - July 1997

The X-ray evolution spanning one long and one short outburst and three quiescent periods is presented in Figure 5.1, for data set P20033. The most noticeable characteristic of the data set is the average count rate; in the third quiescent period (27 counts s^{-1}) the count rate was noticeably higher than the second (19 counts s^{-1}) quiescent period. The average quiescent count rates for this observation and all others in quiescence can be seen in Table 5.4 in Section 5.4.2. On JD 2450517 the optical magnitude rose from an average of 12^{th} mag to approximately 11.4 mag. The X-ray count rate also increased at this time by a factor of 2 with a slightly softer spectrum resembling a mini outburst. In the optical band both outbursts were very similar, however, in the X-ray bands the outbursts were noticeably different. Before the start of the short outburst the flux nearly doubled from 20 to 38 counts s^{-1} before being suppressed to below the quiescent level. The hard X-rays recovered as the optical band returned to quiescence. In the long outburst, the X-ray, behaviour was different from expected, the count rate increased to marginally above the quiescent rate but was not suppressed until 10 days into the outburst. As the optical band began to decline the X-rays became suppressed before quickly recovering. As the optical band reached minimum the hard X-ray count rate rose above the quiescent level before returning to quiescence resembling the U Gem outbursts presented in Chapter 6. Although the quiescent count rates varied dramatically throughout the data set the spectrum was remarkably constant, with a hardness ratio of 1.1. During outburst the hardness ratio dropped to 0.8.

P40012, June 1999

The evolution of the X-ray recovery into quiescence is presented in Figure 5.2, for data set P40012. During the optical maximum the hard X-rays were clearly suppressed and began to recover when the optical band had declined to approximately half of the maximum outburst magnitude. The recovery was earlier than seen in the 1996 outburst in Chapter 4 which occurred as the optical reached quiescence. During the recovery, the hard X-ray count rate reached a peak of approximately 100 counts s^{-1} lasting for approximately 3.5 days, a day longer than was seen in Chapter 4. The X-ray count rate then returned to what was most likely the quiescent count rate.

The spectrum was softer in outburst than quiescence, changing from 0.8 in outburst to 1.1 in quiescence. As the X-ray count rate began to increase the hardness smoothly increased. In the 1996 outburst (see Chapter 4) the hardness varied before increasing as the system returned to quiescence. When the hard X-ray count rate reached maximum in the peak during the hard X-ray recovery the spectrum was still getting harder, reaching maximum as the hard X-rays returned to their quiescent count rate.

P50011, march - June 2000

The X-ray evolution spanning a long and short outburst and two quiescent periods is presented in Figure 5.3, for data set P50011. This observation has an impressive temporal resolution with a cadence of approximately 12 hours. Both outbursts were very similar in the optical and X-ray bands, with the only noticeable difference being the duration. The X-ray suppression was well defined, with a count rate of approximately 10 counts s^{-1}. At the end of the outburst, the hard X-ray recovery began during the decline in the optical band. The count rate rose sharply to a peak of 135 and 170 counts s^{-1} for the long and short outbursts respectively, $4-6$ days after the optical reached quiescence. During quiescence the X-rays were also highly variable, ranging from $20-110$ counts s^{-1}.

Despite the larger error bars in outburst, it is clear that the X-ray were softer; approximately 0.8 for the long outburst and 0.85 for the short outburst. The quiescent spectrum, with a hardness ratio of approximately 1.1, also did not show much variability despite the highly variable count rate during this period.

P50012, August - January 2000

Two concentrated groups of observations in outburst and quiescence are presented in Figure 5.4, for data set P50012. The hard X-ray count rate was approximately a factor of 5 higher in quiescence than in outburst. The spectrum was also softer in outburst with respective hardness ratios of approximately 0.8 and 1.05.

P90007, September - January 2004

Four X-ray outbursts, two fully observed short outbursts and two partially observed long outbursts are presented in Figure 5.5, for data set P90007. Three quiescent periods were also fully observed. The outburst count rates were all lower than in quiescence and all at approximately 10 counts s^{-1}, while the quiescent count rates were highly variable.

The hardness of the spectrum was well defined and shows a drop from approximately 1.1 to 0.8 when the system transitioned from quiescence to outburst. The quiescent spectrum also did not change greatly while the count rate was highly variable.

Light Curve Trends

In all data sets, the X-ray light curves (with the exception of one outburst in the P20033 data set) and hardness ratios presented very consistent behaviour. In all but one outburst the hard X-rays were suppressed to a mean count rate of between 5 and 10 counts s^{-1}. At the end of outburst the hard X-ray recovery began after the optical band had already started to decline, the count rate rose above the quiescent rate before returning to quiescence. There was also evidence for a count rate increase before the hard X-ray suppression, however, it was very rapid with a duration of $\sim$ 12 hours, consistent with Wheatley et al. (2003). The quiescent X-rays were brighter than during outburst and were very variable ranging from approximately $20-75$ counts s^{-1}. The mean quiescent count rates were also very different between quiescent intervals, the mean quiescent count rates can be seen in Table 5.4.

In all observations the spectrum was well defined. Despite the high level of variability in quiescence, the hardness ratios were very constant, with a hardness ratio in all data sets between

1.05 and 1.15. In outburst the spectrum was softer dropping to between 0.75 and 0.85.

5.3.2 Outburst Transition

An increase in the count rate is expected before and after the hard X-ray suppression and was clearly observed in Chapter 4. A detailed plot of the transition of the P50011 data set can be seen in Figure 5.6. Three observations before the X-rays became quenched, starting on JD 2451622 and 2451680.5, were very similar to that seen in Chapter 4 and show evidence of an increased count rate. In the first outburst the count rate, initially at the quiescent rate, increased from 33 to 66 counts s^{-1}. The count rate then dropped to 33 counts s^{-1} before becoming quenched at 9 counts s^{-1}. The second outburst followed a similar pattern. The count rate, increased from 66 to 106 counts s^{-1}. The count rate then dropped to 34 counts s^{-1} and then was quenched with a count rate of 10 counts s^{-1}. A change in the hardness ratio, when the spectrum became softer, in Figure 5.3 also supports this as the transition into outburst. These observations were consistent with the 1996 outburst in Chapter 4. The first outburst in data set P20033 also had an increased count rate immediately before hard X-rays became quenched. The cadence of the P50011 data set was 12 hours, placing a constraint on the duration of the rapid peak of $\leq$ 12 hours. This is consistent with observations by Wheatley et al. (2003) who measured the duration of the increase before outburst to be 12 hours.

An increase in the count rate in the recovery of the hard X-rays was clearly detected in both outbursts in data set P50011 a recovery was also observed after the long outburst in data set P20033. In the P50011 data set the count rate rose gradually, just before the optical band reached quiescence, to a peak of 135 and 170 counts s^{-1} respectively. Approximately 4 – 6 days later the X-ray count rate reached quiescence, which was approximately 2 – 4 days after the optical band reached quiescence. The duration of the hard X-ray recovery lasted nearly as long as the hard X-rays were quenched for, with the peak after the long outburst lasting longer that that of the short outburst.

The cross correlation of all the data sets, including the outburst from Chapter 4, was calculated separately for both the optical rise and decline. The cross correlation is a method of estimating how correlated two time series are, i.e., how correlated the outburst rise and de-

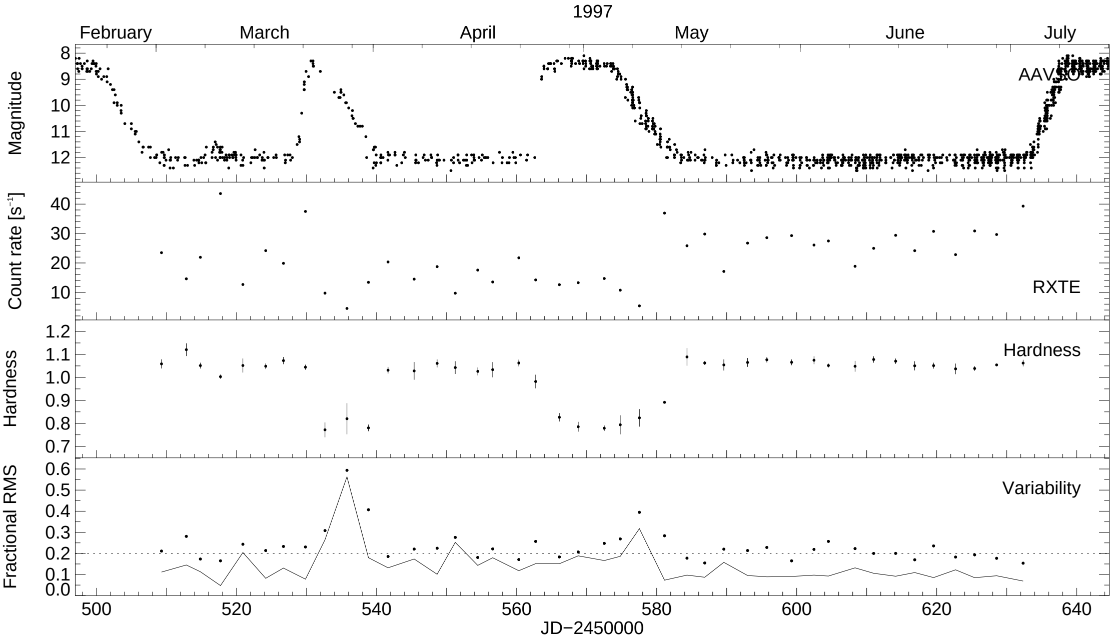

Figure 5.1: Simultaneous *AAVSO* and *RXTE* observations along with the hardness ratio and fractional RMS and expected variability using the observation with the observation ID P20033.

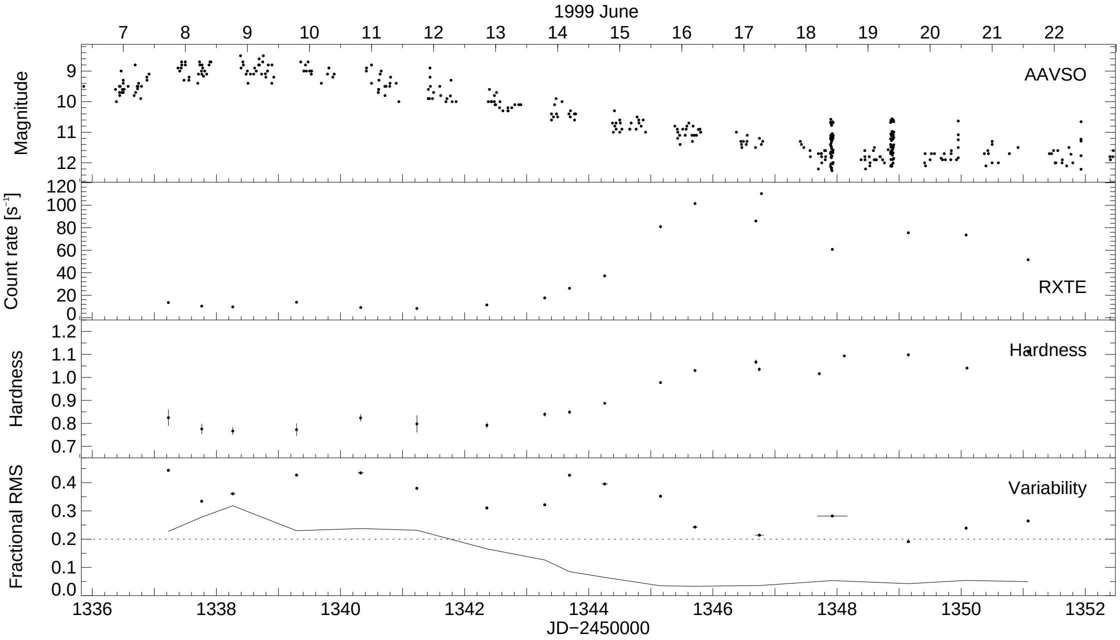

Figure 5.2: Simultaneous *AAVSO* and *RXTE* observations along with the hardness ratio and fractional RMS and expected variability using the observation with the observation ID P40012.

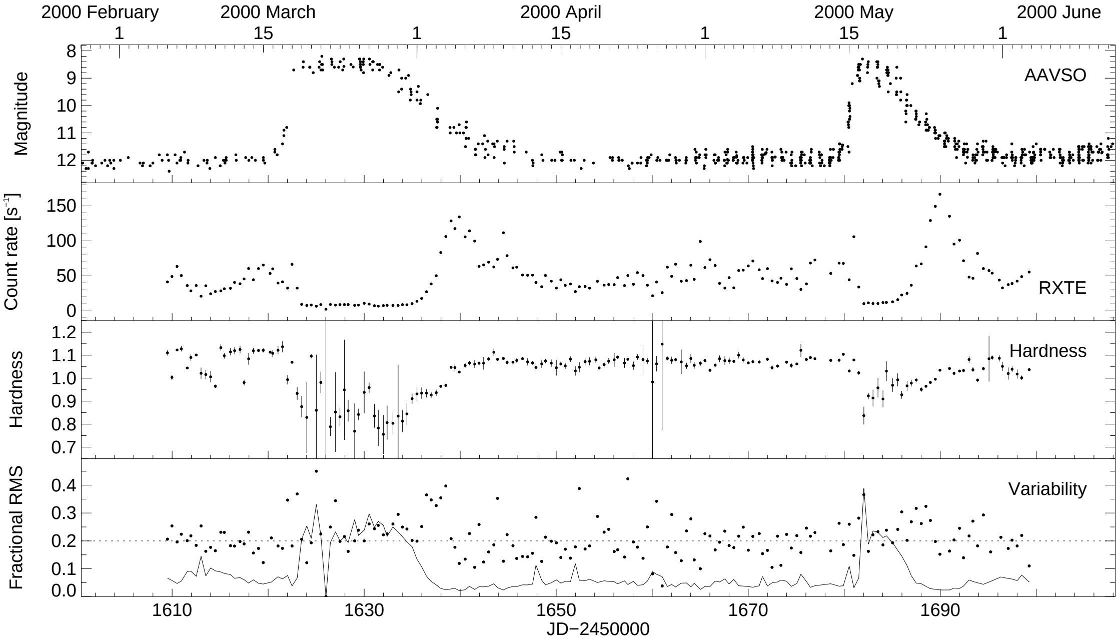

Figure 5.3: Simultaneous *AAVSO* and *RXTE* observations along with the hardness ratio and fractional RMS and expected variability using the observation with the observation ID P50011.

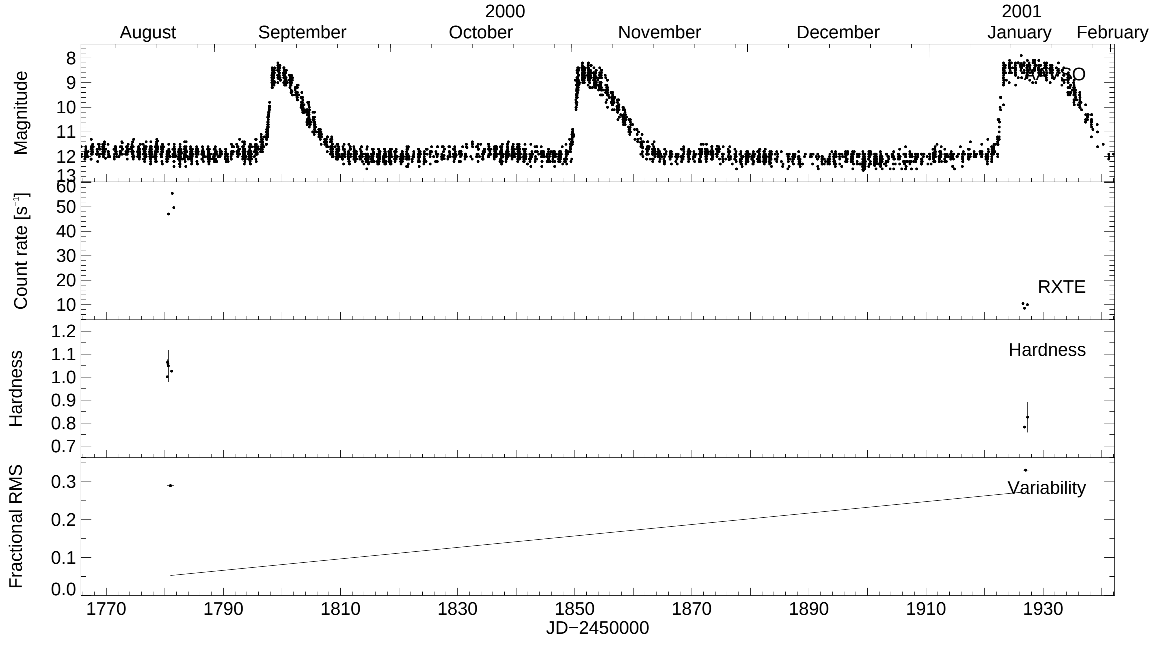

Figure 5.4: Simultaneous *AAVSO* and *RXTE* observations along with the hardness ratio and fractional RMS and expected variability using the observation with the observation ID P50012.

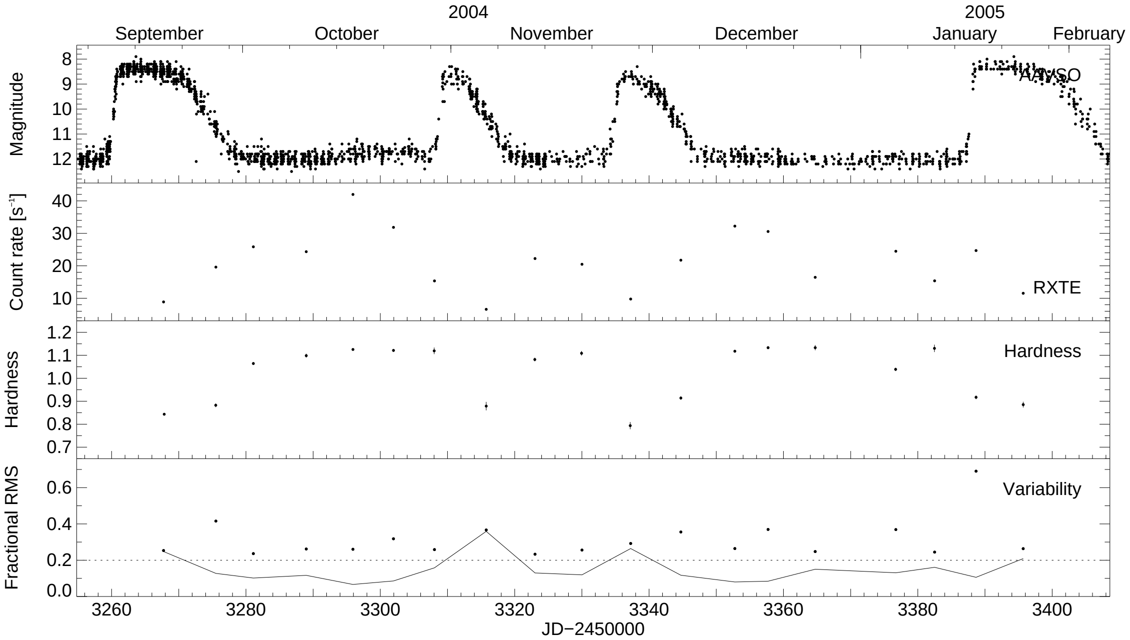

Figure 5.5: Simultaneous *AAVSO* and *RXTE* observations along with the hardness ratio and fractional RMS and expected variability using the observation with the observation ID P90007.

cline are, for each outburst in a given data set, with the rise and decline of a template outburst. This will determine how repeatable the outburst shapes are in the data sets indicating how the timescale of the boundary layer transition vary across the outbursts. The cross-correlation is calculated by shifting one time series and taking the integral of the product of the two time series. When the time series match, the product of the two time series is maximized (Fuller, 1976). Two templates were chosen that, qualitatively, best represented the outburst transition shapes. The rise template used was the first outburst in data set P50011, on JD 2451621.6, and the decline template used was the third outburst in data set P90007, on JD 2453345.5. The optical and X-ray, for the respective rise and decline, were plotted with their respective offsets in Figure 5.7. The time axis uses arbitrary time in days to indicate the separation of the rise and decline in the outburst cycle.

The optical transitions had very similar outburst rise and decline. The rise was less well correlated than the decline and one outburst also had a slower rise than the others. This was most likely due to the faster timescales at the start of outburst. Figure 5.7 also shows that while the quiescent count rates differed in all the data sets all the outburst count rates were very similar. The X-ray transitions all varied from one another and were not as well correlated as in the optical band. The X-ray flux increase at the start of outburst was also much more rapid than the decline. The only outburst that was fully resolved was the data set from Chapter 4, however, three other outbursts showed evidence of an increased count rate. The timing of these peaks were also consistent with occurring at the same time. Both outbursts from data set P50011 showed an increase in the count rate. The last outburst in the P90007 data set, although there were no earlier observations, showed a decline at the same time as in the 1996 outburst.

The recovery of the X-rays, in the right hand column of Figure 5.7, shows that the beginning of the recovery began at different times in each outburst. There was also a variety of durations and peak count rates. The earliest hard X-ray recovery began when the optical band was still close to maximum at 8^{th} mag, while the latest recovery (that of the 1996 outburst began when the optical had nearly reached quiescence. The correlated time of the peaks of the recovery were, within the spread of the optical decline, consistent with occurring at the same time. The first outburst in data set P50011 also appeared to be double peaked.

5.3.3 The X-ray Delay

The only data set with high enough temporal resolution to be able to accurately determine a delay between the optical rise and the X-ray suppression was P50011. The P20033 data set also had a high temporal resolution but the X-ray observations near the hard X-ray suppression were not defined well enough to be able to calculate a delay.

The variable nature of the quiescent X-rays and the cadence of the observations makes it difficult to determine the start of the outburst. However, the hardness ratio was very well defined during quiescence for all data sets and is a good indication of the start of the X-ray outburst. The hardness ratio as well as the X-ray count rate were used to calculate delay times at the start of the X-ray outburst. In both outbursts in the P50011 data set the three observations before the hard X-rays were quenched indicate the end of quiescence. The count rate rapidly increased before being quenched. The spectrum during this interval became softer also indicating the beginning of the transition into outburst. For the long outburst, the optical rise began on JD 2451620.9,

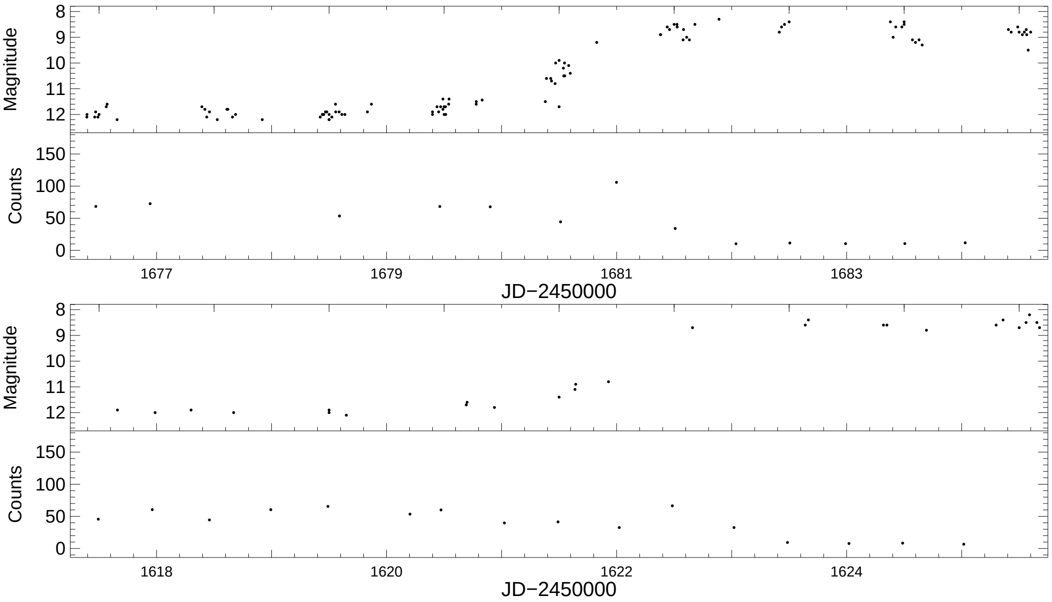

Figure 5.6: Detailed sections of the optical (upper panel) and X-ray (bottom panel) light curves from Figure 5.3 during the transition to outburst.

while the X-ray outburst began on JD 2451622.0, delayed by approximately 0.5 – 1.6 days. For the short outburst, the optical rise began on JD 2451679.8, while the X-ray outburst began on JD 2451680.5, delayed by 0.6 – 1.2 days. The delay can be seen in Figure 5.6. Both these delay times are estimates due to the nature of the sampling of the optical and X-ray data.

5.3.4 Variability

The bottom panel of Figures 5.1 to 5.5 shows the fractional RMS variability of the data (data points) plotted with the variability expected from counting statistics alone (solid line).

All X-ray observations had highly variable count rates. The count rates in outburst were between 5 – 20 counts s^{-1}. In quiescence the count rate varied over a much larger range of 20 – 120 counts s^{-1}, but more commonly between approximately 20 – 50 counts s^{-1}.

The fractional RMS variability ranged from 15 – 45 per cent, data sets with higher exposures on average had a slightly higher fractional RMS variability. The expected variability

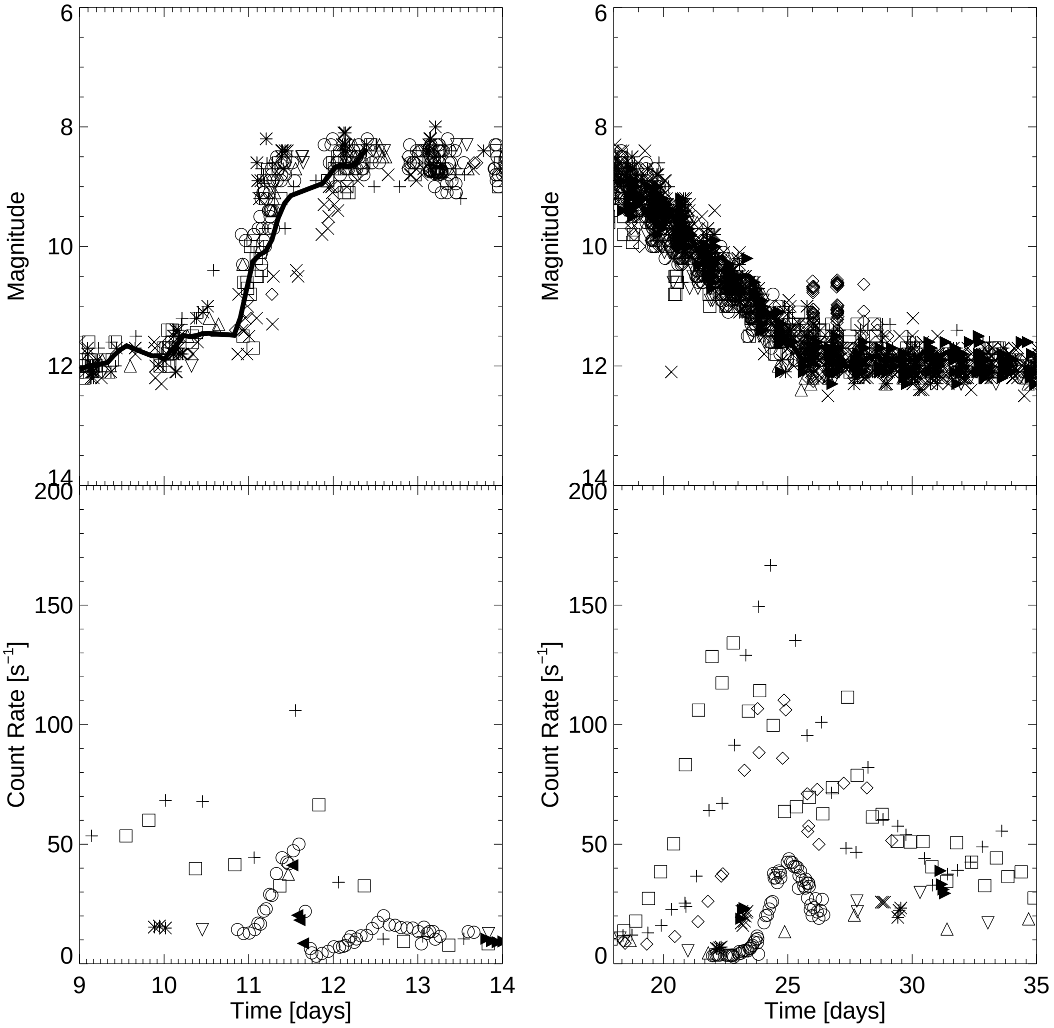

Figure 5.7: All five data sets and also the outburst from Chapter 4, cross correlated and centred around the transition into outburst (left column) and the transition out of outburst (right column). The rise of the first outburst in data set P50011, on JD 2451621.6, and decline of the third outburst in data set P90007, on JD 2453345.5, were used for the respective templates. Symbols relate to the outburst beginning on the following JD: 2450365 - open circle, 2450528 - open upward triangle, 2450563 - open downward triangle, 2451336 - open diamond, 2451622 - open square, 2451680 - plus sign, 2453260 - cross, 2453308 - star, 2453334 - filled right facing triangle, 2453388 - filled left facing triangle.

during outburst was higher due to lower count rates. During the hard X-ray suppression in the P20033 data set on JD 2450536 and 2450577 the fractional RMS variability was approximately 60 per cent and 40 per cent respectively although the expected variability was also high. In data set P20033 it is interesting to note that although the second quiescent section had a lower count rate than both the other quiescent sections all quiescent intervals were equally variably.

Although all observations had high levels of variability, SS Cygni was most variable during the transitions into and out of outburst. In data sets P40012 and P50011, on JD 2451622, 2451636 and 2451686, during the transition the fractional RMS variability reached 45 per cent. An observation covering the transition in the P90007 data set was calculated to have a fractional RMS variability of 70 per cent. High variability has previously also been reported in VW Hyi (Wheatley et al., 1996) and SS Cygni (Wheatley et al., 2003) as well as U Gem (see Chapter 6) where periods of highest variability also occurred during the transition of the boundary layer.

The P50011 data set had the largest range of quiescent count rates, and the fractional RMS variability also varied from observation to observation over the range 10 – 45 per cent. This shows that as well as there being variability present on the time scale of the outburst cycle there was also high levels of rapid variability within each observation on the time scale of the sampling in this data set.

Rapid X-ray Variability

Analysis of Figures 5.1 to 5.5 at the beginning of this section showed that nearly all observations were variable with the highest periods of variability occurring at the start or end of the X-ray suppression. Selected individual sections of the *RXTE* light curve from the P50011 data set, binned in 16 seconds, shows the evolution of the variability throughout an outburst cycle. Light curves plotted in Figure 5.8 show the variability covering consecutive intervals during an outburst cycle. As the observations progress the variability of the count rate in the light curve sections decreased clearly as the system transitioned from quiescence to outburst. As the outburst ended and the hard X-rays recovered the variability in the count rate increased becoming highly variable on very short time scales, varying over the range of 30 – 120 counts s^{-1} on the time scale of minutes. The light curve sections that correspond to the peak of the recovery are plotted on a larger range, the count rate varied over a larger range, 50 – 200 counts s^{-1}, but on a slightly longer time scale. As the system progressed back into quiescence the variability decreased to a similar level as that before the outburst. This is a familiar picture for all the data sets presented in this chapter (see Figure 5.9).

A selection of individual sections of light curve, from Figures 5.1 to 5.5 are shown in Figure 5.9, the top panel is the 16 second binned light curve with the associated hardness ratio below, with the soft S and hard H bands split in the energy range 2.3 – 4.8 keV in the soft band and 4.8 – 20.3 keV in the hard band.

Both panels C and D show a large, short lived spike in the count rate during both an outburst and quiescence section. On JD 2451339.847 the count rate increased by a factor of 9 and on JD 2451343.710 the count rate increased by a factor of 3. Both spikes had a duration of $\sim$ 250 seconds and there was little evidence of a change in the hardness ratio.

The observation in panel J was observed in the P90007 data set during the transition into the final outburst covered by the X-rays. The count rate started to decrease on JD 2453388.106, continuing to decline throughout the observation from 65 to 10 counts s^{-1} in approximately 2.8 hours, until JD 2453388.220. During this transition there was little evidence of a change in the hardness ratio.

The selection of individual light curve sections in Figure 5.8 and 5.9 shows that there were high levels of variability present in all data sets. SS Cygni was variable in quiescence, however, the highest amount of variability was seen during the transitions into and out of outburst. The X-ray count rate changed by a factor of 4 in just 70 seconds, but more commonly varied by a factor of 3 in under a minute. These strong variations were not associated with any significant variations in the hardness ratio indicating that the variability was not due to temperature changes or photoelectric absorption. The variability was most likely due to changes in the accretion rate in the boundary layer.

Resolving the timescales of the X-ray variability allows for the density of the gas to be constrained. If the spectrum of the gas does not change, as indicated by the hardness ratios in Figure 5.9, then the flux will vary based on the density of the gas with a characteristic time of the cooling time scale of the gas.

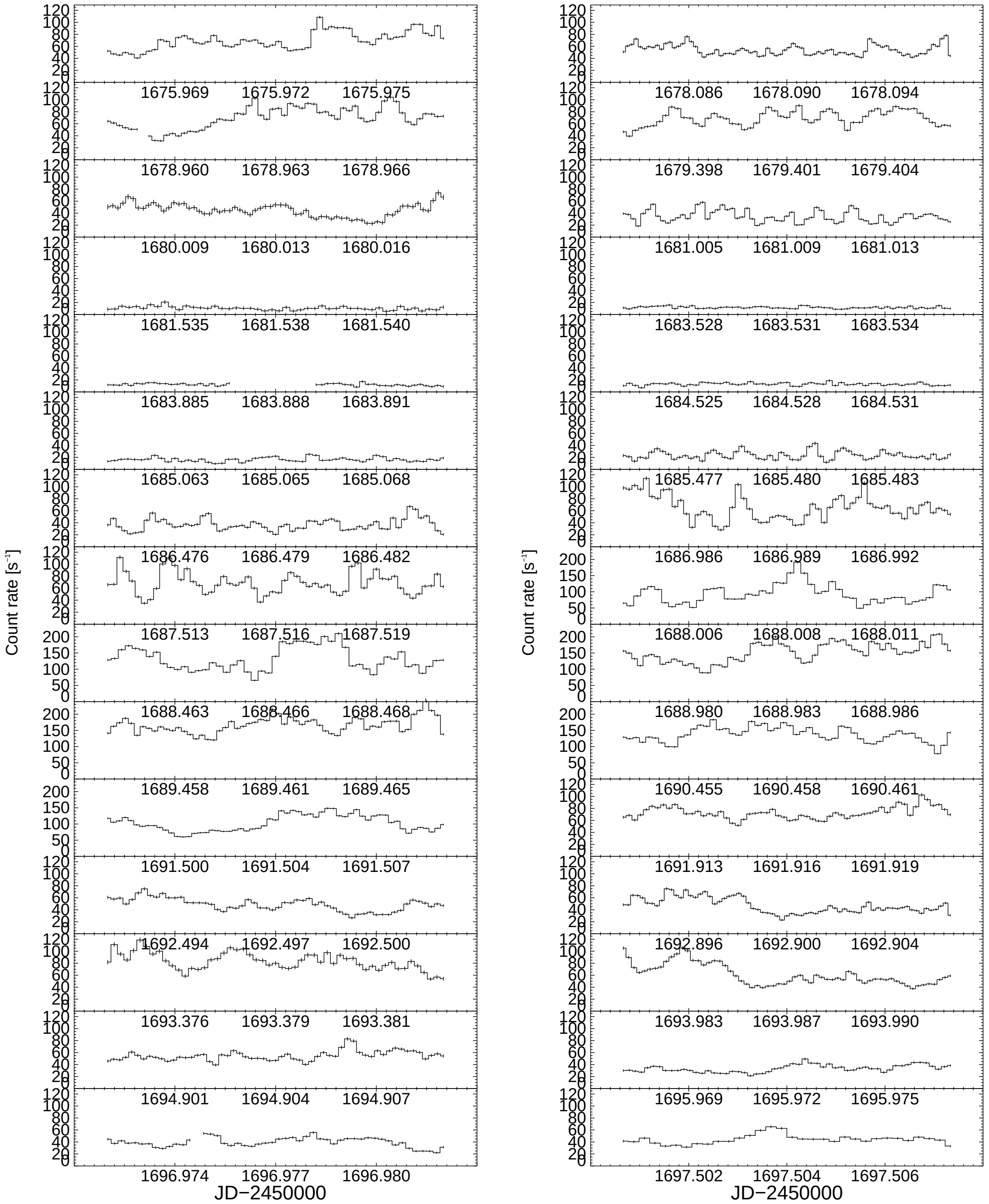

Figure 5.8: Selected individual sections from the *RXTE* light curve, Figure 5.3, of data set P50011 in 16 second binning. Note the top five panels in the right column are plotted on a larger scale.

The volume emissivity of an optically thin gas is $\sim 2 \times 10^{-27} n_e^2 T_e^{1/2}$ ergs s^{-1} cm^{-3} and the thermal energy per unit volume of the X-ray emitting gas is $\frac{3}{2} n_e k T_e$ ergs cm^{-3}, where k is the Boltzmann constant, T_e is the temperature of the gas and n_e is the electron density. The characteristic cooling timescale is the ratio of these, resulting in $t_{cool} = 2 \times 10^{11} T_e^{1/2} n_e^{-1}$ seconds.

On JD 2451664.986, plotted in panel F in Figure 5.9, the count rate dropped by a factor of 2 in approximately 16 seconds. Using a best fit temperature of 20 keV (See Section 5.4.1) the electron number density was $\geq 1.9 \times 10^{14}$ cm^{-3}.

Light Curve Power

The power spectral density (PSD) describes how the power of a time series is distributed with frequency. The purpose of estimating the spectral density is to characterise the frequency content of the signal where variability is distributed over a range of time-scales.

Due to earth occultations and transits through the SAA as well as other timing constraints on the detector it is often not possible to obtain evenly sampled data. It is possible to map unevenly sampled data into evenly sampled times, for example, data can either be set to zero, the nearest neighbour or interpolated. However, these methods do not give good results and often artificially increase the power at low frequencies. A better method to calculate the PSD with unevenly sampled data is the Lomb-Scargle periodogram (Lomb, 1976; Scargle, 1982; Press & Rybicki, 1989). This method only uses the measured points and for evenly sampled data is equivalent to the PSD apart from the normalisation constant. The Miyamoto normalisation ($2\Delta / N\overline{h}^2$, where Δ is the bin time, N is the number of data points with an average of $\overline{h}$) was used to normalise the PSD (Miyamoto et al., 1991). This normalisation is independent of the number of data points, sampling rate and the mean value of the data allowing easy comparison.

If the periodogram is binned in logarithmic space the distribution of the binned periodogram converges to a Gaussian distribution with fewer data points per bin, therefore allowing for finer frequency binning (Papadakis & Lawrence, 1993). Logarithmic binning is also less biased than alternative methods and the data requires less smoothing. The bias is constant and can be easily corrected by using $log[P(f)] = \frac{1}{M} \Sigma_j log[P(f_j)] + 0.253$, where M is the number of points in each bin, j varies over the M consecutive points and 0.253 is a constant bias of this es-

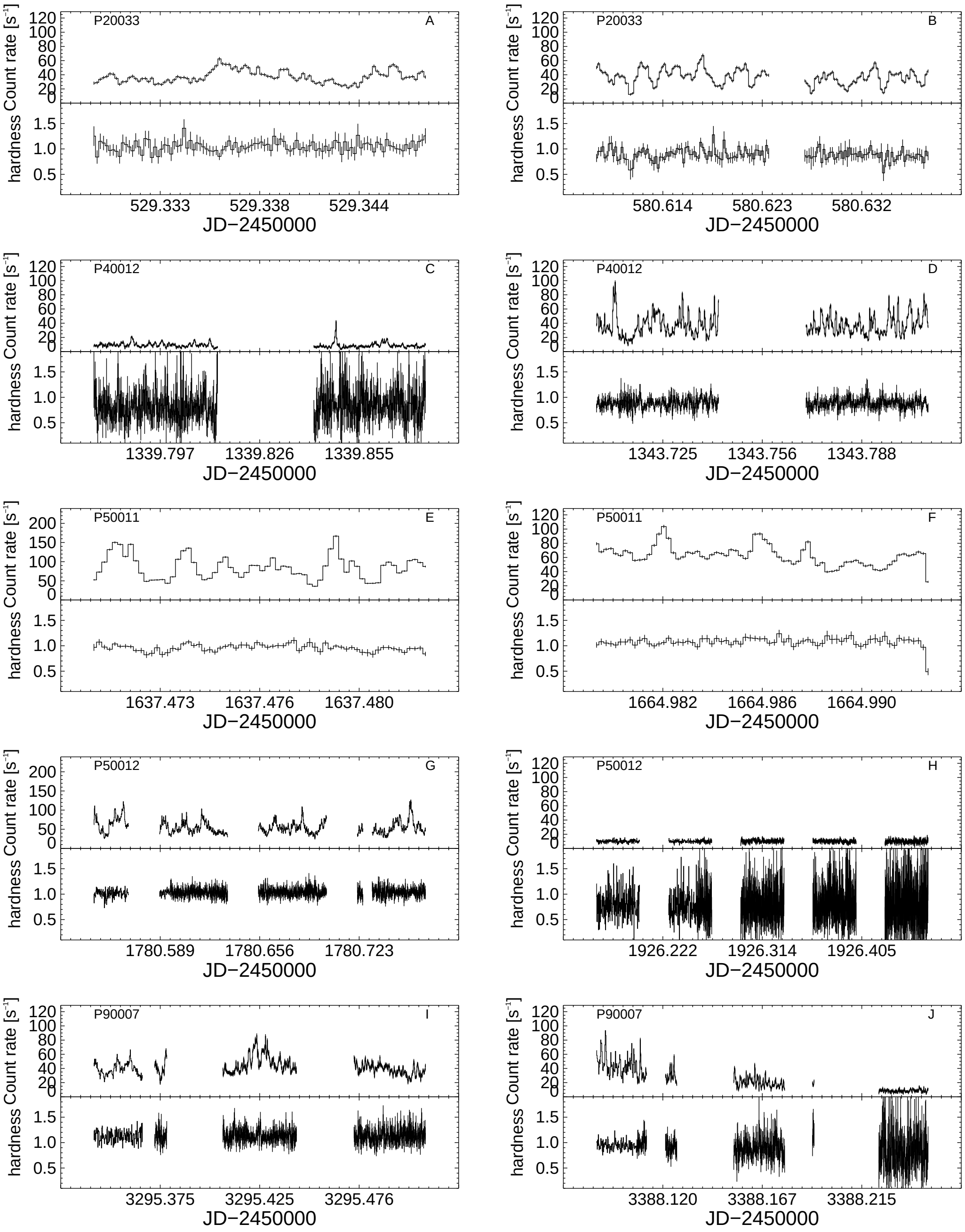

Figure 5.9: Selected individual sections from the *RXTE* light curves in Figures 5.1 to 5.5 in 16 second binning plotted with the respective hardness ratio.

timation. The precision of each estimated point is independent of N, i.e., the standard deviation of each point is always 100 per cent and is the same for all the bins and approximately equal to $\sqrt{0.310/M}$ (Papadakis & Lawrence, 1993).

The PSD shows the contribution of variability on different time scales to the total variability of the light curve. On short time scales the variability is characterised as red noise producing a power law PSD, $P(\nu)$, at frequency ν given by $P(\nu) \propto \nu^{-\alpha}$, where α is the PSD slope. The hard X-ray PSD flattens to $\alpha \sim 0$ at lower frequencies becoming white noise. This frequency break is a sign of characteristic timescales within the X-ray emitting boundary layer. The break frequency is related to the size of the emitting region and it marks a break in the correlation between frequency and amplitude of the variations. Fitting a broken power law to the PSDs in Figure 5.10 resulted in good fits to both the P20033 and P50011 periodograms. The power law slope, break frequencies and resulting χ^2_ν can be seen in Table 5.2. The P50011 periodogram, which had the brightest light curve of the three periodograms, had the steepest power law slope and highest frequency break. The power law fit to the PSD from data set P90007 was not statistically acceptable, with a χ^2_ν of 2.18 (619 d.o.f), the PSD also does not flatten at the best fit break frequency. This indicates that the shorter time scale X-ray variability was not observed.

The PSD from data sets P20033 and P50011 are very similar, while the PSD from data set P90007 is noticeably different. The power law slope is a ratio between the high and low frequency variability. Therefore, with a slightly steeper slope data set P50011 has more low frequency variability, although this is most likely not significant in comparison with the other PSD.

Two break frequencies, high and low, are expected in the PSD, in these PSD only the low frequency break is detected. The data were binned in 16 second bins, not fast enough to resolve the high frequency break indicating that rapid variability occurs on timescales faster than 16 seconds.

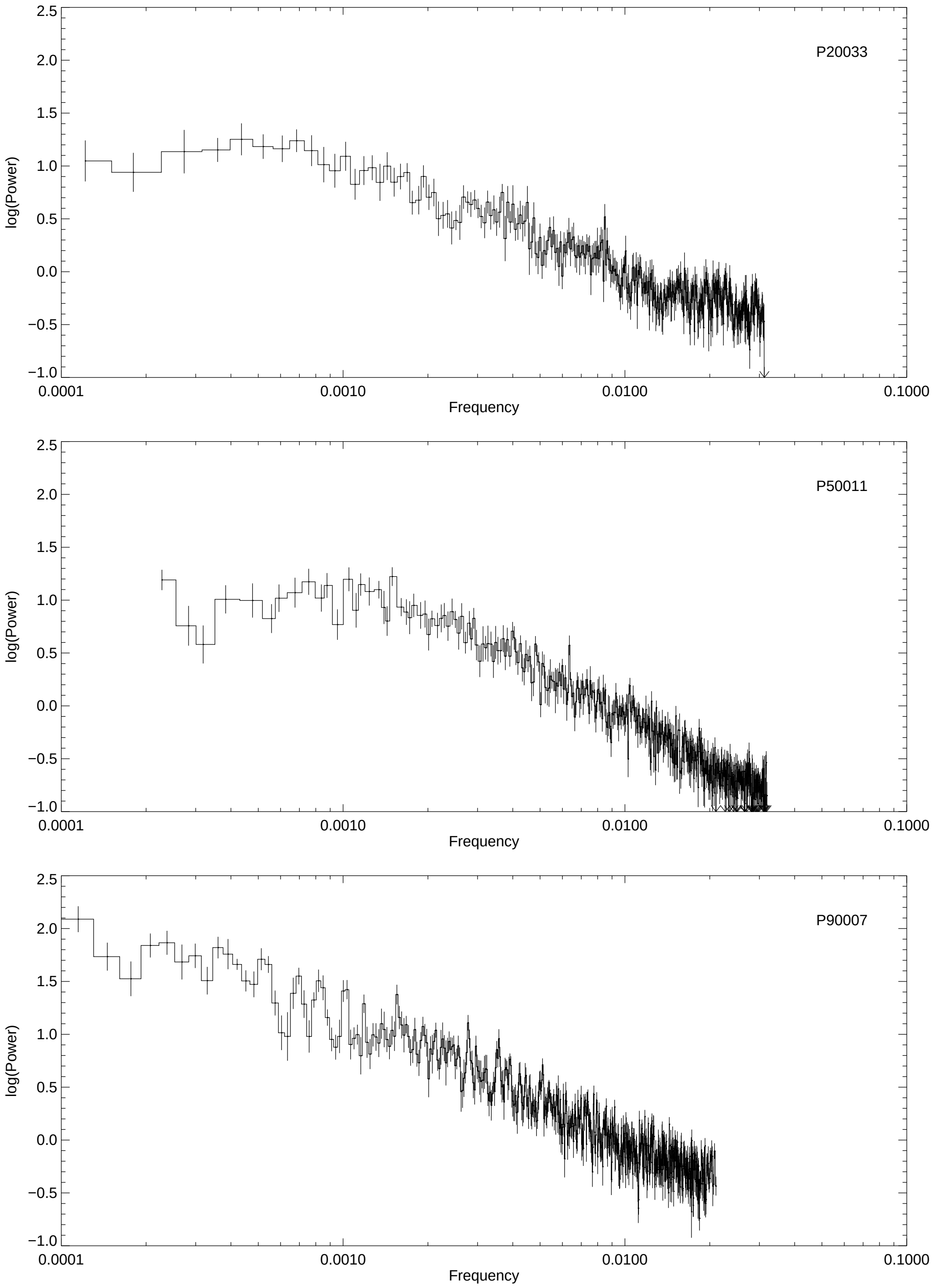

Figure 5.10: Combined power spectra of all individual quiescent sections from the respective light curves in Figures 5.1, 5.3 and 5.5.

Table 5.2: The power law slope, break frequencies and resulting χ^2_ν of fitting a broken power law to the PSD in Figure 5.10.

Observation ID	Power law slope	Frequency	χ^2_ν break [$\times10^{-3}$ Hz]
P20033	1.64	1.49	1.06 (350)
P50011	1.79	2.18	1.29 (437)
P90007	1.45	0.45	2.18 (619)

5.4 Spectral Fitting

The data in this chapter has impressive temporal resolution over many outburst cycles allowing the evolution of the spectral parameters to be studied throughout many quiescent periods.

The data presented in Chapter 4 were found to be well described by both single and multi-temperature models, requiring the addition of a fixed 6.4 keV line and sub-solar metal abundances, a partial covering component was also required for the single temperature models.

5.4.1 Single Temperature Fits

The single temperature model with a 6.4 keV emission line and free metal abundances described the data in Chapter 4 well, it is also a simple model that can be used to characterise the data. Fits to this model can be seen in Figures 5.11 to 5.15.

The best fit model temperatures were well constrained and clearly defined the start and ends of the outbursts in all data sets. Despite the highly variable count rates the best fit temperatures remained remarkably constant. The quiescent temperatures fitted between 15 – 20 keV for all data sets, while in outburst the temperatures became cooler with best fits between 5 – 10 keV, with the majority fitting between 6 – 8 keV. The best fit model temperature in Figure 5.11 also has a slightly lower temperature in the second quiescent interval compared to the third quiescent interval. This indicates that the different flux levels of the quiescent intervals does have an effect on the spectral parameters.

The abundances were fitted as a free parameter to allow the thermal plasma model to provide a better description of the thermal lines. Although the model abundances are not expected to vary over the observation each spectrum was fit independently. For all spectra in the five data sets the abundances were sub solar (relative to abundances of Anders & Grevesse, 1989), with nearly all the best fits resulting in abundances between 0.2 – 0.4 solar. Within error, these abundances were similar with $0.53^{+0.03}_{-0.02}$ and $0.45^{+0.02}_{-0.04}$ solar for the representative spectra found in Chapter 4.

The line strength of the 6.4 keV line, while the system was in quiescence, was consistently between 150 – 250 eV. During outburst the line was noticeably stronger with most fits resulting in line strengths of 300 – 400 eV, the line strength for the P50011 data set, Figure 5.13, was as high as 800 eV.

Examining the trends in Figures 5.11 to 5.15 the best fit abundances and line strengths appear to be correlated. The P50012 data set, due to the large amount of concentrated exposure in quiescence and outburst, was binned into two spectra to test this. Confidence contours were plotted for the fitted values of the 6.4 keV line normalisation and the abundances in Figure 5.16. It should be noted that the 6.4 keV line normalisation is expected to decrease even though the line strength increases due to the decrease in the continuum flux. The confidence contours show that the parameters were weakly correlated. This correlation may be due to the detector not having high enough resolution to separate the fluorescent line from the thermal lines. In outburst, with more cooler gas present in the boundary layer the result is stronger helium like (6.7 keV) than hydrogen like (6.95 keV) line emission. The helium like emission and fluorescent lines may be blended by the detector and fit by the 6.4 keV line. The abundance parameter then fits the hydrogen like emission line and a weaker helium like emission line resulting in lower best fit abundances than expected and higher 6.4 keV line strengths.

Testing the Iron Thermal Emission Lines

To understand how reasonable the best fit line strengths were for the single temperature thermal plasma model a fit was performed using a bremsstrahlung continuum with three fixed emission lines, to the P50012 data set. The line energies were fixed at 6.4, 6.7 and 6.95 keV for a fluorescence line and helium and hydrogen like iron line emission. This model has no dependence on the metal abundances and using three separate emission lines fixed at the correct energy for the respective lines should be able to better determine the 6.4 keV line strengths. The best fit

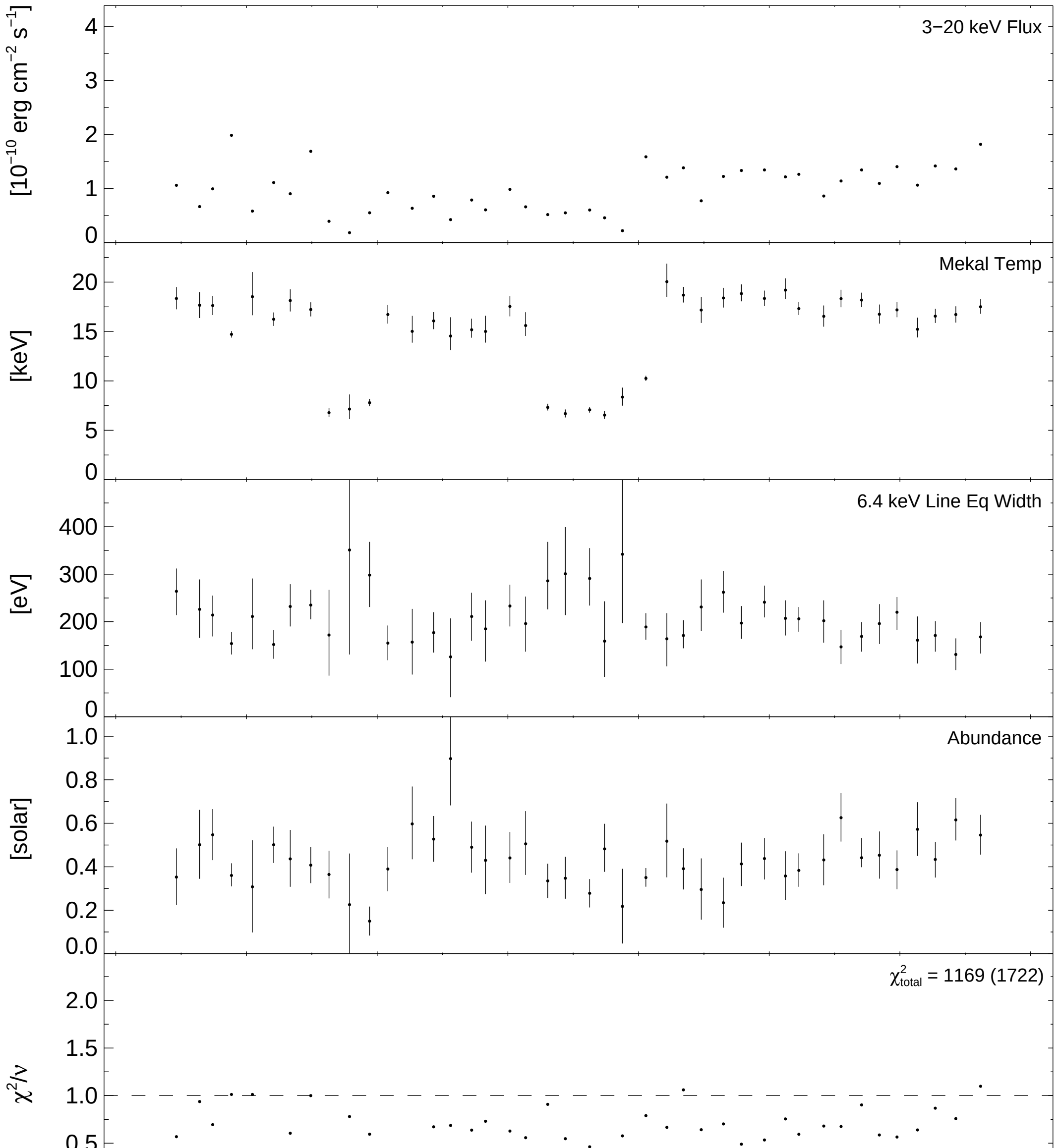

Figure 5.11: Results of fitting the single temperature thermal plasma model with fixed 6.4 keV emission line and free abundances to the data set P20033. All errors are 68 per cent confidence for one parameter of interest ($\Delta\chi^2 = 1.0$).

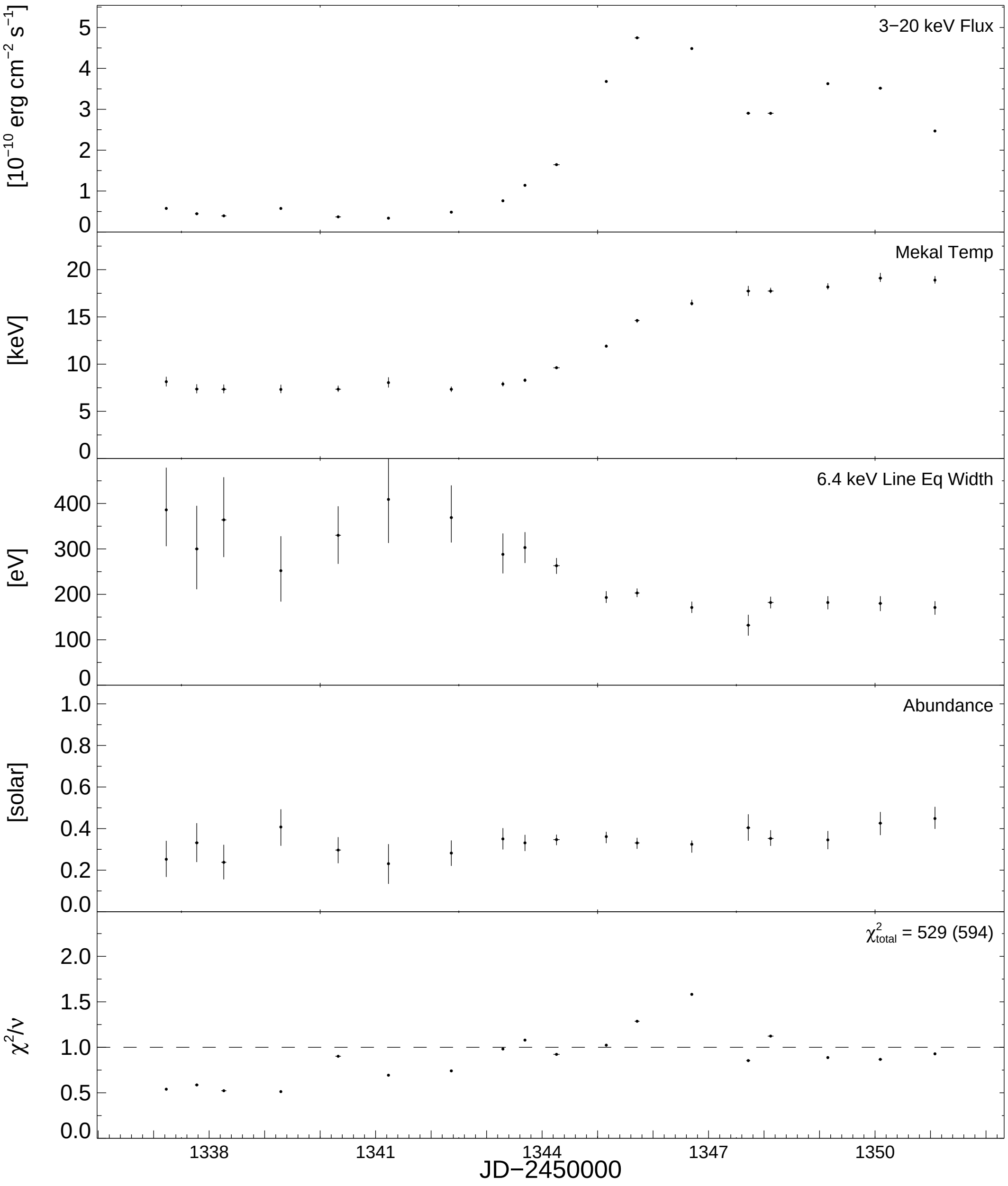

Figure 5.12: Results of fitting the single temperature thermal plasma model with fixed 6.4 keV emission line and free abundances to the data set P40012. All errors are 68 per cent confidence for one parameter of interest ($\Delta\chi^2 = 1.0$).

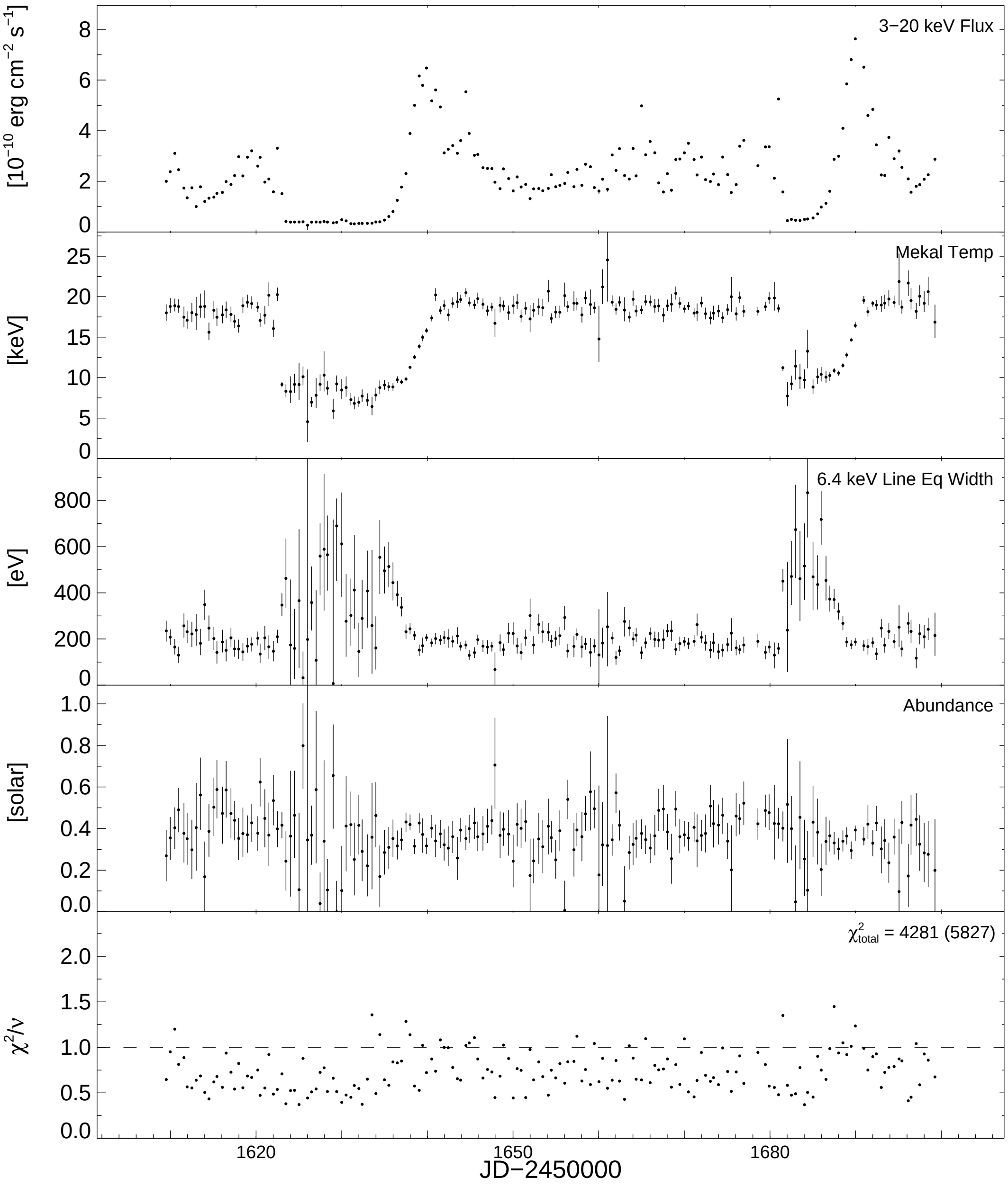

Figure 5.13: Results of fitting the single temperature thermal plasma model with fixed 6.4 keV emission line and free abundances to the data set P50011. All errors are 68 per cent confidence for one parameter of interest ($\Delta\chi^2$ = 1.0).

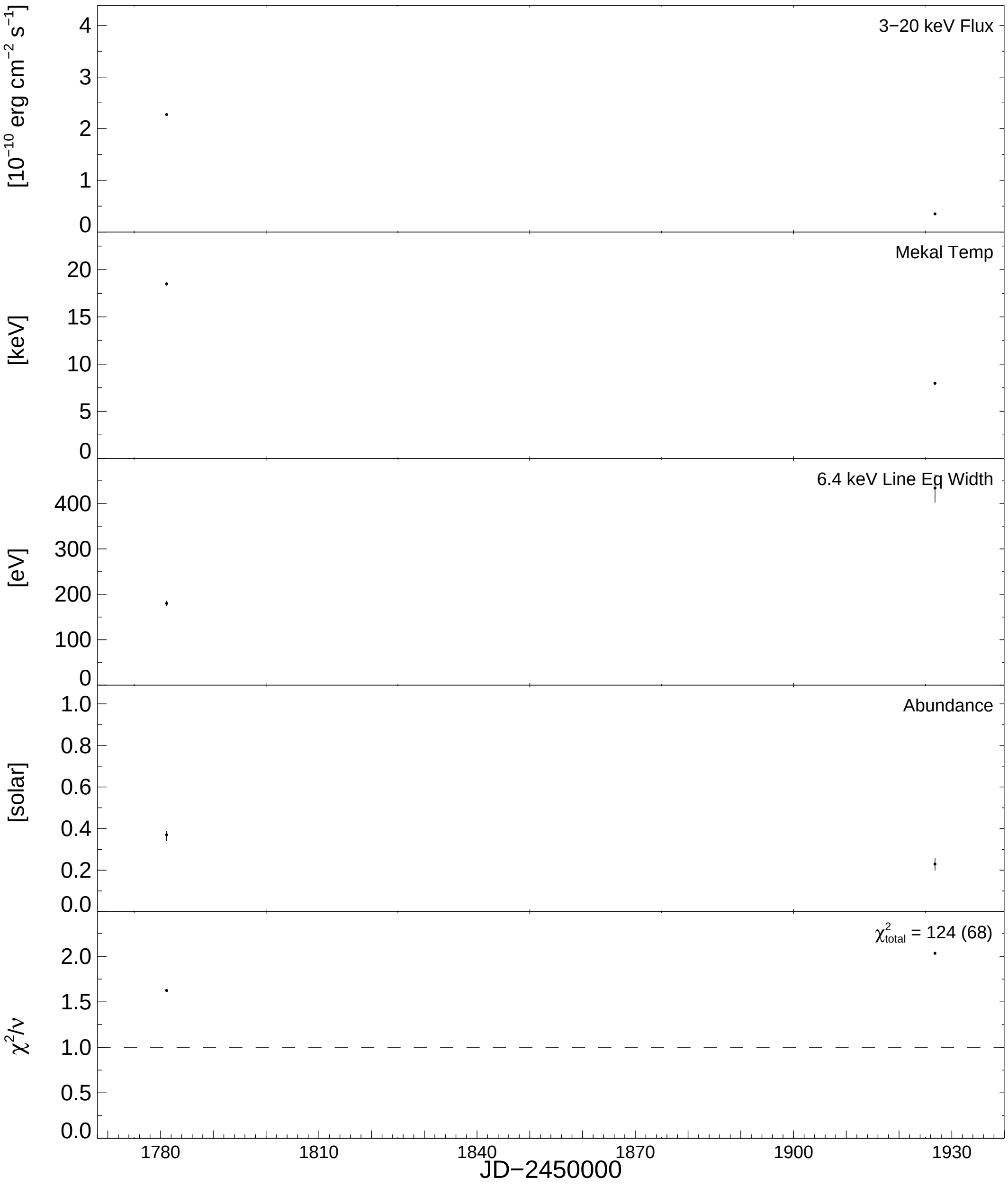

Figure 5.14: Results of fitting the single temperature thermal plasma model with fixed 6.4 keV emission line and free abundances to the data set P50012. All errors are 68 per cent confidence for one parameter of interest ($\Delta\chi^2$ = 1.0).

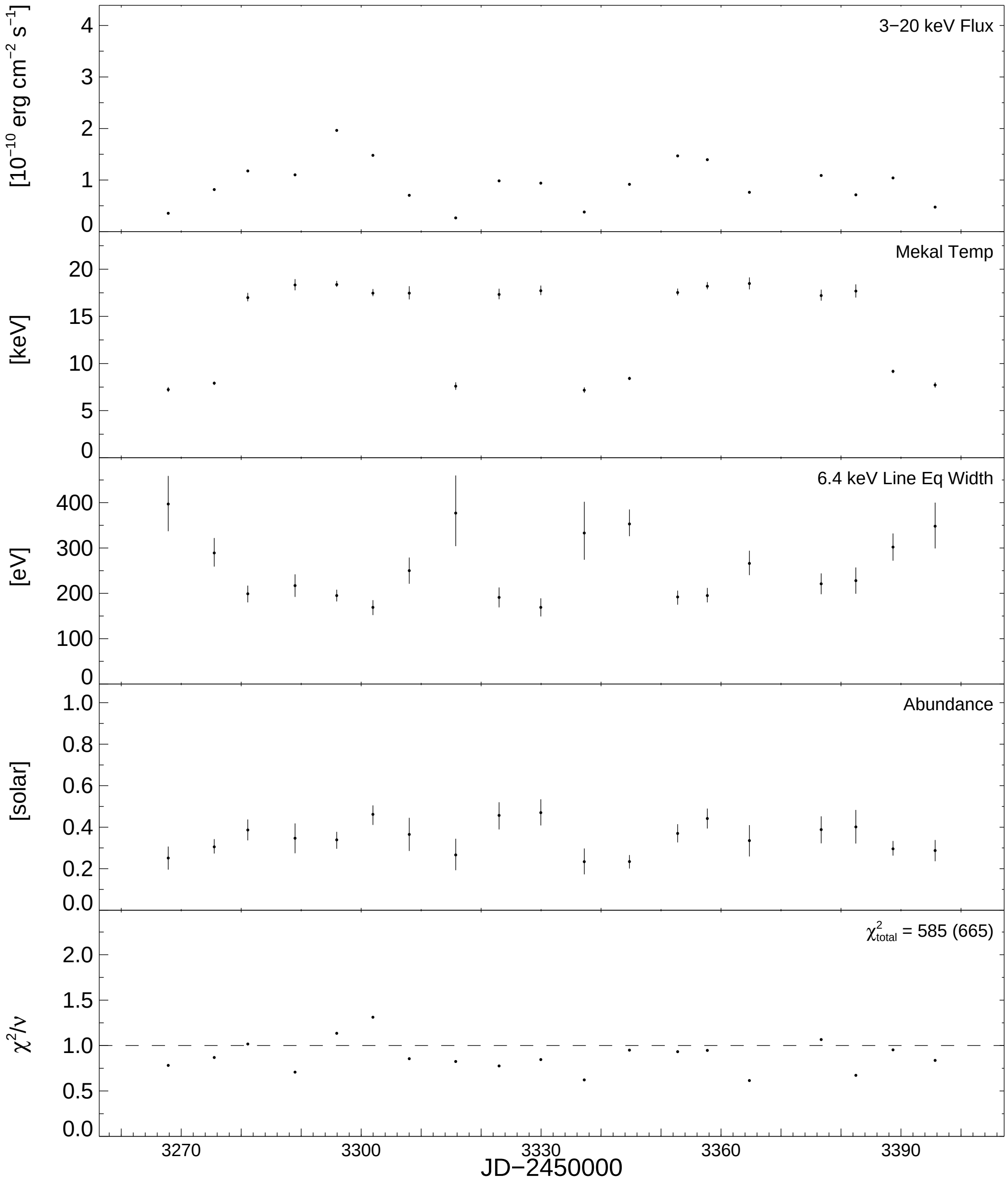

Figure 5.15: Results of fitting the single temperature thermal plasma model with fixed 6.4 keV emission line and free abundances to the data set P90007. All errors are 68 per cent confidence for one parameter of interest ($\Delta\chi^2$ = 1.0).

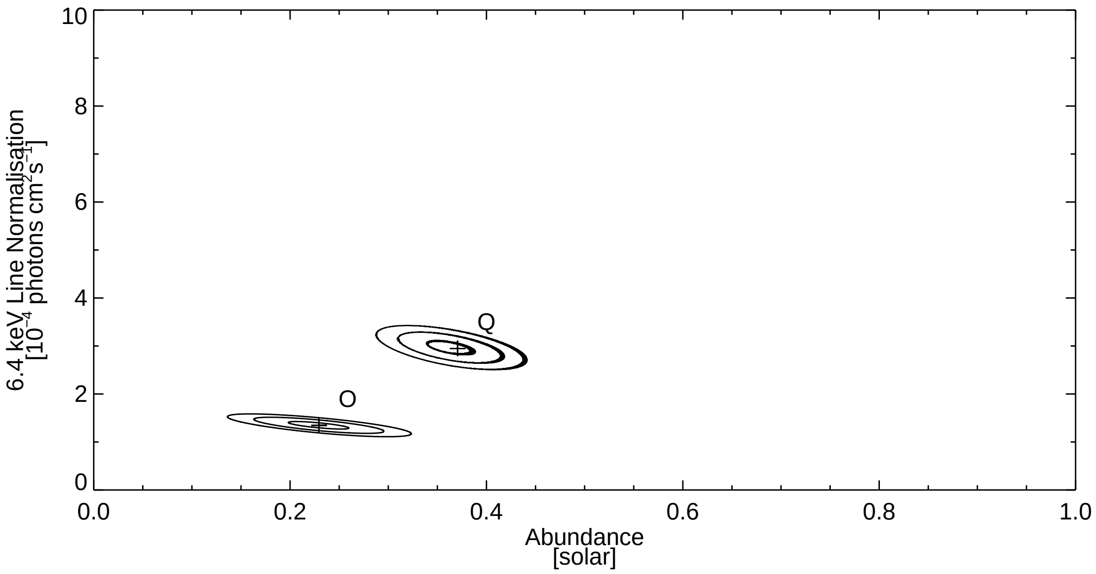

Figure 5.16: Allowed ranges of the 6.4 keV line normalisation and the abundance parameters for the two binned spectra from data set P50012. The spectra are marked quiescence (*Q*) and outburst (*O*). The cross represents the best fitting values for each spectrum. The three contours represent $\Delta\chi$ of 2.3, 4.61 and 9.21, corresponding to 68, 90 and 99 per cent confidence for two parameters of interest (Lampton et al., 1976).

Table 5.3: Fits to the two binned spectra from data set P50012. A bremsstrahlung continuum with three fixed lines at 6.4, 6.7 and 6.95 keV for the fluorescence line, helium like and hydrogen like iron emission lines.

Time [JD]	χ^2_ν	kT [keV]	6.4 keV EW [eV]	6.7 keV EW [eV]	6.95 keV EW [eV]	Flux [2 – 20 keV]
2451781	31 (34)	$19.5^{+0.1}_{-0.2}$	104^{+25}_{-24}	117^{+45}_{-44}	54 ± 28	2.28×10^{-10}
2451926	63 (34)	$8.2^{+0.2}_{-0.2}$	$394.^{+126}_{-95}$	$150.^{+112}_{-121}$	$36.4^{+106}_{36.4}$	3.51×10^{-10}

Table 5.4: Observation times of each pointed *RXTE*/*PCA* of SS Cygni used produce the seven quiescent spectra.

Spectrum ID	Proposal number	Start - End date [JD]	Number of observations	Total exposure [ks]	Mean count rate [counts s^{-1}]
1	P20033	2450509 -2450526.5	7	14	30.5
2	P20033	2450541 -2450560	7	15	18.8
3	P20033	2450584 -2450632	17	30	27.4
4	P50011	2451648 -2451680.5	66	50	75.8
5	P90007	2453281 -2453330	4	42	30.6
6	P90007	2453323 -2453302	5	18	20.7
7	P90007	2453352 -2451682	8	46	23.8
8	P50012	2451926.5 -2451927.5	5	39	8.8

parameters are presented in Table 5.3 and resulted in 6.4 keV line strengths comparable to the fits with the thermal plasma model.

5.4.2 Long Term Quiescent Spectral Evolution

The data sets were binned such that the data in each quiescent interval were combined into a single spectrum resulting in seven spectra. The exposure, start and end times of each spectrum and mean count rates can be found in Table 5.4.

Initially a single temperature thermal plasma model and a 6.4 keV line were fit to the quiescent data. The metal abundances were fit as a free parameter. A number of spectra were well fit by this model but it was unable to fit the spectra with higher exposures, which resulted in χ^2_ν of just less than 2 indicating that the model was not able to fully describe the data. The residuals to this model for spectrum number 5, the poorest fitting spectrum also with a high exposure, are plotted in Figure 5.19, panel A. The residuals show the model was a poor fit, with a deficit in the model between 7.5 – 10 keV and an excess above 10 keV. The total χ^2_ν for this model was 1.33 (268 d.o.f).

The addition of the 6.4 keV line is highly suggestive of Fe Kα fluorescence emission due to illumination of cold gas, which is a strong indication that there was Compton scattering of X-rays. The equivalent widths were also consistent with those expected from a semi-infinite, plane parallel cold slab irradiated by an external source of X-rays (George & Fabian, 1991). Fitting the data with a free reflection component improved the overall χ^2_ν but was unable to improve the poorer fitting spectra from the previous model, which still had an unacceptable χ^2_ν above 1.5 (40 d.o.f) consistent with Chapter 4.

In Chapter 4 the data were found to be well fit by both a single temperature model, with free abundances, with a partial covering absorber and 6.4 keV line (Section 4.3.1) and by a multi-temperature thermal plasma model, with free abundances, and a 6.4 keV line (Section 4.4.3).

Partial Covering absorber

Fitting the data with partial covering absorber resulted in a significant improvement to all spectra. The total χ^2_ν improved from 1.34 (268 d.o.f) to 0.69 (254 d.o.f), an F-test resulted in a probability of 9.0×10^{-34} that this improvement occurred by chance.

Although the single temperature model with partial covering absorber resulted in a good overall fit, the requirement of the 6.4 keV line is a good indication of a reflection continuum present in the spectra. A reflection component was added to the model with the reflector abundances tied to the abundances of the plasma model and the reflection fit as a free parameter. The reflection spectrum was calculated from the code of Magdziarz & Zdziarski (1995). The addition resulted in a small improvement to the overall fit giving a total χ^2_ν of 0.67 (247 d.o.f). The addition was not significant, an F-test resulted in a probability of 0.55, however the fits show that the spectra were consistent with a reflection continuum. The residuals for this model for spectrum number 5 both with and without reflection are plotted in Figure 5.19, panels B and C.

Fits to all the data using the single temperature model with partial covering absorber, 6.4 keV and free reflection component can be seen in Figure 5.17. The quiescent spectra, each with a large amount of exposure, were able to constrain the model parameters. The most striking feature of these fits are the different fluxes between each spectrum, from 0.7×10^{-10} ergs s^{-1} cm^{-2} – 2.3×10^{-10} ergs s^{-1} cm^{-2} the average flux was 1.26×10^{-10} ergs s^{-1} cm^{-2}. The best fit temperature was well constrained with best fits of 13.6 ± 1.0 – 16.3 ± 1.3 keV. Both the best fit abundances and 6.4 keV line equivalent widths were consistent between the spectra with best fits between $0.32 \pm 0.03 - 0.49 \pm 0.06$ solar for the abundances and $158^{+27}_{-31} - 208 \pm 29$ eV for the equivalent widths. The covering fraction parameter was consistent across the spectra, favouring a high covering fraction close to 1 for the majority of spectra. The hydrogen column was barely constrained by a number of spectra, although, all spectra had a consistent nH with a best fit value of $80^{+511}_{-46} - 262^{+71}_{-100}$ atoms cm^{-2}. The contribution from the reflection continuum was well constrained, with a best fit of $0.25^{+0.13}_{-0.15} - 0.88 \pm 0.27$. All spectra, with exception of spectra number 1, were consistent with a constant reflection.

Multi-temperature Models Fits

In Chapter 4 a multi-temperature model was found to give statistically acceptable fits. Multi-temperature continuum models have also been found previously to result in more statistically acceptable fits (Done & Osborne, 1997; Baskill et al., 2005; Okada et al., 2008). The single temperature continuum model was replaced with a multi-temperature model, cemekl in `XSPEC` (built from the mekal code, Singh et al., 1996)). The emission measure follows a power law in temperature, proportional to $(T/T_{max})^{\alpha}$. This allows a full range of temperatures to be fit with T_{max} and α fit as free parameters.

As with the single temperature fits the residuals to the multi-temperature model required a line component fixed at 6.4 keV for fluorescence of neutral iron and free metal abundances. The fit resulted in a total χ^2_ν of 0.77 (261 d.o.f).

Although the multi-temperature model resulted in good fits, the requirement of the 6.4 keV line is an indication of a reflection continuum. A reflection component was added to the model with the reflector abundances tied to the abundances of the plasma model. Fitting the reflection as a free parameter improved the fits resulting in a total χ^2_ν of 0.65 (247 d.o.f). The addition had a significant effect, an F-test resulted in a probability of 4.0×10^{-8}. The residuals

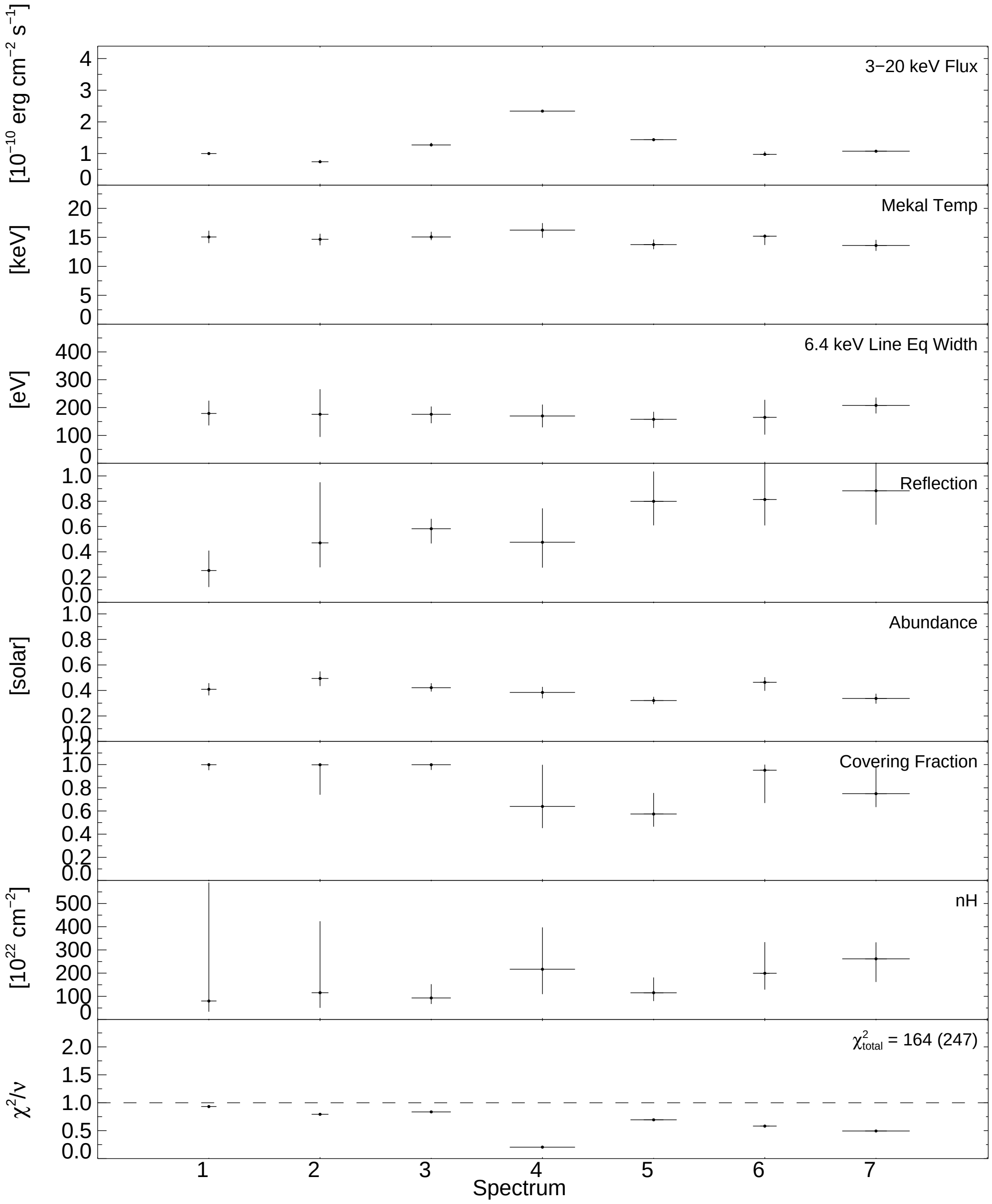

Figure 5.17: Results of fitting the seven quiescent spectra with a single temperature model with free abundances, partial covering component, fixed 6.4 keV emission line and a free reflection component. All errors are 68 per cent confidence for one parameter of interest ($\Delta\chi^2$ = 1.0).

to this model for spectrum number 5 both with and without reflection are plotted in Figure 5.19, panels D and E. The residuals show a marked improvement over the initial single temperature model fits.

Fitted parameters to all the data using the multi-temperature model with 6.4 keV and free reflection component can be seen in Figure 5.18. The quiescent spectra, each with a large amount of exposure, were able to constrain the model parameters. Unlike Section 4.4.3 in Chapter 4, the α parameter was well constrained with best fits of $0.97^{+0.77}_{-1.16} - 1.70^{+1.49}_{-1.92}$. The best fits were consistent with fits by Baskill et al. (2005), who fit an α of 1.41 ± 0.09 in quiescence. The T_{max} parameter was not as well constrained and varied between spectra from between $23^{+4}_{-2}-34^{+5}_{-3}$ keV. Both the best fit abundances and 6.4 keV line equivalent widths were similar between the spectra with best fits between $0.34\pm0.03-0.58\pm0.07$ solar for the abundances and $129\pm26-188\pm15$ eV for the equivalent widths. The contribution from the reflection continuum was well constrained and favoured a low reflection, $0.21^{+0.17}_{-0.12} - 0.51^{+0.08}_{-0.19}$. Based on the strengths of the 6.4 keV line emission, which is consistent with a reflection origin (George & Fabian, 1991), it is hard to believe that the lack of reflection present in spectra 1 and 2 was real. The reflection continuum is constrained by the harder part of the X-ray spectrum, above $\sim$ 10 keV. At these energies the background systematics become important and have the greatest effect, it is likely that this combined with the lower exposures for these two spectra are the cause of the best fit reflection fitting at 0.

In both the single and multi-temperature fits the quiescent spectra had a high temperature and favoured sub-solar abundances of $\sim$ 0.4 solar. Both models had consistent 6.4 keV line strengths of $\sim$ 200 eV strongly indicating the presence of a reflection continuum in the spectra. The high covering fraction and hydrogen column in the single temperature fits also provide evidence of absorbing gas near to the boundary layer, however the partial covering absorber was not needed in the multi-temperature fits suggesting that it may not be present. When fitting the reflection parameter the spectra favoured a higher reflection in the single temperature than multi-temperature model, but was well constrained and low in both models.

It should be noted that the best fit χ^2_ν for all the spectra were low, most likely indicating that the systematic error applied was too high.

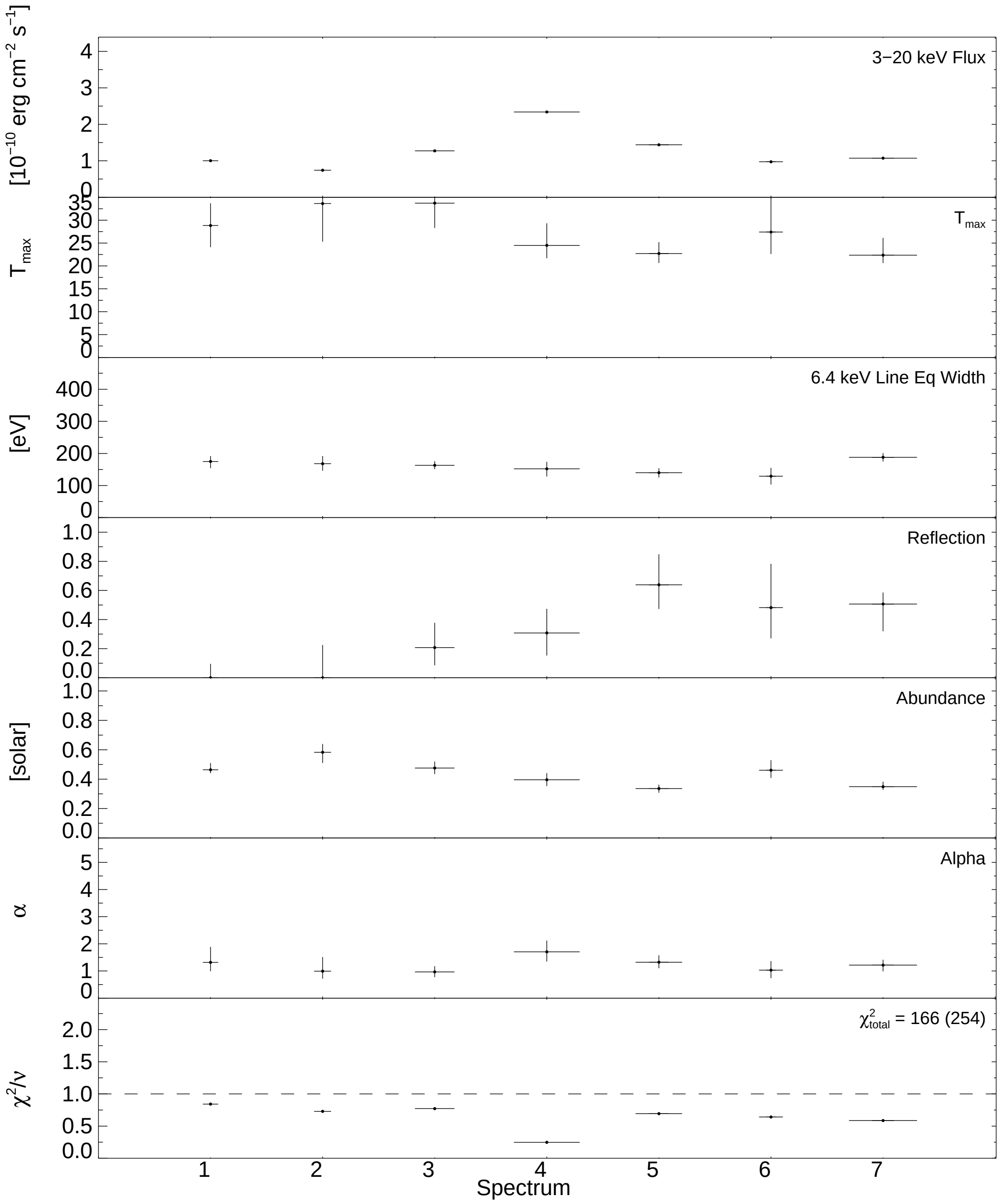

Figure 5.18: Results of fitting the seven quiescent spectra with a multi-temperature model with free abundances, fixed 6.4 keV emission line and a free reflection component. All errors are 68 per cent confidence for one parameter of interest ($\Delta\chi^2$ = 1.0).

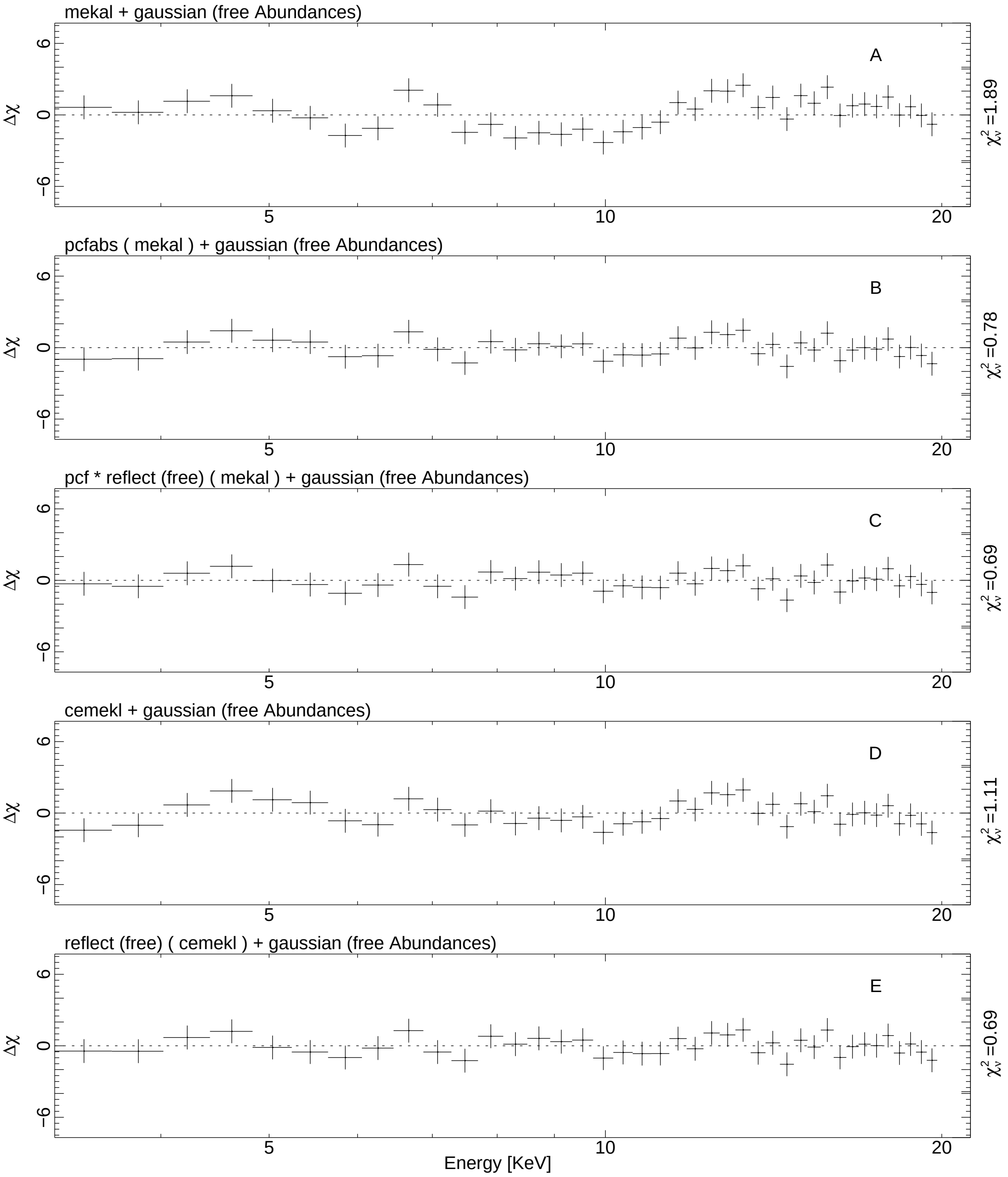

mekal + gaussian (free Abundances)

pcfabs (mekal) + gaussian (free Abundances)

pcf * reflect (free) (mekal) + gaussian (free Abundances)

cemekl + gaussian (free Abundances)

reflect (free) (cemekl) + gaussian (free Abundances)

Figure 5.19: The residuals for spectrum number 5 from Figure 5.17 and 5.18 to the models attempted in this section. The model, as used in `XSPEC`, is labelled above the residuals, with the reduced χ^2 at the end of the individual panel.

5.4.3 Spectral Evolution Through Quiescence

The long term quiescent evolution was studied in detail in Section 5.4.2. This section focuses on the short term spectral evolution throughout a single quiescent interval. The quiescent interval in data set P50011 had the highest exposure covering an entire quiescent interval (from JD 2451648 – 2451680.5, spectrum 4 in Section 5.4.2). To maximise the signal to noise this quiescent period was binned into five spectra and fit with the two best fitting models: a single temperature thermal plasma model with free abundances, partial covering component, fixed 6.4 keV emission line and a free reflection component; and a multi-temperature thermal plasma model with free abundances, fixed 6.4 keV emission line and a free reflection component.

Both models fit the data well resulting in good total χ^2_ν of 0.64 (160 d.o.f) and 0.60 (155 d.o.f) respectively. The best fit parameters for both models are presented in Figures 5.20 and 5.21 respectively. The flux during the quiescent period initially increased from 1.8×10^{-10} ergs s^{-1} cm^{-2} to 2.8×10^{-10} ergs s^{-1} cm^{-2} before decreasing to 2.3×10^{-10} ergs s^{-1} cm^{-2} Both models had well constrained temperature and T_{max} parameters respectively. T_{max} increased for the first half of quiescence, while for the single temperature model the temperature was constant throughout the entire quiescent interval. Both models also fit a slightly lower temperature for the spectrum on JD 2451665.4. The α parameter, for the multi-temperature model, was also well constrained with the best fits between $1.34^{+0.51}_{-0.34} - 1.72^{+0.53}_{-0.44}$, consistent with 1.41 ± 0.09 fit by Baskill et al. (2005). Both the best fit abundances and 6.4 keV line equivalent widths were also similar between the spectra with best fits between $0.32 \pm 0.03 - 0.43^{+0.04}_{-0.05}$ solar for the abundances and $145 \pm 15 - 186 \pm 38$ eV for the equivalent width, consistent with a reflection origin (George & Fabian, 1991). The contribution from the reflection continuum was well constrained and favoured a low reflection. Four of the five spectra were consistent with a constant reflection, at $0.31 \pm 0.01 - 0.38^{+0.19}_{-0.26}$ for the single temperature model and $0.12^{+0.12}_{-0.17} - 0.19^{+0.17}_{-0.11}$ for the multi-temperature model. Fits from both models for the spectrum on JD 2451665.4 favoured a higher reflection, $0.91^{+0.22}_{-0.57}$ and $0.59^{+0.16}_{-0.17}$ for the single and multi-temperature models respectively. Further analysis found that T_{max} and the reflection parameter were weakly correlated. The best fit reflection parameters for both models are lower than in Section 5.4.2. The reflection continuum is constrained by the harder part of the X-ray spectrum, above $\sim$ 10 keV. At these energies the background systematics become important and have the greatest effect and it is likely that this combined with lower exposures than in Section 5.4.2 are the cause of the lower best fit reflection. The covering fraction parameter was consistent across the spectra, favouring a high covering fraction of $0.77^{+0.23}_{-0.33} - 1.00^{+0.00}_{-0.04}$, with the exception of the spectrum on JD 2451665.4 which fit a lower covering fraction of $0.51^{+0.11}_{-0.01}$. The hydrogen column was barely constrained by a number of spectra, although, all spectra had a consistent nH with a best fit value of $177^{+135}_{-82} - 269^{+81}_{-181}$ atoms cm^{-2}.

5.4.4 Model Reflection

Comparing the flux above 7 keV with the 6.4 keV line normalisation (as was done in Section 4.4.4 in Chapter 4), it is possible to get a better understanding of the reflection in the system.

Using the higher signal to noise data from Section 5.4.2 (also see Table 5.4) the line normalisation and the line flux above 7 keV is plotted in Figure 5.22 for the single temperature model with 6.4 keV line and a partial covering absorber. The single temperature model used for Figure 5.22 may over predict the line in outburst because the continuum temperature is lower. At lower temperatures there will be more He like emission which may be fit by the 6.4 keV line. The multi-temperature model allows a range of temperatures to be fit, resulting in a more realistic determination of the thermal lines. The line normalisation and the line flux above 7 keV is also plotted for the multi-temperature model in Figure 5.23. This model includes a reflection component that accounts for the reflected photons present which should be removed from the data leaving only the photons that can cause reflection. After a best fit to the model was found the model reflection parameter was then set to zero and the flux was calculated.

The solid line shows the best fit to all spectra. The spectra are numbered sequentially in time (see Figures 5.17 or 5.18). For the single temperature model all spectra are a good fit to a straight line, with the exception of spectrum number 7. The spectra in the multi-temperature model do not fit the best fit line as well, but are still consistent with a straight line. The residuals to the fit line and the data are plotted in the bottom panel. The line fit resulted in a gradient of 0.046 ± 0.002 (with an intercept of 0.000 ± 0.004), for the single temperature fits. The line fits resulted in a gradient of 0.035 ± 0.002 (with an intercept of 0.008 ± 0.007), for the multi-

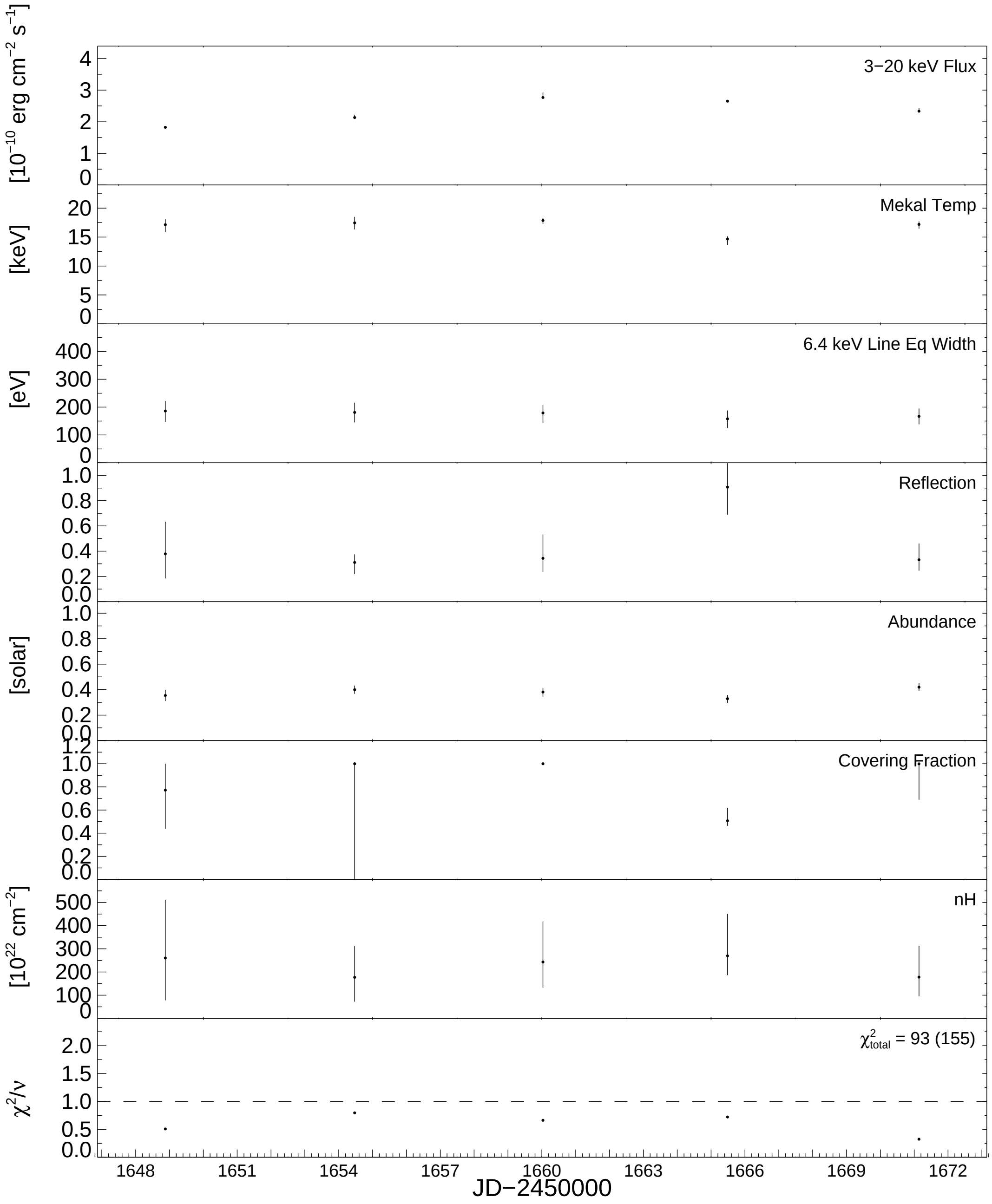

Figure 5.20: Results of fitting the five spectra with a single temperature model with free abundances, partial covering component, fixed 6.4 keV emission line and a free reflection component. All errors are 68 per cent confidence for one parameter of interest ($\Delta\chi^2 = 1.0$).

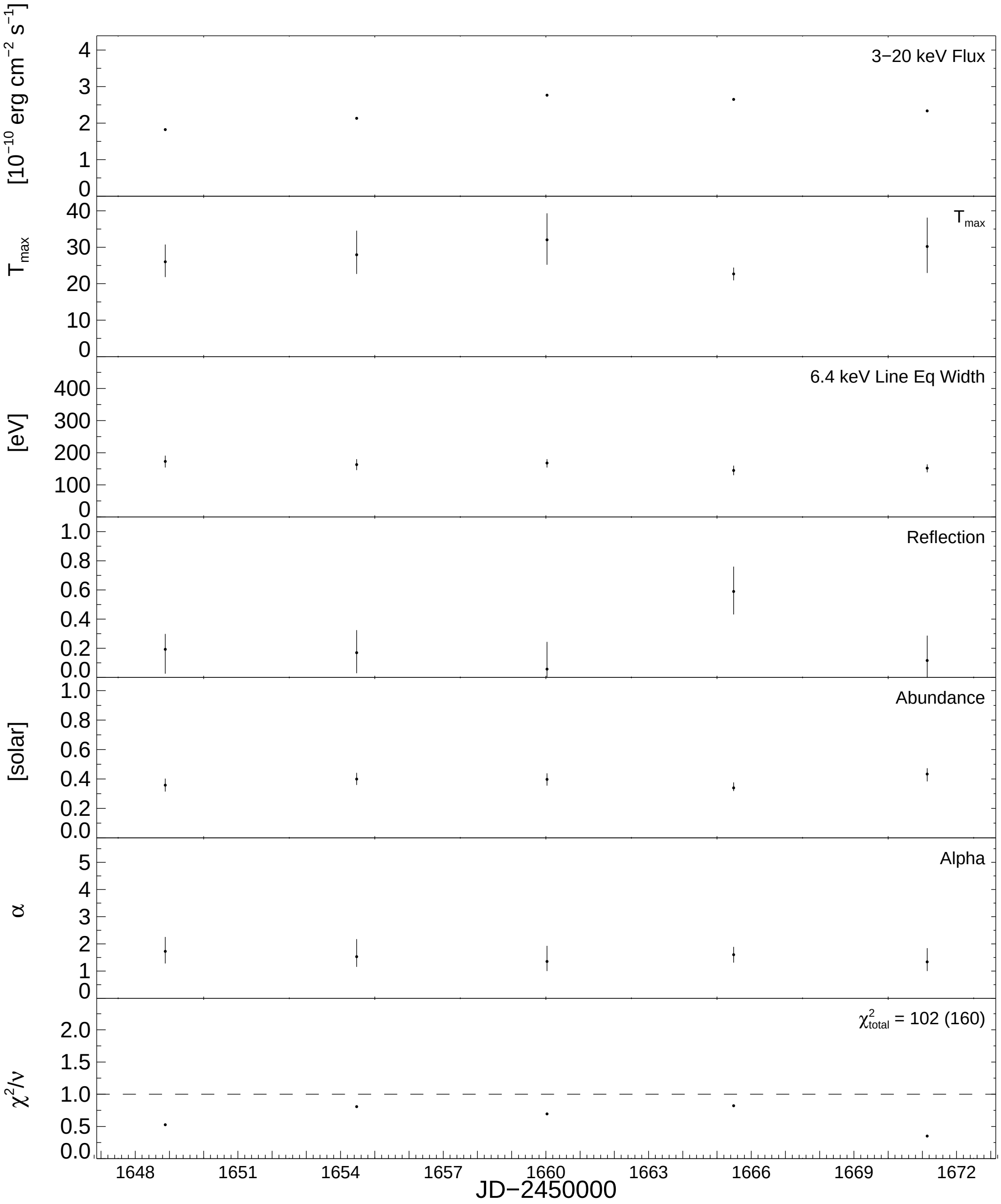

Figure 5.21: Results of fitting the five spectra with a multi-temperature model with free abundances, fixed 6.4 keV emission line and a free reflection component. All errors are 68 per cent confidence for one parameter of interest ($\Delta\chi^2$ = 1.0).

temperature model. Both Figures 5.22 and 5.23 are consistent with a constant reflection in quiescence.

To compare the outburst reflection with that during quiescence the binned outburst spectra from data set P50012 in Section 5.4.1 were fitted with both the single and multi-temperature models. This outburst spectra is plotted on Figures 5.22 and 5.23 respectively and labelled as spectrum number 8. In both models the 6.4 keV line normalisation is greater than the line fit indicating that for both models the spectra are consistent with an increased reflection in outburst.

5.4.5 X-ray Luminosity

Fluxes were calculated for the combined quiescent spectra from the best fitting model over the energy range $2 - 20$ keV, resulting in a range of fluxes of $0.7 - 2.3 \times 10^{-10}$ ergs s^{-1} cm^{-2}. Broadband fluxes were also calculated by integrating over the energy range $0.01 - 100$ keV giving fluxes of $1.3 - 3.9 \times 10^{-10}$ ergs s^{-1} cm^{-2}. Assuming a distance of 166.2 ± 12.7 pc for SS Cygni (Harrison et al., 1999) the corresponding luminosity was calculated to have a range of $4.3 - 12.9 \times 10^{32} (d/166pc)^2$ ergs s^{-1}. Using the relation $L = GM_{wd}\dot{M}/2R_{wd}$ and assuming the mass of the white dwarf in SS Cygni is $M_{wd} = 0.82 M_{\odot}$ and $R_{wd} = 5.9 \times 10^8$ cm (Bitner et al., 2007) the quiescent accretion rates corresponding to the luminosities, were calculated to be $0.5 - 1.29 \times 10^{16}$ g s^{-1}. These accretion rates and associated fluxes and luminosities can be seen in Table 5.5. These accretion rates are substantially higher than calculated for the 1996 outburst in Chapter 4 of 0.3×10^{16} g s^{-1}.

The peak of the transition provides an estimate of the accretion rate at which the boundary layer becomes optically thick to its own emission and the hard X-rays become suppressed. These accretion rates and associated fluxes and luminosities can be seen in Table 5.6. It is interesting to note that the quiescent accretion rate in data set P50011 is higher than the peak accretion rates in both the P20033 and P90007 data sets and is also higher than observed in Chapter 4. This is surprising because while the boundary layer in these data sets is already optically thick in data set P50011 it remains in quiescence and optically thin.

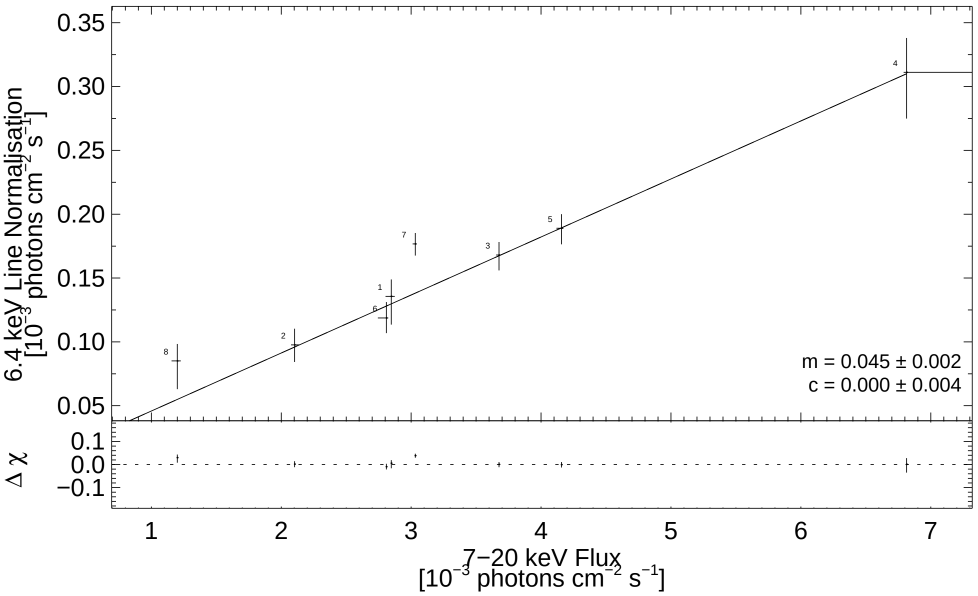

Figure 5.22: The best fit 6.4 keV line normalisation and the continuum flux above 7 keV to the single temperature model with partial covering absorber, 6.4 keV emission line and free abundances. The best fit line to all the data is plotted along with its residuals. All errors are in the 68 per cent confidence interval for one parameter of interest ($\Delta\chi^2 = 1.0$).

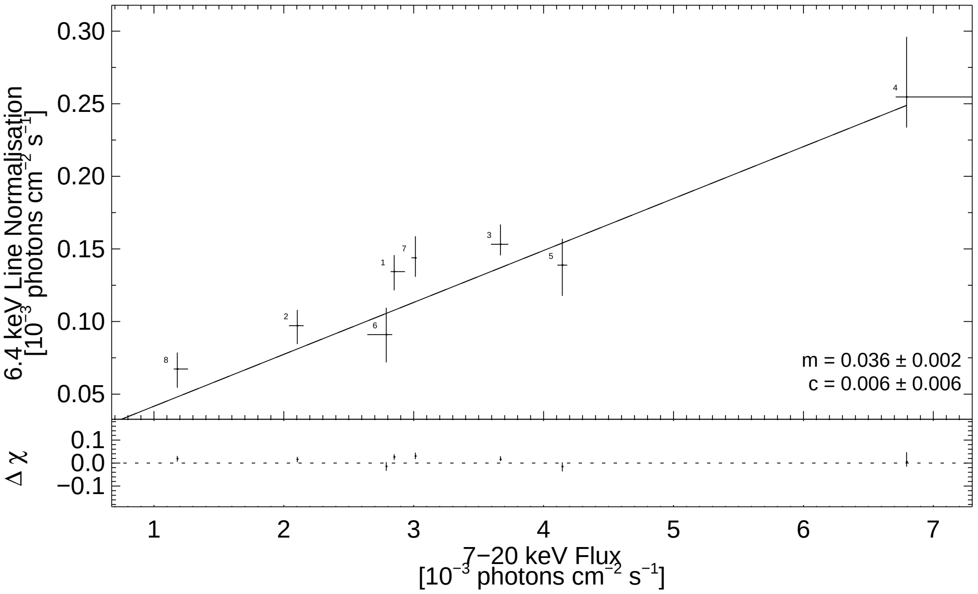

Figure 5.23: The best fit 6.4 keV line normalisation and the continuum flux above 7 keV to the multi-temperature model with free reflection component, 6.4 keV emissions line and free abundances. The best fit line to all the data is plotted along with its residuals. All errors are in the 68 per cent confidence interval for one parameter of interest ($\Delta\chi^2 = 1.0$).

Table 5.5: Luminosities and accretion rates of SS Cygni during quiescence.

Observation ID	Flux[a] [2 – 20 keV]	Flux[a] [0.01 – 100 keV]	Luminosity[b]	Accretion rate[c]
1	10.0	16.3	3.3	4.9
2	7.4	13.2	2.4	3.6
3	12.7	22.1	4.2	6.2
4	23.4	38.8	7.7	10.1
5	14.4	23.9	4.7	7.0
6	9.7	16.7	3.2	4.8
7	10.7	18.2	3.5	5.2

[a] $\times 10^{-11}$ ergs s^{-1} cm^{-2}
[b] $\times 10^{32}(d/166pc)^2$ ergs s^{-1}
[c] $\times 10^{15}$ g s^{-1}

Table 5.6: Luminosities and accretion rates of SS Cygni at the peak of the hard X-ray recovery.

Observation ID	Flux[a] [2 – 20 keV]	Flux[a] [0.01 – 100 keV]	Luminosity[b]	Accretion rate[c]
P20033	16.6	28.3	9.33	10.1
P40012	45.2	81.3	26.8	28.9
P50011	61.5	102.0	33.6	36.3
P90007	14.1	25.5	8.40	9.1

[a] $\times 10^{-11}$ ergs s^{-1} cm^{-2}
[b] $\times 10^{32}(d/166pc)^2$ ergs s^{-1}
[c] $\times 10^{15}$ g s^{-1}

5.5 Discussion

The X-ray data presented in this chapter observed the evolution of 10 outbursts and 7 full periods of quiescence, with a further 4 periods of quiescence partially observed. With the exception of one outburst, all outbursts exhibited very consistent behaviour. The quiescent X-rays were harder and brighter than during optical outburst. Shortly after the optical band entered outburst the X-ray flux was quenched to below the quiescent level. Although the mean quiescent fluxes were very different between data sets, the outburst fluxes, for all data sets, were all very similar. The exception to this outburst pattern was not suppressed until 10 days after the optical rise, however, the spectrum was soft for the duration of the outburst. The behaviour of this outburst closely resembles that presented of U Gem in Chapter 6.

5.5.1 The X-ray Transition

In three of the outbursts presented there was an increased count rate immediately before the hard X-ray suppression making it likely that this event occurs immediately before the X-ray suppression in all SS Cygni outbursts. The cadence of the observation places an upper limit of 12 hours for the duration of this peak. This is consistent with Wheatley et al. (2003) who measured the rise to the peak to take approximately 12 hours. The peak does not reach the same count rate as in the hard X-ray recovery for two of the outbursts, but based on the outburst in Chapter 4 it is likely that the highest part of the peak before the suppression was missed. The observed peaks were also consistent with occurring at the same time before the hard X-ray suppression. When the heating wave reaches the boundary layer the accretion rate rapidly increases before the optically thin boundary layer becomes optically thick and the bremsstrahlung continuum is replaced by a black body continuum. The boundary layer is thought to become optically thick once the accretion rate has reached a critical value (Pringle & Savonije, 1979). Observing the count rate increase before the hard X-ray suppression also places a constraint on the delay between the optical rise and the X-ray drop. The rise in the X-ray count rate occurred $0.5 - 1.6$ days after the beginning of the rise in the optical band. This is consistent with the delay of $0.9 - 1.4$ days measured by Wheatley et al. (2003). This indicates that in SS Cygni the heating wave probably originates from the same place in the accretion disc for all outbursts.

The hard X-ray recovery was clearly observed in a number of outbursts. The beginning of the hard X-ray recovery had a range of times beginning just after the optical outburst started to decline, to when the optical band had nearly reached quiescence, as was observed in Chapter 4. However, the peak of the recovery occurred at similar times. The duration of the recovery typically lasted $3 - 5$ days, ending after the optical band had reached quiescence. The timing of the start of the recovery indicates that the accretion rate in the boundary layer was already decreasing before the cooling front reached it. The range of recovery times and the X-ray outburst returning to quiescence after the optical is presumably an indication that the inner disc is the last part of the accretion disc to return to quiescence. It as also likely that the cooling front propagates throughout the accretion disc before it cools the boundary layer.

All observations showed high levels of variability, $\sim$ 45 per cent, during the transitions, both at the start and at the end of the hard X-ray suppression. This coincides with the boundary layer as it changes state from optically thin to optically thick and vice versa. The averaged PSD also shows that there is variability on timescales faster than 16 seconds. SS Cygni has been found previously to be variable during the transition with amplitude peaks at 45 per cent during X-ray suppression (Wheatley et al., 2003). Variability of VW Hyi has been observed on a timescale of $\sim$ 200 seconds with an amplitude that decreased from $\sim$ 100 per cent at the beginning to $\sim$ 50 per cent at the end of the recovery from outburst (Wheatley et al., 1996). Variability was also found in U Gem during the transition of the boundary layer at the start and end of the X-ray suppression (Chapter 6).

5.5.2 X-rays in Quiescence

During outburst the count rates were suppressed at a very constant level for all but one outburst. The mean quiescent count rates, on the other hand, varied greatly from data set to data set and also within each observation on long and short time-scales. The quiescent spectrum was also harder than that of the outburst spectrum. Despite the high levels of variability in the light curve and the vast differences in the count rates between data sets there was little change in the spectrum.

The spectra from all data sets were combined creating several spectra from the full quiescent intervals with very high signal to noise. These spectra were used to analyse the long term quiescent evolution. The spectra were also combined from the quiescent interval with the highest exposure to analyse the short term quiescent evolution. All spectra constrained the complex single and multi-temperature reflection models, resulting in similar long and short term spectral evolution. Despite the very different fluxes between the quiescent observations the plasma temperatures were well constrained and consistent across all spectra for both the short and long term quiescent intervals and all fitting required sub-solar metal abundances, $0.4-0.5$ solar. Single temperature fits required a partial covering absorber, with all spectra favouring a high covering fraction. This can be interpreted as the X-rays being partially obscured by an absorbing medium.

However, the high covering fraction and the multi-temperature models not requiring this component indicate that this may not be the correct interpretation. The 6.4 keV line strengths in both models were also consistent with a reflection continuum. The reflection continuum significantly improved the fits with all spectra favouring a reflection below 1, with most fitting between 0.2 – 0.6. The line fits of the 6.4 keV line normalisation and the model flux above 7 keV are also consistent with a constant reflection. Approximately 3.5 – 4.5 per cent of the continuum flux in quiescence was fluorescent photons. This indicates that if the inner accretion disc is truncated it is stable and the geometry does not change throughout quiescence. The fraction of fluorescent photons created from the continuum flux > 7 keV are consistent with the spectra that were not quenched in Chapter 4 and also with SU UMa in Chapter 7.

5.5.3 Quiescent Accretion Rates

Hard X-rays are expected to be emitted in low accretion rate systems where $\dot{M} \leq 10^{16}$ g s^{-1} (Pringle & Savonije, 1979; Patterson & Raymond, 1985b). When the accretion rate reaches a critical value the boundary layer becomes optically thick and the hard X-rays become thermalised and emitted in the EUV and soft X-ray bands. (Pringle & Savonije, 1979). The mean fluxes varied between the quiescent intervals, however, spectral fitting resulted in only small differences between the model parameters. This suggests that these flux variations were due to long term accretion rate variations in the quiescent disc. The accretion rate in quiescence, when the disc was optically thin, was observed at higher rates (10.1×10^{15} g s^{-1}) than a number of outburst accretion rates as the boundary layer became optically thick (0.9 and 1.0×10^{16} g s^{-1}), based on the peak of the hard X-ray recovery. This is surprising, analysis by Wheatley et al. (2003) suggested that once the accretion rate reaches a critical value the boundary layer becomes optically thick. However, the accretion rate during the peak, before the outburst and during the recovery, always increases despite the preceding quiescent accretion rate. This indicates that the critical accretion rate is not fixed in SS Cygni. The large range of accretion rates in quiescence may be due to changes in the viscosity of the quiescent accretion disc (Shakura & Syunyaev, 1973; Papaloizou & Stanley, 1986) allowing a higher quiescent accretion rate.

These accretion rates are 2 – 3 orders of magnitude higher than predicted by the DIM, (e.g., Hameury et al., 2000), if the quiescent disc extends down to the white dwarf surface and if the X-rays are emitted by a hot boundary layer (Pringle & Savonije, 1979; Tylenda, 1981; Patterson & Raymond, 1985b). Therefore, the removal of the inner disc by magnetic stress (Livio & Pringle, 1992) or evaporation (Meyer & Meyer-Hofmeister, 1994; Menou, 2000) or by other means makes the truncation of the disc an important ingredient in the DIM resolving the discrepancy between observation and theory.

5.6 Conclusions

The X-ray data presented in this chapter observed the outburst evolution of 10 outbursts and 11 quiescent intervals. With the exception of one outburst of the ten observed, all data exhibited very consistent behaviour. During optical quiescence the X-rays were harder and brighter than in outburst and also substantially variable, and although the quiescent X-rays had a large flux range to outburst flux across all data sets was remarkably constant. A rapid increase in the count rate immediately before the hard X-ray suppression was observed with an upper limit of 12 hours on its duration. The X-ray outburst was also delayed by $0.5 - 1.6$ days after the beginning of the rise in the optical band. At the end of outburst the hard X-ray recovery was also observed. The recovery had a range of start times and durations presumably indicating that the cooling front originates from different parts of the disc.

The quiescent spectrum was harder than in outburst and despite the level of variability during quiescence the spectral parameters were consistent. This indicates that there are long term variations in the accretion rate. The spectra was well fit by a multi-temperature thermal plasma model and was consistent with the presence of a weak reflection continuum. This indicates that the inner disc is likely truncated in quiescence.

The observations presented here have high quiescent accretion rates. The accretion rates before hard X-ray suppression, when the boundary layer becomes optically thick, also varies quite drastically from $0.9 - 3.6 \times 10^{16}$ g s^{-1}. This indicates that the critical accretion rate for the boundary layer to become optically thick is not fixed for SS Cygni.

Chapter 6

The Evolution of U Gem Throughout Outburst

6.1 Introduction

U Gem was discovered as a weak source of hard X-rays in the 0.2 – 10 keV band during outburst using the *A-2* experiment on the *HEAO 1* satellite (Swank et al., 1978). Later, using data from the *Einstein* satellite the X-ray flux was observed to be variable on timescales of 20 seconds during quiescence (Mason & Cordova, 1982). U Gem has strong soft X-ray emission (Cordova & Mason, 1984), later found to be modulated with the orbital period during an unusually long outburst observed with *EXOSAT* (Mason et al., 1988). An optically thin thermal bremsstrahlung model was able to describe *Einstein* data well (Eracleous et al., 1991).

Analysis of quiescent data from *ASCA* taken over a three week period found no noticeable differences in the count rates or spectrum (Szkody et al., 1996). However, an orbital phase dependent variation was observed. Broad deep dips in the X-ray light curve were first discovered by Mason et al. (1988) in decline from outburst using *EXOSAT* and were also seen by Long et al. (1996) in the extreme UV (using the *EUVE* satellite) in quiescence. Dips were found to be centred at phases 0.7 and 0.15 and indicated that the X-ray emission during quiescence must be confined to a small region with absorbing material located at a stable position far out from the orbital plane. The characteristics of the dips were consistent with stream overflow models used to explain dips in low mass X-ray binaries, where the mass transfer stream overflows the disc resulting in complex disc stream interactions where a mixture of cold and hot clouds form near the inner disc (Frank et al., 1987). Baskill et al. (2005) observed U Gem, amongst other dwarf novae, in quiescence also finding orbital dips broadly consistent with photoelectric absorption. Statistically acceptable fits were achieved with a thermal plasma model absorbed by photoelectric absorption by neutral material.

High resolution data were taken from the *Chandra METG* and *HETG* both during quiescence and outburst making it possible, for the first time, to resolve X-ray emission lines. The emission lines imply that the X-ray emission arose from gas with a range of temperatures moving at low velocity (Szkody et al., 2002). Based on the line ratios of forbidden and intercombination lines in Mg `XI` and Si `XIII` triplets the gas is also high-density. The data were fit with a cooling flow model producing reasonable agreement with the quiescent data indicating the source of X-rays is a cooling plasma settling onto the white dwarf. *XMM-Newton* data were also found to be in good agreement with a cooling flow model (Pandel et al., 2005). A study of the emission lines, observed during quiescence and outburst by the *Chandra HETG*, found the fluorescent iron line to be relatively weak compared to the other CVs studied. The Fe `XXV` line was significantly broadened during outburst compared to quiescence indicating the presence of high velocity material near the white dwarf during the outburst (Rana et al., 2006). A high energy component was also seen in the X-ray outburst spectra, in data from *RXTE* and also in the same *Chandra HETG* data. It was attributed to reflection from an optically thick boundary layer (Güver et al., 2006). Mauche et al. (2005), also using the same *Chandra HETG* data, compared U Gem and SS Cygni light curves finding that while hard X-rays in SS Cygni became dimmer during outburst, hard X-rays in U Gem got brighter contrary to observations of most other dwarf novae in outburst. This was originally observed by Swank et al. (1978).

In this chapter two well sampled observations in the hard X-ray band are presented covering outbursts of U Gem. The flux in U Gem is seen to increase in outburst contrary to nearly all other cataclysmic variables, this will be studied to determine if this system is unusual. The two outbursts, separated by seven years, will also be analysed photometrically and spectroscopically

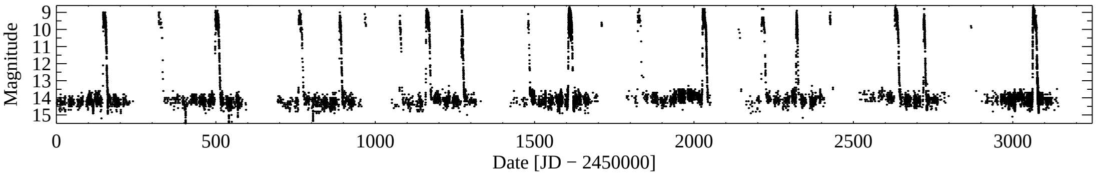

Figure 6.1: An 8 year section of the *AAVSO* light curve of U Gem. Observations presented here cover the first and last outbursts respectively.

to attempt to understand the X-ray evolution throughout outburst.

6.2 Observations

Observation of U Gem using the *RXTE* Proportional Counter Array (*PCA*) began on 1997 November 7 and ended on 1997 December 1. The observations were triggered by the optical rise and began shortly after the start of the outburst was observed by the American Association of Variable Star Observers (*AAVSO*). The observations covered an entire outburst and the following 9 days of quiescence. The second observation started on 2004 February 27 until 2004 March 14 also spanning an entire outburst. A log of observations is given in Table 6.1.

The total exposure was 208 ks (1997) and 155 ks (2004) respectively. Observations were taken in blocks of between 1 – 10 ks for the first observation and blocks of 3 – 12 ks for the second observation. There were also gaps due to Earth occultations and passage of the spacecraft through the South Atlantic Anomaly. Data were taken from the *PCA* experiment on *RXTE*, see Chapter 3. All *RXTE* count rates are presented for three *PCU*s.

For details of the extraction criteria and software used in this chapter see Section 4.2 in Chapter 4. The 1997 outburst was also simultaneously observed with the Extreme Ultra-Violet Explorer (*EUVE*) (Bowyer, 1994), observations began on 1997 November 7 continuously for 7 days until November 14.

Table 6.1: Pointed *RXTE*/*PCA* observations of U Gem used in this analysis.

Proposal ID	Year	Start - End date	Number of observations	Total exposure [ks]	Gain epoch
P20035	1997	Nov 7 - Dec 1	23	208	3
P80011	2004	Feb 27 - Mar 14	17	155	5

6.3 Time Series Analysis

6.3.1 Outburst Light Curves

The simultaneous *AAVSO, EUVE* and *RXTE* light curves of the 1997 and 2004 U Gem outbursts are shown in Figure 6.2. The left set of panels shows the 1997 outburst with the 2004 outburst on the right. The top panels are plots of the respective *AAVSO* optical light curves, directly below is the extreme UV band from the *EUVE* of the 1997 outburst. The *EUVE* mission ended in 2001, there has unfortunately not been a mission to replace it since. Finally the bottom plots shows the *RXTE* count rate averaged over 3 *PCU*s. Both outbursts have been plotted with the same time duration. In both the 1997 and 2004 outburst, as is typical with fast-rise slow-decline outbursts of dwarf novae, the optical light curve rose rapidly until reaching its maximum. In 1997 the optical flux reached maximum on JD 2450760 at approximately $m_{vis} = 9.2$ mag, where it gently declined for eleven days to approximately $m_{vis} = 10$ mag. It then declined much more rapidly before reaching quiescence four days later on JD 2450765. The 2004 outburst had a similar outburst shape. The outburst reached maximum on JD 2453063, when it slowly declined for twelve days before declining more rapidly, reaching quiescence a further 4 days later on JD 2453079.

The beginning of both the 1997 and 2004 X-ray observations were triggered by observations of the rise in the optical band by the *AAVSO*. Since the X-ray observations were triggered by the optical rise there must be a delay since the rise in the EUV band is clearly observed. However, it is hard to determine the magnitude of the delay because the X-ray count rate was already high. Although the second X-ray observation for both data sets has a higher count rate than the preceding and following observations it is unclear if these were part of a rapid flux increase that was seen in SS Cygni (See Chapters 4 and 5). The flux reached maximum on JD

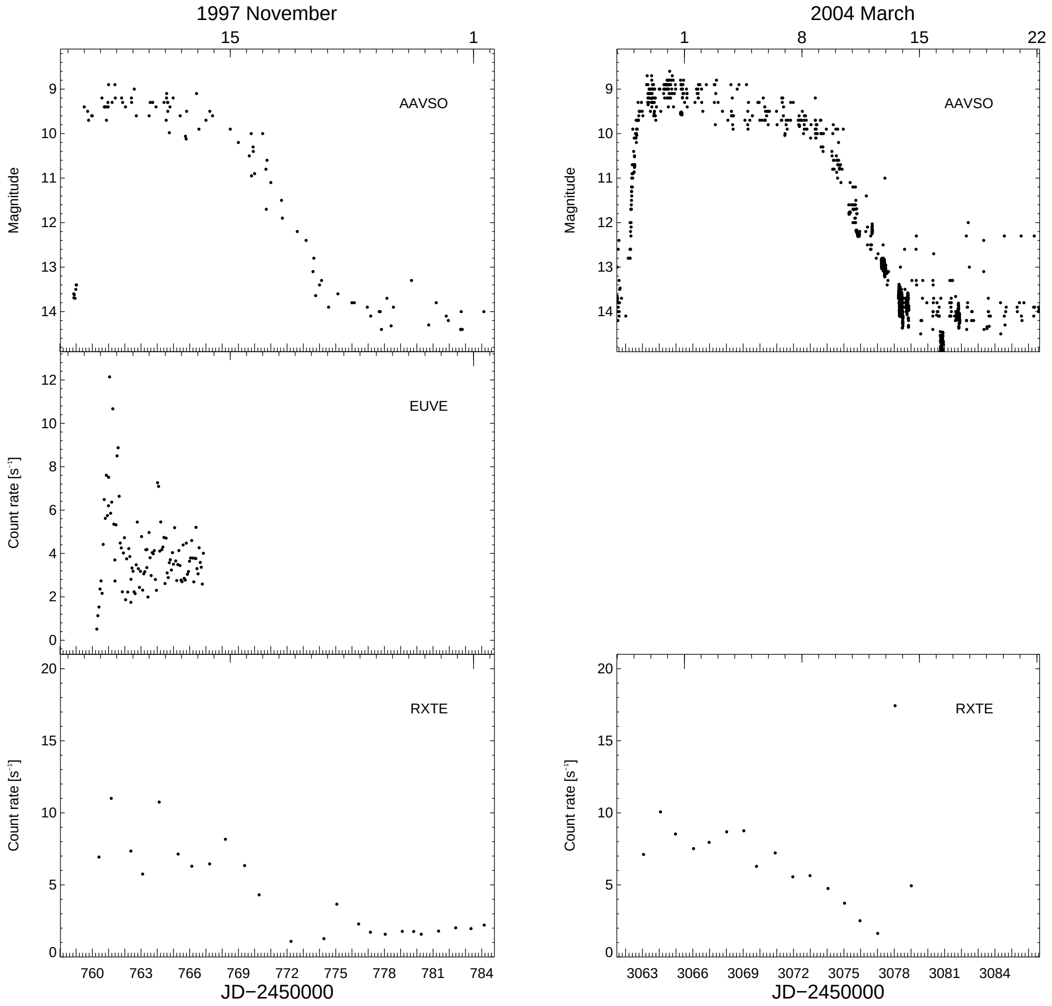

Figure 6.2: Simultaneous *AAVSO*, *EUVE* and *RXTE* observations for the 1997 and 2004 outbursts of U Gem. The left set of panels shows the 1997 outburst, while the right panels shows the 2004 outburst.

2450760 and JD 2453063 in 1997 and 2004 respectively. In the EUV it is possible to see a delay of approximately 1.0 – 1.4 days, measured from when the optical was brighter than 13^{th} mag to when the EUV count rate begins to increase. Wheatley et al. (2003) resolved the beginning of an SS Cygni outburst in X-rays. They observed a delay of 0.9 – 1.4 day in the X-ray band after the beginning of the rise in the optical, the EUV did not begin to rise for another 0.6 days.

A consistently high count rate was observed during both the 1997 and 2004 outbursts and unlike SS Cygni and SU UMa the hard X-rays were not immediately quenched. In 1997, while the count rate was high, there was variability between neighbouring observations before the count rate later stabilised at 7 counts s^{-1} on JD 2450765. At its highest count rate the 2004 outburst was slightly brighter than that of 1997. The count rate remained high for approximately 6 days before rapidly declining on JD 2450700 reaching quiescence three days later. The 2004 outburst had a more stable count rate throughout the outburst at 8 counts s^{-1} with a smaller amount of variation. The count rate started to decline at a slightly slower rate than in 1997 on JD 2453072 reaching quiescence six days later.

Although the observed outburst characteristics of U Gem were very different to SS Cygni, its behaviour near the end of outburst was similar to that exhibited by SS Cygni (Chapter 4). In both observations, as the outburst progressed, the count rate decreased. Before reaching quiescence the X-ray count rate dropped below the quiescent level to near zero before recovering and returning to quiescence. This behaviour was also similar to the second X-ray outburst (JD 2450560) in Figure 5.1 in Chapter 5, which was not quenched until 10 days into the outburst. A day after the 2004 flux reached minimum, on JD 2453078, there was a very large, but short lived, peak in the X-rays with a flux increase almost twice that of the maximum outburst flux. Similarly, three days after the 1997 flux reached minimum there was also a small peak on JD 2450775. It is possible that this flux increase did occur in the 1997 outburst but was missed and only the beginning or end of a large count rate increase was observed. Using the cadence of the observations before and after it is possible to place an upper limit on the duration of the count rate increase of approximately 2 days, similar to the duration of the hard X-ray recovery seen in SS Cygni in Chapter 4. Due to the cadence of the observation of approximately 1 day, it is also highly likely that a similar increase was missed at the start of the outburst. The rapid count rate

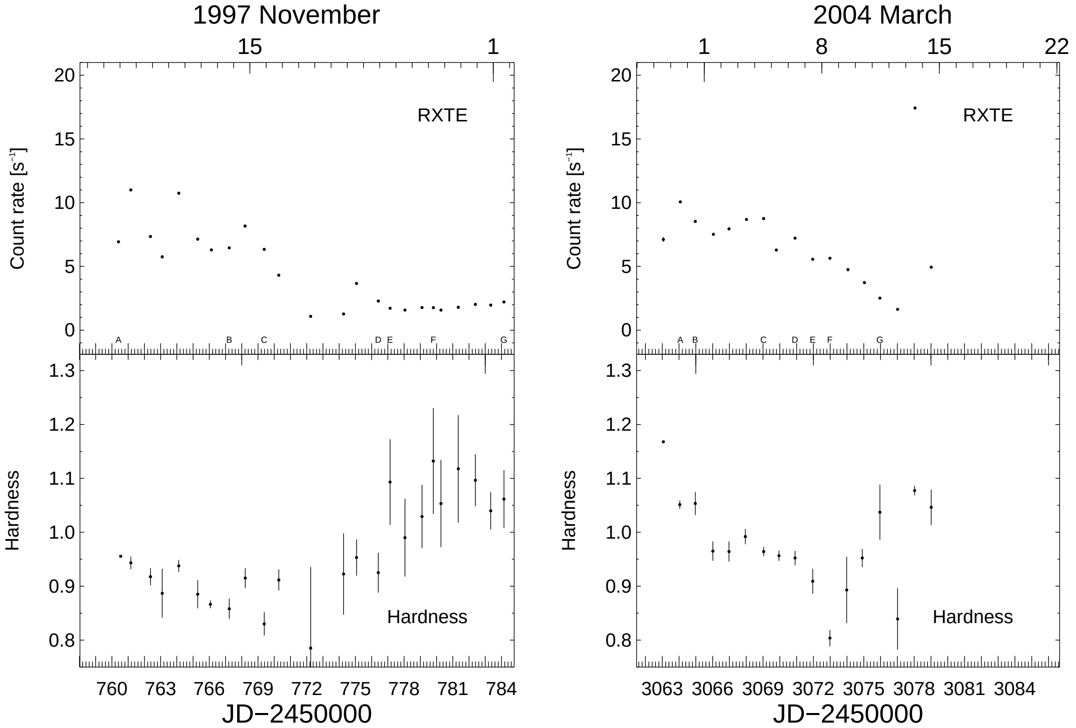

Figure 6.3: The *RXTE* light curves (top) are presented with their respective hardness ratios (bottom). The 1997 outburst is seen in the left set of panels and the right panels shows the 2004 outburst. The letters correspond to the individual light curves plotted in Figure 6.4.

increase seen in SS Cygni in Chapter 4 lasted only approximately half a day.

6.3.2 Hardness Ratios

In order to examine the spectral variation in the hard X-ray band the *RXTE* light curves were divided into soft, S, and hard, H, bands to make the hardness ratio, H/S. The bands were split so there were approximately an equal number of counts in each band, that is 2.3 – 5.8 keV in the soft and 5.8 – 20.3 keV in the hard band for the 1997 data and 2.5 – 5.7 keV in the soft and 5.7 – 20.2 keV in the hard band for the 2004 data[1]. Plots of the 1997 and 2004 outburst light curves and hardness ratios can be seen in Figure 6.3.

---

[1] It should be noted that the channel ranges were slightly different between the two observations due to a shift in the gain epoch in the detector in the time between the two observations.

The quiescent U Gem spectrum had a hardness ratio of approximately 1.1 (observed at the end of the 1997 observation). At the start of the 1997 outburst the spectrum had a hardness ratio of approximately 0.95, already softer than in quiescence indicating that the transition into outburst had already occurred by the time the observation had begun. The spectrum in SS Cygni rapidly softened during the transition into outburst (see Chapter 4). In the second X-ray outburst in Figure 5.1 in Chapter 5 the spectrum also softened while the X-ray count rate was still high. As the 1997 outburst progressed the spectrum softened further. It should be noted that although the count rate was very variable between neighbouring sections of the light curve there was not a corresponding change in the spectrum. Prior to the optical flux reaching minimum, at the end of outburst, the hardness ratio varied between approximately 0.85 – 0.92 before hardening as the small peak appeared in the X-ray count rate. The spectrum continued to harden after the system reached quiescence, reaching approximately 1.1 five days after the X-ray flux was quenched, remaining at this value until the end of the observation.

The 2004 outburst followed a similar evolution but was both brighter and harder than in 1997. The hardness, initially just below 1.2, quickly dropped to near 1.0 on JD 2453066, where it further continued to soften, at a similar rate seen in 1997, to 0.9. This indicates that the end of the transition was observed in the 2004 outburst. As the X-ray count rate began to decline on JD 2453074 the spectrum began to harden. Just prior to the large spike in the count rate the spectrum softened from 1.04 to 0.84, before returning to near 1.05 at the end of outburst.

Both observations exhibited a softening of their respective spectrum during outburst with the hardness ratio dropping to between 0.8 and 0.9, however, the 2004 spectrum was harder. As the X-ray count rates declined both spectra hardened reaching what is most likely a quiescent hardness of 1.05 – 1.1. This is similar to what was observed during outburst in SS Cygni, (see Chapter 4), the hardness ratio dropped as the X-rays were quenched to near 0.9 and during the X-ray recovery the spectrum hardened to approximately 1.2.

6.3.3 Orbital Dips

U Gem is a high inclination system, observed to be at an angle of $i \sim 72$ degrees (Unda-Sanzana et al., 2006). Mason et al. (1988) discovered broad deep dips in the X-ray light curve during the decline from outburst, which they suggested were due to the high inclination. They found the dips centred at phases 0.7 and 0.15. Later Long et al. (1996) and Szkody et al. (1996) also observed dips in the EUV band (using *EUVE*), during outburst and the decline from outburst, and in the X-ray band (using *ASCA*), during quiescence. They also found the dips to be located at a phase of 0.7.

Szkody et al. (1996) observed orbital dips in the energy range 0.5 – 6 keV during quiescence using the *SIS* detector on board *ASCA*. They were not able to detect the dips in the harder 2 – 10 keV band using the *GIS* detector. In order not to remove the orbital dips that may be present in the *RXTE* light curves data were extracted in the energy range 2.5 – 7.5 keV. Absorption dips were previously detected in the UV and soft X-ray bands using detectors able to detect much softer photons than *RXTE* (below 2.5 keV) thus the data presented here may not show dips if the absorption occurs below 2.5 keV. The light curves were phase folded using the ephemeris of Echevarría et al. (2007) and plotted over two periods. Individual light curve sections providing the greatest coverage of phases 0.15 and 0.7 are presented in Figure 6.4, where letters correspond to the labels in Figure 6.3.

With the exception of panels 1997A and 2004D there is no evidence of dips in the *RXTE* observations of U Gem, this is most likely because the X-rays observed by *RXTE* are too hard to be absorbed. Both light curves 1997A and 2004D show the presence of a dip between phases 0.7 and 0.9 with a shallower dip at phase 0.1 - 0.3 for 1997A and at phase 0.3 - 0.5 for 2004D. Figure 6.5 shows the hardness ratio, H/S, plots of panels 1997A and 2004D, the bands were split at 2.5 – 5.0 and 5.0 – 7.5 keV, with approximately an equal number of counts in each band. The dip in plot 1997A is not accompanied by any hardness variation yet the dip in plot 2004D does correspond with a strong hardening of the spectrum at phase 0.7 – 0.9, the spectrum also hardens slightly at phase 0.3 – 0.4. The dips in plot 1997A were most likely caused a lack of phase coverage not removing an anomalous features in the light curve. However, the hardening of the spectrum suggests that the dips in plot 2004D are caused by absorbing material as found by Szkody et al. (1996).

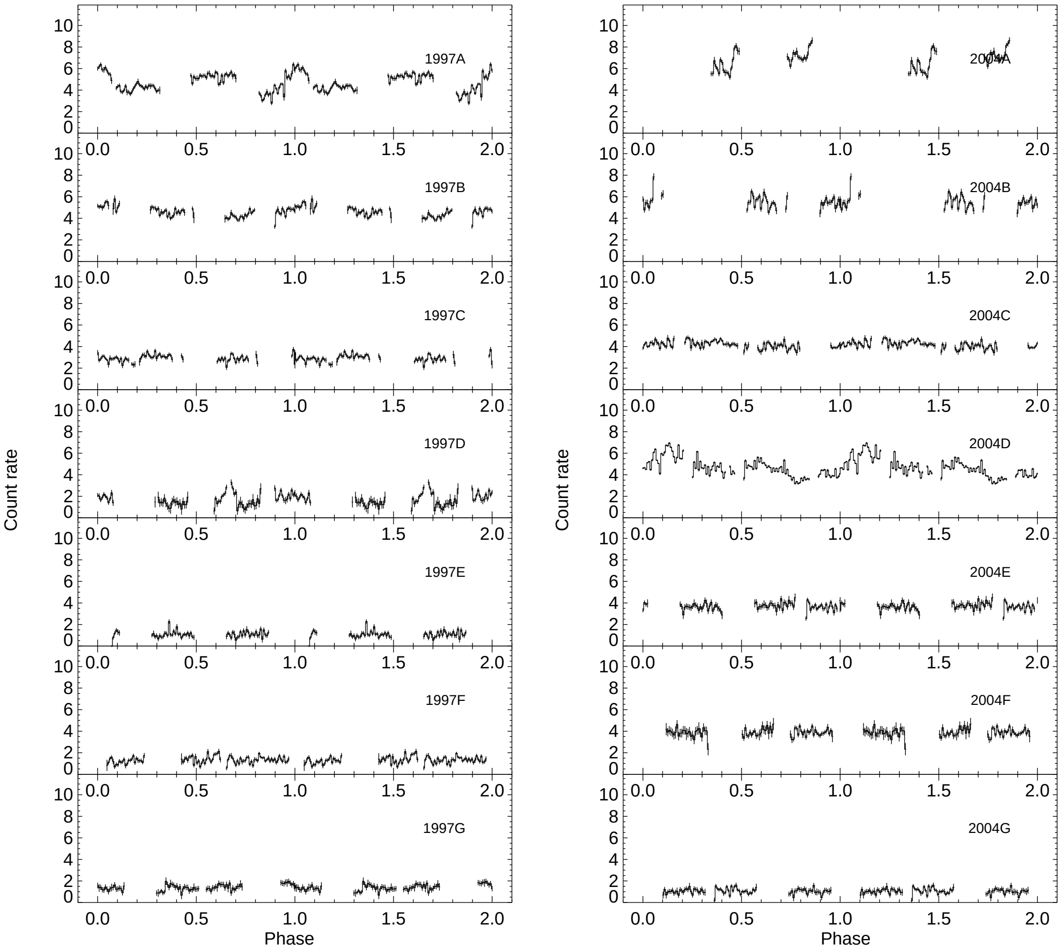

Figure 6.4: Phase folded plots of individual sections from the entire *RXTE* light curve of U Gem. The light-curves were extracted in the energy range of 2.5 − 7.5 keV and in 64 second bins. Panels on the left show sections from the 1997 outburst and panels on the right show sections from the 2004 outburst. Labels 1997A-G and labels 2004A-G correspond to the labels A-G on the 1997 and 2004 plots on Figure 6.3.

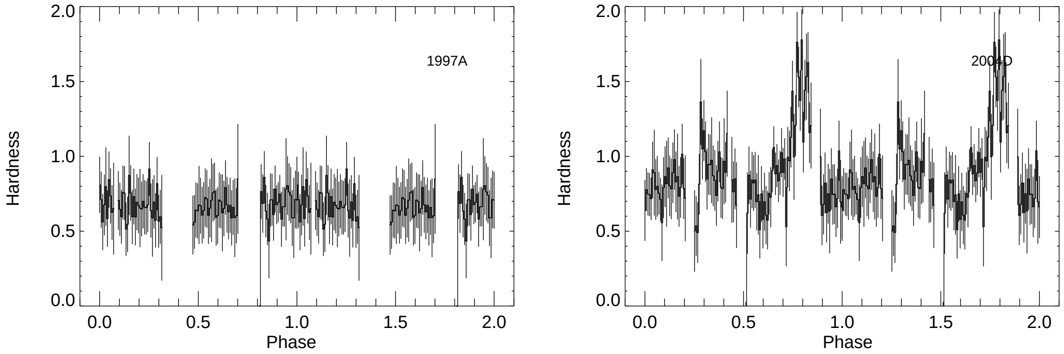

Figure 6.5: Phase folded hardness ratios of the light curves, 1997A and 2004D, from Figure 6.4 showing orbital dips. The light curves were split at 5 keV and in 64 second bins.

6.3.4 Variability

Figure 6.6 shows the *RXTE* light curve (bottom panels) binned at 64 seconds. The upper plot shows the fractional RMS variability of the data (data points) plotted with the variability expected from counting statistics alone (solid line).

During the quiescent period, in the 1997 observation, the mean count rate was stable. However, at the start of the observation the mean count rate varied dramatically between neighbouring sections in both the 1997 and 2004 light curve.

Comparing the calculated fractional RMS variation (data points) to the expected variability (solid line), during optical outburst, shows that the variability in both observations is dominated by counting statistics. However, there were a number of sections that show real variability. The variability during the quiescent period at the end of the 1997 observation was calculated to be less than that expected from noise alone, this is most likely caused by the error on the background being overestimated[2]. During this section of the observation the count rate was low and errors in the background will have a stronger effect.

Significant variability was seen in both observations at the very start of outburst, most likely the end of the transition into outburst and during the transition back to quiescence. Comparing the variability of two segments of the light curve near to the end of the outburst, both having similar average count rates (e.g., JD 2450770 and JD 2450775), shows that there is more

---

[2] http://astrophysics.gsfc.nasa.gov/xrays/programs/rxte/pca/chisquare.html

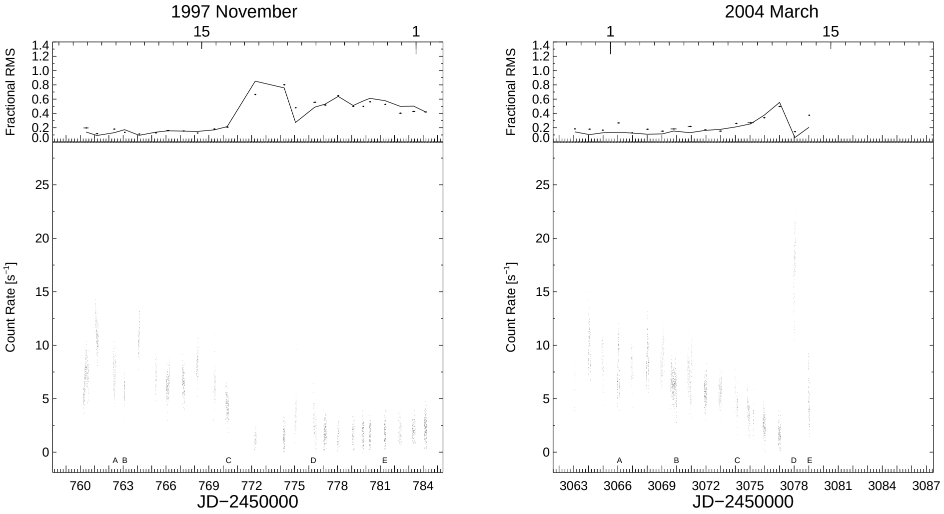

Figure 6.6: The *RXTE* light curve and fractional RMS variability of U Gem. The upper panels show the fractional RMS variability measured within each observing interval (data points) plotted with the expected fractional RMS variability from counting statistics (solid line), below is the 64 second binned light curve.

variability in the latter segment. This variability coincides with the boundary layer as it transitions from an optically thin to an optically thick state as the system moves out of outburst. Significant variability was also seen throughout the 2004 outburst. Both VW Hyi (Wheatley et al., 1996) and SS Cygni (Wheatley et al., 2003, Chapter 5) were also found to be variable with periods of highest variability occurring during the transition of the boundary layer at the start and end of the X-ray suppression.

Sections of the *RXTE* light curve are plotted with 64 second bins in Figure 6.7 showing the variability during specific intervals. A number of the 64 second binned light curve sections show only small amounts of variability while other sections were highly variable.

Light curves presenting variations are plotted in more detail along with their hardness ratio in Figure 6.8 showing short term variability. Panel 1997C got brighter and softer on JD 2450769.38. The remainder of the light curve was not variable and the hardness ratio did not show any variation. The sudden increase in flux seen in the light curve coincided with a drop in hardness, the extra counts were soft and lasted approximately 240 seconds. Assuming a thermal

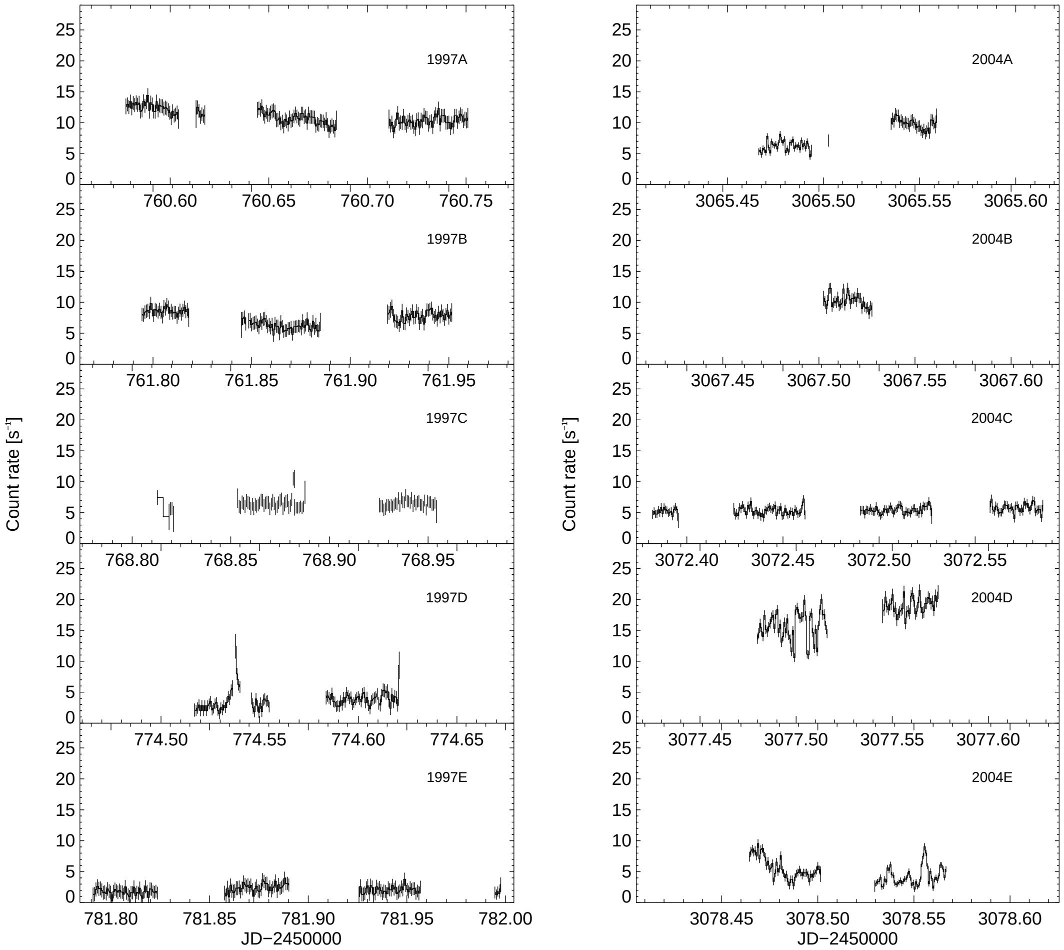

Figure 6.7: Individual sections from the entire *RXTE* light curve of U Gem in 64 second binning. Panels on the left show sections from the 1997 outburst and panels on the right show sections from the 2004 outburst. Letters A-E correspond to the labels on Figure 6.6.

Table 6.2: The χ^2_ν statistics calculated using the average count rate for each panel of Figure 6.8.

	Light curve		Hardness ratio	
Plot panel	χ^2 (dof)	Probability	χ^2 (dof)	Probability
1997C	85 (47)	P=1	44 (47)	P=0.39
1997D	259 (48)	P=1	71 (48)	P=0.98
2004D	927 (46)	P=1	41 (46)	P=0.32
2004E	587 (51)	P=1	36 (51)	P=0.06

bremsstrahlung continuum with a temperature of 7.5 keV (see Section 6.4) and a distance of 96.4 ± 4.6 pc (Harrison et al., 1999) the corresponding luminosity was calculated to be 1.2×10^{32} ergs s^{-1} cm^{-2}. It is likely that this was a flare from the secondary star. By comparison panel 1997D got brighter, over a period of approximately 15 minutes. The count rate was low increasing the uncertainty in the hardness ratio, however, this feature did appear to be harder indicating that the origin was most likely in the boundary layer. It is hard to determine if the variability in the remainder of the light curve is accompanied with any hardness variation.

Panel 2004D showed strong variability and the high count rate afforded a suitably small error on the hardness ratio to be able to determine that the variability did not coincide with a hardness change. As with 1997D, it is hard to determine if the variability in 2004E was accompanied with any hardness variation. The features seen in the light curve did not correlate with the hardness with the exception of the drop in count rate at the beginning of the light curve being accompanied by a small drop in hardness. Variability of VW Hyi has been observed on a time-scale of ~ 200 seconds with an amplitude that decreased from ~ 100 per cent at the beginning to ~ 50 per cent at the end of the recovery from outburst (Wheatley et al., 1996). SS Cygni was also found to be variable during the transition with amplitude peaks at 45 per cent during X-ray suppression (Wheatley et al., 2003, Chapter 5).

Table 6.2 shows the χ^2 statistic for all four light curves and associated hardness ratios calculated using the average of the light curve as the model count rate for each panel. The χ^2 shows that the variability in the light curves was real. There is a significant probability that there was variability in the 1997 hardness ratios, the variation is most likely due to a hardness variation caused by the features present in the light curves. The variability in the hardness ratios seen in the 2004 outburst light curves were not statistically significant.

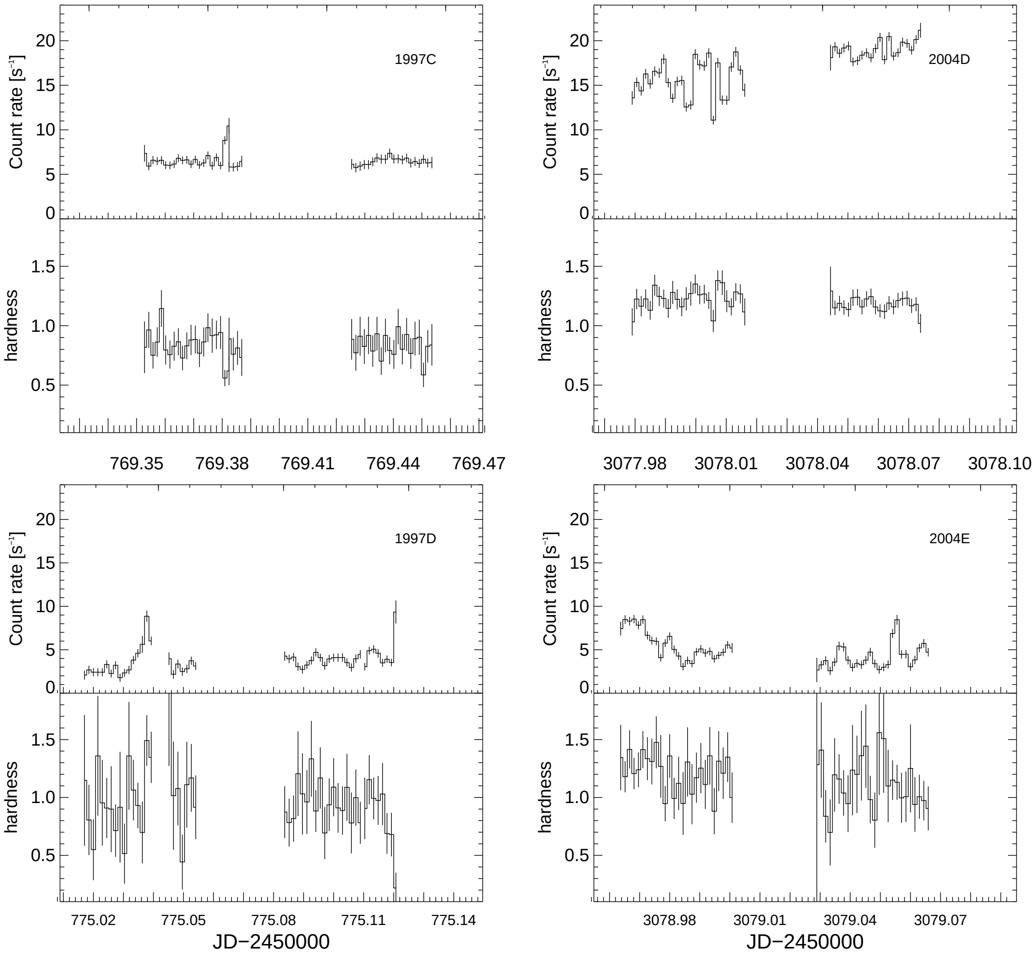

Figure 6.8: The *RXTE* 3 − 20 keV light curve and hardness ratio of the two variable sections of the 1997 and 2004 outburst. Labels correspond to those in Figure 6.7 and 6.6 plotted in 128 second binning with their corresponding hardness ratio plotted directly below.

6.4 Spectral Fitting

The two outbursts presented here were observed once a day, excluding Earth occultations, for 24 days in November 1997 and 16 days in March 2004. The data were re-binned such that all data taken from a single day of observation were binned into one spectra for fitting. Analysis of SS Cygni in Chapter 4, Section 4.4.1 found that a systematic error of 0.5 per cent was required on the data. Analysis of the fainter SU UMa data in Section 7.4 in Chapter 7, where the background dominates the data, found that SU UMa required a systematic error on the background of 0.5 per cent. A systematic error of 0.5 was applied to the data and to the background.

The spectrum throughout the observation was well parameterised by a thermal bremsstrahlung model with a free line emission component. The best fit parameters for this fit can be seen in Figure 6.9. The line width and line energy were fit as free parameters to better understand the distribution of the line emission in the spectrum. The model resulted in a total χ^2_ν of 1.20 (960 d.o.f) for the 1997 observation and 1.23 (579 d.o.f) for the 2004 observation. Figure 6.10 shows the cumulative histogram plots of χ^2_ν resulting from fits of all spectra to the current model. The histograms show that both fits are reasonable, but not formally acceptable.

During the 1997 observation both the best fit temperature and line strength were well constrained and constant, or slightly decreasing, despite large variations in the flux. When the outburst started to decline the best fit parameters became less well constrained. As the system transitioned back into quiescence the temperature dropped slightly, but only briefly before rising and stabilising in quiescence at approximately 14 keV. When the temperature dropped the line strength greatly increased before returning back to a similar value as prior to this. In the 2004 observation the spectra, again, fit with a lower temperature during outburst than during quiescence. It was more apparent in this observation that the temperature dropped during outburst. What is surprising is that the temperature was higher than the 1997 fits but also with a stronger line. As the temperature declined the line strength also declined, this is contradictory to what is expected. As the continuum temperature drops the thermal lines are expected to get stronger to compensate. As the observation moved into quiescence and the temperature rose the line strength continued to drop as expected.

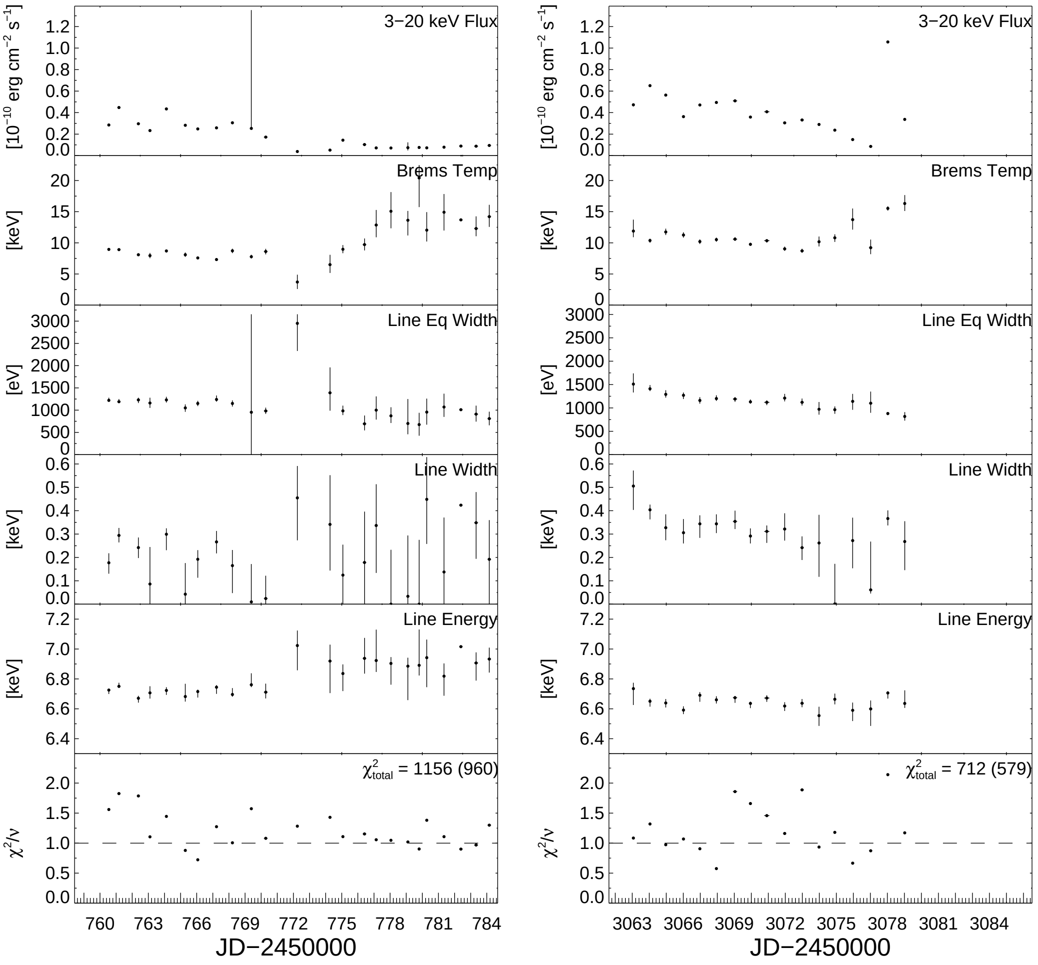

Figure 6.9: The results of fitting a thermal plasma model to the 1997 and 2004 X-ray spectra. This model consists of a bremsstrahlung plasma model and a free emission line. All errors are in the 68 per cent confidence interval for one parameter of interest ($\Delta\chi^2$ = 1.0).

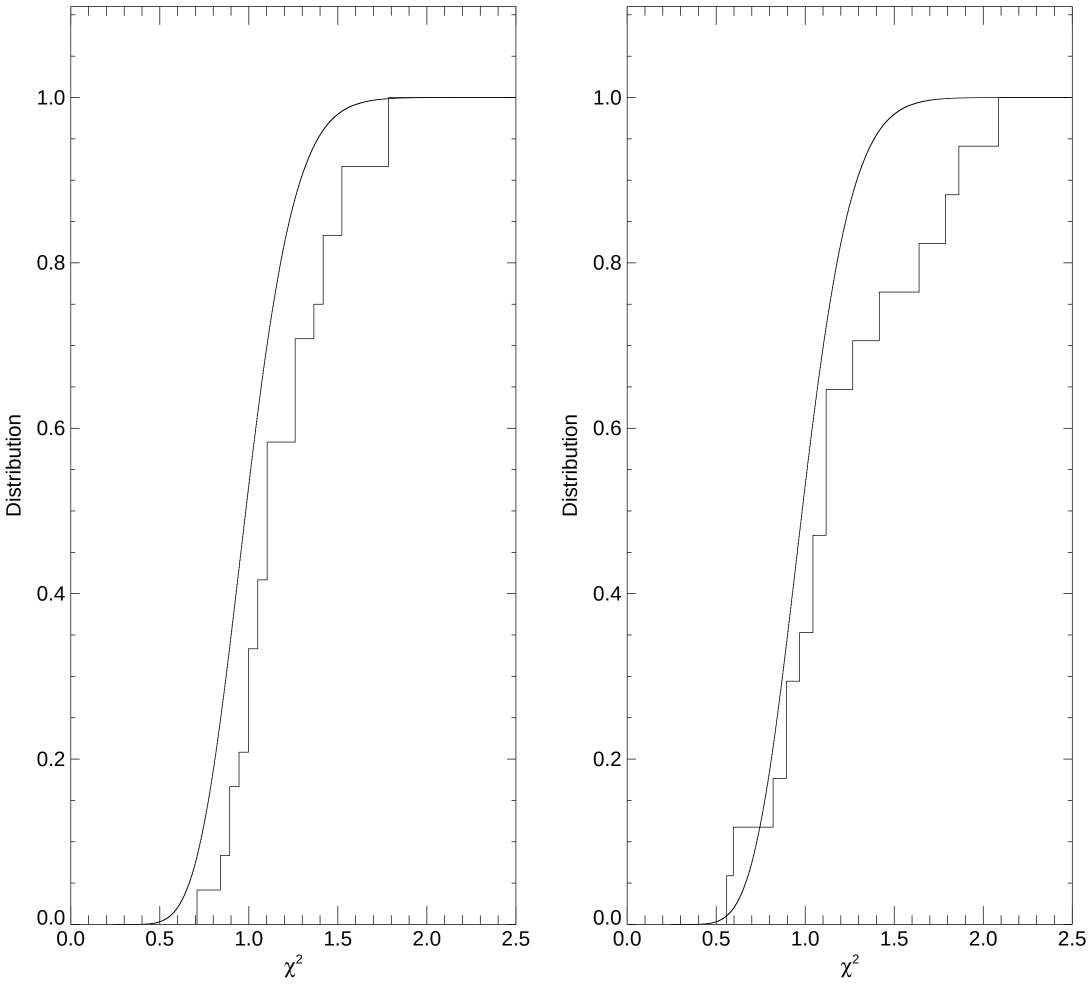

Figure 6.10: Cumulative histogram plots of χ_ν^2 resulting from fits of all spectra to the bremsstrahlung plasma model and a free emission line. The cumulative χ^2 distribution (curve) is also plotted.

The spectra near the spike are interesting in that the spectrum before the spike was much cooler than that during the spike, although it is close to the confusion limit of the *RXTE* detector (Jahoda et al., 2006). However, the increased flux did not affect the temperature, the spectrum following had a much lower flux yet was hotter. A similar rise in flux was seen at the start and end of outburst in observations of SS Cygni in Chapters 4 and 5, with the timescales of these events being similar in both systems. In SS Cygni, at the end of outburst, the temperature rose as the X-ray flux recovered before dropping back to the quiescent level.

Both observations, during outburst, required an emission line at approximately 6.7 keV. In 1997 as the observation progressed and the temperature increased the line profile changed from being dominated by a $\sim$ 6.7 keV component to being dominated by a $\sim$ 6.9 keV component. This was caused by the line profile switching from being dominated by He like to H like iron lines. The 2004 outburst did not have a similar shift in the line energy most likely because there was not enough quiescent observations to observe this. The data were only able to constrain the line width during the outburst. During the transition and in quiescence in the 1997 observation the line width was not well constrained. At the start of the 2004 outburst the best fit required a relatively broad line of 0.5 keV. As the boundary layer transitioned into outburst the line width decreased to near 0.35 keV, before decreasing further when the X-ray flux declined.

To fit a more realistic model to the data a single temperature plasma model was used, mekal in `XSPEC` (Mewe et al., 1985, 1986; Liedahl et al., 1995). The model includes thermal line emissions from abundant elements. The data required an emission line near 6.5 keV, most likely an iron fluorescence line, so a fixed emission component at 6.4 keV was added to the model. The addition to the model improved the fits in both observations: the total χ^2_ν for the 1997 observation decreased from 1.49 (1032 d.o.f) to 1.17 (1008 d.o.f) and the 2004 observation decreased from 3.27 (630 d.o.f) to 1.26 (613 d.o.f).

Fits to the data with the abundances as a free parameter showed that the best fit abundances varied between 0.6 – 1.4 solar (relative to abundances of Anders & Grevesse, 1989). The timescales for these changes to occur were too short to be physical so the abundances were fixed. Previous studies found the abundances of U Gem to be $1.03^{+0.17}_{-0.15}$ and $1.23^{+0.20}_{-0.16}$ solar in quiescence (Baskill et al., 2005) and 1.3 ± 0.22 solar in outburst Güver et al. (2006). To deter-

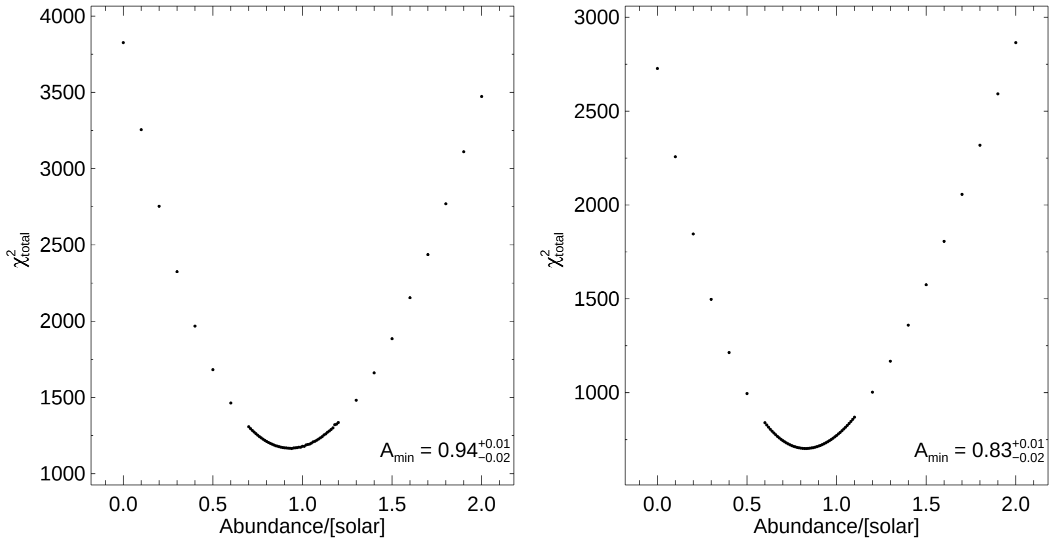

Figure 6.11: Abundances plot with the best fitting total χ^2 of all the data for a thermal plasma model with a fixed emission line at 6.4 keV. A higher number of fits were performed near the minimum to resolve the parameter with higher accuracy. The 1997 outburst is plotted in the left column and the 2004 outburst is plotted in the right column.

mine the value of the model abundance the parameter for each spectrum was fixed at a value between 0 – 2 and a fit was made. A higher number of fits was performed near the minimum to resolve it better. The total χ^2 was calculated and the resulting distribution of abundances and total χ^2 was plotted in Figure 6.11. This method has to assume the correct model is being used for the system. In using a single temperature model lower temperature gas may not be modelled causing the abundances to compensate for this resulting in a biased result. This accounts for the difference in best fit abundances with (Baskill et al., 2005) and Güver et al. (2006). However, using this model produces satisfactory fits to all spectra. A value of 0.9 solar was chosen for the abundances to fit the remaining data.

Fitting the current model with the new abundances did not result in a significant improvement to either observation, however, the model is more realistic with the metal abundances the same for all spectra. The total χ^2_ν was 1.17 (1008 d.o.f) for the 1997 outburst and 1.16 (613 d.o.f) for the 2004 outburst. See Figure 6.12 for the best fit parameters of this fit. As with the previous model the fitted temperature was lower in outburst than during quiescence. The plasma model required a slightly lower temperature to be fit, approximately 7 keV and 11 keV in outburst and 12 keV and 14 keV during quiescence for the 1997 and 2004 observations respectively. Unsurprisingly there was a similar trend in the best fit temperatures compared to the bremsstrahlung model. In the 1997 outburst the temperature was well constrained and constant until the system transitioned to quiescence when the temperature dropped briefly before rising and stabilising in quiescence at the higher temperature. Similarly, in 2004 the spectra fit with a lower temperature in outburst than in quiescence. The temperature also dropped as the outburst progressed until the disc transitioned into quiescence when the temperature increased. The cooler spectrum before the spike was most likely due to the low count rate reaching the confusion limit of the detector. The best fit temperature of the 2004 observation was also noticeably higher than the best fit of the 1997 observation. This temperature difference was also seen in fits using the bremsstrahlung continuum model indicating that the temperature was higher during the 2004 observation.

With the thermal lines being modelled by the thermal plasma model the 6.4 keV line no longer compensates for the previously un-modelled iron lines resulting in a weaker line equivalent width. In both observations the line strength weakened as the outburst progressed, before getting slightly stronger in quiescence, this is opposite to what is expected. However, it is misleading to directly compare the line strengths between the two observations because of the difference in continuum temperature between the two observations. The best fit line strength was more prominent in the 2004 data, however, this is expected due to a higher continuum temperature.

To understand why the model did not fit a number of the 2004 spectra as successfully as the 1997 spectra, two of the poorer fitting spectra from the 2004 observation are plotted in Figure 6.13. The crosses show the data points for the observed spectra while the line represents the folded model. The bottom panel shows the residuals (the data minus the folded model scaled by the error). The spectra shown, although poor fitting, do not have any clear distinguishing features in the residuals to indicate where the model should be improved, with the exception of a shallow dip just above 10 keV in the bottom plot. A physical model would not be able to fit many of the data points seen in the residuals of these two plots while also fitting the remainder

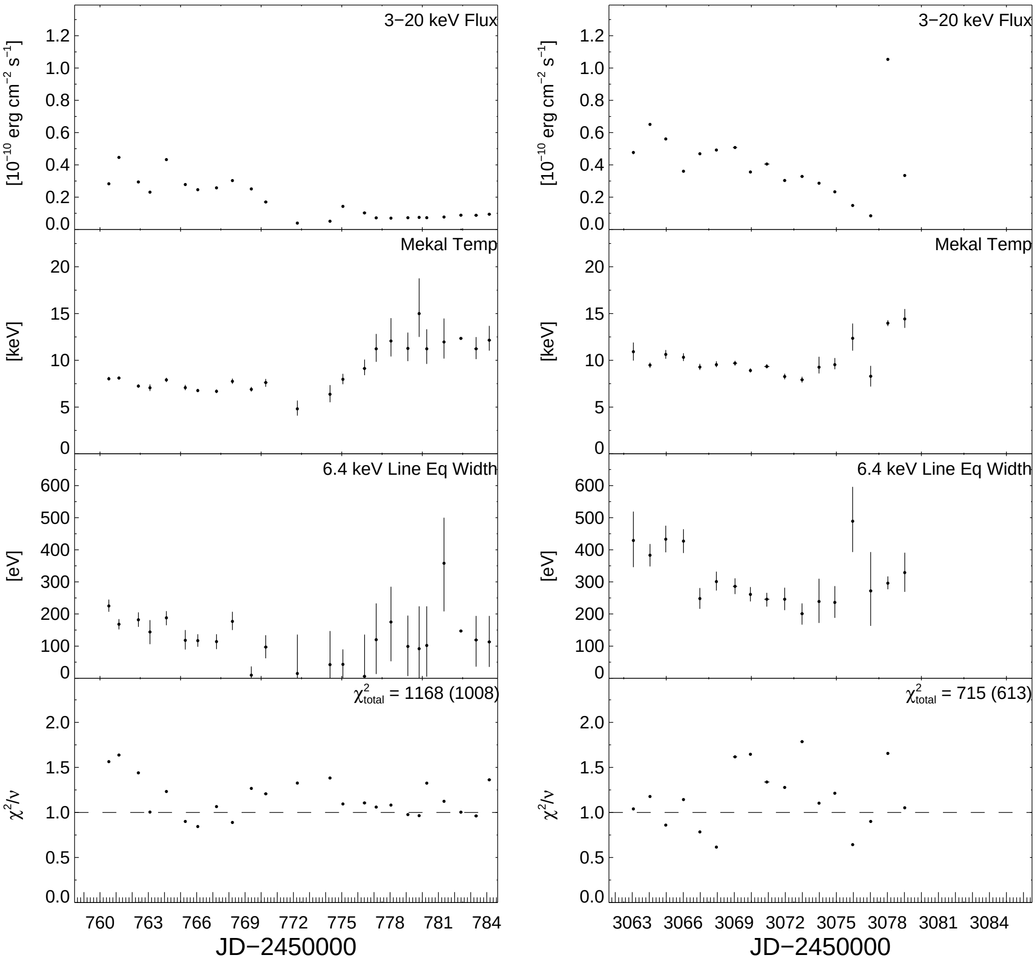

Figure 6.12: The results of fitting a thermal plasma model to the 1997 and 2004 X-ray spectra. This model consists of a single temperature thermal plasma model with the abundances fixed to 0.9 solar and a fixed 6.4 keV emission line. All errors are in the 68 per cent confidence interval for one parameter of interest ($\Delta\chi^2$ = 1.0).

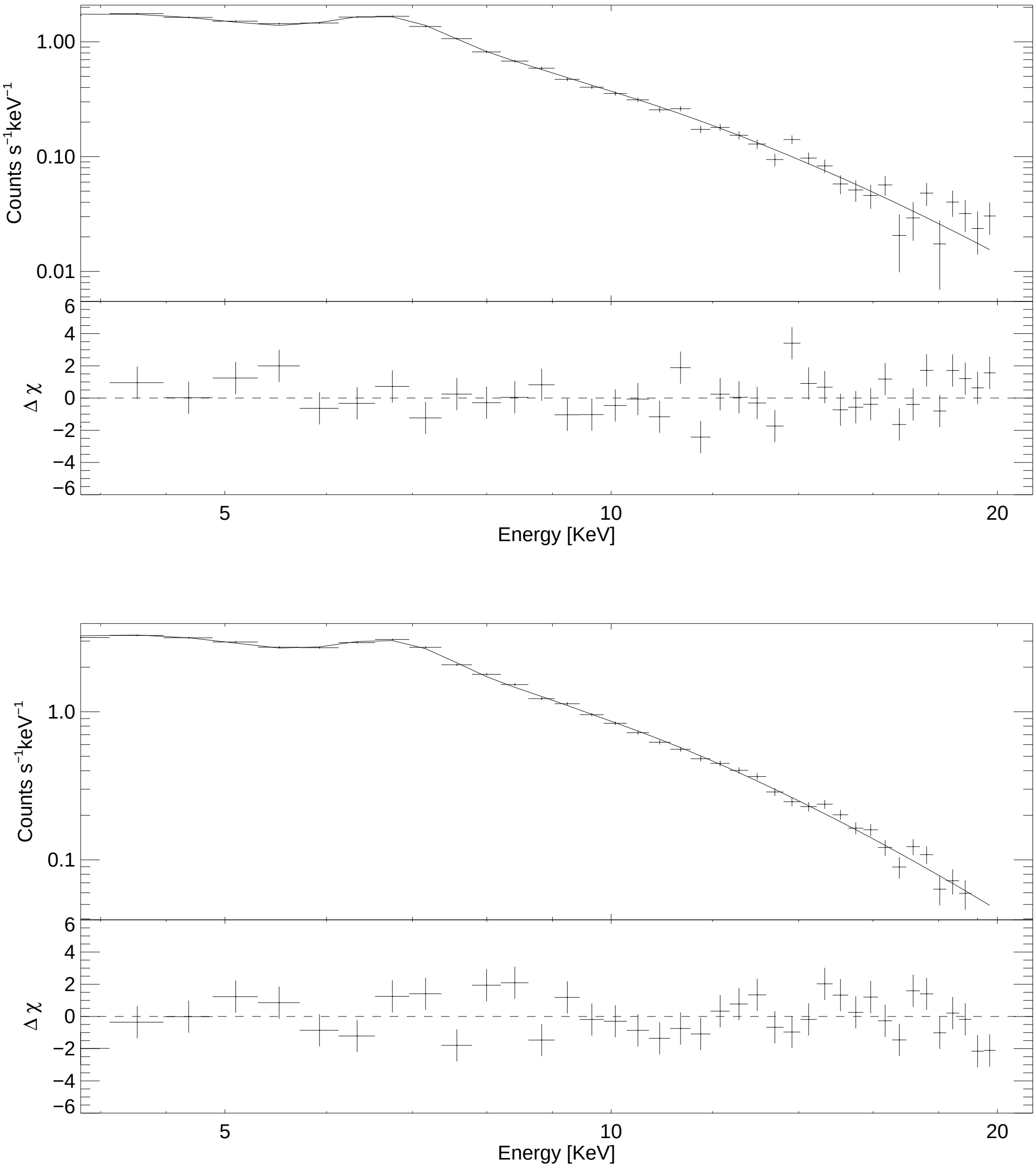

Figure 6.13: The data (crosses) and model (line) plotted in the top panels, the residuals (data minus folded model) is plotted directly below its respective model. The top of the pair of plots is the 7th spectrum from the 2004 observation, with a χ^2_ν of 1.62 (36 d.o.f) and the bottom plot is the 16th spectrum also from the 2004 observation with a χ^2_ν of 1.65 (36 d.o.f). The model used includes a single temperature plasma model with an emission line fixed at 6.4 keV.

of the data. This may be an indication that the current model being used is incorrect since it is not able to describe the data very well.

In an attempt to improve the model a number of additional components were tested. A second thermal plasma model was added to model low temperature gas with the metal abundances fixed at 0.9 for both thermal plasma models. Although a good fit with a total χ^2_ν of 1.16 (960 d.o.f) and 1.06 (579 d.o.f), for the 1997 and 2004 respectively, was produced the data only wanted to fit one component and was not able to constrain the second thermal plasma model.

Studying the residuals in more detail a small number of spectra had an excess in the model near $7-8$ keV. To test if this was caused by an absorbing component an absorption edge was added to the model. The model produced good fits with a total χ^2_ν of 1.17 (960 d.o.f) for 1997 and 1.10 (579 d.o.f) for 2004, the improvement to the fit of the 1997 data was not significant with an F-test probability of 0.80. The improvement to the 2004 data was significant with an F-test probability of 3.9×10^{-4}. Although the overall improvement of the fits was significant, the poorer fitting spectra before this addition were only marginally improved, but still poor.

The need for a 6.4 keV line is highly suggestive of iron Kα fluorescence emission due to illumination of cold gas and the significant improvement to the 2004 fits with the addition of the edge component suggest there is reflection present in the system. The strengths of the fluorescent line in the 1997 outburst were also consistent with a reflection origin. The fluorescent line strengths in the 2004 outburst were very strong, this may be due to blending of the fluorescence line and the He like thermal iron line by the detector which were both being fit by the 6.4 keV line. A reflection component (calculated from the code of Magdziarz & Zdziarski, 1995), with the reflection albedo fixed at 1, was added to the model. The model angle was set to 72 degrees (Unda-Sanzana et al., 2006) and the reflector abundances were set to the abundances of the thermal plasma model. The addition to the model resulted in only a slight improvement to the 1997 best fit resulting in a total χ^2_ν of 1.14 (1008 d.o.f) and did not improve the 2004 best fit, resulting in a total χ^2_ν of 1.28 (613 d.o.f). Allowing the reflection to be a free parameter did not improve the fits for either observation and the data was also not able to constrain the model.

The data were not able to constrain the reflection component making it difficult to analyse its evolution during outburst. However, it is possible to get an understanding of the reflection

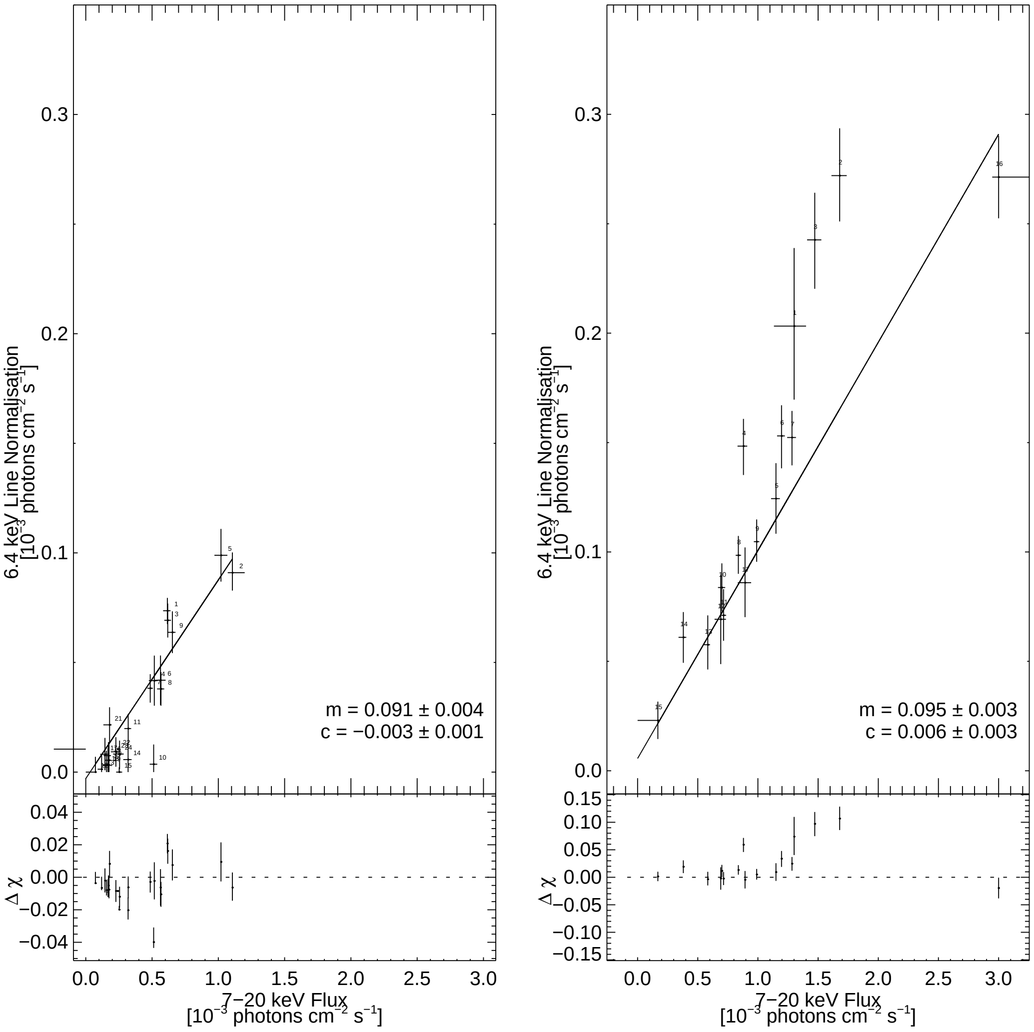

Figure 6.14: The best fit 6.4 keV line normalisation and the flux above 7 keV, also plotted is the best fit line to all data points. The bottom panel shows the residuals between the best fit line and the data. Data from the 1997 observation is plotted on the left, while data from the 2004 observation is plotted on the right. Numbers next to the data points rank spectra relative to the time they were observed.

in the system by comparing the flux above 7 keV with the 6.4 keV line normalisation (see Section 4.4.4 in Chapter 4). The left plot of Figure 6.14 shows that in the 1997 data there is a good correlation with the flux between 7 – 20 keV and the line normalisation. This indicates that there is no change in reflection during this observation. The 2004 observation also shows that a good correlation with the exception of the four spectra above the line. The four spectra above the line were consecutive in time, from the beginning of the outburst indicating that at the beginning of the observation the reflection was higher than during the rest of the observation, maybe due to a large influx of gas into the boundary layer at the beginning of the outburst.

Both observations have consistent gradients of 0.091 ± 0.004 for 1997 and 0.095 ± 0.003 for 2004 and the line of best fit also passed close to zero. The line and continuum flux produced were consistent between observations and are consistent with the geometry of the disc not significantly changing during outburst in the seven years between the two observations. Approximately 9 per cent of photons contribute to the reflection, this is over twice that seen in SU UMa (4 per cent in Chapter 7) although this fraction consists mostly of quiescent observations. The fraction of fluorescent photons produced is, however, similar to the fraction during outburst in SS Cygni in Chapter 4 (10 per cent).

Using a distance of 96.4 ± 4.6 pc to U Gem (Harrison et al., 1999) the fluxes were calculated from the best fitting model by integrating over a broad energy range, 0.01 – 100 keV. Using the relation $L = GM_{wd}\dot{M}/2R_{wd}$ the accretion rates were calculated using a value of $M_{wd} = 1.20M_{\odot}$ for the mass of U Gem and $R_{wd} = 3.9 \times 10^{8}$ cm for the radius (Echevarría et al., 2007). The flux, luminosity and accretion rates were calculated for an outburst and quiescent spectrum from each observation, the spectrum observed during the peak of the 2004 spike was also chosen. The flux, luminosities and accretion rates are presented in Table 6.3. Both U Gem observations have comparable luminosities and accretion rates during quiescence and outburst respectively. The accretion rate calculated during the spike was over an order of magnitude higher than during quiescence.

Table 6.3: Luminosities and accretion rates of selected spectra from the 1997 and 2004 observations of U Gem.

Time	State	Flux[a]		Luminosity[b]	Accretion rate[c]
[JD]		[2 – 20 keV]	[0.01 – 100 keV]		
2450764	OB	4.3	6.9	7.7	3.7
2450777	Q	0.7	1.1	1.2	0.6
2453064	OB	6.5	10.3	11.4	5.5
2453077	Q	0.8	1.4	1.5	0.7
2453078	spike	10.5	16.9	18.6	9.1

[a] $\times 10^{-11}$ ergs s^{-1} cm^{-2}
[b] $\times 10^{31}(d/96pc)^2$ ergs s^{-1}
[c] $\times 10^{14}$ g s^{-1}

6.5 Discussion

Previous analysis of U Gem has been based upon a small number of snapshot observations with a short duration observed during either an outburst or quiescent period. The data presented here span 24 days from the start of the November 1997 outburst and 16 days from the start of the March 2004 outburst and allows the evolution of the outburst to be studied in unprecedented detail.

6.5.1 X-ray Quenching

The outbursts of U Gem in the optical band presented here do not differ greatly from wide outbursts seen in SS Cygni or other dwarf nova, a rapid rise with a flat top during outburst and a slow decline. Time scales over which the outbursts proceeded also had a similar duration, with the two U Gem outbursts lasting 3 – 4 days longer than SS Cygni.

The outburst X-ray luminosity of U Gem was calculated to be between $0.8 - 1.1 \times 10^{32}(d/96pc)^2$ ergs s^{-1}, similar to that found for SU UMa ($0.7 \times 10^{32}(d/260pc)^2$ ergs s^{-1}, Chapter 7) and SS Cygni ($\sim 1.9 \times 10^{32}(d/166pc)^2$ ergs s^{-1}, Chapter 5) during the hard X-ray suppression. Baskill et al. (2005) observed RU Peg, a U Gem system, in outburst and calculated a luminosity of 9.4×10^{31} ergs s^{-1}. In quiescence, U Gem had a luminosity of $1.2 - 1.5 \times 10^{31}$ ergs s^{-1}. Both SS Cygni and SU UMa had substantially higher luminosities between $2.5 - 3 \times 10^{32}(d/260pc)^2$ and $3 - 8 \times 10^{32}(d/166pc)^2$ ergs s^{-1}. GW Lib had an X-ray luminosity of 9×10^{28} ergs s^{-1} (Byckling et al., 2009). It is also the only other dwarf nova to increase in X-ray luminosity during outburst. Based on this U Gem can be characterised as being unusually faint during quiescence, rather than unusually bright during outburst. This may be due to the high inclination of U Gem, at 72 degrees (Unda-Sanzana et al., 2006). Studying non-magnetic cataclysmic variables observed by *ROSAT*, van Teeseling et al. (1996) found the emission measure to be anti-correlated with the system inclination. However, GW Lib, like U Gem, is more luminous during outburst but has a low inclination (van Spaandonk et al., 2010) conflicting with this theory.

In hard X-rays U Gem is observed to brighten during outburst, this was first observed by Swank et al. (1978). The two outbursts presented here, separated by seven years, show that the brightening of hard X-rays observed during outburst is a phenomenon consistently seen in U Gem outbursts. This characteristic is also in contradiction to the observed behaviour of most other DN systems. The X-ray count rate in SS Cygni was observed by Wheatley et al. (2003) to rise by a factor of four in half a day, but was then suddenly quenched to near zero in less than 3 hours. Near the end of the optical outburst the hard X-ray count rate recovered again before declining. This behaviour is seen in observations presented in Chapters 4 and 5 and in 6 outbursts of SU UMa presented in Chapter 7. Observation of VW Hyi (Pringle et al., 1987; Wheatley et al., 1996) show that the flux drops by at least a factor of 2 and both YZ Cnc and WX Hyi (Hartmann et al., 1999; van Teeseling & Verbunt, 1994) also show more luminous hard X-rays in quiescence than outburst. Hard X-rays are also suppressed during superoutburst in WZ Sge (Wheatley & Mauche, 2005). The only other dwarf nova to be seen to brighten in outburst was GW Lib where the peak flux was 3 orders of magnitude brighter in outburst than in quiescence. It seems to have an unusually low quiescent X-ray luminosity (Byckling et al., 2009). Despite the very obvious difference in the hard X-ray outburst of U Gem and other DN systems, the U Gem X-ray flux was quenched below the quiescent level for a short time just prior to the end of the outburst. However, a rapid drop in the X-rays as the EUV rose was not observed. Shortly after, the count rate sharply rose forming a spike before returning to the quiescent count rate. Presumably this was the boundary layer as it transitioned from an optically thick to optically thin state. With an upper limit of 2 days for the duration of the peak it is conceivable that this peak is similar to the hard X-ray recovery seen in SS Cygni in Chapter 4, which had a duration of a day and a half.

6.5.2 X-ray Origin

It is not currently known where hard X-rays originate from in outburst. Patterson & Raymond (1985a) argue that the hard X-rays are produced in an optically thin region surrounding the optically thick outburst boundary layer. Eclipse observations of OY Car provide competing evidence against this in the form of a second source of X-rays. Observations by Naylor et al. (1988) in UV and X-ray bands suggest that there is an extended vertical disc structure. While observations by Mauche & Raymond (2000) in extreme-ultraviolet suggest that the extended source is from optically thick boundary radiation being scattered into the line of sight by the accretion disc wind. The increased X-ray flux during outburst and the dips observed in Section 6.3.3 in the light curve suggests that the X-rays originate from the inner part of the accretion disc with a scale height not much greater than the disc thickness. This supports models where the mass transfer stream overflows the disc resulting in complex disc stream interactions explaining dips in low mass X-ray binary light curves (Frank et al., 1987).

Dips in the light curve are thought to be caused by a thickening of the accretion disc near the circularisation radius. The stream impacts the edge of the disc partially penetrating the disc edge and partially flowing above and below the disc. The overflowing stream settles at the circularisation radius where a complicated interaction occurs between the disc and the mass transfer stream. Cold clouds form out of the disc plane creating a non-axisymmetric ring occultating the central source at phases 0.3 and 0.7 – 0.9 (see Figure 1 in Frank et al., 1987). Marsh et al. (1990) presented Doppler images of U Gem showing the stream penetrating the outer edge of the disc, with velocities intermediate between those expected for an unimpeded stream and co-rotation with the disc.

6.5.3 Spectral Evolution

Reassuringly both U Gem outbursts have a similar spectral evolution to SS Cygni during outburst. The spectrum softens during outburst and hardens when the system transitions back to quiescence with what is most likely the boundary layer transition. It is a good indicator of changing accretion rates, as the outburst X-ray count rates are dominated by softer X-rays. Both observations also show variability at the very start of outburst and during the transition back to quiescence coinciding with the disc changing state as the system moves out of outburst. VW Hyi (Wheatley et al., 1996) and SS Cygni (Wheatley et al., 2003) were also found to be variable during transition of the boundary layer at the start and end of the X-ray suppression. From the spectral fits it is clear that although the 1997 and 2004 observations exhibit the same general behaviour, i.e., emitting more X-rays from cooler gas during outburst, they were very different from each other. Most noticeably the temperature of the system during outburst in 2004 is higher than in 1997. There is also an indication of more reflection at the beginning of the 2004 outburst, but only when the flux was higher than was reached in the 1997 outburst.

The difference in the hard X-ray flux during the 1997 and 2004 observations is difficult to understand. It may be possible that all X-ray outbursts are different which is hard to determine having only two observations. It is also conceivable that there has been an underlying change in the system in the interim period between the two observations.

6.6 Conclusions

The two outbursts presented here show that the brightening of hard X-rays during outburst is a regular phenomenon exhibited by U Gem in outburst. U Gem can be characterised as being unusually faint during quiescence, rather than unusually bright during outburst. Although the two outbursts have the same general behaviour their individual light curves differ significantly. Despite the differences between these two observations and also with the well known dwarf nova SS Cygni they do reassuringly have a similar spectral evolution. Both systems emit cooler X-ray during outburst which gets replaced by a hotter continuum as the system transitions into quiescence.

While it is not currently known where hard X-rays come from in outburst the reflection is constant throughout the outburst and quiescence. The dips in the light curve suggest that the X-rays originate from the inner part of the accretion disc with a scale height not much greater than the disc thickness.

Chapter 7

X-ray Observations of SU UMa Throughout Six Normal Outbursts

7.1 Introduction

Following the X-ray detections of SS Cygni (Rappaport et al., 1974) and U Gem (Swank et al., 1978) , SU UMa was observed with the Imaging Proportional Counter (*IPC*) detector on the *Einstein* X-Ray Observatory by Cordova & Mason (1980). It was detected with a flux of 1.3×10^{-11} ergs s^{-1} cm^{-2} (0.6 counts s^{-1}) in the $0.1 - 4.5$ keV energy range of the *IPC* (assuming a spectral temperature of 10 keV). At energies below 0.7 keV they observed several areas of weaker emission forming a ring symmetrically located about the position of the dwarf nova. Later observations showed no evidence of this extended emission (Cordova & Mason, 1984). Using further observations with the *Einstein* observatory, Cordova & Mason (1984) found X-rays from SU UMa to be variable on short timescales. Eracleous et al. (1991) fitted an optically thin thermal bremsstrahlung model to the *Einstein* spectrum. Based on models by Pringle & Savonije (1979) and Tylenda (1981) the hard X-ray emission was consistent with being from a hot optically thin boundary layer between the disc and star.

SU UMa was observed twice in quiescence and once in outburst with *ROSAT* by Silber et al. (1994). Hot optically thin emission was observed and in outburst the observed count rate dropped by a factor of 3. Both the quiescent and outburst spectrum were well fitted by a bremsstrahlung model with temperatures of $2.6^{+1.2}_{-0.6}$ and $2.2^{+1.9}_{-0.8}$ keV respectively. In quiescence the boundary layer was responsible for 20 per cent of the total luminosity yet only 1 per cent during outburst. Silber et al. (1994) suggested that either the missing flux is an undetected extreme ultraviolet component or the boundary layer luminosity is carried away as kinetic energy by a wind during outburst. Baskill et al. (2005) presented SU UMa in outburst with *ASCA*, amongst a large number of other dwarf novae. They found a statistically acceptable fit to the spectrum using a thermal plasma model absorbed by photoelectric absorption by neutral material with a similar outburst temperature to that of SS Cygni of $5.1^{+0.5}_{-0.4}$ keV. SU UMa was again observed during a quiescent period using *XMM-Newton* (Pandel et al., 2005) where a large number of emission lines were detected. The observed lines indicated that the X-ray emitting plasma covers a wide range of temperatures, prompting the use of a cooling flow model to fit the spectra. Their model gave a good agreement to the data suggesting the source of X-rays is from a cooling plasma settling onto the white dwarf through a disc boundary layer. High resolution data taken from the *Chandra HETG* during quiescence showed the presence of a weak fluorescent iron line indicating there may be reflection present in the system (Rana et al., 2006). They also found the Fe XXVI line to be absent from the spectra indicating a lower temperature in the emitting region compared to other sources studied. Using the G line ratio of Fe XXV (defined as the ratio of the sum of the forbidden and intercombination lines with the resonance line) which is sensitive to electron temperature, they were able to determine that the plasma in quiescence is collisionally ionised.

Previous analysis of SU UMa has been based upon a number of snapshot observations, with short durations either during an outburst or quiescent period, making it difficult to draw firm conclusions about the evolution of the emitted X-ray through outburst.

Observations have shown that the X-ray spectrum in quiescence is a hot optically thin plasma. Observed lines indicate that the X-ray emitting plasma covers a wide range of temperatures and is consistent with a cooling plasma settling onto the white dwarf through a disc boundary layer.

In outburst the hard X-rays are usually suppressed and replaced with an intense extreme

Table 7.1: Pointed *RXTE*/*PCA* observations of SU UMa used in this analysis.

Proposal ID	Year	Start - End date	Number of observations	Total exposure [ks]	Gain epoch
P60005	2001	Mar 25 - Jun 21	193	336	5

ultraviolet component. This is thought to be due to the boundary layer becoming optically thick to its own emission as the accretion rate increases during outburst. However, the X-ray flux evolution through the outburst cycle is not well reproduced by the standard disc instability model, (e.g., Lasota, 2001).

In this chapter the evolution through outburst of SU UMa is investigated and observations in the X-ray band covering six outbursts are presented. The outbursts and quiescence of SU UMa will be explored and discussed photometrically and spectroscopically and the prototype SU UMa system will be compared with other dwarf novae. In Section 7.2 observations and data analysis are presented. In Section 7.3 the outbursts are compared with each other and in Section 7.4 the SU UMa spectra is modelled.

7.2 Observations

SU UMa was monitored using the *RXTE* Proportional Counter Array (*PCA*) beginning on 2001 March 28 and ending on 2001 June 21. The observation spanned six normal outbursts. A log of observations is given in Table 7.1. The total exposure was 336 ks and observations were taken in blocks of between $1-14$ ks exposure with additional gaps due to Earth occultations and passage of the spacecraft through the South Atlantic Anomaly (SAA). All *RXTE* count rates are presented for three *PCU*s.

For details of the extraction criteria and software used in this chapter see Section 4.2 in Chapter 4. On 2000 May 13 *PCU*0 suffered a loss of propane from its veto layer resulting in a higher number of false events being observed in that detector. As a result this detector was not used in the extraction of this data set.

7.3 Time Series Analysis

The *RXTE* observations covered six normal outbursts of SU UMa. Figure 7.1 shows the X-ray observations plotted with optical observations from the *AAVSO*. The optical data consist of visual observations (85 per cent) and V band CCD observations (15 per cent) with an average cadence of 5 hours. In outburst the optical band rapidly brightened from approximately 14^{th} to 12^{th} mag in approximately 0.5 days before declining back into quiescence. Outbursts were nearly equally spaced, lasting approximately 2 days with the quiescence periods lasting approximately 10 days.

In the hard X-ray band as the system entered outburst the X-rays became suppressed to near zero. The X-ray flux remained suppressed for most of the duration of the outburst, recovering during optical decline. The outbursts are shown in more detail in Figure 7.2, there was no sign of a peak preceding the X-ray suppression, as was observed in SS Cygni. The cadence of X-ray observations at the beginning of the outbursts was typically 12 hours.

Also plotted in Figure 7.1 is the X-ray hardness ratio which was created using counts in the energy bands $2.0-3.7$ keV and $3.7-18.5$ keV. During quiescence the hardness ratio does not show any obvious variations, although on JD 2452012 for approximately 4 days a higher X-ray count rate was accompanied by a harder spectrum. The χ^2 during this period, using the average of the hardness ratio as the model hardness, results in the χ^2_ν of 1.4 (3 d.o.f) with a probability of 0.76 suggesting that this feature is significant. Despite large error bars during outburst it is clear that the system was softer during outburst than during quiescence. This has also been seen in other dwarf novae (e.g., Baskill et al., 2005). Closer inspection of Figure 7.1 shows that the softening of the spectrum coincides with the hard X-rays becoming quenched.

To make comparison between the outbursts a composite light curve was made of the six outbursts. The cross correlation was calculated separately for both the optical and X-ray data sets and the second outburst (JD 2452017) was chosen as a template outburst. Due to the low cadence of both the optical and X-ray data the template outburst was interpolated and then used to calculate the cross correlation. The times were shifted to maximise the cross correlation and the composite light curve is plotted in Figure 7.3. The top plot shows the composite light curve using the optical template and the bottom plot shows the composite light curve using the

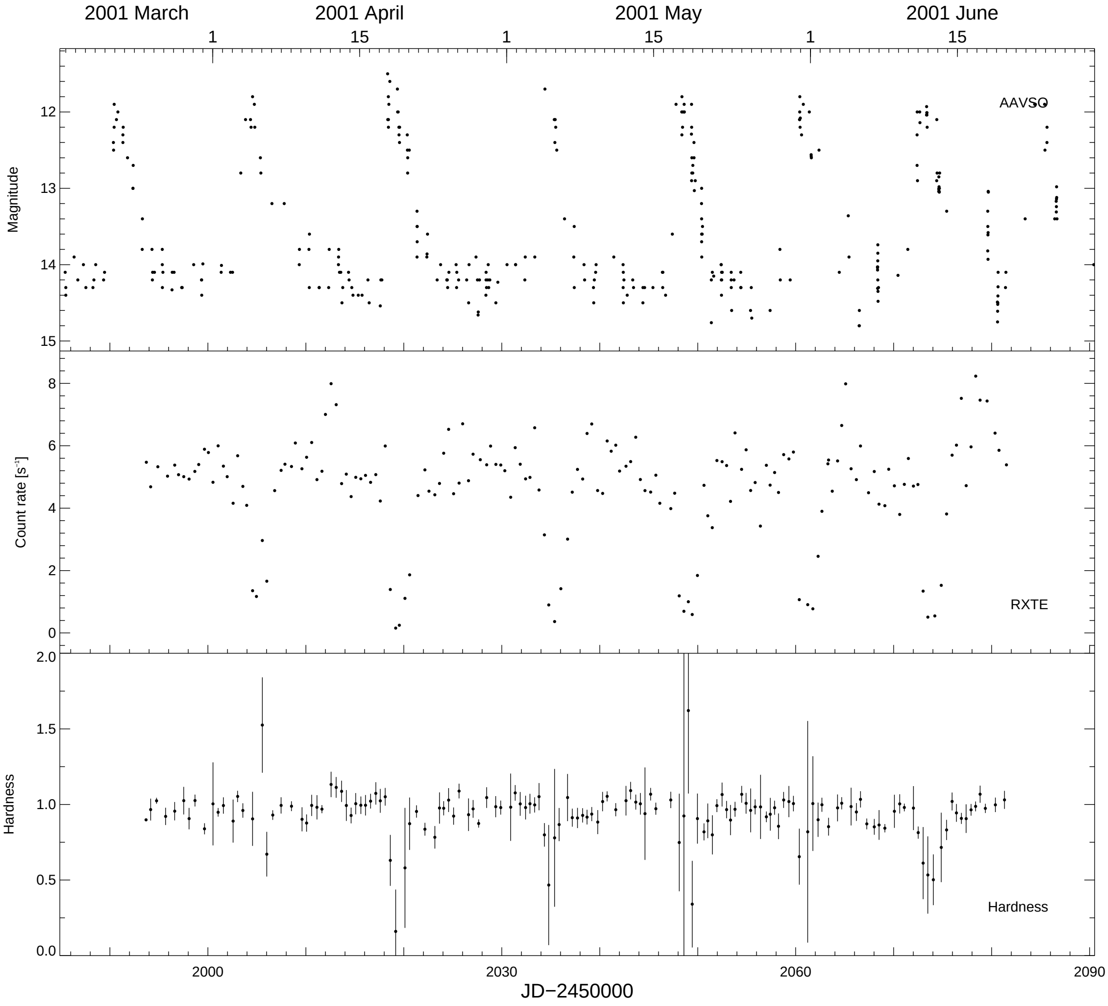

Figure 7.1: *AAVSO* (upper panel) and *RXTE* (middle panel) observations of SU UMa during the March - June 2001. The X-ray hardness ratio, defined as the hard band (3.7 – 18.5 keV) divided by the soft band (2.0 – 3.7 keV) is also plotted (bottom panel).

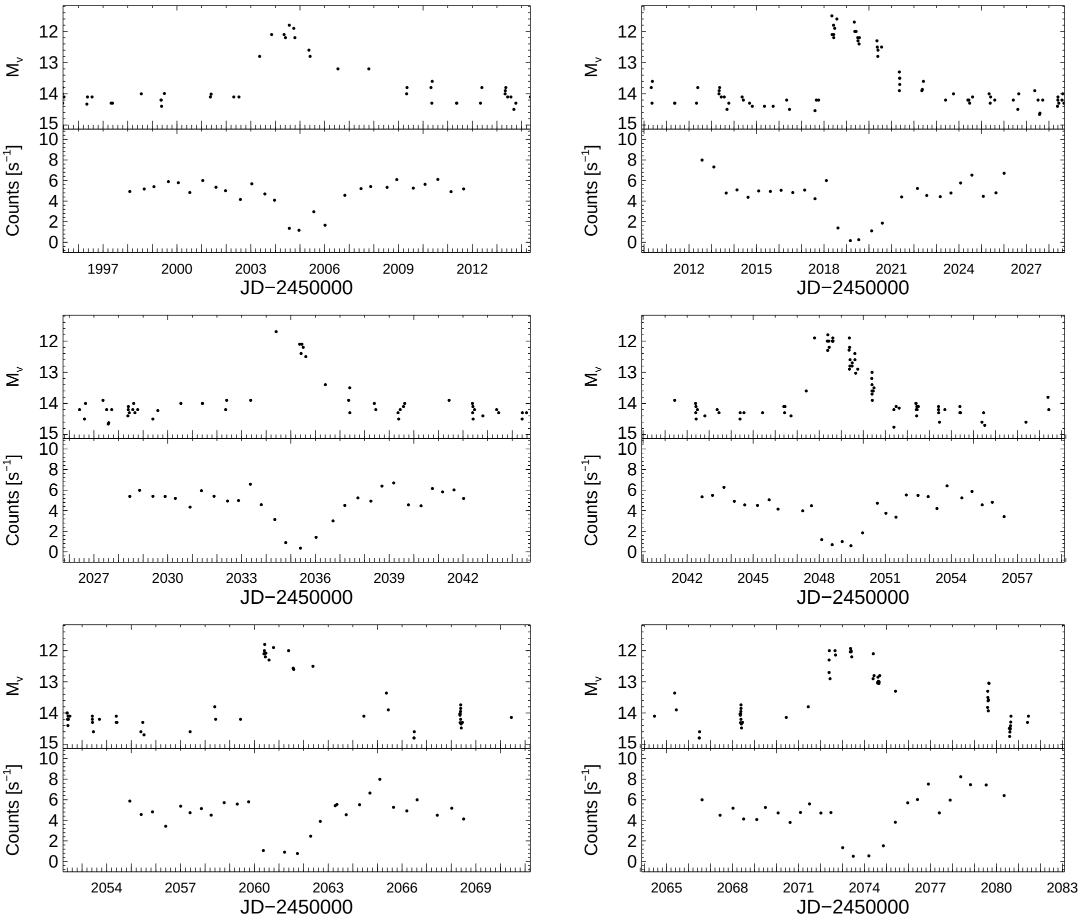

Figure 7.2: Detailed optical (upper panel) and X-ray (bottom panel) light curves from Figure 7.1.

Table 7.2: Optical and X-ray times for the flux to reach mid-point of the transition to outburst, including the cadence of the optical and X-ray observations respectively.

Optical time [JD]	Cadence [days]	X-ray time [JD]	Cadence [days]	Delay [days]
2452003.0	0.79	2452004.1	0.60	1.12
2452017.9	0.47	2452018.4	0.46	0.45
2452033.6	1.03	2452034.3	0.42	0.68
2452047.5	0.39	2452047.8	0.42	0.34
2452059.8	0.88	2452060.1	0.68	0.25
2452071.8	0.88	2452072.7	0.47	0.86

X-ray template. The composite light curve shows that for the six outbursts the shapes were highly repeatable. In both the optical and X-ray bands the quiescent periods following outburst were more variable than prior to the outbursts. A peak in the count rate immediately before outburst was also not observed in the composite light curve, which has an average separation of points of only 2 hours. The X-ray suppression was remarkably rapid and was not resolved in the composite light curve, suggesting it occurred faster than two hours.

Figure 7.3 also shows there was a delay between the start of outburst in the optical and X-ray bands, however, due to the sparse sampling of both optical and X-ray data it is difficult to determine the precise duration of the delay. To quantify the delay the data were interpolated and times when the X-ray and optical flux crossed the mid point between outburst and quiescence were calculated, these times are shown in Table 7.2. The delays show that the X-ray suppression follows the optical rise by $0.25 - 1.12$ days later, with a median delay of 0.57 days. The range in delay times can be accounted for by the cadence of the observations (also listed in Table 7.2).

In order to determine whether the X-ray flux increased during quiescence, as predicted by the disc instability model, a linear least squares fit was performed to the quiescent intervals, plotted in Figure 7.4. The X-ray observations were selected when the optical light curve was fainter than 14^{th} mag. There was short timescale variability in the light curves, but the quiescent trend is well represented by the best fit lines. The fits show that the quiescent X-ray count rates either remained constant or decreased. The gradients of the line fits are presented in Table 7.3. Figure 7.5 shows the composite light curve of Figure 7.4 with a linear least squares fit to all the quiescent data. The fit was applied to the interval where the optical was fainter than 14^{th} mag in

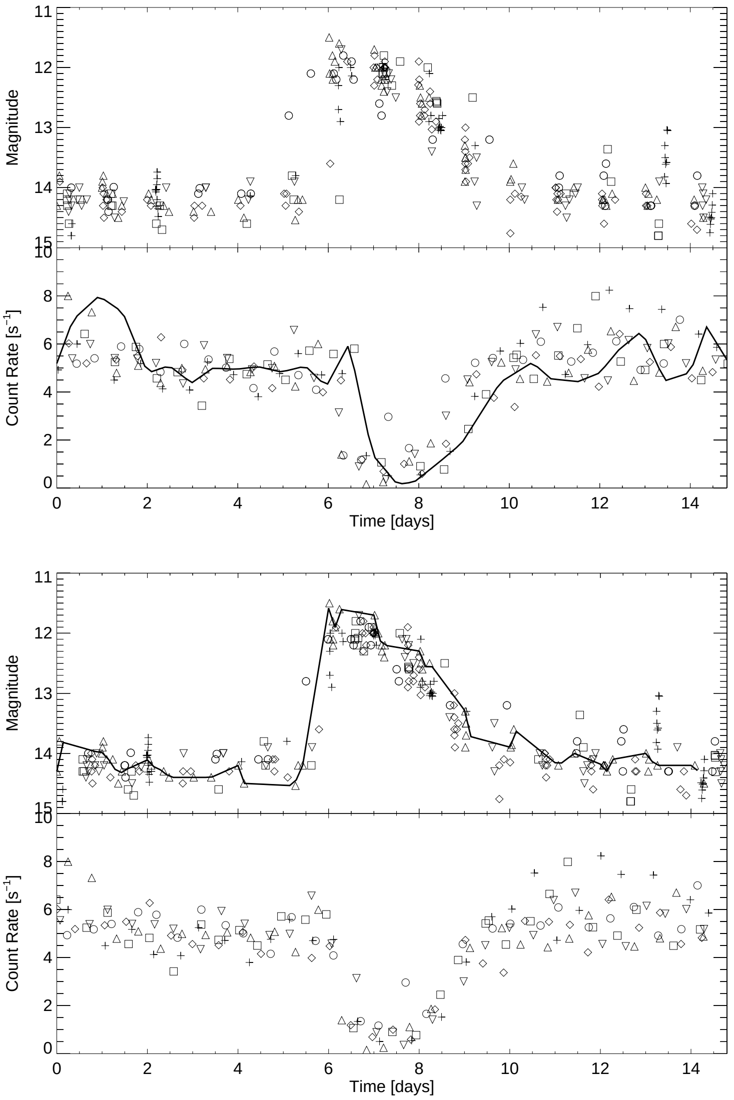

Figure 7.3: The auto correlation of the *AAVSO* (upper panel) and *RXTE* (bottom panel) outbursts from Figure 7.1 overlaid. The second outburst (thick line) was used as the template. Symbols relate to the outburst as follows: 1^{st} - circle, 2^{nd} - upward triangle, 3^{rd} - downward triangle, 4^{th} - diamond, 5^{th} - square, 6^{th} - plus sign.

Table 7.3: Gradients for the linear least squares fits to the quiescent X-ray data from Fig 7.4 and Fig 7.5.

Quiescence interval [JD]	Gradient [counts s^{-1} $days^{-1}$]
2451999	$+0.01 \pm 0.02$
2452013	-0.22 ± 0.02
2452028	$+0.00 \pm 0.01$
2452042	-0.14 ± 0.02
2452055	$+0.06 \pm 0.02$
2452068	-0.38 ± 0.03
Composite	-0.09 ± 0.02

all six cycles. It shows that, in addition to short timescale variability, there was an overall decline in the hard X-ray flux during quiescence. The mean count rate decreased from a maximum of 5.8 counts s^{-1}, with a gradient of 0.09 counts s^{-1} day^{-1}, although the average decline is not well represented by a straight line (χ^2_ν = 4.9 (5 d.o.f)). A similar decline during quiescence has previously been seen in SS Cygni by McGowan et al. (2004).

7.4 Spectral Fitting

7.4.1 Combined Quiescence Spectrum

To maximise the signal to noise the data were first binned into two spectra. Observations with count rates lower than 3 $counts^{-1}$ (per 3 *PCU*s), based on Figure 7.1, were considered to be in outburst and were combined into one outburst spectrum, with 48.4 ks of exposure. All remaining data were combined into one quiescent spectrum, with 251 ks of exposure. The source was not detected above 12 keV in outburst and thus data were not fitted above this energy. The data were initially fitted with the error on the background set to zero, this will be addressed in more detail further on in this section. SS Cygni was found to require a systematic error of 0.5 per cent on the data (Section 4.4.1 Chapter 4), this systematic error was also added to the SU UMa data presented here.

A bremsstrahlung continuum model was fitted to the data; the resulting fit was poor for both the outburst and quiescence spectra. Although this model is not physically realistic it is,

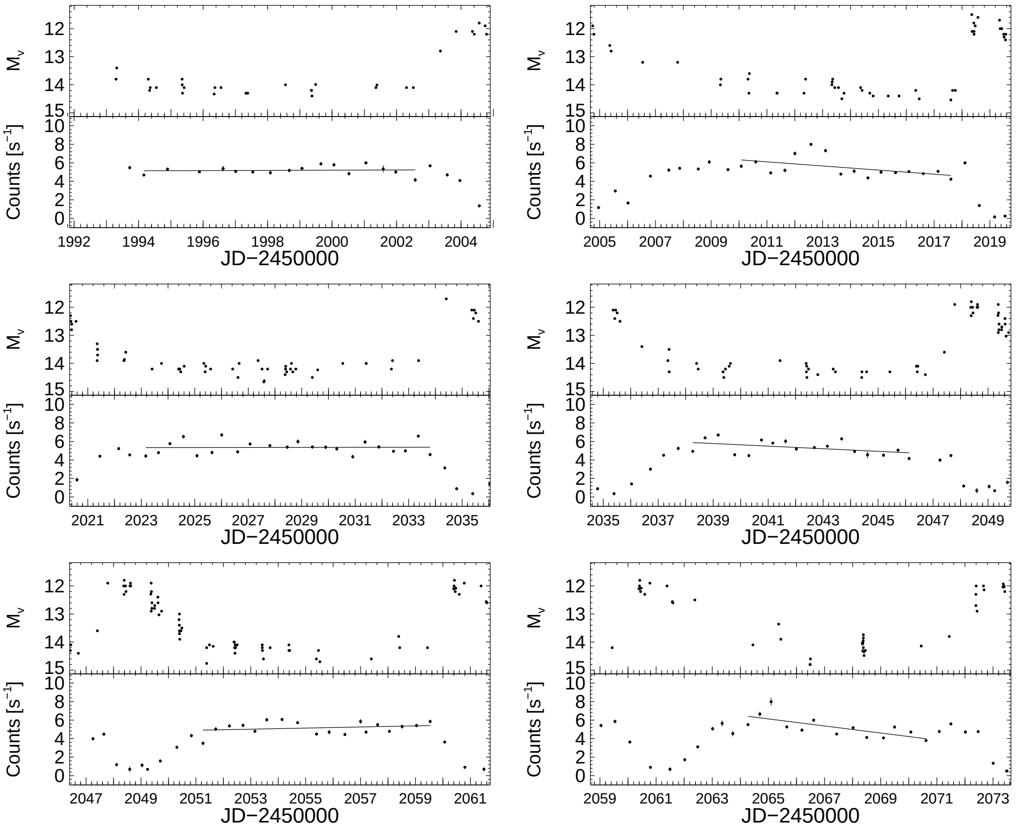

Figure 7.4: Individual optical (upper panel) and X-ray (bottom panel) light curves from Figure 7.1 centred around the quiescent intervals. Each quiescent X-ray interval is also plotted with a linear least squares fit at times when the optical magnitude was fainter than 14^{th} mag.

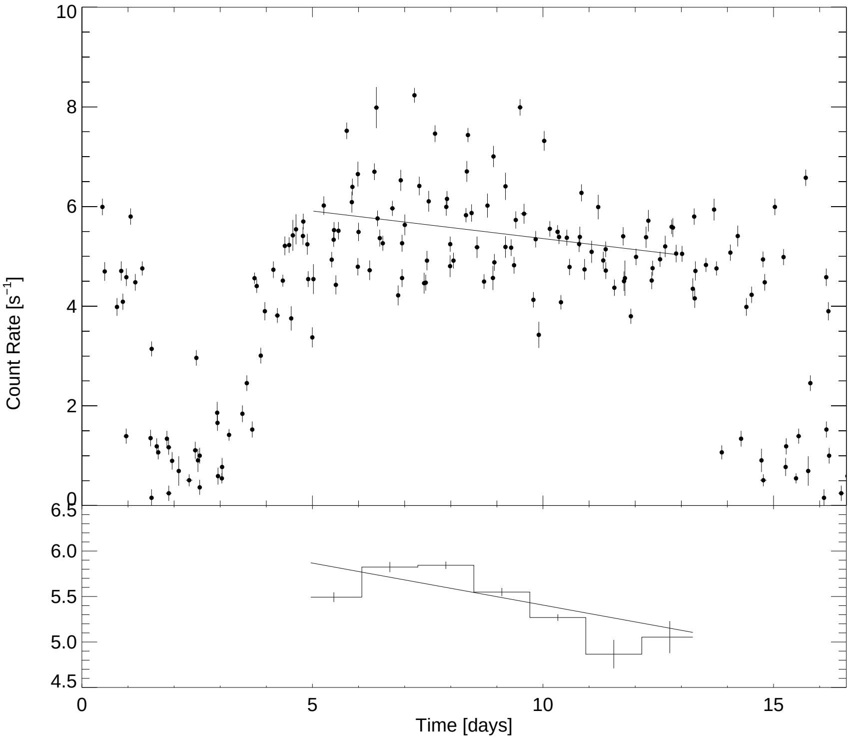

Figure 7.5: Composite X-ray light curve from Figure 7.3 centred around the quiescent interval with a linear least squares fit to the quiescent data (top panel) and to the binned quiescent data (bottom panel) at times when the optical magnitude was fainter than 14th mag.

however, useful to parameterise the system. The residuals of both spectra showed the model had a deficit between 6 – 7 keV, most likely due to a mixture of a fluorescent and thermal iron lines. Adding a free emission line to the model dramatically improved the fit to the data resulting in a χ^2_ν of 3.46 (33 d.o.f) for the quiescent spectra and a χ^2_ν of 0.58 (12 d.o.f) for the outburst spectra. The outburst χ^2_ν is worryingly low, indicating that model might be fitting photon noise in the detector or that the error bars have been overestimated. However, the probability of a fit resulting in a χ^2_ν lower than this value is 14 per cent and so it is possible that a fit with this χ^2_ν can occur by chance. Figure 7.6 shows the best fit for the spectra with this model in quiescence and outburst.

To fit a more realistic model to the data a single temperature plasma model was used (the mekal model in `XSPEC`, Mewe et al., 1985, 1986; Liedahl et al., 1995). Applying this model to the quiescent spectra did not result in a good fit with a χ^2_ν of 13 (36 d.o.f). The residuals, Figure 7.7 panel A, show that there is an excess in the model between 6 – 8 keV. Comparing the plotted model and data it is apparent that this excess comes from the modelled line emission in the thermal plasma model. Reducing the strength of the thermal lines can be achieved by lowering the metal abundances. Making the model abundances a free parameter gave a significant improvement to the fit resulting in a χ^2_ν of 3.6 (35 d.o.f) with an F-test probability of 2×10^{-11}. The residuals to this model can be seen in Figure 7.7 panel B. The best fit abundances were found to be lower than solar levels (Anders & Grevesse, 1989) at 0.64 solar. Sub-solar abundances have been found for other dwarf novae (Baskill et al., 2005).

The modification to the model reduced the size of the excess in the residuals (Figure 7.7 panel B) but it was still poorly fitting in the 6 – 8 keV energy range. The residuals show a deficit in the model between 6 – 7 keV providing evidence for a 6.4 keV fluorescence line of neutral iron, also seen in SU UMa by Rana et al. (2006). A narrow Gaussian component fixed at 6.4 keV was added to the model, the result of this addition is seen in Figure 7.7 panel C. The fit produces a χ^2_ν of 2.01 (34 d.o.f). The addition of the narrow emission line improved the fit between 6 – 8 keV, but it was unable to remove the residual feature near 7 keV. Adding a partial covering component to the model significantly improved the fit to the SS Cygni data in Chapter 4, but making the addition to the SU UMa data did not improve the fit, resulting in a χ^2_ν of 2.11

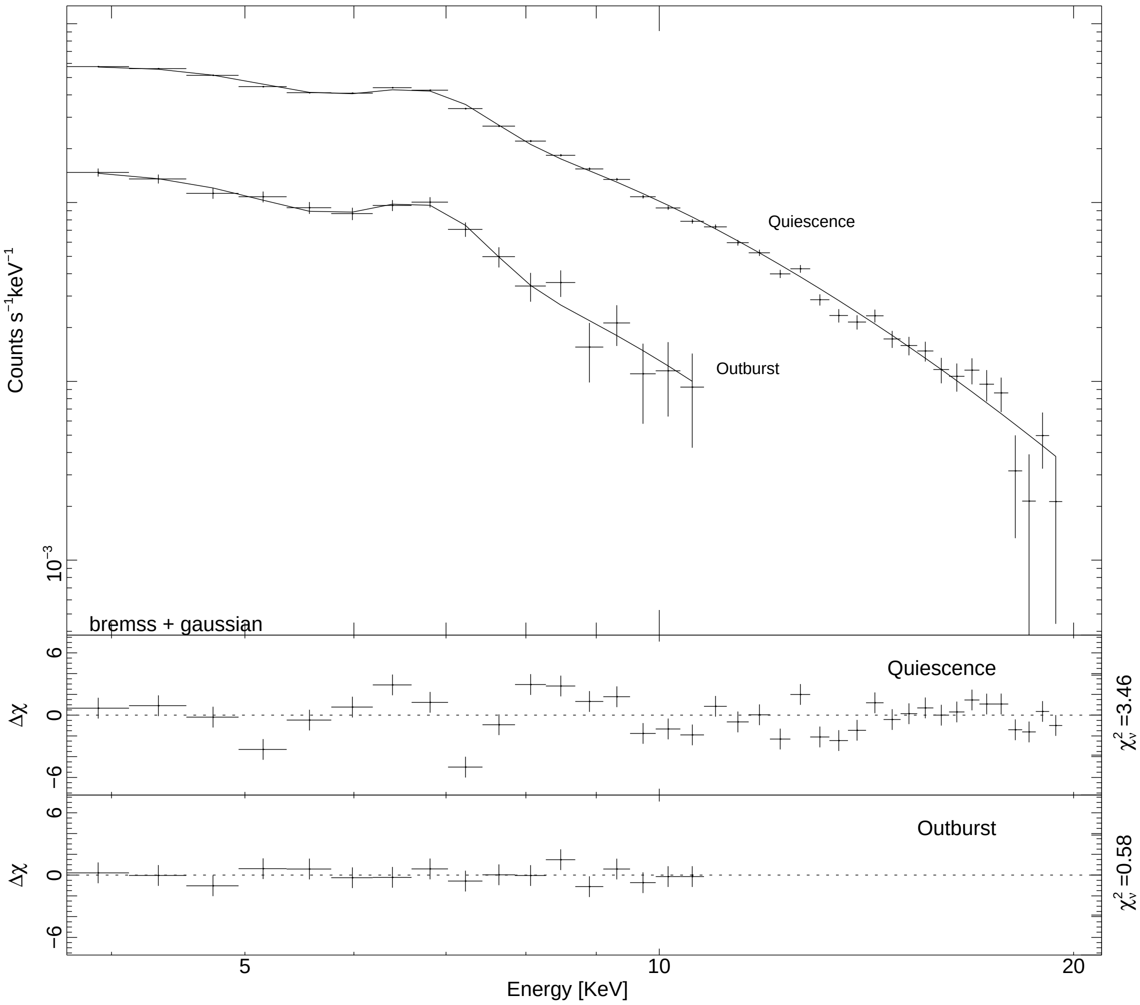

Figure 7.6: The top panel shows the data (crosses) and the folded model of a bremsstrahlung continuum with an emission line (curve) for the two spectra in outburst and quiescence. The panels below show the residuals for this model. The χ^2_ν produced by the fit is at the end of the individual panel. All errors are in the 68 per cent confidence interval for one parameter of interest ($\Delta\chi^2 = 1.0$).

(32 d.o.f). The residuals for this model are plotted in Figure 7.7 panel D.

7.4.2 Background Systematics

The unacceptably high χ^2_ν produced by these fits indicates that either the model is inadequate, or systematic uncertainties are present in the data that are not fit by the model. Extensive analysis of the calibration and background model for the *PCA* was carried out by Jahoda et al. (2006). They determined that the energy calibration has deviations of ≤ 1 per cent from power law fits to the Crab Nebula and unmodeled variations in the instrumental background at ≤ 2 per cent below 10 keV and ≤ 1 per cent between $10 - 20$ keV. When `saextrct` generates the data files the error is calculated as the square root of the number of counts in the data file. This is correct for the data, however, the background is estimated from the average of a huge amount of data and so the resulting error on the background is overestimated[1]. A value of zero was used as the background error in the fitting in Section 7.4.1. However, SU UMa is a faint system, so background systematics are likely to contribute significantly.

To investigate the level of systematic error required on the background, the data were re-binned forming eight spectra. Using the same criteria as above, observations with count rates lower than 3 counts^{-1} (per 3 *PCU*s), based on Figure 7.1, were binned into one outburst spectrum containing 48 ks of exposure. One spectrum was made for each quiescent period between the outbursts with each quiescent spectrum containing an average of 36 ks of exposure. SU UMa is a much fainter system than either SS Cygni or U Gem, where the source counts dominate the spectrum, allowing the instrumental systematic error to be estimated. SS Cygni was found to require a systematic error of 0.5 per cent on the data (Section 4.4.1 Chapter 4), this systematic error was added to the spectrum in quadrature as before. A series of fits were made with the systematic error on the background selected in the range $0 - 2$ per cent, as identified by Jahoda et al. (2006). The data were fitted using the current best model: a thermal plasma model with free abundances and a narrow emission line fixed at 6.4 keV. Figure 7.8 shows the cumulative histogram plots of the best fit χ^2_ν distributions, with the cumulative plot of the χ^2 distribution (curve) on the same plot. The plots show that a systematic error of 0 and 0.1 per cent in the

---

[1] http://astrophysics.gsfc.nasa.gov/xrays/programs/rxte/pca/chisquare.html

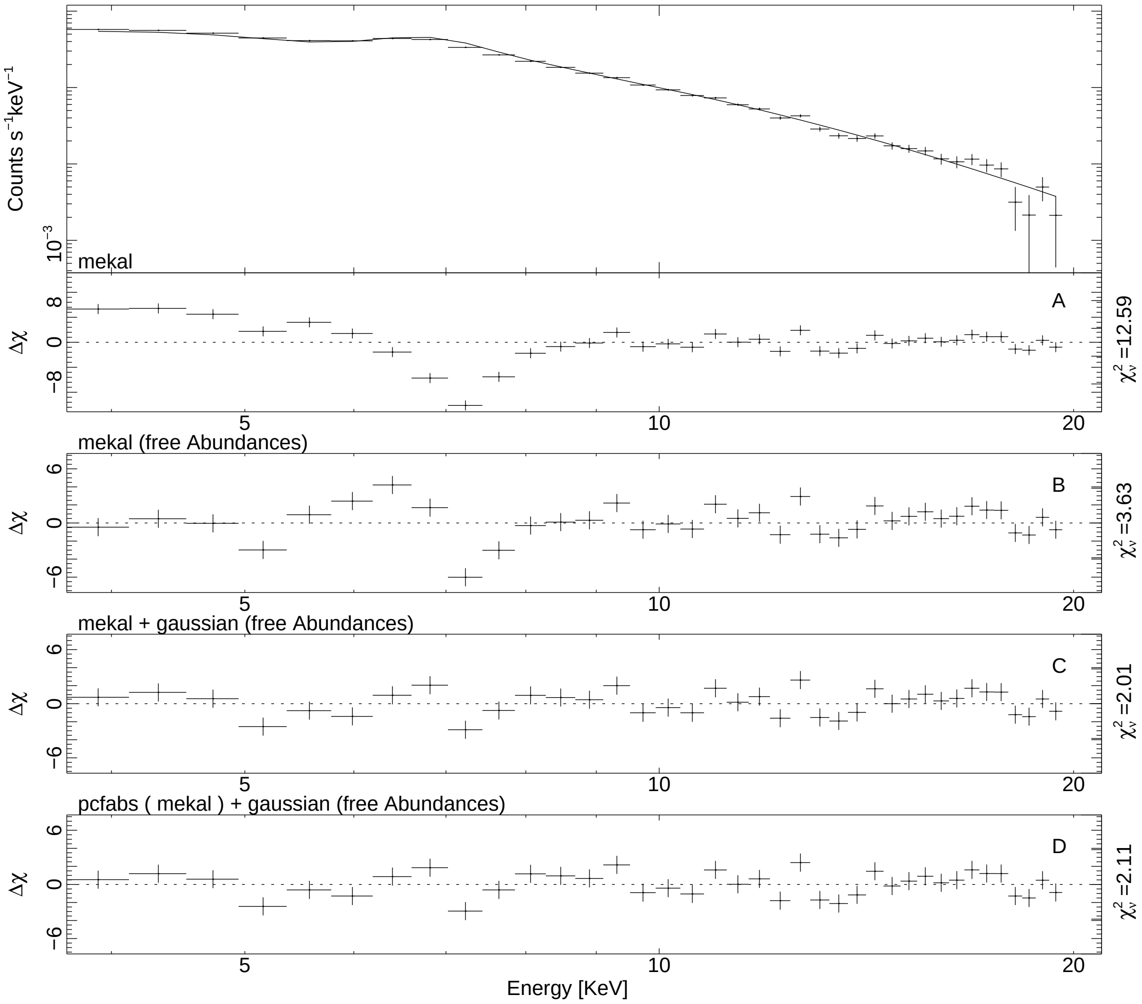

Figure 7.7: The top panel shows the data (crosses) and the folded model of a bremsstrahlung continuum with emission line (curve) for the quiescence spectra (from Figure 7.6). The panels below show the residuals for this model and fits to subsequent models. The model, as used in `XSPEC`, is labelled above the pair of residuals, with the χ^2_ν at the end of the individual panel. All errors are in the 68 per cent confidence interval for one parameter of interest ($\Delta\chi^2 = 1.0$).

background underestimates the error resulting in distributions that are greater than 1. Similarly a systematic error of between 1.3 and 2 per cent overestimate the error and result in distributions that are less than 1. A systematic error between 0.3 and 1 per cent produces a distribution that is closest to a χ^2 distribution, with a background systematic error of 0.5 per cent producing the best result. Since this is within the range identified by Jahoda et al. (2006) and produced acceptable fits to the model, this value was adopted and applied to all data.

Fitting the quiescent and outburst spectrum with the new background systematic applied resulted in an acceptable χ^2_ν for all spectra. The best fitting thermal plasma model with a narrow emission line was improved, giving an acceptable fit with a χ^2_ν of 0.99 (34 d.o.f) to the combined quiescent spectrum in Section 7.4.1. The addition of a partial covering absorption component to the model, again, did not significantly improve the fit resulting in a χ^2_ν of 1.03 (32 d.o.f).

7.4.3 Time Resolved Spectra

The best fit parameters resulting from the fit to the thermal plasma model with narrow emission line are shown in Figure 7.9, χ^2 residuals for all spectra can be seen in Figure 7.10. The top seven panels are the quiescent spectrum with the outburst spectra in the bottom panel. The flux of the quiescent spectra varies during the observation with the seventh spectrum emitting more X-rays on average than the other quiescent spectra. The system was also fainter and softer in outburst than in quiescence. Within error the temperature of the quiescent spectra were consistent with each other at an average temperature of 7.8 ± 0.3 keV. The outburst spectrum fitted a lower temperature of 3.8 ± 0.4 keV. The best fit free abundances were also consistent with each other with an average abundance of 0.64 ± 0.01 solar. The outburst spectrum was less well constrained fitting an abundance of 0.62 ± 0.25, however it was still consistent with the quiescent spectra. The 6.4 keV line strength was weaker in the earlier quiescent intervals, but within the error all spectra were consistent with each other, with an average equivalent width of 91 ± 35 eV during quiescence. The best fit line strength during outburst was consistent with the quiescent spectrum but was poorly constrained (102 ± 102 eV). These equivalent widths were also consistent with equivalent widths expected from a semi-infinite, plane parallel cold slab irradiated by an external source of X-rays (George & Fabian, 1991). Fitting a reflection continuum (calculated from the

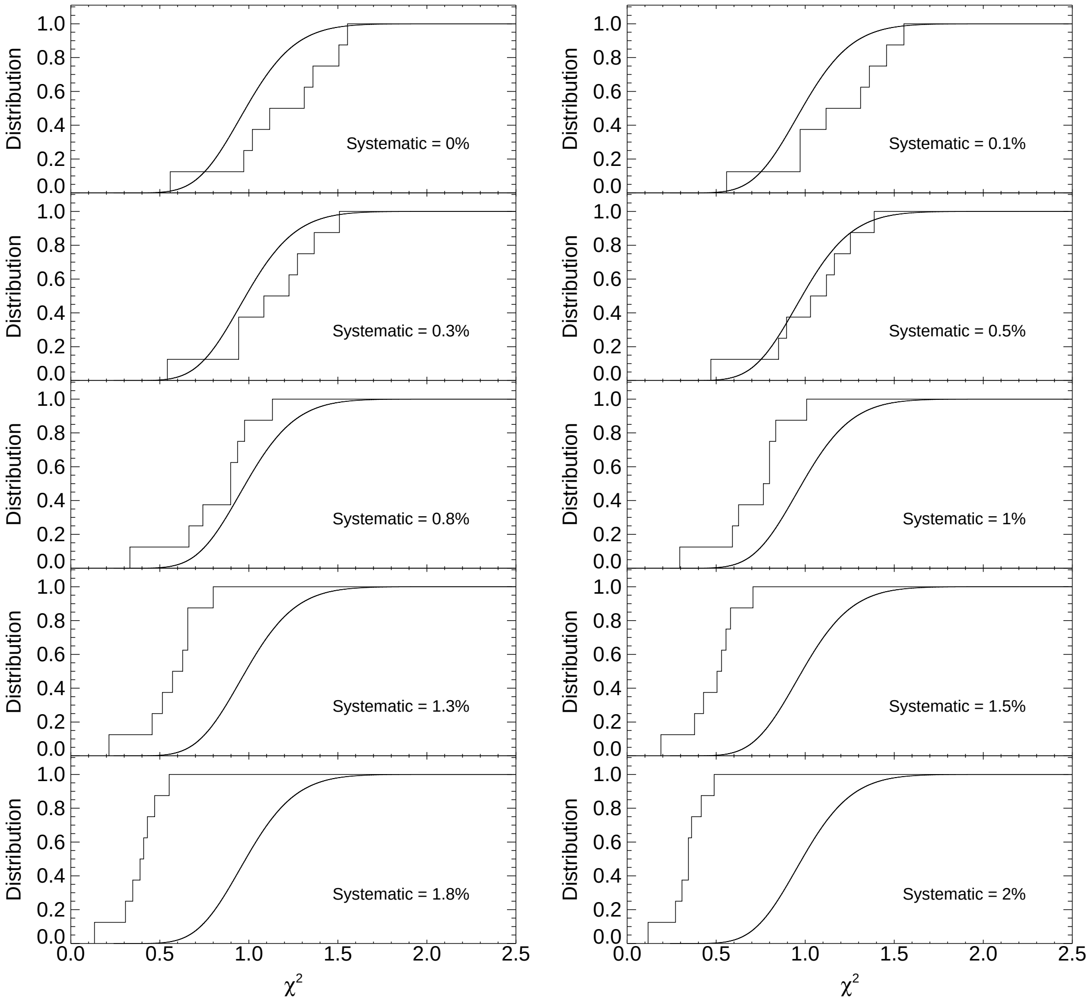

Figure 7.8: Cumulative histogram plots of χ^2_ν resulting from fits of all spectra to the thermal plasma model with a narrow emission line. The foreground systematic error was fixed at 0.5 for all fits while the background systematic was varied from 0 to 2 per cent.

code of Magdziarz & Zdziarski, 1995), with the reflection albedo fixed at 1 and the reflector abundances tied to the abundances of the plasma model, does not improve the best fit. However, it does show that the data were consistent with a reflection continuum with a total best fit χ^2_ν of 1.3 (251 d.o.f).

Comparing the flux above 7 keV with the 6.4 keV line normalisation (as was done in Section 4.4.4 in Chapter 4), it is possible to get a better understanding of the reflection in the system. The line normalisation and the line flux above 7 keV are plotted in Figure 7.11 which shows the fraction of continuum photons that produce line photons. The figure shows there is a good correlation with the flux between $7-20$ keV and the line normalisation. The gradient of the line shows that $\sim$ 4 per cent of hard X-rays give rise to fluorescent photons. The linear fit is consistent with no change in reflection during these observations.

7.4.4 Multi-Temperature Model Fits

The X-ray spectrum originates from an optically thin plasma that probably consists of a wide range of temperatures, previously modelled as a cooling flow (Wheatley et al., 1996; Pandel et al., 2005). A multi-temperature model was fit to the combined quiescent spectrum (cemekl in `XSPEC`, Singh et al., 1996) which showed that $\alpha \geq 0.8$, $T_{max} = 12^{+2}_{-4}$ keV and abundance $= 0.59 \pm 0.05$ with a χ^2_ν of 0.97 (33 d.o.f) confirming low abundances. T_{max} and α are consistent with *ASCA* observations of other dwarf novae in quiescence (Baskill et al., 2005).

7.4.5 Fluxes and Luminosity

Fluxes were calculated from the best fitting model over the energy range $2-20$ keV. Broadband fluxes were calculated by integrating over the energy range $0.01-100$ keV. They are presented in Table 7.4 along with the luminosities and associated accretion rates. Assuming a distance of 260^{+190}_{-90} pc to SU UMa (Thorstensen, 2003) the average X-ray luminosity of the system was calculated to be $2.6 \times 10^{32}(d/260pc)^2$ ergs s^{-1} in quiescence and $0.7 \times 10^{32}(d/260pc)^2$ ergs s^{-1} in outburst. It should be noted that although the outburst flux is consistent with that calculated by Baskill et al. (2005) it is close to the confusion limit of the *RXTE* detector (Jahoda et al., 2006). The accretion rates were calculated using the relation $L = GM_{wd}\dot{M}/2R_{wd}$. The mass of

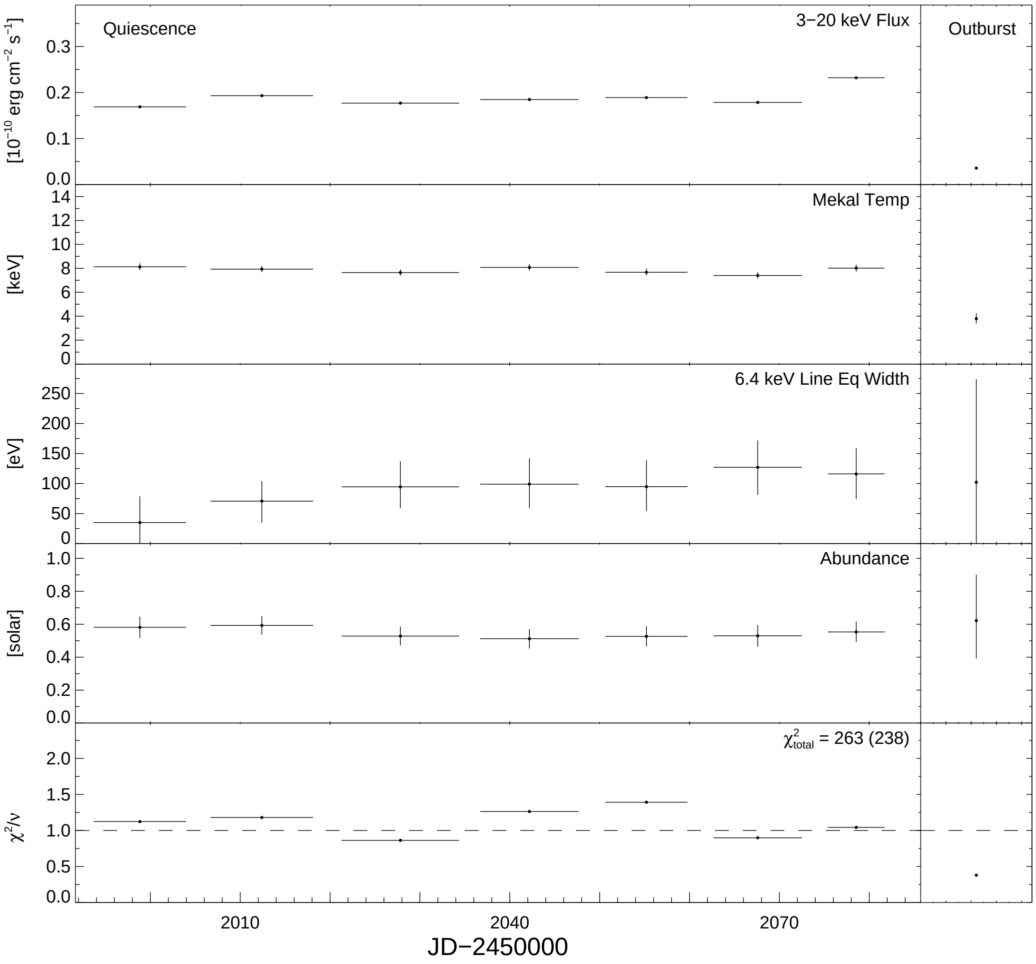

Figure 7.9: Thermal plasma model with the addition of a fixed 6.4 keV emission line component due to fluorescence. X-axis error bars mark the start of the first observation until the end of the last observation of the original spectra used to produce that spectrum. The spectra to the far right of the plot contains all outburst data and is thus plotted separately. All errors are in the 68 per cent confidence interval for one parameter of interest ($\Delta\chi^2$ = 1.0).

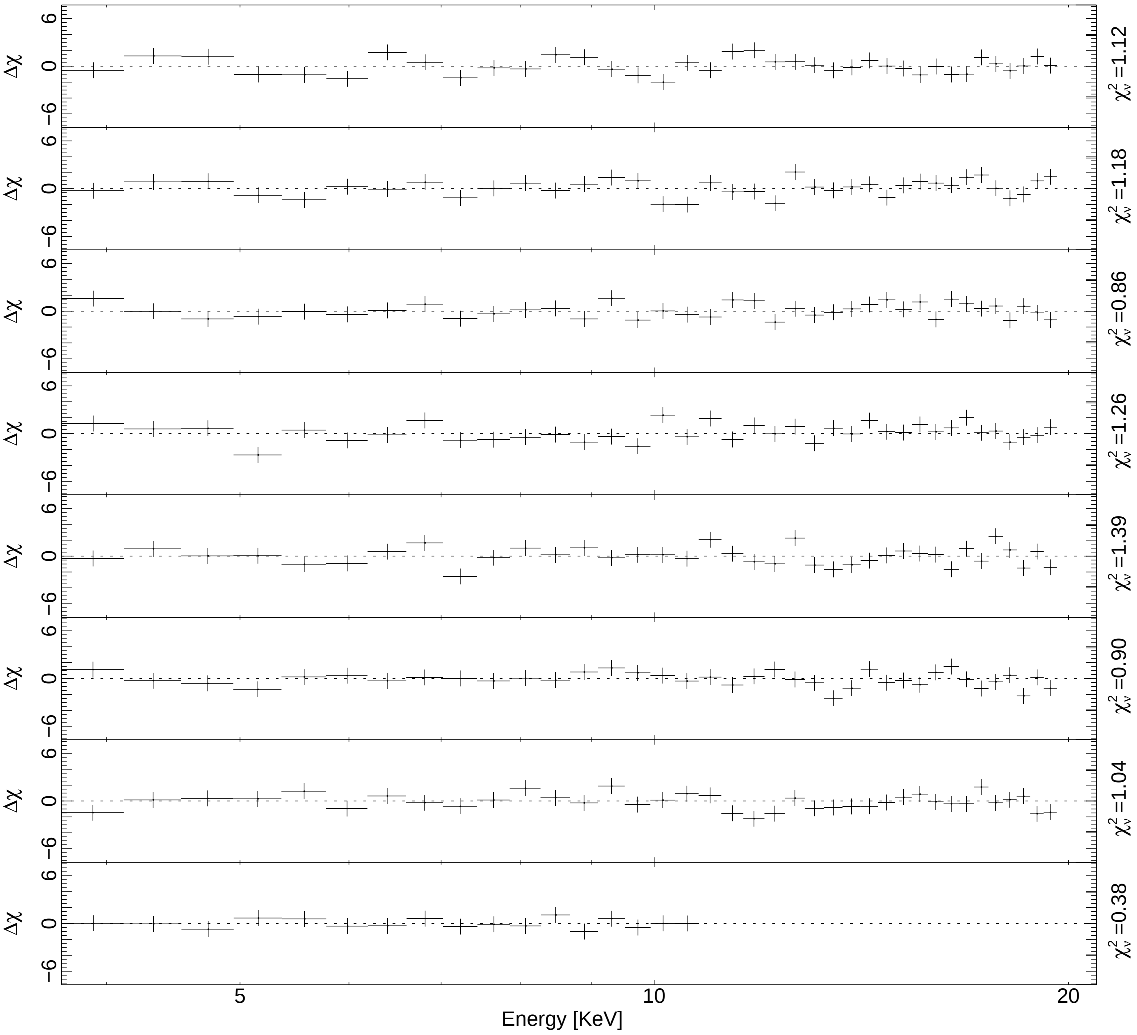

Figure 7.10: χ^2 residuals for all spectra plotted in Figure 7.9 using a thermal plasma model with a fixed 6.4 keV emission line. The first seven spectra are the quiescent spectra with the outburst spectra in the bottom panel. All errors are in the 68 per cent confidence interval for one parameter of interest ($\Delta\chi^2 = 1.0$).

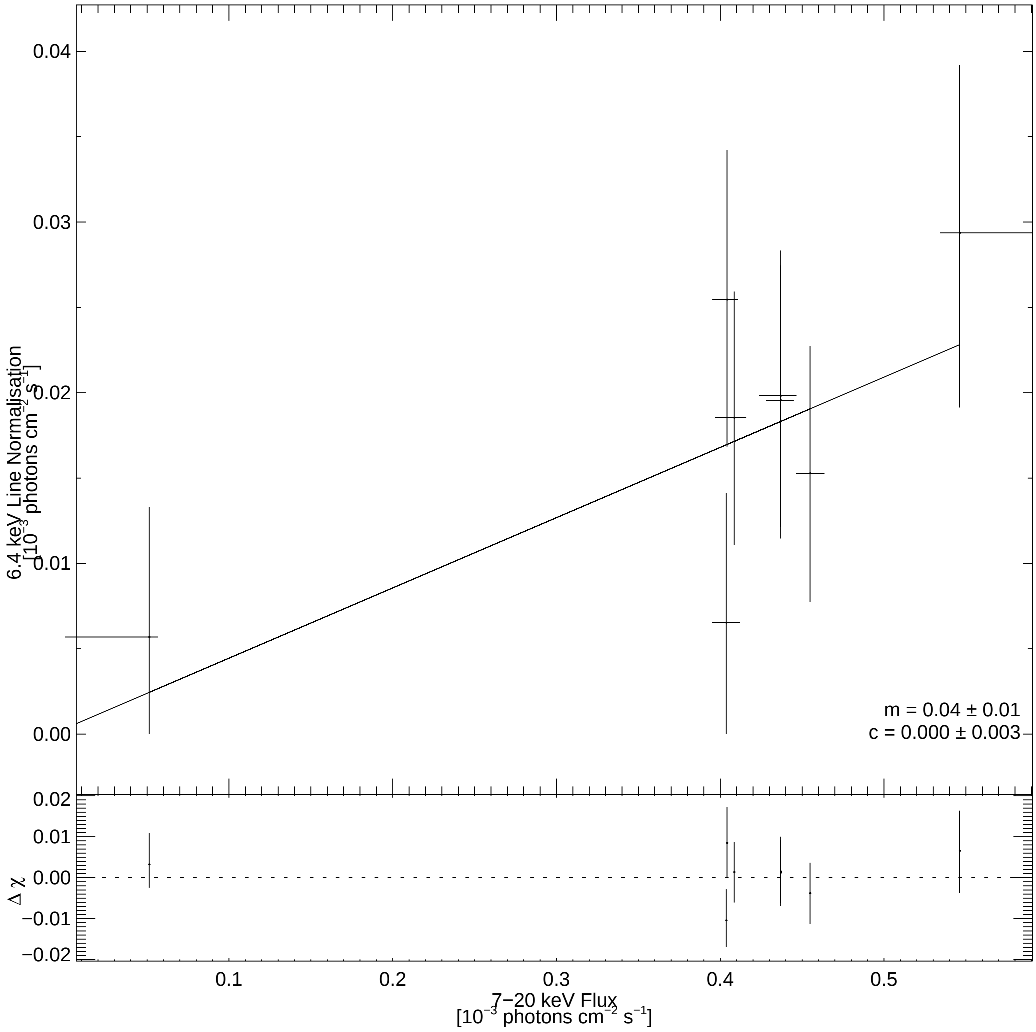

Figure 7.11: The best fit 6.4 keV line normalisation and the continuum flux above 7 keV. Also plotted is the best fit line to the data points. The bottom panel shows the residuals between the best fit line and the data. All errors are in the 68 per cent confidence interval for one parameter of interest ($\Delta\chi^2 = 1.0$).

Table 7.4: Fluxes, luminosities and associated accretion rates for SU UMa.

Spectra number	Flux[a]		Luminosity[b]	Accretion rate[c]
	[2 – 20 keV]	[0.01 – 100 keV]		
1	1.7	2.8	2.3	3.8
2	1.9	3.2	2.6	4.3
3	1.8	3.0	2.4	4.0
4	1.8	3.1	2.5	4.1
5	1.9	3.2	2.6	4.2
6	1.8	3.0	2.4	4.0
7	2.3	3.9	3.1	5.2
Outburst	0.4	0.9	0.7	1.2

[a] $\times 10^{-11}$ ergs s^{-1} cm^{-2}

[b] $\times 10^{32}(d/260pc)^2$ ergs s^{-1}

[c] $\times 10^{15}$ g s^{-1}

the white dwarf in SU UMa has not been directly calculated owing to its low inclination. Based on the work of Knigge (2006) white dwarfs in binaries were found to have an average mass of $M_{wd} = 0.75M_{\odot}$ and $R_{wd} = 7.7 \times 10^8$ cm. These values were used to calculate the accretion rates presented here. The calculated luminosities correspond to an average accretion rate during quiescence of 4.2×10^{15} g s^{-1} and 1.2×10^{15} g s^{-1} during outburst. However, the accretion rate is not thought to drop during outburst, instead the luminosity is probably dominated by an intense extreme ultraviolet component.

7.5 Discussion and Conclusions

X-ray observations of SU UMa spanning six normal outbursts has been presented. The X-ray flux evolution of SU UMa has been studied in much greater detail than has been possible with the brief snapshot observations that previous analysis has relied on.

All six outbursts showed consistent X-ray behaviour. At the start of outburst the X-rays were suddenly quenched to near zero, the X-ray count rate dropping by nearly a factor of 4. This was consistent with snapshot observations by Silber et al. (1994) who measured the *ROSAT* X-ray count rate to be a factor of 3 lower in outburst. A larger drop in X-rays was measured from *RXTE* data since the spectrum gets softer as well as fainter. Observation of VW Hyi, also a SU UMa type variable, showed the flux to drop by a factor of 6 (Wheatley et al., 1996).

Calculating times for the optical and X-ray fluxes to cross the mid-transition point indicated that the X-ray suppression lags behind the optical rise by about half a day. This is an indication of the time the heating wave in the disc takes to propagate to the boundary layer. SS Cygni has also been observed to have a delay between optical and X-ray outbursts, with the beginning of X-ray outburst lagging behind the optical by 0.9 – 1.4 days (Wheatley et al., 2003). The shorter delay for SU UMa suggests that the time for the heating wave to travel through the disc is shorter, perhaps due to its smaller accretion disc.

The lack of an X-ray flux increase at the start of any of the outbursts is puzzling since the boundary layer is only thought to become optically thick once the accretion rate has reached a critical value (Pringle & Savonije, 1979). In SS Cygni, the X-rays do increase before being suddenly suppressed (Wheatley et al., 2003). It may be that the quiescent accretion rate in SU UMa is already close to the critical rate. However, our estimated accretion rate in quiescence (4.2×10^{15} g s^{-1}) is below the expected critical value of 2×10^{16} g s^{-1}, although this does depend on the white dwarf mass and radius, the viscosity of the disc and temperature of the shocked gas (Pringle & Savonije, 1979). In SS Cygni the transition was seen at an accretion rate of 1×10^{16} g s^{-1} (Wheatley et al., 2003). Alternatively, the observations presented here might have missed the flux increase. The optical rise in SS Cygni was approximately 1.5 days with an associated duration of 12 hours for the rise in the hard X-rays. The optical rise in SU UMa was approximately 1 day but the average separation of points in the composite light curve of Figure 7.3 results in an upper limit of 2 hours to the duration of a peak that occurs at the same outburst phase and with the same duration in each case. An increase in flux was also not seen in VW Hyi (Wheatley et al., 1996), although these observations had a cadence of one observation a day.

The X-ray suppression occurred very rapidly and was not resolved in our composite light curve, with a cadence of 2 hours (Figure 7.4). This is similar to SS Cygni where the suppression occurred in less than 3 hours (Wheatley et al., 2003).

The X-ray recovery began while the optical band was in decline from outburst. This was earlier than seen in VW Hyi where the X-ray recovery occurred at the end of the optical outburst (Wheatley et al., 1996). Presumably this was due to a cooling front reaching the boundary layer before passing through the whole disc, perhaps suggesting that the cooling wave in SU UMa does not start at the outer edge of the disc.

The X-ray count rates measured for SU UMa tend to decrease during quiescence, dropping by 12 per cent over 8 days. This has also been seen in SS Cygni by McGowan et al. (2004), where the decrease was by 40 per cent over 31 days. It is interesting to note that in both cases the count rate drops by about 1.7 per cent day^{-1}, perhaps indicating similar timescales acting in the inner accretion discs. The decrease in X-ray flux is in direct conflict with the disc instability model which predicts increasing quiescent accretion rates (e.g., Lasota, 2001).

The X-ray spectrum of SU UMa in outburst was softer and fainter than during quiescence, in common with other dwarf novae (e.g., Baskill et al., 2005). The X-rays observed during quiescence arise from an optically thin region that is probably replaced by an unseen optically thick emitting region that most likely dominates during outburst. Spectral fitting of the data shows that a thermal plasma model with sub-solar abundances of 0.64 ± 0.01 and a 6.4 keV line describes the data well. The data are also consistent with the presence of a constant reflection continuum.

The luminosity during outburst, 7×10^{31} ergs s^{-1}, was similar to that calculated by Baskill et al. (2005) for SU UMa with *ASCA*. Other systems observed by *ASCA* in outburst include RU Peg (9.4×10^{31} ergs s^{-1}), a U Gem system. During quiescence SU UMa had an average luminosity of $2.6 \times 10^{32} (d/260pc)^2$ ergs s^{-1}, about as luminous as SS Cygni (3.6×10^{32} ergs s^{-1}) but more luminous than U Gem (2.8×10^{31} ergs s^{-1}). T Leo, a SU UMa system, was also calculated to be less luminous with a luminosity of 1.8×10^{31} ergs s^{-1}. The average luminosity during quiescence corresponds to a quiescent accretion rate of 4.2×10^{15} g s^{-1}. This was similar to the quiescent rate of 3×10^{15} found by Wheatley et al. (2003) and in Chapter 4 for SS Cygni and was two and a half orders of magnitude higher than predicted by the disc instability model, (e.g., Hameury et al., 2000).

Chapter 8

Discussion

8.1 Dwarf Novae in X-rays

The three dwarf novae SS Cygni, U Gem and SU UMa were presented in this thesis in far greater temporal resolution than ever before using pointed *RXTE*/*PCA* observations. Nearly all previous analysis of dwarf novae has been based upon a number of snapshot observations, with a short duration either during an outburst or quiescent period. A total of 562 pointed observations were presented with a combined exposure of 1.54 Ms. These observations covered a total of 19 outburst and 16 quiescent intervals allowing the X-ray flux evolution throughout outburst and quiescence to be studied in far greater detail than has been previously possible.

8.2 Temporal Evolution

8.2.1 The Outburst Cycle

All three systems have a very similar outburst shape in the optical band. The optical magnitude rises rapidly until reaching the respective maximum visual magnitude within ~ 1 day. The light curve remains at maximum for between $2 - 9$ days before starting its decline and returning to quiescence, as is typical of fast rise slow decline outbursts.

Although the behaviour in the optical band is similar there is a larger distinction in the hard X-ray band between the three systems. During outburst both SS Cygni and SU UMa present a clear picture of the X-ray nature of most dwarf novae: the hard X-rays in outburst were quenched below the quiescent flux level. This was observed in 16 of the 17 outbursts observed in comparison with the 16 quiescent intervals. Unlike in quiescence, the outburst count rates in both SS Cygni and SU UMa were very similar for all outbursts, the spectrum also became softer. In contradiction to this observed behaviour the hard X-rays in U Gem brightened during outburst. A comparison of X-ray luminosities shows that U Gem is unusually faint during quiescence, see Table 8.1 and 8.3. This may be due to the high inclination of U Gem, at 72 degrees (Unda-Sanzana et al., 2006). Studying non-magnetic cataclysmic variables observed by *ROSAT*, van Teeseling et al. (1996) found the emission measure to be anti-correlated with the system inclination. This suggests that the X-rays originate from the inner part of the accretion disc with a scale height not much greater than the disc thickness, where most of the X-ray flux in high inclination systems is absorbed by the accretion disc. The only other dwarf nova observed to brighten in outburst is GW Lib (Byckling et al., 2009). However, GW Lib has a low inclination (van Spaandonk et al., 2010) conflicting with this theory.

8.2.2 The X-ray Transition

As SS Cygni entered outburst the hard X-ray flux quickly increased before being rapidly quenched. At this time the boundary layer transitioned from optically thin to optically thick, the hard X-ray spectrum softens and is replaced by an intense extreme ultraviolet component as the hard X-rays are suppressed. An increase in flux at the start of the SU UMa outbursts was not observed. The observations presented may have missed the flux increase, however, the data places an upper limit of about 2 hours on its duration. This is substantially shorter than the peak seen in SS Cygni which was $\leq$ 12 hours. This suggests that a flux increase in SU UMa would be much more rapid than in SS Cygni, which is plausible since both the outburst recurrence times and orbital period are much shorter. Alternatively, the accretion rate may not need to significantly increase before the optically thin boundary layer becomes optically thick, as it does in SS Cygni.

A delay between the optical and X-ray outbursts was observed in both SS Cygni and SU UMa. The delay in SS Cygni was between 0.5 – 1.6 days, while SU UMa had a delay of $\sim$ 0.5 days. The delay is an indication of the time the heating wave in the disc takes to propagate to the

Table 8.1: Fluxes, luminosities and associated accretion rates during quiescence.

Time	Flux[a]		Luminosity[b]	Accretion rate[c]
[JD]	[2 – 20 keV]	[0.01 – 100 keV]		
		sscyg		
2450366.3	6.2	11.0	3.6	3.4
2450518	10.0	16.3	3.3	4.9
2450550	7.4	13.2	2.4	3.6
2450609	12.7	22.1	4.2	6.2
2451664	23.4	38.8	7.7	10.1
2453293	14.4	23.9	4.7	7.0
2453327	9.7	16.7	3.2	4.8
2453367	10.7	18.2	3.5	5.2
P50012	21.7	37.5	7.4	10.0
		ugem		
2450777	0.7	1.1	0.12	0.06
2453077	0.8	1.4	0.15	0.07
		suuma		
2451999	1.7	2.8	2.3	3.8
2452010	1.9	3.2	2.6	4.3
2452028	1.8	3.0	2.4	4.0
2452042	1.8	3.1	2.5	4.1
2452055	1.9	3.2	2.6	4.2
2452068	1.8	3.0	2.4	4.0
2452078	2.3	3.9	3.1	5.2

[a] $\times 10^{-11}$ ergs s^{-1} cm^{-2}

[b] $\times 10^{32}$ ergs s^{-1}

[c] $\times 10^{15}$ g s^{-1}

Table 8.2: Fluxes, luminosities and associated accretion rates during the boundary layer transition.

Time	Flux[a]		Luminosity[b]	Accretion rate[c]
[JD]	2 – 20 keV	0.01 – 100 keV		
		sscyg		
P10040	21.0	38.0	11.0	12.0
P20033	16.6	28.3	9.33	10.1
P40012	45.2	81.3	26.8	28.9
P50011	61.5	102.0	33.6	36.3
P90007	14.1	25.5	8.40	9.1
		ugem		
P80011	10.5	16.9	1.86	0.91

[a] $\times 10^{-11}$ ergs s^{-1} cm^{-2}

[b] $\times 10^{32}$ ergs s^{-1}

[c] $\times 10^{15}$ g s^{-1}

Table 8.3: Fluxes and luminosities during the hard X-ray quenching.

Time	Flux[a]		Luminosity[b]	Accretion rate[c]
[JD]	[2 – 20 keV]	[0.01 – 100 keV]		
		sscyg		
P50012	3.2	5.7	1.9	-
		ugem		
2450764	4.3	6.9	0.8	-
2453064	6.5	10.3	1.1	-
		suuma		
P60005	0.4	0.9	0.7	-

[a] $\times 10^{-11}$ ergs s^{-1} cm^{-2}

[b] $\times 10^{32}$ ergs s^{-1}

[c] $\times 10^{15}$ g s^{-1}

boundary layer. The consistent delays indicate that, in relation to the boundary layer, the heating waves in SS Cygni and SU UMa may originate at a similar location in the accretion disc.

A peak in the X-rays at the end of the outburst was observed in both SS Cygni and U Gem; as the system returned to quiescence the hard X-ray flux increased before declining back to the quiescent count rate. As with the start of the outburst, the count rate in SU UMa returned to quiescence without a peak. The boundary layer transitioned from optically thick to optically thin and the extreme ultraviolet spectrum was replaced by the quiescent hard X-ray spectrum. An increase in flux was also not seen in VW Hyi (Wheatley et al., 1996), although these observations had a cadence of one observation a day.

The peak of the recovery in both SS Cygni and U Gem occurred as the optical band reached quiescence. The start of the U Gem recovery occurred at the end of the optical outburst, while in SS Cygni the start of the hard X-ray recovery had a range of times. The recovery began from when the optical band was close to maximum to when the optical band had nearly reached quiescence. The X-ray recovery in SU UMa began when the optical band had declined approximately half way to quiescence. The X-ray flux returned to quiescence shortly after the optical band reached quiescence indicating that the inner disc is the last part of the accretion disc to return to quiescence. The start of the recovery occurring before the optical outburst reached quiescence indicates that the accretion rate in the boundary layer was already decreasing before the cooling front reached it. The cooling front then reached the boundary layer as the hard X-ray recovery reached the peak. The cooling wave then returned the inner disc to quiescence.

8.2.3 Quiescent Evolution

The disc instability model predicts increasing quiescent accretion rates, (e.g., Lasota, 2001). However, the X-ray flux measured for SU UMa tends to decrease during quiescence (Collins & Wheatley, 2010). SS Cygni has also shown evidence of being constant or decreasing in quiescence (McGowan et al., 2004). Observations of dwarf novae during quiescence often show a decrease of the optical and UV flux between outbursts also (Smak, 2000).

8.3 Spectral Evolution

The quiescent X-ray spectrum of all three dwarf novae was harder than during outburst. The X-rays observed during quiescence arise from an optically thin boundary layer that was probably replaced by an unseen optically thick emitting region that most likely dominates during outburst.

8.3.1 Spectral Modelling

All three dwarf novae were well described by a single temperature thermal plasma model. The spectra required the addition of a fixed 6.4 keV emission line and a significant improvement was also made fitting the spectra with sub-solar abundances. SS Cygni had an abundance of between $0.2 - 0.5$ solar with most spectra requiring metal abundances of 0.4 solar. U Gem required higher abundances of 0.9 solar, while SU UMa required abundances of 0.6 solar. The high signal to noise spectra were also able to constrain multi-temperature models, also requiring a fixed 6.4 keV emission line and sub-solar abundances.

8.3.2 Reflection

The continuum emission can be reflected from any optically thick surface, however the geometry of the boundary layer is complex. Reflection is expected from the optically thick boundary layer and inner disc if it extends down to the white dwarf surface, the X-ray emission will also illuminate the white dwarf surface. In addition, X-rays may be scattered into the line of sight by the photoionised accretion disc wind (Mauche & Raymond, 2000).

The need for a 6.4 keV line is highly suggestive of Fe Kα fluorescence emission due to illumination of cold gas, which is a strong indication that there is Compton scattering of X-rays. Line strengths are also consistent with that of a reflection origin (George & Fabian, 1991). Model fits significantly improved with the addition of a reflection component to the spectra with high signal to noise.

Models favour a high reflection during the hard X-ray suppression and low reflection during quiescence, consistent with Done & Osborne (1997). This provides evidence for a truncated disc in quiescence, although the timing of the reflection change, occurring at the same time as the spectrum change, is surprising. It would be expected that the reflection should, for example, decrease after the spectrum hardens at the end of the hard X-ray suppression, and not at the same time. At the end of the hard X-ray suppression the spectrum hardens indicating that the inner disc should have emptied. This suggests that the observed changes in the spectrum may be due to the boundary layer itself and not disc truncation.

Neither U Gem or SU UMa are bright enough to constrain a complex reflection model, but the line strengths in both systems are consistent with a reflection continuum. Comparison of the 6.4 keV line flux and the continuum flux (> 7 keV) capable of producing this line shows that that both SS Cygni and U Gem have an increased amount of reflection during outburst. During quiescence, approximately 4 per cent of the continuum flux are fluorescent photons for both SS Cygni and SU UMa. In outburst this increased to 10 per cent for SS Cygni and approximately 9 per cent for U Gem.

8.3.3 Luminosities and Accretion Rates

Quiescence

Hard X-rays are expected to be emitted in low accretion rate systems where $\dot{M} \leq 10^{16}$ g s^{-1} (Pringle & Savonije, 1979; Patterson & Raymond, 1985b). During quiescence SS Cygni has a large range of luminosities, using the parallax distance of 166.2 ± 12.7 pc (Harrison et al., 1999), calculated luminosities were $2.4 - 7.7 \times 10^{32}$ ergs s^{-1}. SU UMa was about as luminous as SS Cygni, its luminosities were much more constant but also over a shorter time span reducing the chance of observing long term variations. Luminosities, using the parallax distance of 260^{+190}_{-90} pc (Thorstensen, 2003), were calculated at 2.6×10^{32} ergs s^{-1}. U Gem is over $20 - 50$ times fainter than both SS Cygni and SU UMa. Using the parallax distance of 96.4 ± 4.6 pc (Harrison et al., 1999), the luminosity was calculated to be 1.2×10^{31} ergs s^{-1}. Both SS Cygni and SU UMa luminosities are comparable to Z Cam, during transition and outburst, and RU Peg, in outburst (Baskill et al., 2005). While T Leo was found to be as bright as U Gem during quiescence.

Using the relation $L = GM_{wd}\dot{M}/2R_{wd}$ and assuming the mass and radius of the white dwarf is $M_{wd} = 0.82 M_{\odot}$ and $R_{wd} = 5.9 \times 10^{8}$ cm (Bitner et al., 2007) for SS Cygni, and

$M_{wd} = 1.20 M_{\odot}$ and $R_{wd} = 3.9 \times 10^8$ cm (Echevarría et al., 2007) for U Gem. SU UMa does not have a measured mass, however, using an estimate of $M_{wd} = 0.75 M_{\odot}$ and $R_{wd} = 7.7 \times 10^8$ cm (Knigge, 2006) the respective accretion rates are calculated in Table 8.1 along with the quiescent fluxes and luminosities.

SS Cygni and SU UMa had comparable accretion rates. The accretion rate for SS Cygni was in the range $3.6 - 10.1 \times 10^{15}$ g s^{-1} and SU UMa had an average accretion rate of 4.2×10^{15} g s^{-1}. The accretion rate in U Gem was nearly two orders of magnitude lower at 6.0×10^{13} g s^{-1}. If the low luminosity in quiescence is a result of the high inclination in U Gem and a significant proportion of the X-ray flux is absorbed by the accretion disc (van Teeseling et al., 1996), then this accretion rate is an underestimate.

In quiescence, SS Cygni was observed to accrete at a higher rate than accretion rates the boundary layer has been calculated to become optically thick at (see Tables 8.1 and 8.2). This is surprising, analysis by Wheatley et al. (2003) suggested that once the accretion rate reaches a critical value the boundary layer becomes optically thick. However, the accretion rate during the peak, before outburst and during the recovery, always increases despite the preceding quiescent accretion rate. This indicates that the critical accretion rate is not fixed, in SS Cygni. The large range of accretion rates in quiescence may be due to changes in the viscosity of the quiescent accretion disc allowing a higher quiescent accretion rate (Shakura & Syunyaev, 1973; Papaloizou & Stanley, 1986).

Outburst

When the accretion rate reaches a critical value the boundary layer becomes optically thick, hard X-rays become thermalised and are emitted in the EUV and soft X-ray bands. (Pringle & Savonije, 1979; Wheatley et al., 2003).

During the outburst transition the flux of both SS Cygni and U Gem was observed to increase rapidly above the quiescent level, although this was only observed at the end of the outburst for U Gem. The flux in SU UMa is immediately quenched and recovers without an increase in the flux above the quiescent level. This indicates that in both SS Cygni and U Gem the accretion rate must rise substantially before the boundary layer becomes optically thick, while

SU UMa has a quiescent accretion rate close to that required for the boundary layer to become optically thick, alternatively transitions occurs much more rapidly. At the peak of the hard X-ray recovery, a good indicator of the outburst accretion rate, the luminosities were calculated to be in the range $8.4 - 33.6 \times 10^{32}$ ergs s^{-1} for SS Cygni and 1.9×10^{32} ergs s^{-1} for U Gem. These luminosities correspond to accretion rates of $0.9 - 3.6 \times 10^{16}$ g s^{-1} and 0.9×10^{15} g s^{-1} respectively. See Table 8.2 for the fluxes, luminosities and accretion rates during the peak transition. These accretion rates assume that the hard X-rays represent the full accretion rate. If there is an un-observed soft X-ray component then these accretion rates will be an underestimate.

During outburst U Gem gets brighter with a luminosity of $7.7 - 1.1 \times 10^{31}$ ergs s^{-1}. This is comparable with SU UMa in outburst with a luminosity of 7×10^{31} ergs s^{-1} indicating that U Gem is unusually faint during quiescence, rather than unusually bright in outburst. See Table 8.3 for all outburst fluxes, luminosities. The accretion rates are not presented in Table 8.3 since the hard X-rays become thermalised and emitted as soft X-rays resulting in a significantly underestimated accretion rate.

8.4 Future Work

One of the most important questions for future work is quiescence. Accounting for three quarters and half of the outburst cycle in SS Cygni and U Gem respectively it is not as well understood as outburst. Quiescence also poses a problem for the disc instability model. The quiescent accretion rate for SS Cygni and SU UMa are over two orders of magnitude higher than disc instability model predictions (e.g., Hameury et al., 2000), while the accretion rate in U Gem is consistent with the disc instability model. The quiescent X-ray flux also decreases in both SS Cygni and SU UMa contrary to model predictions. Observations of the quiescent evolution of U Gem are needed to determine if the quiescent X-ray flux also decreases.

Another important question for future work is the origin of the hard X-ray emission during outburst. Once this is understood the geometry of the inner accretion disc and boundary layer will be able to be probed more accurately.

The evolution of the three systems presented showed that they have a remarkable number of similarities as well as differences. This study needs to be extended and good X-ray coverage is needed of more dwarf novae to build up an understanding of the population.

Bibliography

Anders E., Grevesse N., 1989, Geochim. Cosmochim. Acta, 53, 197

Arnaud K. A., 1996, in Jacoby G. H., Barnes J., eds, ASP Conf. Ser. 101: Astronomical Data Analysis Softwae and Systems V XSPEC: The First Ten Years. pp 17–+

Aschenbach B., 1991, in Klare G., ed., Reviews in Modern Astronomy Vol. 4 of Reviews in Modern Astronomy, First Results from the X-Ray Astronomy Mission ROSAT.. pp 173–187

Balbus S. A., Hawley J. F., 1991, ApJ, 376, 214

Baskill D. S., Wheatley P. J., Osborne J. P., 2005, MNRAS, 357, 626

Benlloch S., Rothschild R. E., Wilms J., Reynolds C. S., Heindl W. A., Staubert R., 2001, A&A, 371, 858

Bevington P. R., Robinson D. K., 1992, Data reduction and error analysis for the physical sciences. New York: McGraw-Hill, —c1992, 2nd ed.

Bitner M. A., Robinson E. L., Behr B. B., 2007, ApJ, 662, 564

Blackburn J. K., 1995, in Shaw R. A., Payne H. E., Hayes J. J. E., eds, Astronomical Data Analysis Software and Systems IV Vol. 77 of Astronomical Society of the Pacific Conference Series, FTOOLS: A FITS Data Processing and Analysis Software Package. pp 367–+

Bowyer S., 1994, Science, 263, 55

Bradt H., 1982, Advances in Space Research, 2, 315

Bradt H. V., Rothschild R. E., Swank J. H., 1993, AASPP, 97, 355

Bradt H. V., Swank J. H., Rothschild R. E., 1990, Advances in Space Research, 10, 297

Buat-Ménard V., Hameury J.-M., Lasota J.-P., 2001a, A&A, 366, 612

Buat-Ménard V., Hameury J.-M., Lasota J.-P., 2001b, A&A, 369, 925

Byckling K., Osborne J. P., Wheatley P. J., Wynn G. A., Beardmore A., Braito V., Mukai K., West R. G., 2009, MNRAS, 399, 1576

Cannizzo J. K., 1993, The Limit Cycle Instability in Dwarf Nova Accretion Disks. Accretion Disks in Compact Stellar Systems, pp 6–+

Cannizzo J. K., Mattei J. A., 1992, ApJ, 401, 642

Ceraski W., 1908, Astronomische Nachrichten, 177, 173

Chandrasekhar S., 1960, Proceedings of the National Academy of Science, 46, 253

Chandrasekhar S., 1961, Hydrodynamic and hydromagnetic stability

Charles P. A., 2002, The Observatory, 122, 77

Coburn W., Heindl W. A., Gruber D. E., Rothschild R. E., Staubert R., Wilms J., Kreykenbohm I., 2001, ApJ, 552, 738

Coburn W., Heindl W. A., Rothschild R. E., Gruber D. E., Kreykenbohm I., Wilms J., Kretschmar P., Staubert R., 2002, ApJ, 580, 394

Coburn W., Heindl W. A., Wilms J., Gruber D. E., Staubert R., Rothschild R. E., Postnov K. A., Shakura N., Risse P., Kreykenbohm I., Pelling M. R., 2000, ApJ, 543, 351

Collins D. J., Wheatley P. J., 2010, MNRAS, 402, 1816

Cordova F. A., Mason K. O., 1980, Nature, 287, 25

Cordova F. A., Mason K. O., 1984, MNRAS, 206, 879

Done C., Osborne J. P., 1997, MNRAS, 288, 649

Dove J. B., Wilms J., Nowak M. A., Vaughan B. A., Begelman M. C., 1998, MNRAS, 298, 729

Echevarría J., de la Fuente E., Costero R., 2007, AJ, 134, 262

Eggleton P. P., 1983, MNRAS, 204, 449

Eracleous M., Halpern J., Patterson J., 1991, ApJ, 382, 290

Fabian A. C., Barcons X., 1992, ARA&A, 30, 429

Frank J., King A. R., Lasota J.-P., 1987, A&A, 178, 137

Fuller W. A., 1976, Introduction to statistical time series / Wayne A. Fuller. Wiley, New York :

Gammie C. F., Menou K., 1998, ApJ, 492, L75+

George I. M., Fabian A. C., 1991, MNRAS, 249, 352

Giacconi R., Gursky H., Waters J. R., 1964, Nature, 204, 981

Giacconi R., Kellogg E., Gorenstein P., Gursky H., Tananbaum H., 1971, ApJ, 165, L27+

Giles A. B., Jahoda K., Strohmayer T., 1998, Advances in Space Research, 22, 965

Glasser C. A., Odell C. E., 1994, IEEE TRANSACTIONS ON NUCLEAR SCIENCE, 41

Gruber D. E., Heindl W. A., Rothschild R. E., Coburn W., Staubert R., Kreykenbohm I., Wilms J., 2001, ApJ, 562, 499

Güver T., Uluyazı C., Özkan M. T., Göğüş E., 2006, MNRAS, 372, 450

Hōshi R., 1979, Progress of Theoretical Physics, 61, 1307

Hameury J.-M., Lasota J.-P., Dubus G., 1999, MNRAS, 303, 39

Hameury J.-M., Lasota J.-P., Warner B., 2000, A&A, 353, 244

Hanke M., Wilms J., Nowak M. A., Pottschmidt K., Schulz N. S., Lee J. C., 2009, ApJ, 690, 330

Harrison T. E., McNamara B. J., Szkody P., McArthur B. E., Benedict G. F., Klemola A. R., Gilliland R. L., 1999, ApJ, 515, L93

Hartmann H. W., Wheatley P. J., Heise J., Mattei J. A., Verbunt F., 1999, A&A, 349, 588

Hayashida K., Inoue H., Koyama K., Awaki H., Takano S., 1989, PASJ, 41, 373

Heindl W. A., Coburn W., Gruber D. E., Pelling M. R., Rothschild R. E., Wilms J., Pottschmidt K., Staubert R., 1999, ApJ, 521, L49

Heindl W. A., Coburn W., Gruber D. E., Rothschild R. E., Kreykenbohm I., Wilms J., Staubert R., 2001, ApJ, 563, L35

Heise J., Mewe R., Brinkman A. C., Gronenschild E. H. B. M., den Boggende A. J. F., Schrijver J., Parsignault D. R., Grindlay J. E., 1978, A&AP, 63, L1

Hellier C., 2001, Cataclysmic Variable Stars. Cataclysmic Variable Stars, Springer, 2001

Hind J. R., Hansen P. A., 1855, Astronomische Nachrichten, 39, 131

Hjellming M. S., Webbnik R. F., 1987, ApJ, 318, 794

Howell S. B., Nelson L. A., Rappaport S., 2001, ApJ, 550, 897

Iben I. J., Livio M., 1993, PASP, 105, 1373

Iben I. J., Tutukov A. V., 1993, ApJ, 418, 343

Inoue H., 2001, Progress of Theoretical Physics Supplement, 143, 99

Ishida M., Okada S., Hayashi T., Nakamura R., Terada Y., Mukai K., Hamaguchi K., 2009, PASJ, 61, 77

Ivanova N., Taam R. E., 2004, ApJ, 601, 1058

Jahoda K., Markwardt C. B., Radeva Y., Rots A. H., Stark M. J., Swank J. H., Strohmayer T. E., Zhang W., 2006, ApJS, 163, 401

Jahoda K., Swank J. H., Giles A. B., Stark M. J., Strohmayer T., Zhang W., Morgan E. H., 1996, in Siegmund O. H., Gummin M. A., eds, Proc. SPIE Vol. 2808, p. 59-70, EUV, X-Ray, and Gamma-Ray Instrumentation for Astronomy VII, Oswald H. Siegmund; Mark A. Gummin; Eds. Vol. 2808 of Presented at the Society of Photo-Optical Instrumentation Engineers (SPIE) Conference, In-orbit performance and calibration of the Rossi X-ray Timing Explorer (RXTE) Proportional Counter Array (PCA). pp 59–70

King A. R., 1988, QJRAS, 29, 1

King A. R., Shaviv G., 1984, Nature, 308, 519

Knigge C., 2006, MNRAS, 373, 484

Kolb U., Stehle R., 1996, MNRAS, 282, 1454

Koyama K., 1988, Comments on Astrophysics, 12, 287

Kraft R. P., 1962, ApJ, 135, 408

Kraft R. P., 1964, ApJ, 139, 457

Kraft R. P., Mathews J., Greenstein J. L., 1962, ApJ, 136, 312

Kreykenbohm I., Coburn W., Wilms J., Kretschmar P., Staubert R., Heindl W. A., Rothschild R. E., 2002, A&A, 395, 129

Kreykenbohm I., Wilms J., Coburn W., Kuster M., Rothschild R. E., Heindl W. A., Kretschmar P., Staubert R., 2004, A&A, 427, 975

Kuster M., Wilms J., Staubert R., Heindl W. A., Rothschild R. E., Shakura N. I., Postnov K. A., 2005, A&A, 443, 753

Lampton M., Margon B., Bowyer S., 1976, ApJ, 208, 177

Lasota J.-P., 2001, New Astronomy Review, 45, 449

Levine A. M., Bradt H., Cui W., Jernigan J. G., Morgan E. H., Remillard R., Shirey R. E., Smith D. A., 1996, ApJ, 469, L33+

Liedahl D. A., Osterheld A. L., Goldstein W. H., 1995, ApJ, 438, L115

Littlefair S. P., Dhillon V. S., Marsh T. R., Gänsicke B. T., 2006, MNRAS, 371, 1435

Littlefair S. P., Dhillon V. S., Marsh T. R., Gänsicke B. T., Southworth J., Watson C. A., 2006, Science, 314, 1578

Livio M., Pringle J. E., 1992, MNRAS, 259, 23P

Lomb N. R., 1976, Ap&SS, 39, 447

Long K. S., Mauche C. W., Raymond J. C., Szkody P., Mattei J. A., 1996, ApJ, 469, 841

Lubow S. H., Shu F. H., 1975, ApJ, 198, 383

Magdziarz P., Zdziarski A. A., 1995, MNRAS, 273, 837

Markoff S., Nowak M. A., Wilms J., 2005, ApJ, 635, 1203

Marsh T. R., Horne K., Schlegel E. M., Honeycutt R. K., Kaitchuck R. H., 1990, ApJ, 364, 637

Marshall H. L., 2000, New Astronomy Review, 44, 555

Mason K. O., Cordova F. A., 1982, Advances in Space Research, 2, 109

Mason K. O., Cordova F. A., Watson M. G., King A. R., 1988, MNRAS, 232, 779

Mattei J. A., Mauche C., Wheatley P. J., 2000, Journal of the American Association of Variable Star Observers (JAAVSO), 28, 160

Mauche C. W., Mattei J. A., Bateson F. M., 2001, in P. Podsiadlowski, S. Rappaport, A. R. King, F. D'Antona, & L. Burderi ed., Evolution of Binary and Multiple Star Systems Vol. 229 of Astronomical Society of the Pacific Conference Series, Optical and EUV Light Curves of Dwarf Nova Outbursts. pp 367–+

Mauche C. W., Raymond J. C., 2000, ApJ, 541, 924

Mauche C. W., Wheatley P. J., Long K. S., Raymond J. C., Szkody P., 2005, in Hameury J.-M., Lasota J.-P., eds, The Astrophysics of Cataclysmic Variables and Related Objects Vol. 330 of Astronomical Society of the Pacific Conference Series, Chandra HETG Spectra of SS Cyg and U Gem in Quiescence and Outburst. pp 355–+

McBride V. A., Wilms J., Coe M. J., Kreykenbohm I., Rothschild R. E., Coburn W., Galache J. L., Kretschmar P., Edge W. R. T., Staubert R., 2006, A&A, 451, 267

McBride V. A., Wilms J., Kreykenbohm I., Coe M. J., Rothschild R. E., Kretschmar P., Pottschmidt K., Fisher J., Hamson T., 2007, A&A, 470, 1065

McGowan K. E., Priedhorsky W. C., Trudolyubov S. P., 2004, ApJ, 601, 1100

Medvedev M. V., Menou K., 2002, ApJ, 565, L39

Menou K., 2000, ArXiv Astrophysics e-prints

Mewe R., Gronenschild E. H. B. M., van den Oord G. H. J., 1985, A&AP, 62, 197

Mewe R., Lemen J. R., van den Oord G. H. J., 1986, A&AP, 65, 511

Meyer F., Meyer-Hofmeister E., 1981, A&A, 104, L10+

Meyer F., Meyer-Hofmeister E., 1983, A&A, 121, 29

Meyer F., Meyer-Hofmeister E., 1994, A&A, 288, 175

Mitsuda K., Bautz M., Inoue H., Kelley R. L., Koyama 2007, PASJ, 59, 1

Miyamoto S., Kimura K., Kitamoto S., Dotani T., Ebisawa K., 1991, ApJ, 383, 784

Mukai K., Kinkhabwala A., Peterson J. R., Kahn S. M., Paerels F., 2003, ApJl, 586, L77

Mukai K., Wood J. H., Naylor T., Schlegel E. M., Swank J. H., 1997, ApJ, 475, 812

Narayan R., Popham R., 1993, Nature, 362, 820

Naylor T., Bath G. T., Charles P. A., Hassal B. J. M., Sonneborn G., van der Woerd H., van Paradijs J., 1988, MNRAS, 231, 237

Nowak M. A., Juett A., Homan J., Yao Y., Wilms J., Schulz N. S., Canizares C. R., 2008, ApJ, 689, 1199

Nowak M. A., Wilms J., Heindl W. A., Pottschmidt K., Dove J. B., Begelman M. C., 2001, MNRAS, 320, 316

Nowak M. A., Wilms J., Heinz S., Pooley G., Pottschmidt K., Corbel S., 2005, ApJ, 626, 1006

O'Donoghue D., Chen A., Marang F., Mittaz J. P. D., Winkler H., Warner B., 1991, MNRAS, 250, 363

Okada S., Nakamura R., Ishida M., 2008, ApJ, 680, 695

Oppenheimer B. D., Kenyon S. J., Mattei J. A., 1998, AJ, 115, 1175

Osaki Y., 1974, PASJ, 26, 429

Osaki Y., 1996, PASP, 108, 39

Paczyński B., 1971, ARA&A, 9, 183

Paczynski B., 1976, in Eggleton P., Mitton S., Whelan J., eds, Structure and Evolution of Close Binary Systems Vol. 73 of IAU Symposium, Common Envelope Binaries. pp 75–+

Paizis A., Nowak M. A., Wilms J., J-L. Courvoisier T., Ebisawa K., Rodriguez J., Ubertini P., 2005, A&A, 444, 357

Pandel D., Córdova F. A., Mason K. O., Priedhorsky W. C., 2005, ApJ, 626, 396

Papadakis I. E., Lawrence A., 1993, MNRAS, 261, 612

Papaloizou J. C. B., Stanley G. Q. G., 1986, MNRAS, 220, 593

Patterson J., Kemp J., Harvey D. A., Fried R. E., Rea R., Monard B., Cook L. M., Skillman D. R., Vanmunster T., Bolt G., Armstrong E., McCormick J., Krajci T., Jensen L., Gunn J., Butterworth N., Foote J., Bos M., Masi G., 2005, PASP, 117, 1204

Patterson J., Raymond J. C., 1985a, ApJ, 292, 550

Patterson J., Raymond J. C., 1985b, ApJ, 292, 535

Pickering E. C., Fleming W. P., 1896, ApJ, 4, 369

Ponman T. J., Belloni T., Duck S. R., Verbunt F., Watson M. G., Wheatley P. J., Pfeffermann E., 1995, MNRAS, 276, 495

Postnov K. A., Yungelson L. R., 2006, Living Reviews in Relativity, 9, 6

Pottschmidt K., Kreykenbohm I., Wilms J., Coburn W., Rothschild R. E., Kretschmar P., McBride V., Suchy S., Staubert R., 2005, ApJ, 634, L97

Pottschmidt K., Wilms J., Chernyakova M., Nowak M. A., Rodriguez J., Zdziarski A. A., Beckmann V., Kretschmar P., Gleissner T., Pooley G. G., Martínez-Núñez S., Courvoisier T. J.-L., Schönfelder V., 2003, A&A, 411, L383

Pottschmidt K., Wilms J., Nowak M. A., Pooley G. G., Gleissner T., Heindl W. A., Smith D. M., Remillard R., Staubert R., 2003, A&A, 407, 1039

Prat L., Rodriguez J., Cadolle Bel M., Kuulkers E., Hanke M., Tomsick J., Corbel S., Coriat M., Wilms J., Goldwurm A., 2009, A&A, 494, L21

Pratt G. W., Hassall B. J. M., Naylor T., Wood J. H., Patterson J., 1999, MNRAS, 309, 847

Press W. H., Rybicki G. B., 1989, ApJ, 338, 277

Pringle J. E., 1977, MNRAS, 178, 195

Pringle J. E., 1981, ARA&A, 19, 137

Pringle J. E., Bateson F. M., Hassall B. J. M., Heise J., van der Woerd H., Holberg J. B., Polidan R. S., van Amerongen S., van Paradijs J., Verbunt F., 1987, MNRAS, 225, 73

Pringle J. E., Savonije G. J., 1979, MNRAS, 187, 777

Pringle J. E., Wade R. A., 1985, Astronomy Express, 1, 159

Rana V. R., Singh K. P., 2003, Bulletin of the Astronomical Society of India, 31, 347

Rana V. R., Singh K. P., Schlegel E. M., Barrett P. E., 2006, ApJ, 642, 1042

Rappaport S., Cash W., Doxsey R., McClintock J., Moore G., 1974, ApJ, 187, L5+

Rappaport S., Joss P. C., Verbunt F., 1983, ApJ, 275, 713

Rappaport S., Verbunt F., Joss P. C., 1983, ApJ, 275, 713

Reig P., Coe M. J., 1998, MNRAS, 294, 118

Ricketts M. J., King A. R., Raine D. J., 1979, MNRAS, 186, 233

Rothschild R. E., Blanco P. R., Gruber D. E., Heindl W. A., MacDonald D. R., Marsden D. C., Pelling M. R., Wayne L. R., Hink P. L., 1998, ApJ, 496, 538

Rothschild R. E., Boldt E. A., Holt S. S., Serlemitsos P. J., Garmire G. P., Agrawal P. C., Riegler G. R., Bowyer S., Lampton M., 1979, Space Science Instrumentation, 4, 269

Rothschild R. E., Wilms J., Tomsick J., Staubert R., Benlloch S., Collmar W., Madejski G., Deluit S., Khandrika H., 2006, ApJ, 641, 801

Scargle J. D., 1982, ApJ, 263, 835

Schreiber M. R., Gänsicke B. T., 2001, A&A, 375, 937

Schreiber M. R., Gänsicke B. T., Hessman F. V., 2000, A&A, 358, 221

Schreiber M. R., Hessman F. V., 1998, MNRAS, 301, 626

Seward F. D., Charles P. A., 1995, Exploring the X-Ray Universe. Exploring the X-Ray Universe, by Frederick D. Seward and Philip A. Charles, pp. 414. ISBN 0521437121. Cambridge, UK: Cambridge University Press, November 1995.

Shakura N. I., Syunyaev R. A., 1973, A&A, 24, 337

Silber A., Vrtilek S. D., Raymond J. C., 1994, ApJ, 425, 829

Singh K. P., White N. E., Drake S. A., 1996, ApJ, 456, 766

Smak J., 1984a, Acta Astronomica, 34, 161

Smak J., 1984b, PASP, 96, 5

Smak J., 1999, Acta Astronomica, 49, 383

Smak J., 2000, New Astronomy Review, 44, 171

Spruit H. C., Ritter H., 1983, A&A, 124, 267

Stelzer B., Wilms J., Staubert R., Gruber D., Rothschild R., 1999, A&A, 342, 736

Suchy S., Pottschmidt K., Wilms J., Kreykenbohm I., Schönherr G., Kretschmar P., McBride V., Caballero I., Rothschild R. E., Grinberg V., 2008, ApJ, 675, 1487

Swank J. H., Boldt E. A., Holt S. S., Rothschild R. E., Serlemitsos P. J., 1978, ApJ, 226, L133

Szkody P., Long K. S., Sion E. M., Raymond J. C., 1996, ApJ, 469, 834

Szkody P., Mattei J. A., 1984, PASP, 96, 988

Szkody P., Nishikida K., Raymond J. C., Seth A., Hoard D. W., Long K. S., Sion E. M., 2002, ApJ, 574, 942

Taam R. E., Spruit H. C., 1989, ApJ, 345, 972

Thorstensen J. R., 2003, AJ, 126, 3017

Thorstensen J. R., Wade R. A., Oke J. B., 1986, ApJ, 309, 721

Truss M. R., Wynn G. A., Wheatley P. J., 2004, MNRAS, 347, 569

Tsunemi H., Kitamoto S., Okamura S., Roussel-Dupre D., 1989, ApJ, 337, L81

Tutukov A. V., Fedorova A. V., Yungelson L. R., 1982, Soviet Astronomy Letters, 8, 198

Tylenda R., 1981, Acta Astronomica, 31, 267

Unda-Sanzana E., Marsh T. R., Morales-Rueda L., 2006, MNRAS, 369, 805

Ungut A., Yule A. J., Taylor D. S., Chigier N. A., eds, 1978, The UCSD/MIT hard X-ray and low energy gamma-ray experiment for HEAO-1 - Design and early results

van der Woerd H., Heise J., 1987, MNRAS, 225, 141

van Spaandonk L., Steeghs D., Marsh T. R., Torres M. A. P., 2010, MNRAS, 401, 1857

van Teeseling A., Beuermann K., Verbunt F., 1996, A&A, 315, 467

van Teeseling A., Verbunt F., 1994, A&A, 292, 519

Verbunt F., Bunk W. H., Ritter H., Pfeffermann E., 1997, A&A, 327, 602

Verbunt F., Zwaan C., 1981, A&A, 100, L7

Vogt N., 1982, ApJ, 252, 653

Warner B., 1987, MNRAS, 227, 23

Warner B., 1995, Cataclysmic variable stars. Cambridge Astrophysics Series, Cambridge, New York: Cambridge University Press, —c1995

Watson M. G., 1995, Advances in Space Research, 16, 15

Watson M. G., King A. R., Heise J., 1985, Space Science Reviews, 40, 127

Wheatley P. J., Mauche C. W., 2005, in Hameury J.-M., Lasota J.-P., eds, The Astrophysics of Cataclysmic Variables and Related Objects Vol. 330 of Astronomical Society of the Pacific Conference Series, Chandra X-ray Observations of WZ Sge in Superoutburst. pp 257–+

Wheatley P. J., Mauche C. W., Mattei J. A., 2003, MNRAS, 345, 49

Wheatley P. J., Verbunt F., Belloni T., Watson M. G., Naylor T., Ishida M., Duck S. R., Pfeffermann E., 1996, A&A, 307, 137

White N. E., 1995, Advances in Space Research, 16, 29

Whitehurst R., 1988, MNRAS, 232, 35

Wilms J., Nowak M. A., Dove J. B., Fender R. P., di Matteo T., 1999, ApJ, 522, 460

Wilms J., Nowak M. A., Pottschmidt K., Pooley G. G., Fritz S., 2006, A&A, 447, 245

Wood J., Horne K., Berriman G., Wade R., O'Donoghue D., Warner B., 1986, MNRAS, 219, 629

Wood J. H., Horne K., Berriman G., Wade R. A., 1989, ApJ, 341, 974

Yoshida K., Inoue H., Osaki Y., 1992, PASJ, 44, 537

Zhang W., Morgan E. H., Jahoda K., Swank J. H., Strohmayer T. E., Jernigan G., Klein R. I., 1996, ApJ, 469, L29+